

MAGNETOM Flash

Issue Number 70 • 1/2018
ISMRM Edition

Not for distribution in the US

Page 02

Editorial Comment:
Diffusion MRI
past and future
Denis Le Bihan

Page 10

Clinical acceleration:
from the console
James Hancock

Page 60

Single-breathhold
CS 3D SPACE MRCP
Valérie Laurent, et al.

Page 73

Cost-effectiveness of
MRI for detection of
prostate cancer
Vikas Gulani, et al.

Page 84

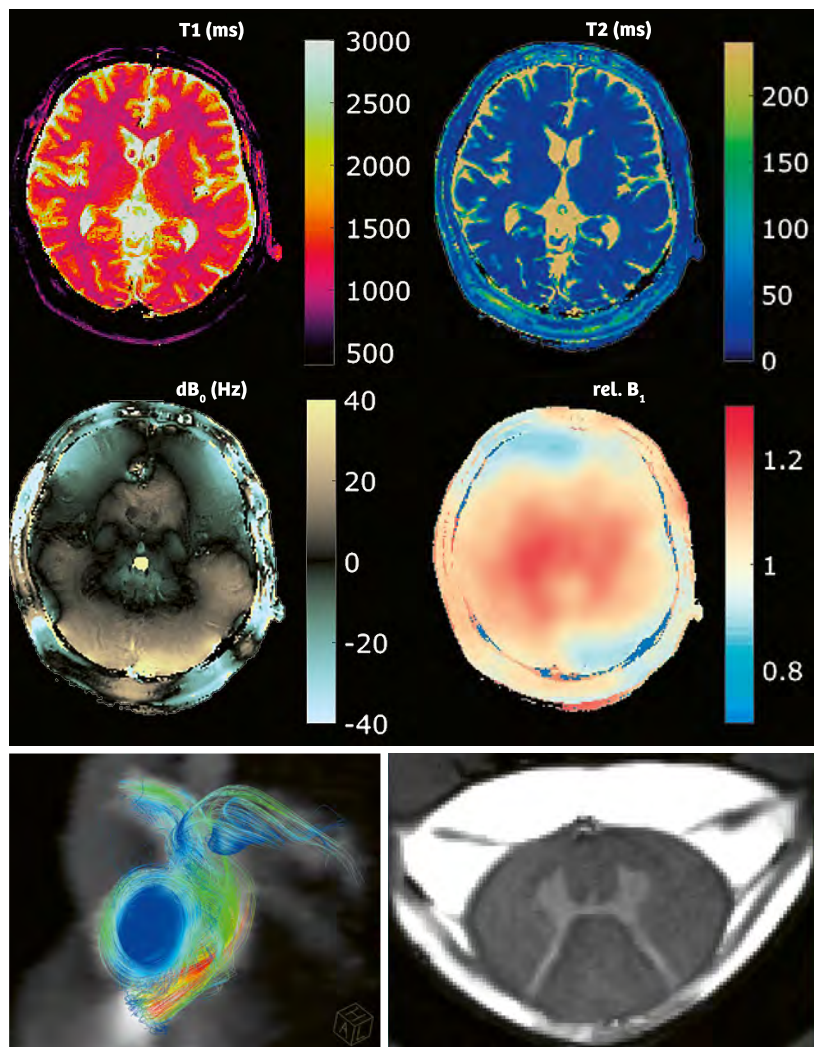
4D Flow in congenital
heart disease
Timothy C. Slesnick, et al.

Page 112

MRI of the cervical
spinal cord at 7T
Virginie Callot, et al.

Page 120

MRF² – MR Field
Fingerprinting
Mathias Nittka





Denis Le Bihan, M.D., Ph.D., has achieved international recognition for his outstanding contributions to the development of innovative MRI methods, in particular diffusion MRI. His focus has been on applying these methods to areas of scientific and clinical importance. He completed his training in medicine and physics in Paris before moving to the United States in 1987. He worked as a Research Section Chief in the Clinical Center at NIH, Bethesda, Maryland, USA, and as a Clinical Associate Professor of Radiology at Georgetown University, Washington, DC, USA. In 1994, he accepted a post at the Service Hospitalier Frédéric Joliot of the French Atomic Energy Commission, in Orsay, France, an internationally recognized MRI and PET facility. In 2000, he was appointed director of the Federative Research Institute of Functional Neuroimaging (Orsay/Paris, France). In 2007, Denis Le Bihan founded NeuroSpin, a new Institute of the CEA aimed at developing and using ultra high field magnetic resonance to understand the brain, from mouse to man. He also holds Visiting Professor positions at Kyoto University (Graduate School of Medicine), the Kyoto Prefectural Faculty of Medicine, and the National Institutes of Physical Sciences in Okazaki, Japan.

Denis Le Bihan belongs to several professional societies. Commensurate with his prolific research, he has authored or co-authored over 400 articles, book chapters, and review articles in the fields of MRI, imaging, neuroscience, and radiology. For his contributions, in 2001, he was awarded the Gold Medal of the International Society for Magnetic Resonance in Medicine. He is also the 2002 recipient of the Lounsbery Award from the National Academy of Sciences (USA) and French Academy of Sciences, and the corecipient of the Louis D. Award of the Institut de France in 2003. Le Bihan also received the prestigious Honda Prize (2012), the Louis Jeantet Foundation Award (2014), and gave the Lauterbur lecture at the 2014 ISMRM meeting. He is a full member of the French Academy of Sciences, the Academy of Technologies, the Academy of Pharmacy, and a corresponding member of the National Academy of Medicine.



Diffusion MRI past and future: an overview

Dear readers and colleagues,

I am very pleased that Siemens Healthineers has chosen to include diffusion and IVIM MRI among the themes being covered by this issue of MAGNETOM Flash and extremely honored to have been invited to write this editorial.

Diffusion MRI has been extraordinarily successful over the past 30 years (over 1,290,000 entries in Google Scholar for “diffusion MRI” as of April 2018). Its main clinical domain of application has been neurological disorders, particularly the management of acute stroke patients. However, it has also rapidly become a standard for the investigation of brain white matter, as Diffusion Tensor Imaging (DTI) can reveal abnormalities in white matter fiber structure in neurological or psychiatric disorders. DTI and its variants have also made it possible to obtain stunning 3D color maps of brain connectivity. Besides their obvious clinical and research potential, these maps now feature in anatomical textbooks on brain white matter (which has become very colorful thanks to diffusion MRI), and the subject of works of art. For the past few years, these brain connection maps, obtained from Siemens Healthineers MRI scanners, have even been printed on the card keys ISMRM participants receive when checking into their hotels during the annual meetings (I have a whole collection!). This is a real mark of recognition!

A virtual biopsy

Diffusion MRI was conceived in 1984 with an inspirational goal: To use a noninvasive technique to provide information on tissue at the microscopic level, while MR images remain at a macroscopic (millimetric) resolution, in other words, a kind of virtual, noninvasive biopsy. Beyond the invention of diffusion MRI, this goal has driven, and is still driving, my efforts, and those of many teams around the world, to develop and apply this powerful concept to biomedical research and clinical practice. Diffusion MRI involves investigating the diffusion of water molecules in tissue (the diffusion of other molecular moieties can also be studied using MR diffusion spectroscopy). One way of looking at the method is to think of the water molecules as spies probing the tissue for us on a microscopic scale, providing an imprint onto the diffusion MRI signal of what they have ‘seen’ during their Brownian motion driven displacements: fibers, macromolecules, cell membranes, all the obstacles that prevented them from diffusing freely. Of course, it is important to bear in mind that this microscopic information is averaged out within each voxel, although it is still possible to obtain information on the

degree of homogeneity or heterogeneity of the diffusion process within each voxel. This concept, inferring information on tissue microstructure in images with a macroscopic resolution has proved extremely useful in clinical practice, providing exquisite contrast not readily available with other imaging modalities, including MRI, without the need for contrast agents. For instance, brain cell swelling occurring right at the onset of ischemia (due to cytotoxic edema) is only revealed by diffusion MRI, well before any detectable changes in T1 or T2 may be cached. In the 1990s, for the first time, this discovery by Michael Moseley’s team allowed the objective diagnosis of stroke at the acute phase and the development of thrombolytic agents. This completely changed our views on the management of acute stroke patients, improving the clinical outcome of many patients worldwide.

However, diffusion MRI is also increasingly being used with great success outside the brain to investigate a broad variety of illnesses, especially cancer, whether breast, prostate, or liver, as reported in the article by Petralia et al. in this issue of MAGNETOM Flash. It is perhaps not so well known that my experience of diffusion MRI also started in the liver. Back in the early 1980s (I was then a medical resident in neurosurgery and radiology, and a Ph.D. student in nuclear and elementary particles physics), I was asked whether MRI could differentiate liver tumors from angiomas. At the time, MRI contrast media were not clinically available. I quickly came back with a vague idea that, perhaps, a molecular diffusion measurement would result in low values in solid tumors, due to molecular movement ‘restriction’, while diffusion would be slightly enhanced in flowing blood. Based on Stejskal and Tanner’s pioneering NMR work in the 1960’s, I thought that specific diffusion coding could be accomplished using magnetic gradient pulses, but there was a problem with integrating these pulses into those used in the MRI sequence for spatial encoding. This may seem trivial, but in fact, it was a major hurdle. Some colleagues remarked at that time that it was not even possible to obtain images of diffusion *in vivo* and that my first (I)SMRM presentation in 1985 was nothing more than a collection of artifacts. I had to gather all my courage to continue. The innovative element of my approach was that it proposed *localizing* the diffusion measurements, that is obtaining *maps* of the diffusion coefficients in tissue. This had never been done before, especially *in vivo*, with any technique. I was very excited and, in a matter of weeks “diffusion MRI”, as we know it, was born, implemented, and validated. In my first diffusion MRI papers (published in Radiology and the

journal of the French Academy of Sciences, *Comptes rendus*) I introduced the “b factor” to quantify the degree of diffusion weighting (as TE is for T2) from the gradient pulses magnitude and duration with the presence of cross-terms between diffusion and the multiple imaging gradient pulses (which were of course not taken into account by Stejskal and Tanner), the ADC concept, IVIM (IntraVoxel Incoherent Motion), and all the conceptual and technical ingredients that still ensure the success of diffusion MRI.

There were, indeed, many technical issues that still needed to be resolved, and the first trials conducted in the liver at 0.5T were very disappointing. The method never really worked, mainly because of huge motion artifacts due to respiration (we had to wait until 1999 when Professor Yamada and his team in Japan published a landmark paper proving that my idea of differentiating between angiomas and liver tumors was not misguided). First, the signal-to-noise ratio was very low. Second, gradient hardware rarely enabled us to reach strengths beyond 8 or 10 mT/m (at the price of very large eddy current artifacts) and the limit for the b values was around 100 or 200 mm/s². Third, there was no EPI, just conventional 2D FT spin-echo sequences. The acquisition times necessary for diffusion encoding were very long (close to 10 minutes per b value) and, as respiratory gating was not yet available either, motion artifacts caused by body movement were atrocious. So, I gave up, and quickly switched to the brain, which was my own area of expertise after all. I scanned my own brain and that of some of my colleagues before investigating patients. It worked beautifully and resulted in a great achievement: Diffusion MRI was established.

Strong gradient hardware makes all the difference

It took some time for diffusion MRI to come into clinical use, as it was without doubt a very innovative and “out of the box” concept for the time. Today, however, diffusion MRI has become a cornerstone of modern medical imaging. The method became clinically relevant in the 1990s when it was coupled to EPI (Echo-Planar Imaging), which reduced motion artifacts and acquisition times dramatically. EPI requires strong gradient hardware and in light of its potential for the management of acute stroke patients, MRI manufacturers built on diffusion EPI to provide robust and efficient technical solutions for the healthcare sector. Undeniably, the field of diffusion MRI has evolved considerably over the last 30 years, benefiting especially from improvements in gradient hardware, which is without doubt the most important component of efficient encoding of microscopic diffusion movements. Siemens Healthineers teams must be highly commended

for their outstanding Connectome Gradient systems. This type of hardware enables gradient strengths of 100 or even 300 mT/m and b values higher than 20 000 s/mm² are within reach. Back in the 1980s, I could not never have imagined that the b values would increase 100-fold in 30 years (sadly, the b value is not a stock on the market).

This race toward larger gradient strength is not at all anecdotal. First, technically, it allows shorter TEs to be used for any given b value. This, in turn, increases the signal-to-noise ratio, which is of particular interest for tissue with short T2, such as body tissue, especially when going to high field (as shown at 7T in the spinal cord by Massire et al. in this issue of MAGNETOM Flash). More importantly, however, it allows us to reach higher b values. But why is this important for clinical needs? Diffusion driven displacements of water molecules are encoded in the MRI signal through variations of the magnetic field in space caused by magnetic field gradient pulses. The overall effect of diffusion in the presence of gradient pulses is a signal attenuation and the MRI signal becomes ‘diffusion-weighted’. The signal attenuation is more pronounced when using large b values. As diffusion-weighted images also depend on other parameters, such as T1 and T2, we often calculate the ADC (Apparent Diffusion Coefficient) which depends solely on diffusion. The ADC is obtained from images acquired using only 2 different b values. When diffusion is free (no obstacles to water molecules), the ADC does not depend on the b values, so the choice of b values is just to provide the best ADC accuracy for an expected range of ADC values given the presence of noise. For instance, in the brain, the theoretically optimal pair of b values is 0 and 1000 s/mm², while in most body tissue 0 and 600 or 800 s/mm² would probably be the preferred values. Since this is what makes the diffusion MRI contrast so sensitive to tissue features), in most tissue, diffusion fortunately becomes non-Gaussian due to the many obstacles hindering water diffusion. As a result, the amount of diffusion-driven signal attenuation decreases when the b value increases. In other words, the ADC value decreases when high b values are used, whether in the brain or the body. In short, the higher the b values, the more sensitive the diffusion images are to tissue microstructure features. A consequence of non-Gaussian diffusion is that, in order to make meaningful comparisons across literature or across sites in the case of multicenter studies, it is important to report which b values have been used to acquire data.

Tractography also greatly benefits from high b values. In some tissue, notably brain white matter, but also heart/muscle fibers, diffusion is ‘anisotropic’, strongly depending on the direction of the gradient pulses used to provide diffusion sensitivity. Proper handling of anisotropic

diffusion requires the diffusion tensor imaging (DTI) method which we introduced with Peter Basser in the early 1990s. In conjunction with algorithms connecting voxels based on their individual diffusion features, DTI and its variants have served as the basis for brain white matter tractography since it was introduced. Switching to high b values decreases the contribution of non-axonal water diffusion to the diffusion MRI signal, allowing higher specificity and resolution in fiber delineation.

In fact, it is important to report not only the b values, but also the precise timing of the gradient pulses (which determines the 'diffusion time') used for diffusion encoding, as different time profiles could lead to different diffusion effects even with the same b value. This is due to the fact that there is a higher chance of water molecules interacting with tissue microscopic features when long rather than short diffusion times are used. Thus, comparing ADC values obtained with the same b values but using short and long diffusion times provides us with additional information on the tissue microstructure. In the brain, the NODDI and CHARMED models, for instance, exploit this time dependence to differentiate cellular components (cell body, dendrites) or evaluate their size (the axonal diameter, for example). Short diffusion times require very powerful gradients to ensure they can reach sufficiently high b values. To do this, in practice, diffusion gradient pulses are made to oscillate rapidly and the Pulsed Gradient Spin-Echo sequence (PGSE) becomes an Oscillating Gradient Spin-Echo sequence¹ (OGSE). To date, access to OGSE has been the privilege of researchers working with preclinical MRI scanners equipped with extremely powerful gradient systems (reaching 1 or even 2 T/m). Now, with Siemens Healthineers advanced MAGNETOM Prisma MRI scanners, OGSE has become available to clinicians as well as to their patients. Comparing ADC values at short and long diffusion times could reveal differences between tissue in terms of cellularity and membrane permeability to water (linked to aquaporin receptors expression, for instance). This has huge potential in oncology for diagnosing and staging malignant lesions or monitoring treatment efficacy.

Beyond image acquisition: The expanding world of data processing and artificial intelligence

At the other end of the b value spectrum there is an offshoot of diffusion MRI which should not be overlooked: IVIM² (IntraVoxel Incoherent Motion) MRI. Flow of blood water in randomly oriented capillaries (at voxel level)

"Postprocessing is a very important step enabling us to fully exploit the benefits of the method and access the wealth of information it provides."

mimics a random walk (pseudodiffusion) which results in a pseudodiffusion effect when using diffusion MRI. The effect is seen at very low b values only because the pseudodiffusion coefficient, D^* , associated with blood flow, is higher than the water diffusion coefficient. True diffusion and pseudodiffusion can thus be separated using dedicated algorithms. The idea of using diffusion MRI to obtain images of perfusion has been regarded controversial, but also ground-breaking, and IVIM MRI is enjoying a spectacular renaissance in the assessment of tissue perfusion in clinical practice, especially in the field of cancer imaging (as reported in the article by Granata et al. in this issue of MAGNETOM Flash). A key feature of IVIM diffusion MRI is that it does not involve contrast agents. This means that it could serve as an interesting alternative to contrast-enhanced perfusion MRI in certain patients with contraindications for contrast agents, such as those with renal failure at risk of Nephrogenic Systemic Fibrosis (NSF) or those requiring multiple MRI examinations, since gadolinium might accumulate in brain tissue. It is important to keep in mind, though, that IVIM MRI is a somewhat challenging method because separating perfusion and diffusion requires high signal-to-noise ratios.

It is undeniable that, with the availability of versatile MRI hardware and sequences, important progress has been made in our understanding of the diffusion processes at play in tissue, resulting in increasingly sophisticated models. Diffusion is a genuine physical process that occurs naturally in tissue, as opposed to T1 or T2 which are only defined in the MRI context. Postprocessing is, thus, a very important step enabling us to fully exploit the benefits of the method and access the wealth of information it

¹ Some of the concepts and information presented in this paper are based on research and are not commercially available.

² WIP, the product is currently under development and is not for sale in the US and in other countries. Its future availability cannot be ensured.

“This information is likely to prove be extremely useful when it comes to providing our patients with individual or personalized diagnostic strategies in the era of precision medicine.”

provides; information that is not easily visible on raw diffusion-weighted images, or even the ‘simple’ ADC. During the postprocessing phase, signals from images are combined using algorithms and evaluated using mathematical and physical diffusion models. These models, such as the popular Kurtosis model, are designed to handle non-Gaussian diffusion. Finally, model outputs are transformed into a series of parametric maps, showing the means, but also heterogeneity, of parameters across tissue and organs. Once these diffusion related parameters have been estimated, it is also possible to generate a posteriori virtual diffusion-weighted images mimicking contrast, which can be obtained at any b value. Post-processing is obviously the cornerstone of tractography, providing 3D maps of brain connections from DTI images, but also information on axon fiber diameter or orientation coherence. Another important objective of postprocessing software is to ‘clean’ raw data, realigning images affected by organ motion, correcting geometric distortions induced by gradient pulses, or extracting meaningful signals from background noise. In summary, postprocessing is the key to fully exploiting the benefits of IVIM and diffusion MRI.

Model sophistication, however, should not be an obstacle to clinical application. Diffusion MRI must remain user-friendly and provide clinicians with the information they need to assess their patients’ illnesses. For instance, instead of analyzing several parameters separately, such as IVIM, ADC, or kurtosis, which are not easy to interpret, software could digest this overwhelming information and provide semi-automatic analysis of lesions (through indices or scores) including diagnosis or lesion stage. Final decisions, would, of course, be made by clinicians. This is where artificial intelligence comes in to play in the field of diffusion MRI. For instance, each parameter might have a given threshold to differentiate benign and malignant tissue. Those parameters could be combined to give a summary diagnostic score based on the number of parameters supporting malignancy. Score maps can be generated providing diagnosis, but also showing which areas of lesions are likely to be most malignant thus suggesting the best locations for biopsies. An alternative method, using the Bayesian approach, is to weight each parameter value with population-based

statistics to provide an overall probability for each tissue type (e.g., malignant versus benign or malignancy types). Another approach is to calculate a signature index from the ‘proximity’ or resemblance of the diffusion MRI signal profile of a examined tissue (information obtained using a set of limited key b values and/or diffusion times selected for their higher sensitivity to underlying tissue microstructure) to a database or library of ‘signature’ signal profiles. The profiles in the database are acquired from a reference cohort of patients with established malignant and benign tissue in a given organ, or even simulated using complex models. With this ‘signature index’, highly accurate diagnosis or tissue staging can be readily and automatically obtained without having to calculate any model parameter. This signature can also be adjusted to reveal more specific features, for instance to provide an estimation of radiogenomic biomarkers, such as the presence or absence of hormone receptors Her2 and PgR in breast cancer lesions. This information is likely to prove be extremely useful when it comes to providing our patients with individual or personalized diagnostic strategies in the era of precision medicine.

A promising future

In yet another application, voxels exhibiting high IVIM pseudodiffusion from fast flow can also be flagged and then connected using algorithms, similar to those used for tractography, to generate a completely new kind of IVIM based angiogram without the need for contrast agents. It is important to acknowledge that there is a wealth of information concealed in the diffusion MRI signal, so it is really up to our imagination to devise new ideas, methods, or algorithms to make the most of this treasure trove. For instance, the extreme sensitivity of diffusion MRI to minute changes in cell size (e.g., swelling) makes diffusion MRI a completely new approach for functional MRI, as neural activation is associated with cell swelling, a much more direct connection than with BOLD fMRI which relies on the neurovascular coupling principle. Moreover, considering that diffusion MRI is inextricably linked to tissue microstructure, it should come as no surprise that diffusion MRI can also provide information on tissue elasticity. Indeed, diffusion features, especially through the synthetic indices

presented above, have been successfully quantitatively converted into tissue shear stiffness (in kPa) with extraordinary accuracy in the liver, and without the need for the vibration devices or phase sensitive MR sequences used with conventional MR Elastography (MRE). Research is currently being conducted to examine the possibility of using virtual MRE performed through diffusion MRI in staging liver fibrosis. Ironically, I now find myself involved in trials of diffusion MRI in the liver, the same place I was in more than 30 years ago, but this time with much greater success and using a totally unexpected twist in the method, far beyond my wildest dreams at the time (as far as diffusion MRI is concerned, at least). Moreover, the intravoxel phase dispersion resulting from propagating shear waves induced by mechanical vibrations can be emulated, and transformed into virtual elastograms through the IVIM effect, for any organ and for any combination of vibration frequency or amplitude. This is something that is not easy to achieve with conventional MRE hardware and has produced new and exciting contrast, as we have discovered, to our surprise, in the liver, the breast, and the brain.

From its conception, it took about 10 years for diffusion MRI to enter the routine clinical field in hospitals, a further 10 years from the first DTI papers to the start of generalized usage of tractography in the brain, and

perhaps another 20 years for IVIM to be used clinically to evaluate perfusion in the body. Diffusion MRI is clearly a mind opener. Molecular diffusion has a 'life' of its own and remains a powerful, genuinely multidisciplinary concept at our fingertips with which we can investigate cell physiology, tissue structure, and ultimately life. After all, all biological processes require molecules to interact, for DNA replication, protein transcription, protein and enzyme activity, cross-membrane transport, and much more. However, for molecules to interact, they must first meet, and diffusion is the universal process that nature and evolution have capitalized upon for this purpose. In a sense, diffusion rates set life's speed limit, just as the speed of light sets the limit in the physical world. Diffusion MRI has a bright future ahead and will keep Siemens Healthineers teams busy for years to come, integrating those very promising innovations into their MRI scanners for the benefit of healthcare professionals and patients alike.



Denis Le Bihan

The statements by Siemens' customers presented here are based on results that were achieved in the customer's unique setting. Since there is no 'typical' hospital and many variables exist (e.g., hospital size, case mix, level of IT adoption), there can be no guarantee that other customers will achieve the same results.

Editorial Board

We appreciate your comments.

Please contact us at magnetomworld.team@siemens-healthineers.com



Antje Hellwich
Editor-in-chief



Renate Jerecic, Ph.D.
Head of Collaborations



Wellesley Were
MR Business Development
Manager Australia and
New Zealand



Gary R. McNeal, MS (BME)
Advanced Application Specialist,
Cardiovascular MR Imaging
Hoffman Estates, IL, USA

Review Board

Daniel Fischer
Head of Outbound Marketing MR Applications

Christian Geppert, Ph.D.
Head of Cardiovascular Predevelopment

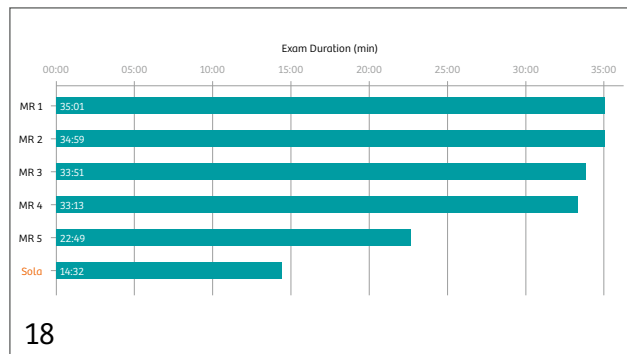
Berthold Kiefer, Ph.D.
Head of Oncological Applications

Heiko Meyer, Ph.D.
Head of Neuro Applications

Efrén Ojeda
MR Marketing Application Center

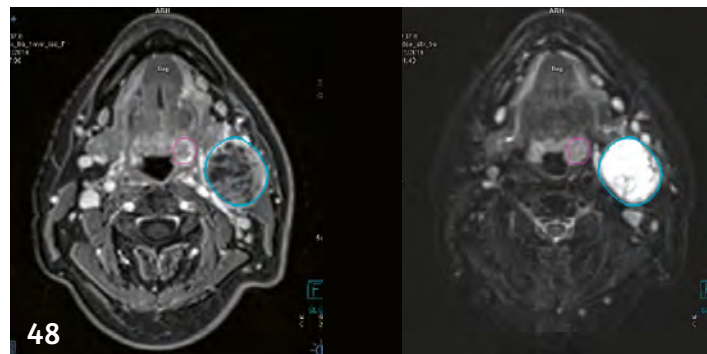
Gregor Thörmer, Ph.D.
Global Segment Manager Men's and Women's Health

Content

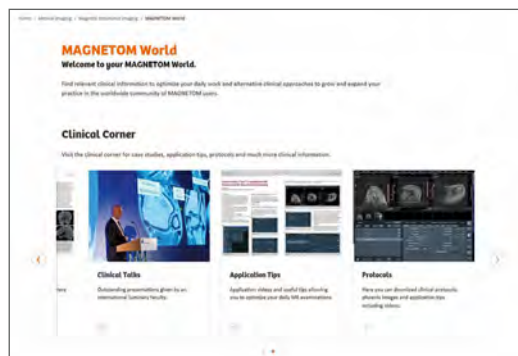


18

MAGNETOM Sola⁴ allows to shorten examination time by 50%



RT-simulation in a patient with head and neck cancer



Learn from the experience of other MAGNETOM users

The MAGNETOM World is the community of Siemens Healthineers MR users worldwide, providing you with relevant clinical information. Here you will find application tips and protocols to optimize your daily work. Lectures and presentations from experts in the field will allow you to be exposed to new ideas and alternative clinical approaches.

Put the advantages of the MAGNETOM World to work for you!

[siemens.com/magnetom-world](https://www.siemens.com/magnetom-world)

Editorial Comment

- 2 Diffusion MRI past and future
Denis Le Bihan, Saclay, France

Spotlight

- 10 Clinical acceleration: from the console
James Hancock, Benson Radiology, North Adelaide, Australia
- 18 MAGNETOM Sola: Adaptive and anticipatory, predictive and profitable
Ulrike Attenberger, et al., Heidelberg University, Mannheim, Germany

Oncological Imaging

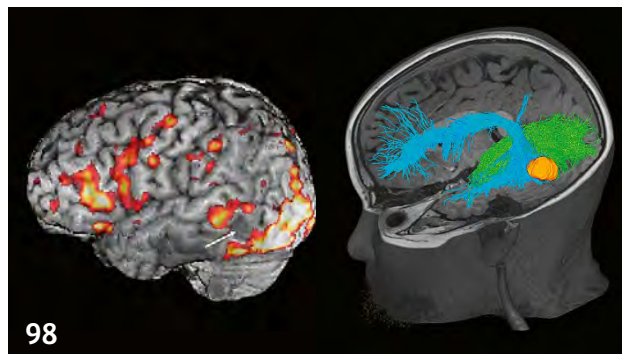
- 24 Technical advances in combined MR/PET: Bringing multiparametric hybrid imaging to a new level
Sergios Gatidis, et al., University of Tübingen, Germany
- 32 Whole-body MR diffusion imaging in oncology: origins, practice, and outlook
Giuseppe Petralia, et al., European Institute of Oncology, Milan, Italy
- 41 How-I-do-it: Whole-body MRI at 1.5T – step-by-step
Will McGuire, et al., Paul Strickland Scanner Centre, Mount Vernon Hospital, Northwood, Middlesex, UK
- 48 MR-simulation for radiotherapy treatment planning of head and neck cancer using 3T MAGNETOM Vida
Daniela Thorwarth, et al., University of Tübingen, Germany



60 Single-breath-hold Compressed Sensing 3D SPACE MRCP¹



76 Compressed Sensing Cardiac Cine¹



98 Advanced neuroimaging and pediatric epilepsy surgery

Abdominal Imaging

- 51 Dynamic contrast-enhanced magnetic resonance imaging, diffusion kurtosis imaging, and intravoxel incoherent motion diffusion-weighted imaging: MRI functional parameters in the assessment of pancreatic cancer
Roberta Fusco, et al., Istituto Nazionale Tumori IRCCS "Fondazione G. Pascale", Naples, Italy
- 60 A single-breath-hold magnetic resonance cholangiopancreatography using Compressed Sensing¹: A pilot study at 1.5T and 3T
Valérie Laurent, et al., Nancy University Hospital, France
- 67 How-I-do-it: Fast and efficient liver imaging with Primovist®/Eovist®
Gregor Thörmer, Siemens Healthineers, Erlangen, Germany

Men's Health

- 73 Cost-effectiveness of MR imaging-guided strategies for detection of prostate cancer in biopsy-naïve men
Vikas Gulani, Case Western Reserve University, Cleveland, OH, USA

Cardiovascular Imaging

- 76 Impact of Compressed Sensing Cardiac Cine¹ in a busy clinical practice
Jérôme Garot, Institut Cardiovasculaire Paris Sud, Massy, France
- 79 MyoMap quantification of myocardial toxicity following concurrent chemoradiotherapy for esophageal carcinoma
Gary Liney, et al., Liverpool Cancer Therapy Centre, Sydney, Australia

Pediatric Imaging²

- 84 4-dimensional phase contrast imaging in congenital heart disease: How we do it
Timothy C. Slesnick, et al., Emory University School of Medicine, Children's Healthcare of Atlanta, GA, USA
- 98 Advanced neuroimaging and pediatric epilepsy surgery
Michael Kean, et al., Royal Children's Hospital, Melbourne, VIC, Australia

Neurology

- 107 How-I-do-it: Dot for productivity
Kevin Dirlam, Halifax Health, Daytona Beach, FL, USA
- 112 MR imaging of the cervical spinal cord at 7T³: a multiparametric portfolio
Virginie Callot, et al., Aix-Marseille University, Marseille, France

Technology

- 120 Magnetic Resonance Field Fingerprinting (MRF²)
Mathias Nittka, Siemens Healthineers, Erlangen, Germany
- 124 Definitions of RF receiver channels and coil density
Mathias Blasche, Siemens Healthineers, Erlangen, Germany

Meet Siemens Healthineers

- 130 Introducing Hannah Hale, Magnet Engineer at Siemens Magnet Technology, Oxford, UK, and Kieran O'Brien, ultra-high-field research team, Bowen Hills, Australia

¹ WIP, the product is currently under development and is not for sale in the US and in other countries. Its future availability cannot be ensured.

² MR scanning has not been established as safe for imaging fetuses and infants less than two years of age. The responsible physician must evaluate the benefits of the MR examination compared to those of other imaging procedures.

³ MAGNETOM 7T and higher field strengths is ongoing research. All data shown are acquired using a non-commercial system under institutional review board permission. MAGNETOM 7T and higher field strengths are still under development and not commercially available yet. Its future availability cannot be ensured.

⁴ MAGNETOM Sola is not commercially available in all countries. Due to regulatory reasons the future availability cannot be guaranteed.

Clinical acceleration: from the console

James Hancock

Benson Radiology, North Adelaide, Australia

In Clinical MR the challenge to scan faster, in higher resolution and with consistent reproducibility always has been and always will be the challenge that drives technological development within the modality. Traditional thinking in MR dictates that speed comes at the cost of compromised image quality and is achieved with a decrease in spatial resolution or at risk of increased artifacts often at the expense of signal-to-noise ratio (SNR).

The implementation of technology such as Compressed Sensing (CS), CAIPIRINHA and Simultaneous Multi-Slice (SMS) is changing our thinking on just what is possible and providing maximum flexibility in imaging. Imaging is now being better tailored to the patient and their capabilities rather than the patient having to bend to the requirements of the imaging. This is a fundamental principle of Siemens BioMatrix technology.

With a big focus on body imaging applications Benson Radiology installed a 3T MAGNETOM Vida system into a private imaging department in the central business district of Adelaide, South Australia in July 2017. Without access to government-based medical rebates the quality, speed and reproducibility of examinations performed on the MAGNETOM Vida system are key to a successful business outcome. The MAGNETOM Vida offers technology like Compressed Sensing (CS), CAIPIRINHA and Simultaneous Multi-Slice (SMS) providing maximum flexibility in imaging.

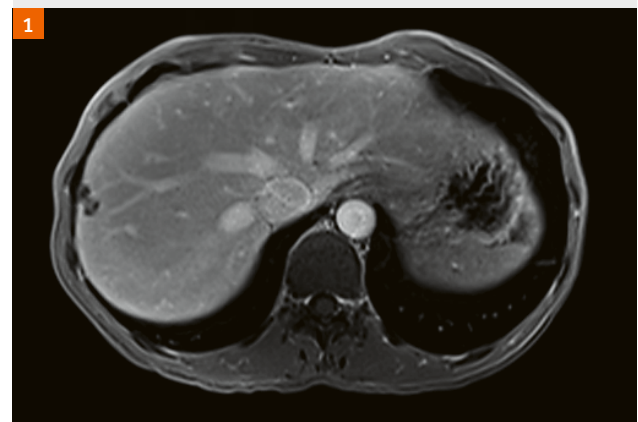
CAIPIRINHA

CAIPIRINHA (Controlled Aliasing in Parallel Imaging Results in Higher Acceleration) is a unique *k*-space acquisition scheme for parallel imaging techniques (PAT) that improves the SNR of a sequence by up to 18% compared to conventional acceleration of the same sequence with SENSE or GRAPPA. With a particular focus on body imaging, Benson Radiology is leveraging the combination of very high coil density with CAIPIRINHA

VIBE to fit an imaging solution to the capabilities of the patient. In a competent breath-holder this allows traditional breath-hold examinations to be acquired at higher spatial resolutions than ever before. Here we use the SNR gain from the parallel imaging technique combined with high coil density to improve fine edge sharpness and better delineate the conspicuity of pathology in the abdomen.

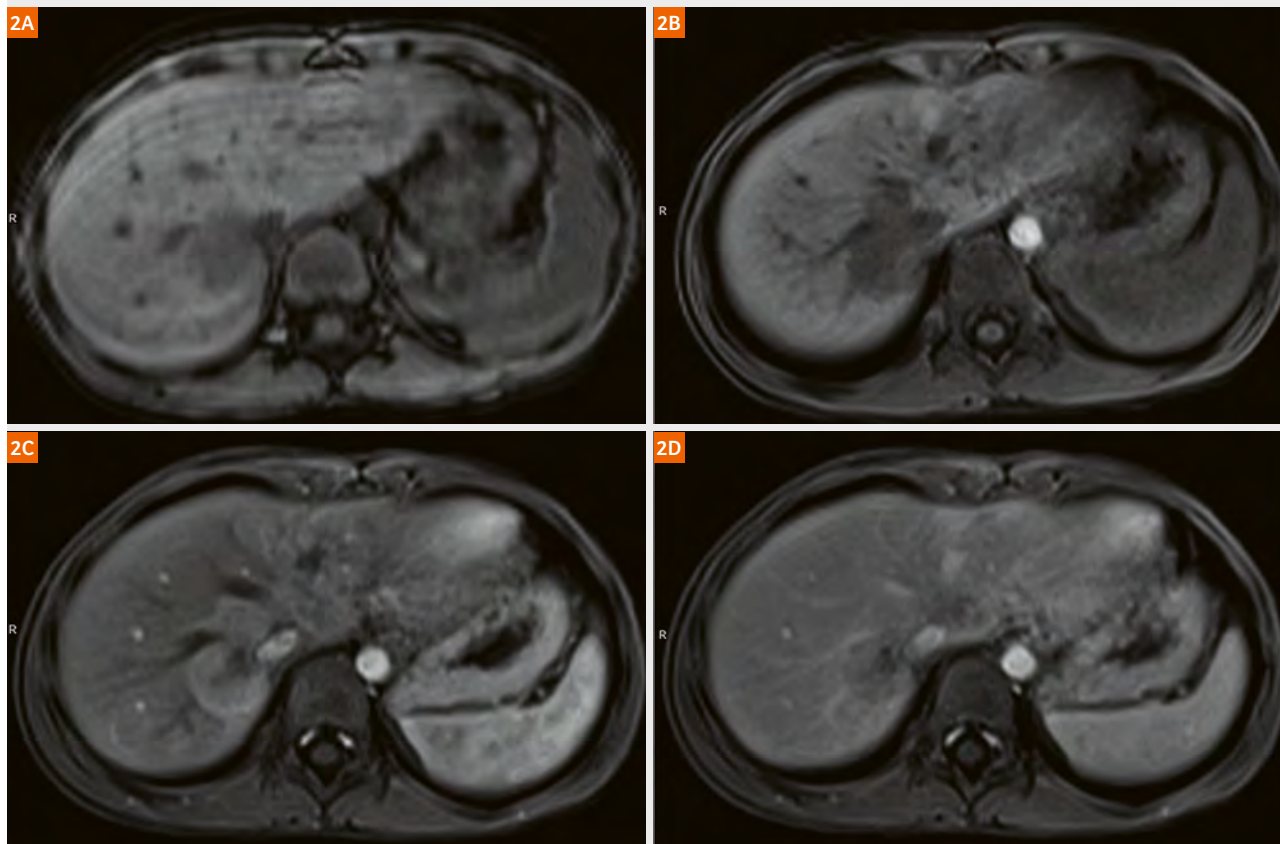
In the subset of patients where the ability to hold ones breath is compromised acceleration factors can be increased, thereby driving down scan time to achieve robust reproducible outcomes without the traditional sacrifice in spatial resolution or the risk of imaging artifacts traditionally associated with high PAT factors. This is achievable at both 1.5T and 3T field strengths.

Figure 1: T1 VIBE CAIPIRINHA post contrast



1.3 x 1.3 x 2 mm, 88 slices, complete liver coverage. Achieved using CAIPIRINHA total acceleration factor of 5. High resolution clearly defines liver lesion with features suggestive of hemangioma in this delayed dataset acquired 5 minutes following administration of gadolinium contrast. Scan time of 16 seconds.

Figure 2: T1 VIBE CAIPIRINHA post contrast at 1.5T



(2A) Traditional 2D T1 FLASH in-phase acquisition time of 11 seconds adversely affected by poor breath-hold in a 7-year-old male with a liver lesion. Repeat imaging using CAIPIRINHA (1.25 x 1.2 x 3 mm) with an acceleration factor of 4 reduced the breath-hold time to 7 seconds and allowed artifact free images to be obtained pre (2B), and post contrast (2C) arterial and (2D) venous.

Simultaneous Multi-Slice (SMS)

With a focus on body imaging, diffusion-weighted imaging (DWI) is always going to be a key aspect of the imaging service offered at Benson Radiology. DWI offers well-known benefits in abdominal and pelvic imaging.

Conventional EPI-DWI techniques can be acquired in multiple ways, including a free-breathing (FB) approach with the use of navigators or with multiple breath-hold techniques. Breath-hold techniques are constrained by the breath-hold capacity of the patient as well as the reproducibility of these breath-holds. This further constrains the usefulness of the technique as b-values become limited, as does the spatial resolution that can be achieved. If using a free breathing technique the acquisition time itself is the tradeoff. Here navigating the approach can become inefficient depending on the patients respiratory cycle. Multiaverage free breathing, while the current gold standard at our institution, is still

a lengthy approach. This is despite making use of parallel imaging techniques like GRAPPA for acquisition acceleration. The conventional EPI-DWI approach is inefficient as every imaging slice has to be excited individually, then the diffusion encoding gradients applied, and finally the image information acquired with EPI encoding. This process needs to be repeated multiple times, once for each imaging slice, until the entire volume of interest is covered.

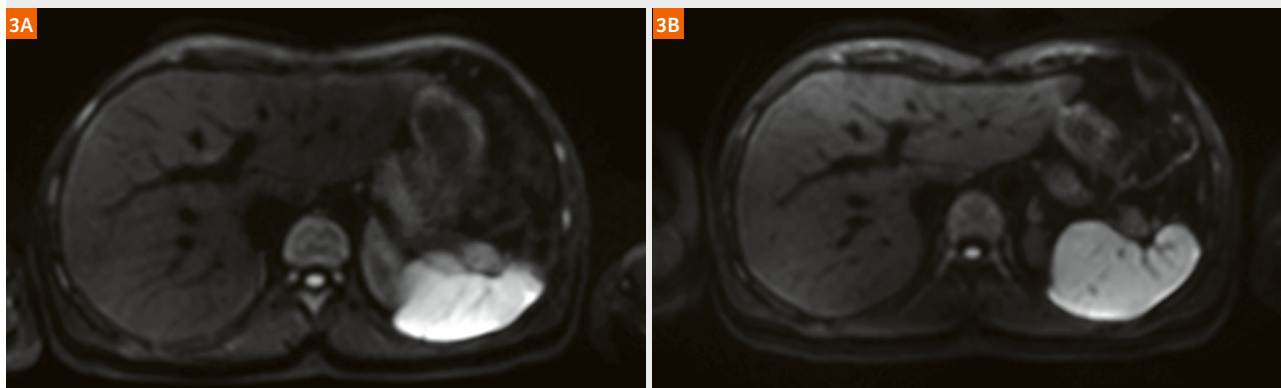
The inefficiencies mentioned above can be overcome with Simultaneous Multi-Slice acquisition combined with a free breathing approach, which we have implemented at our institution. Instead of successive excitation of slices, slices are excited simultaneously with a multiband pulse and blipped-CAIPIRINHA SMS-EPI ensures preservation of high SNR and low artifact levels. Since multiple slices are excited simultaneously, the overall TR for a desired spatial coverage or number of slices is reduced, leading to a scan time reduction by the same factor. The big advantage of

SMS over other acceleration techniques is that it does not suffer from the typical square-root of acceleration factor SNR penalty due to data under-sampling.

The inclusion of SMS or simultaneous multi-slice acquisitions has been very well received on our MAGNETOM Vida system given the amount of body imaging that the system is performing. For liver imaging we traditionally used a free breathing approach, combining a PAT factor of 3 and a very high number of averages to allow for signal rich b800 imaging across a broad spectrum of patient sizes. Our scan times with 3 b-values within the sequence were around 5:27. Switching to a SMS 2 PAT 2 approach we can achieve very comparable results in just 2:58 seconds (see Fig. 3).

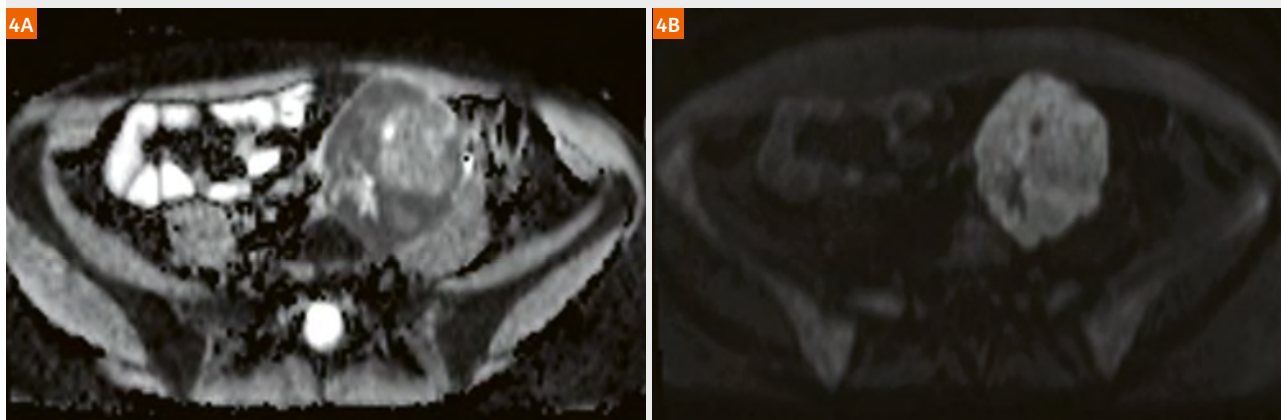
We now routinely use a PAT factor of 2 and an SMS factor of 2 for our abdominal diffusion imaging. As described above, we have used some of the speed improvements for image quality. We have traded off some of the acceleration for better SNR in the higher b800 images via a higher number of averages 7–10 whereby the spatial resolution has improved with an increase in the relative image matrix. Further we have gone from 36 slices acquired at 5 mm to 40 slices at 5 mm ensuring slightly more coverage within the standard protocol, meaning fewer adjustments at the console for technologists based on patient and liver size.

Figure 3: SMS DWI in the liver



(3A) PAT 3 b800 DWI and (3B) SMS 2 PAT 2 b800 DWI of the liver in the same patient at similar slice locations comparing image quality. (3A) was acquired on a 3T MAGNETOM Skyra system with a scan duration of 5:27, TR 6300 ms. (3B) was acquired on a 3T MAGNETOM Vida system with a scan duration of 2:58, TR 3000 ms.

Figure 4: SMS DWI of a pelvic mass



(4A) ADC map and (4B) SMS 2 PAT 2 b1000 DWI in the pelvis of a patient with a likely paraganglioma/pheochromocytoma. SMS DWI acquired with 3 b-values, b1000 with 12 averages. Scan time 3:18.

In prostate imaging we see a very broad spectrum of patient sizes. Traditionally, maintaining resolution and SNR from the center of larger patients has been challenging, especially at higher b-values. SMS combined with the Body 30 coil allows us to take the associated decrease in scan time and translate this to SNR in our higher b-values. This approach has allowed a 3 b-value DWI sequence to be acquired in 4:26 combining SMS 2 PAT 2 with the b1000 making use of 23 averages. Comparatively the traditional PAT 2, 3 b-value DWI approach was a 5:28 acquisition. Clinically this results in reproducible image quality in a wider variety of patients in a shorter scan time than the non SMS technique.

Compressed Sensing (CS)

With a focus on body imaging, cardiac and liver MRI are two of the most challenging examinations for producing consistent reproducible image quality in a given time period. Traditionally it has been difficult to overcome the challenges associated with patient limitations such as breath-holds and ECG gated acquisitions without sacrifice in other areas.

Both cardiac and liver MR are making use of compressed sensing (CS) techniques to overcome these challenges. Benson Radiology has embraced the use of CS accelerated cine imaging in cardiac MR for all indications. This has enabled real-time cine MRI for short axis (SA) and other stack imaging to be completed with a spatial

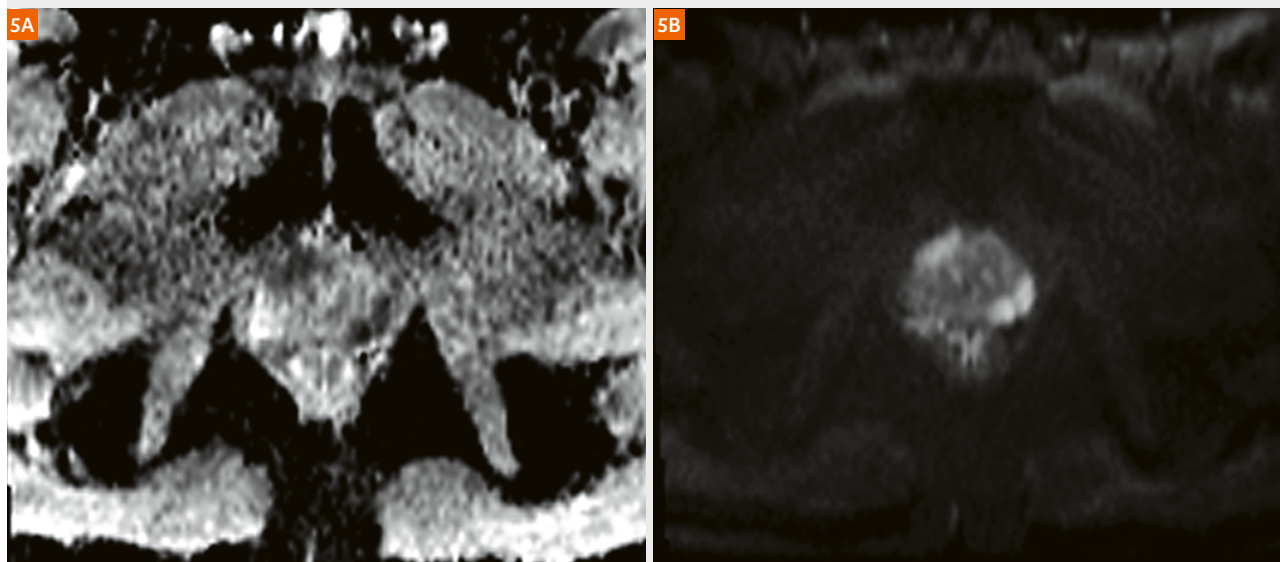
and temporal resolution that compares to segmented acquisitions. The traditional segmented approach to a 10–12 slice SA stack for the left ventricle can take as long as 6 minutes. Using CS, we are acquiring the stack in 25 seconds. If the patient is able to hold their breath this sequence can be split into 2 acquisitions or if the patient is respiratory challenged they can breathe quietly away for the duration of the acquisition. The benefits of this approach are three fold:

- Acquisition of high-resolution cardiac cine images – independent of patient's breathing capability and in the presence of arrhythmia.
- Capture across the whole cardiac cycle for precise quantification.
- Increase the number of patients eligible for cardiac MRI at our facility.

Prior to compressed sensing, when encountering arrhythmias, the technologist would tend to take three approaches to overcome the issue and all of these techniques have drawbacks.

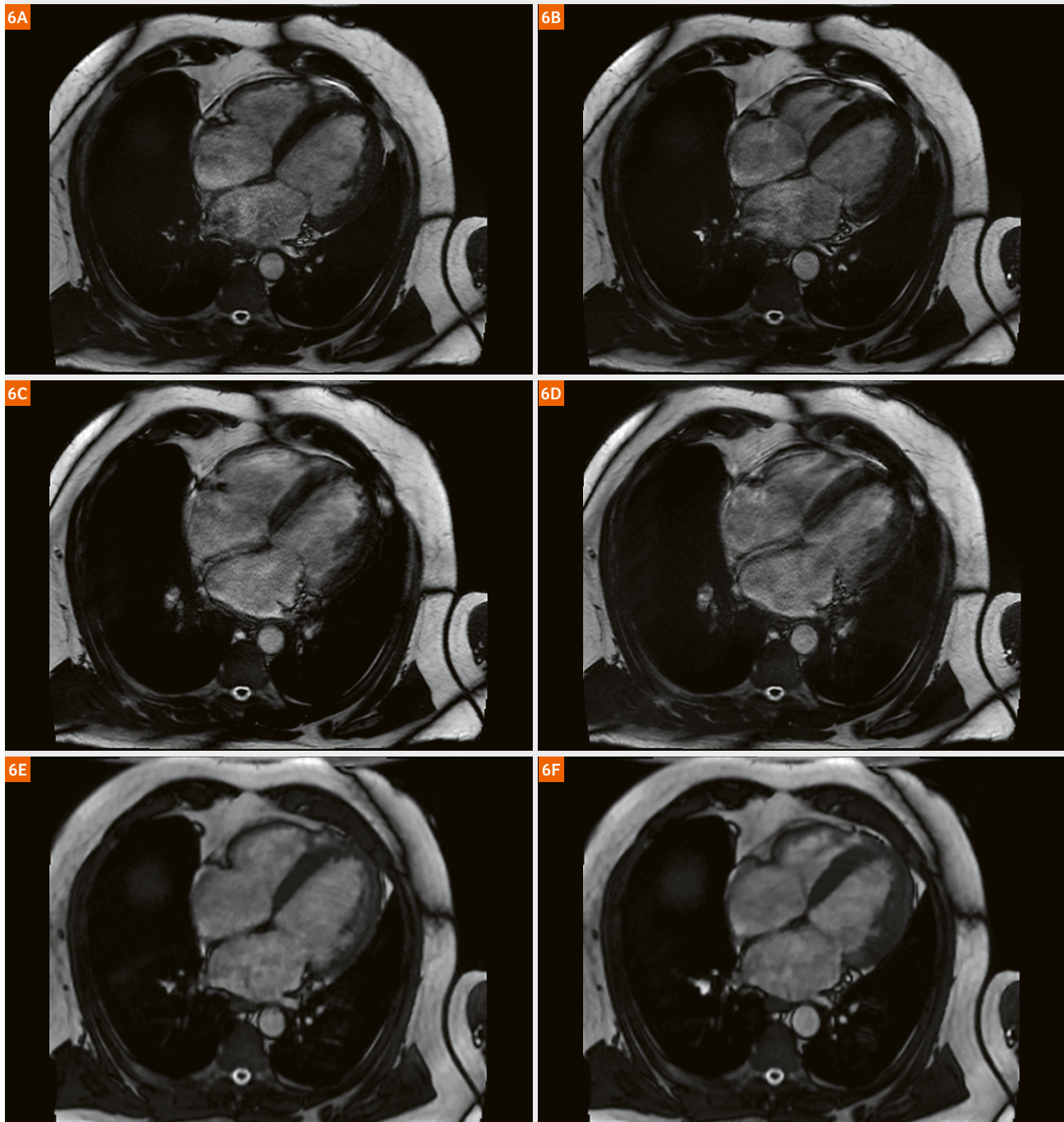
Prospectively gating offers an approach whereby the heart rhythm is studied and the technologist tries to pick an acquisition window which compensates for the arrhythmia by shortening the RR period. Although this can be effective, the downside is you sacrifice acquisition of the entire cardiac cycle, meaning your quantification will suffer.

Figure 5: SMS DWI prostate



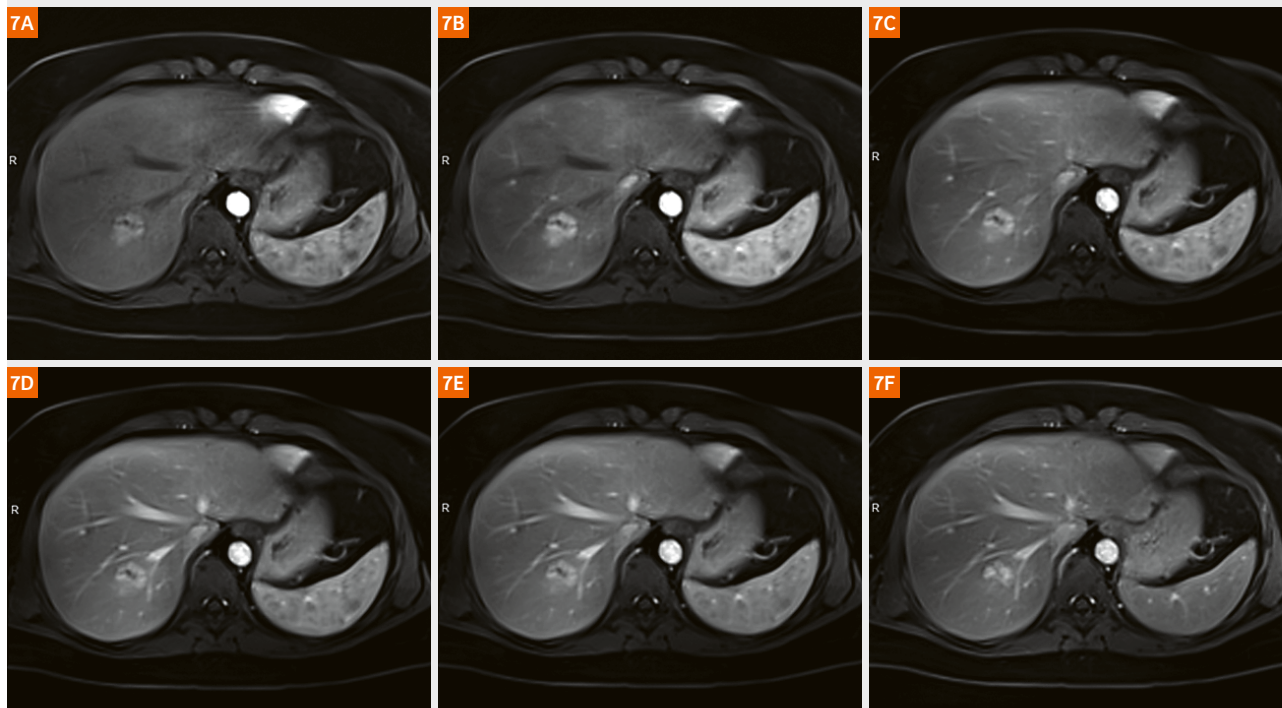
(5A) ADC map and (5B) b1000 for apical prostate cancer. Left posterolateral PZ and right anterolateral PZ both graded as PI-RADS 5. Images acquired using SMS 2 PAT 2. Increased number of averages (23) used in acquiring the b1000 produces noise free images and high clarity in the corresponding ADC map. Scan duration 4:26.

Figure 6: CS in the presence of cardiac arrhythmia



ED and ES 4-chamber true cine using multiple approaches in the same patient with chronic cardiac arrhythmia (**6A, B**) prospective approach demonstrates acceptable image quality however with underestimation of true ES. Acquisition time 11.32 seconds. (**6C, D**) Arrhythmia rejection technique demonstrates unacceptable image quality due to chronic arrhythmia lengthening breath-hold times to an unobtainable level for the patient. Acquisition time 35.41 seconds. (**6E, F**) Compressed Sensing technique demonstrates optimal image quality and samples entire cardiac cycle allowing better quantification of ES versus either of the previous techniques. Acquisition time sub 2 seconds.

Figure 7: CS GRASP VIBE liver



Compressed Sensing T1 Fatsat GRASP VIBE. 6 of 21 phases shown here. Technique is acquired in free breathing with a contrast timing independent acquisition running over approximately 5 minutes. (7A–C) are very early, mid and late arterial phases. (7D, E) are venous phases and (7F) being a delayed phase at nearly 5 minutes post contrast. Arterial enhancement, with contrast retention, central scar and minimal background T1/T2 change favours diagnosis of FNH.

Another available tool is the arrhythmia rejection tool, whereby we set an acceptance window and the scanner rejects any RR periods which do not fall within this window. The downside of this is that if the patient has a chronic arrhythmia then the scan time can increase beyond the ability of the patient to hold their breath.

Prior to CS this leaves the technologist with nowhere to go other than to use real time imaging with poor spatial and temporal resolution. CS has changed this. Using compressed sensing the heart can be imaged with both high spatial and temporal resolution in a robust reproducible fashion independent of the patient's breath-hold ability and in the presence of considerable arrhythmia.

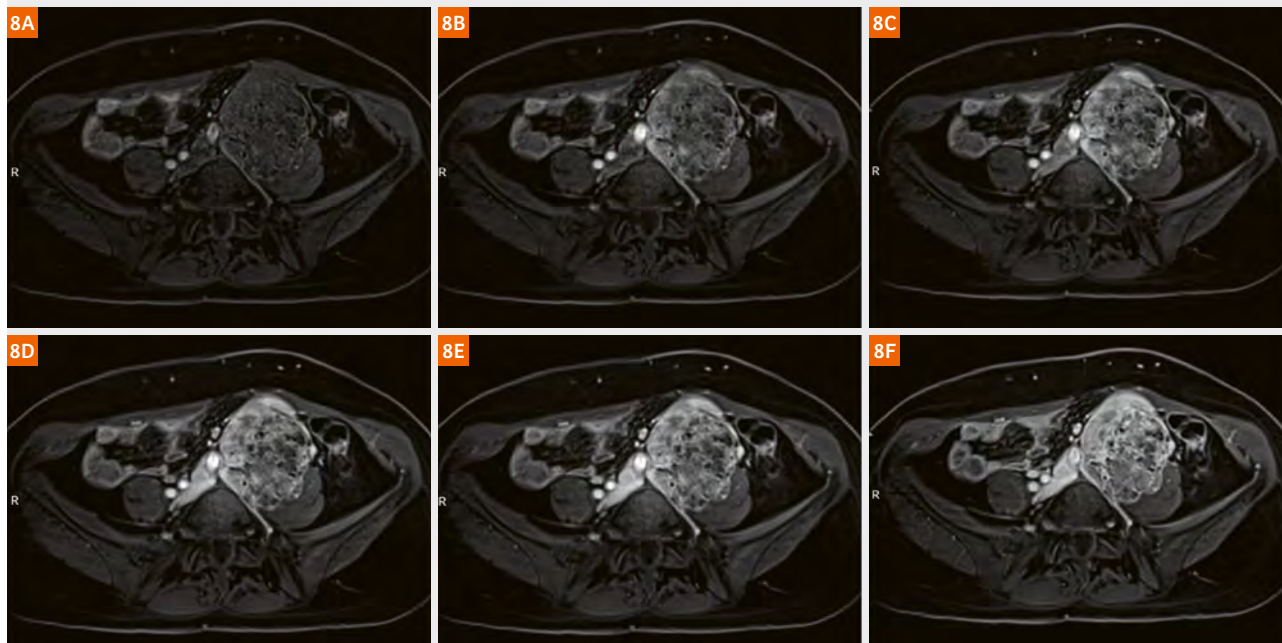
In the liver or any abdominal/pelvic indication that requires a dynamic contrast injection, the quality of the final images is reliant on both a skilled technologist who can trigger the acquisition for an accurate arterial phase or phase(s) and a compliant patient who can follow breathing instructions at the right time and also maintain a breath-hold for the duration of the acquisition. In the liver in particular temporal resolution in lesion characterization is becoming important for diagnosis.

Compressed Sensing GRASP-VIBE offers a technique for patients with limited breath-hold capability or who are unable to follow breathing commands. The technique takes the pressure off technologists as the critical timing-dependent arterial phase of an acquisition is removed. The acquisition is a simple push-button exam.

The acquisition is performed in one continuous run, using a golden-angle stack-of-stars radial scheme that gives robustness towards motion and the flexibility to choose the temporal resolution. The sequence itself guides the user on the correct time point for contrast administration. Reconstruction is performed using a Compressed Sensing GPU accelerated algorithm.

This new approach gives us a reliable post contrast technique on any patient. It is changing the way abdominal post contrast imaging is reviewed and making it a more dynamic cine experience at each slice location for the radiologist. Radiologists receive a temporal dataset which can be viewed akin to a cine series allowing contrast arrival, enhancement and wash out to be viewed on a slice by slice basis. The high temporal resolution is particularly useful for HCC detection and small thrombus within vessels. The insensitivity to breathing

Figure 8: CS GRASP VIBE pelvic mass



Compressed Sensing T1 Fatsat GRASP VIBE. 6 of 21 phases shown here from the same patient as Figure 4. Patient with a likely paraganglioma/pheochromocytoma. Starting with (8A) plain phase (8B–D) arterial time points to (8E, F) venous and delayed.

motion is particularly useful when combined with Primovist contrast where a subset of patients find holding their breath for a traditional arterial phase an issue. The dedicated arterial, venous and transitional phase datasets can be individually reconstructed and displayed as separate series for review in the traditional manner also.

Worldwide MRI is continuing to operate in an environment where the volume of exams is ever increasing with pressure on technologists and radiologists to maintain both image quality and diagnostic confidence. This continues against a background of decreasing reimbursements from government while patients expect high quality exams in an ever decreasing amount of time. Siemens Healthineers continue to innovate to provide solutions to these problems with yet more applications in SMS and CS coming soon to a magnet near you.

Contact

James Hancock
Modality Manager – MRI
Benson Radiology
229 Melbourne Street
North Adelaide, South Australia, 5006
Tel.: (08) 8239 0550
Mobile: 0434 279 466
James.Hancock@bensonradiology.com.au





Siemens Healthineers
welcomes the epoc
Blood Analysis System
to our critical-care
portfolio!

Right result. Right here. Right now.

Improve outcomes and workflow, while transforming care delivery across clinical pathways. The epoc Blood Analysis System gives you lab-quality results here and now.

Improve your workflow and help your clinicians make faster decisions with the handheld epoc® analyzer, which goes wherever patients are located and provides lab-quality results on the spot. Simplify inventory management, reduce costs, and maximize efficiency with the epoc system's single-use test cards that require no refrigeration.

As the newest member of the Siemens Healthineers portfolio, the epoc system helps to improve the patient experience and outcomes by providing the right test in the right place at the right time.

Download the Summary of Analytical Methods and Performance at siemens.com/epoc.

MAGNETOM Sola: Adaptive and anticipatory, predictive and profitable

Ulrike Attenberger, M.D.¹; Johannes Budjan, M.D.²; Katrin Koziel³

¹ Vice Chair of Clinical Operations, Head of Oncologic and Preventive Imaging

² Section Chief of MRI, Head of Multiparametric Imaging

³ Lead Technician, SMRT policy board member

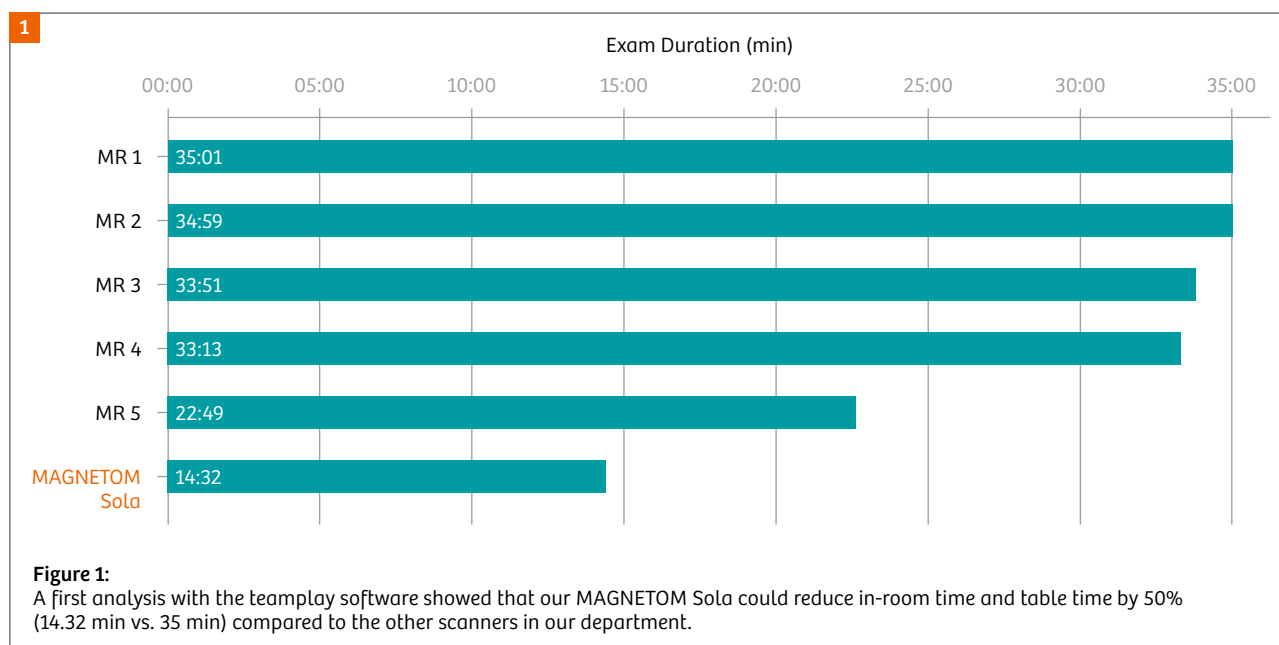
Department of Clinical Radiology and Nuclear Medicine, University Medical Center Mannheim, Medical Faculty Mannheim, Heidelberg University, Mannheim, Germany

Radiology in a changing environment

Today's radiology departments operate in a changing environment.

- A. The demographic change means that the number of elderly, multimorbid patients is increasing.
- B. Economic pressure is growing worldwide, making cost-efficiency a major topic in healthcare.
- C. For personalized treatment and precision medicine, institutions increasingly require robust and consistent imaging data as input for quantifying imaging data and characterizing tissue.

Along with data from deeper levels of information, right down to the genomic level, imaging is the foundation of precision medicine. Merging imaging data with genomic data and molecular information will provide new insights for developing targeted therapies and personalized treatment. Due to the specificity of the data it produces, MRI will play a major role in precision medicine. As well as providing high-resolution anatomical and morphological information, it also supplies functional and molecular data. However, if MRI is to be the key enabler for radiomics and precision medicine, its data must be robust, reproducible, and of a high quality. Until recently, variations in patient anatomy and physiology have been



The statements by Siemens' customers presented here are based on results that were achieved in the customer's unique setting. Since there is no 'typical' hospital and many variables exist (e.g., hospital size, case mix, level of IT adoption), there can be no guarantee that other users will achieve the same results.

a major obstacle to this. In addition, every technician in a radiology department has a different skill level and an individual way of interacting with the patient and the scanner. This often reduces the reproducibility of scans and leads to repeat scans, both of which are significant cost factors for the institution itself and the healthcare system as a whole. In view of all these aspects, radiology departments seeking to expand precision medicine need highly reliable and productive MRI scanners that deliver standardized, high-quality imaging.

BioMatrix® @ 1.5T: Reducing unwanted variations with MAGNETOM Sola

The need for a new MRI scanner

In our MR department, we have two 3T scanners (a MAGNETOM Trio and a MAGNETOM Skyra) and three 1.5T scanners (two MAGNETOM Avintos and a now-replaced MAGNETOM Sonata). We perform a broad spectrum of examinations on these scanners, with a special focus on oncological (including whole-body studies), cardiac, breast, and neuro imaging. In recent years, we were using our dependable MAGNETOM Sonata system almost exclusively for cardiac and neuro imaging. At the same time, we were experiencing increasing demand for, in particular, MSK and oncological abdominal studies. The latter was driven by growth in targeted therapies and the need for frequent follow-up examinations. Eventually, this increase in MR examination requests meant that we had to upgrade. We needed a reliable scanner that would allow us to perform the full spectrum of MR examinations and provide high-quality, robust, and standardized results. In addition, as a university hospital, financial considerations played a significant role in our decision-

making. This meant that, besides meeting the needs of our clinical departments regarding timely appointments for a large number of patients and fulfilling our demand for high-quality studies, we also paid particular attention to examination duration and patient throughput.

Against this backdrop, we had the opportunity to host the world's first installation of a MAGNETOM Sola¹, Siemens Healthineers' latest 1.5T MRI system, which promised to be the perfect match for our needs.

MAGNETOM Sola

MAGNETOM Sola is the first 1.5T system to be equipped with BioMatrix technology, and uses the latest advances in hardware and sequence developments. It features a 70 cm open bore, 204 channels (up to 64 of which can be used simultaneously within one FOV), a 45/200 XQ gradient system, a large FOV of 50 x 50 x 50 cm³, and a dockable table with new BioMatrix Sensors for respiratory and cardiac motion. The syngo MR XA11 software platform provides compressed sensing acceleration for abdominal imaging with inline reconstruction of GRASP-VIBE, and for cardiac examinations with real-time cine imaging during free-breathing. Simultaneous multi-slice acceleration can be used in both TSE sequences and diffusion-weighted imaging, and can substantially shorten acquisition times in MSK and body imaging. Various Dot engines (e.g. Whole-Body, Cardiac, Large Joint, Spine, and Brain) provide consistent examination quality and scan times, so that even less-experienced technicians can perform complex studies in a standardized manner.

¹ MAGNETOM Sola is not commercially available in all countries. Due to regulatory reasons the future availability cannot be guaranteed.

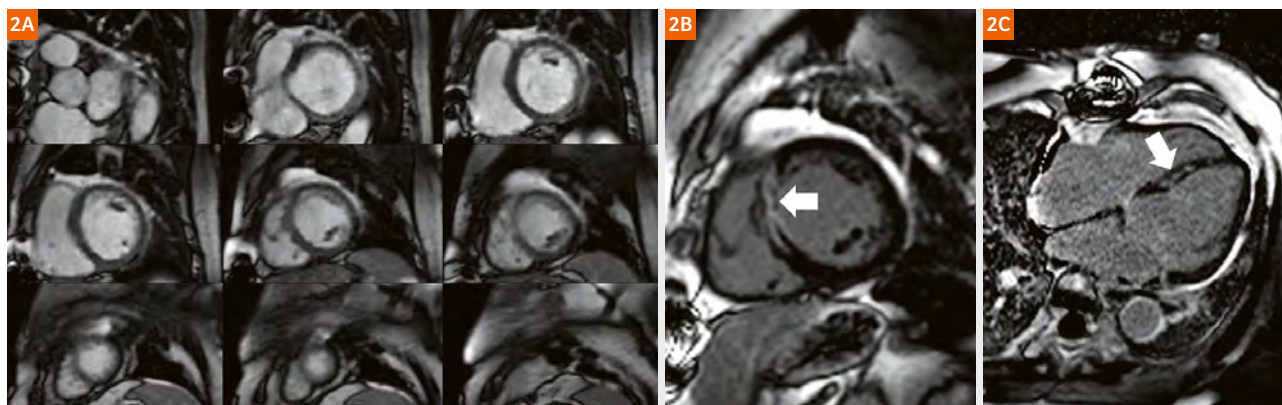


Figure 2:

Free-breathing cardiac MRI protocol with (2A) compressed sensing accelerated cine sequences and (2B) respiratory motion-corrected (MOCO) phase sensitive inversion recovery (PSIR) images with PSIR HeartFreeze. Gadolinium was injected prior to scanning, and acquisition of the entire protocol took 12 minutes. Both hypokinetic wall movement and septal late gadolinium enhancement (arrows) were consistent with post-ischemic scarring.

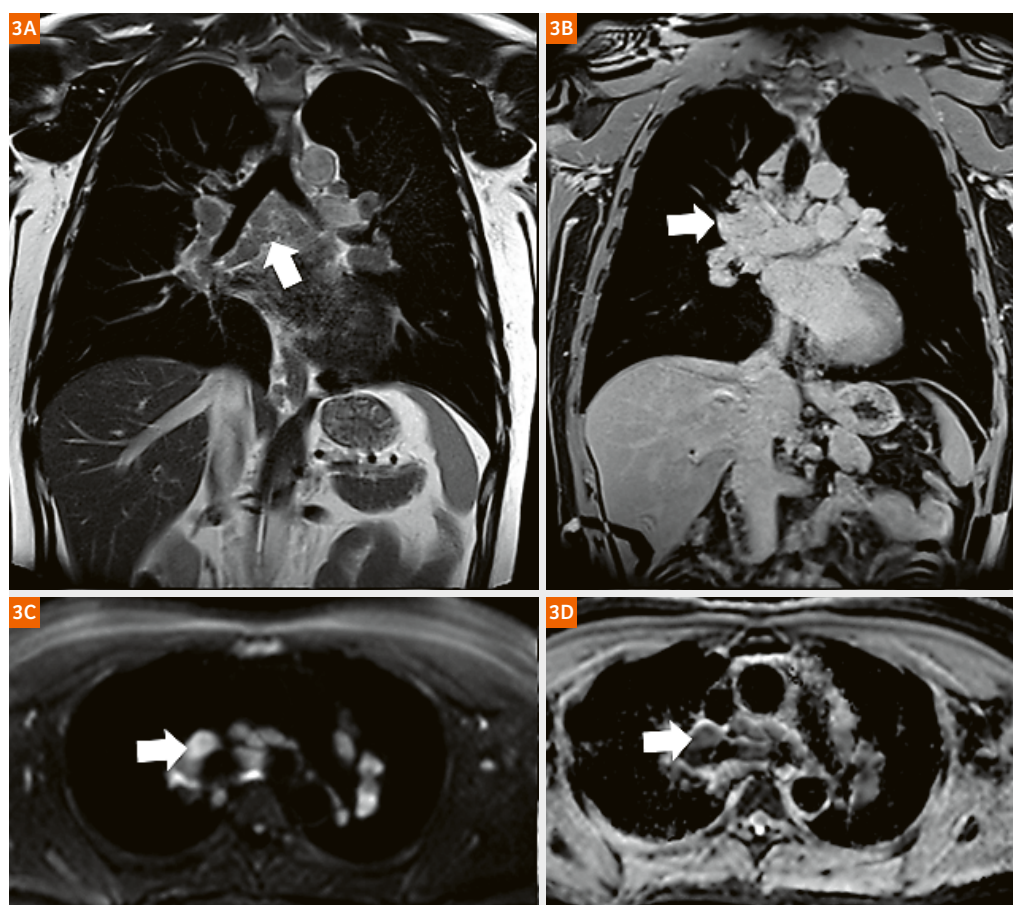


Figure 3: Thoracic MRI of a patient with known sarcoidosis. Morphological (3A: T2-weighted; 3B: T1-weighted) and diffusion-weighted imaging shows significant mediastinal and hilar lymph node enlargement (arrows). Total examination time for the entire protocol (including Trufi and axial morphological sequences) was 12 minutes.

In the first two months after the MAGNETOM Sola was installed, we performed the mandatory CE certification study. During this time, patients undergoing a clinically indicated examination on one of our MAGNETOM Avanto 1.5T systems were scanned for a second time using the MAGNETOM Sola. We compared image quality between both systems, and patients were asked to report on their experience (e.g., on noise and comfort levels).

For the examination protocols, we aimed to limit total examination time to a maximum of 20 minutes with highly standardized setups. We used the Dot engines to design different imaging strategies for different patient groups. With the Dot engines, the technician chooses a strategy (e.g., whole abdomen in a patient with limited breath-holding capabilities) and the protocol is automatically adapted to the patient's specific needs (e.g., by reducing the maximum breath-hold time or automatically choosing free-breathing sequences). The various protocol steps provide guidance for technicians who are new to the system so that they can perform reproducible, high-quality exams.

Using simultaneous multi-slice acceleration in diffusion-weighted imaging means that state-of-the-art DWI is

available in all oncological imaging protocols and at reasonable acquisition times. The same acceleration technique allowed us to set up very short, high-quality MSK protocols.

With the semiautomatic Cardiac Dot Engine and the compressed sensing accelerated acquisition of the function module (i.e., the long- and short-axis cine sequences), comprehensive protocols including late gadolinium enhancement can be acquired in under 15 minutes. Moreover, both the examination time and image quality are less dependent on the individual technician's experience.

Even during the CE certification process, feedback about average examination times per protocol has allowed us to identify outliers and optimize the protocols to improve both image quality and acquisition speed. A first analysis indicated that the MAGNETOM Sola will allow us to shorten our average examination time by 50%. As we are approaching the end of the certification process and are on the verge of having the MAGNETOM Sola as part of our scanner fleet for clinical routine, we now feel very well prepared to face the challenges of the future.

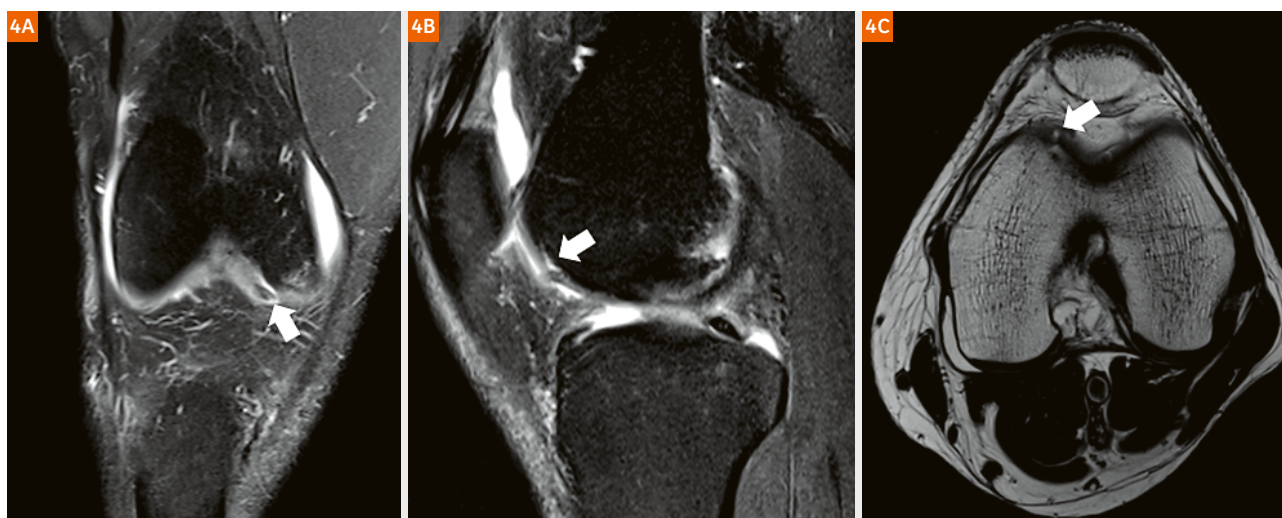


Figure 4: Time-efficient, 10 minute knee protocol acquired with the Knee Dot Engine. A small chondral defect with minimal delamination in the medial femoral condyle is clearly visible in the PD (4A: coronal; 4B: sagittal) and T2-weighted sequences.

The technician's perspective

Katrin Koziel

The idea behind installing the MAGNETOM Sola in Mannheim was to improve image quality and comparability at 1.5T, and to introduce young and inexperienced technicians to a tool that would guide them through all examinations.

Thinking back to my first introduction to Dot engines and my immediate dislike of them, I was skeptical about the idea. As a senior technician, I have reservations about whether automated processes in MRI examinations that require no memorization, no knowledge of sequences, and no details about the technical context of the patient's clinical picture and feasible imaging options are really as easy as they sound. However, my years in clinical routine have taught me that there is a not-so-fine line between using one's knowledge and overachieving without thinking. It is easy to get lost in details that are of no use to making a diagnosis when you are good at your job but bored by routine scanning. Also, we tend to welcome a new technique if it fits our needs, but might reject the same technique if we feel threatened by it. So I told myself to keep an open mind, see what improves, and then decide if it is useful.

First, the hardware: The built-in BioMatrix interfaces are a great feature for accurate patient positioning (Select&GO). Both myself and all the attending junior and senior technicians were hooked immediately. The dockable table with eDrive support and AutoDocking is much easier to control and use than the dockable table we know from

older systems. The new design also has fewer grooves so it is easier to clean and disinfect. Also, the open-bore design with light strips inside the bore is always helpful with the patients.

The new "control center" with a two-monitor system is a great innovation. Planning the examination on the left monitor while simultaneously being able to work with the images on the right monitor without changing platforms is a big improvement. Learning to use all the features on the right monitor will take some time, but it is definitely worth the effort. We're still discovering new tricks every day. As for the new BioMatrix Sensor for respiratory motion, we are really impressed with the image quality possible for non-breath-hold sequences, especially for heart examinations with compressed sensing. This is also where the DotGO workflow comes in. The new possibilities offered by systems equipped with AI is really superb. In the whole-body workflow, for example, we can finally plan using the overview images – just as we have been able to do with CT for decades. The "mother engine" creates the number of stacks needed to cover the entire region of interest, and even names the stacks correctly (chest I, chest II, abdomen, pelvis). This is a relief for all junior technicians, who initially struggle to get their sequences right, fully cover the scanning area, make sure the patient is breathing as instructed, and name the sequences. The scanner also counts and renames the sequences with the vertebrae in all spine examinations, which makes our radiologists very happy because technicians sometimes forget the naming.

Yet although these are great innovations, we still have to remember to encourage our young technicians to keep learning so that they can eventually do themselves what the technology is doing for them now. I want my coworkers to be able to scan without fear of failing. The new techniques on this high-end scanner allow them to do so without having years of experience in MRI. Eventually, though, they will have to use an older scanner without this support, and they will need to do their job just as well.

Nonetheless, I am looking forward to discovering even more features as we continue to learn with our scanners. I want to embrace the possibilities of the new techniques and continual progress in technology without losing the strategic understanding of how important it is to have well-trained technicians.

.....

Contact

Professor Ulrike I. Attenberger, M.D.
Vice Chair of Clinical Operations
Head of Oncologic and Preventive Imaging
Institute of Clinical Radiology and Nuclear Medicine
University Medical Center Mannheim
Theodor-Kutzer-Ufer 1–3
68167 Mannheim
Germany
Tel.: +49 621 383 2067
Ulrike.Attenberger@medma.uni-heidelberg.de



Future perspectives: workflow optimization with BioMatrix technology @ 1.5T and teamplay

A major goal linked to our MAGNETOM Sola will be to reduce the department's in-room and table times to 30 and 20 minutes respectively, regardless of the type of exam. The combination of technologies such as BioMatrix and the Dot engines, and acceleration techniques such as compressed sensing and simultaneous multi-slice will make the MAGNETOM Sola the highly efficient workhorse for our clinical routine. What is more, we want to go even further and use the software product teamplay to continuously benchmark our in-room times with the MAGNETOM Sola against our best practice and achieve further optimization. In-depth, real-time feedback about protocol performance down to the sequence level will allow us to adjust every protocol step regarding the balance of acquisition time and, e.g., image resolution. Using teamplay data and a standalone version of the Dot Cockpit means we can efficiently identify protocols that require improvement, and directly adjust protocols or even sequence parameters without having to interrupt the clinical workflow at the scanner itself. The updated protocols will be delivered to our MAGNETOM Sola via the teamplay cloud, and teamplay can then deliver direct feedback on the impact of protocol adaptations. This closes the loop of monitoring/benchmarking, identifying areas for improvement, adapting the protocols, and integrating the modifications into clinical routine. We will focus on shortening our slot times and increasing our patient throughput while achieving consistently high quality. With teamplay, we can constantly measure our productivity growth and calculate the financial benefit. This will allow us to continually optimize and adjust our scanning strategies so that we can better address the challenges of the future.



teamplay

Get the most out of your data in radiology and cardiology

To advance digitalization in healthcare, teamplay¹ is a departmental performance management solution that brings together healthcare professionals in a team effort. By connecting medical institutions and their imaging devices, teamplay apps aspire to create the biggest radiology and cardiology team in the world and provide its members with tools to tackle big data and the challenges of increasing cost pressure.

The cloud-based solution teamplay with its apps will help you make prompt and well-informed decisions by offering an intelligible overview of your performance data. It monitors quantities such as imaging throughput or

dose levels, utilization of staff, rooms and resources of your whole department down to every device and procedure, simplifying your reporting and showing you where workflows need adjustments. It links you to other users of teamplay and their data to offer comparable benchmarks² and an effortless exchange of images and reports with other healthcare providers.

¹ Please check if teamplay is available in your country.

² Availability of Benchmarking option depends on a minimum number of considered subscribers to guarantee customer anonymity and data protection.

Technical advances in combined MR/PET: Bringing multiparametric hybrid imaging to a new level

Regine M. Perl; Christian P. Reinert; Konstantin Nikolaou; Sergios Gatidis

Department of Radiology, Diagnostic and Interventional Radiology, University of Tübingen, Germany

Introduction

With the introduction of the Siemens Healthineers Biograph mMR in 2010, a new exciting chapter in clinical radiology was opened [1]. For the first time, the simultaneous acquisition of metabolic information from PET, and both anatomic and functional data from MRI became possible for whole-body applications. The first patient scans and small clinical studies showed promising results and demonstrated the potential of this novel modality [2].

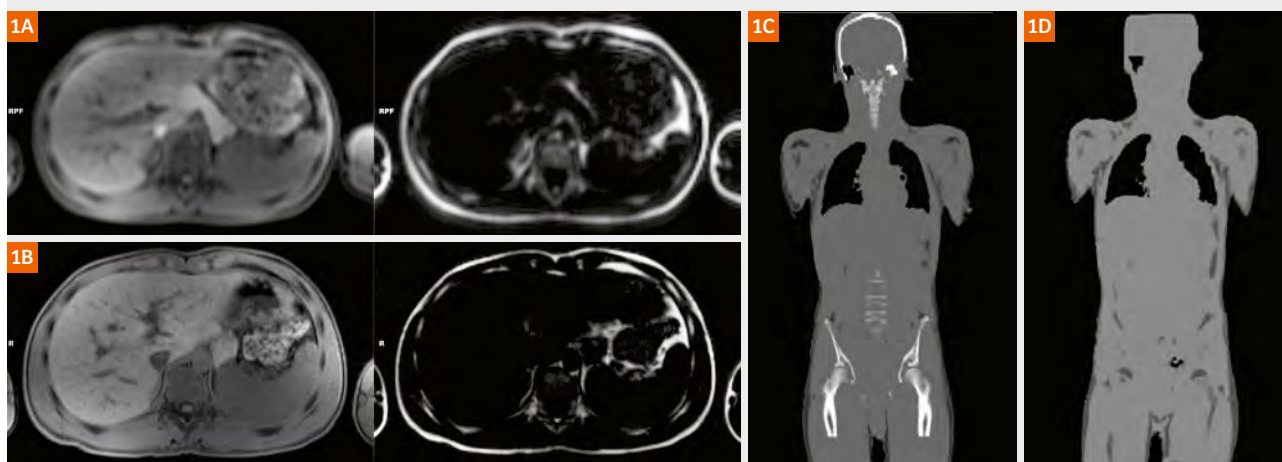
Besides the combined diagnostic information of PET and MRI, a major advantage of MR/PET is the possibility of simultaneous data acquisition of these two modalities. Thus, MR measurement time can be exploited for simultaneous PET data sampling. This in turn allows for longer PET acquisition times and potential reduction in tracer

dose and radiation exposure [3]. Furthermore, this opens the possibility for MR-based PET motion correction.

However, the transfer to clinical routine application proved to be more difficult than expected. Besides issues of reimbursement, the main reasons for this trend were the high complexity of the MR/PET systems, long examination times and – compared to state-of-the-art MR scanners – suboptimal MR workflow and lack of advanced MR techniques. Furthermore, MR specific technical challenges such as MR-based PET attenuation correction needed further improvement [4].

Since these first experiences, significant scientific and technological effort has been invested into further development of clinical MR/PET. Thus, MR/PET has evolved to a routine clinical modality for multiple indications

Figure 1: Advances in MR-based PET attenuation correction.



With the introduction of the CAIPIRINHA acceleration technique (1B), T1-weighted Dixon MR can now be acquired with substantially higher resolution and shorter acquisition times reaching full diagnostic quality in contrast to the initial version (1A) that was only used for the purpose of attenuation correction.

Atlas-based attenuation correction (1C) compared to segmentation-based attenuation correction (1D). Bone structures are considered in the atlas-based approach improving PET quantification accuracy also in the vicinity of skeletal structures.

including oncologic imaging, pediatric imaging and CNS imaging. In the course of this development and especially with the introduction of the *syngo* MR E11P software version in 2017 the Biograph mMR has been equipped with state-of-the-art MR technology and improved PET capabilities transforming the system to a high-performance clinical imaging tool.

This article will give an overview of current advances in MR/PET technology focusing on optimization of PET acquisition and reconstruction, reduction in acquisition time and improvement of diagnostic MR image quality.

Optimizing PET acquisition and reconstruction

The PET part of hybrid MR/PET has been discussed in the past especially due to the challenge of MR-based PET attenuation correction [5]. The problems associated with estimation of bone attenuation and attenuation by objects outside the MR field-of-view have been solved in the meantime so that the PET image quality of the Biograph mMR is qualitatively as well as quantitatively fully on a par with current PET/CT systems [6, 7, 8]. The recent technical advances introduced with the *syngo* MR E11P software upgrade include the HUGE (B_0 -Homogenization Using Gradient Enhancement) technique and atlas-based attenuation correction.

Atlas-based attenuation correction has been introduced early in the development of MR/PET scanners and is now clinically available for the Biograph mMR scanners. The MR-based PET attenuation correction procedure is based on a T1-weighted dual echo Dixon sequence with subsequent segmentation of fat and water tissue and addition of bone structures using an underlying atlas (Fig. 1). Using this technique, PET quantification becomes very accurate even in the vicinity of skeletal structures [9].

Another improvement in PET attenuation and scatter correction is the separate measurement of the peripheral MR field-of-view using the HUGE technique. Using a dedicated continuous table-movement sequence, patient

arms which cannot be imaged with conventional sequences in larger patients due to B_0 -field inhomogeneities in the peripheral field-of-view, can be imaged and added to the attenuation correction map. This results in a significant improvement in PET quantification due to improved scatter and attenuation correction [9, 10].

MR-based PET motion correction has been a scientific topic of interest for many years since MR/PET became clinically available [11]. With the *syngo* MR E11P software version, MR-based motion correction became clinically available for MR/PET. Respiratory motion states are imaged in MRI generating a motion model. Using this model, PET data can subsequently be corrected for motion-induced displacements yielding PET data of higher spatial and quantitative accuracy.

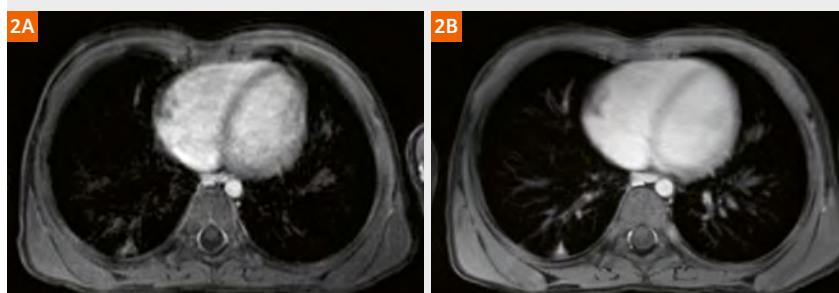
Reducing scan times

A crucial step for the clinical introduction of MR/PET is the acceleration of image acquisition and thus reduction of scan times. This is mostly achieved by accelerating MRI as MRI is usually the more time-consuming part.

The implementation of advanced parallel imaging with CAIPIRINHA [12] on the Biograph mMR allows for faster imaging and higher image quality in several ways. First and most importantly, the attenuation correction Dixon VIBE sequence can be substantially accelerated (from 18 s to 13 s per bed position) while also improving image resolution and quality (Fig. 1); in cases where acquisition time matters (e.g. children¹ or elderly), even a reduction to 7 seconds is feasible using maximum acceleration. This results in image data that can be used not only for attenuation correction but also for diagnostic purposes; furthermore, breath-hold duration can be reduced resulting in better patient comfort and reduced motion artifacts.

¹ Siemens Healthineers Disclaimer does not represent the opinion of the authors: MR scanning has not been established as safe for imaging fetuses and infants less than two years of age. The responsible physician must evaluate the benefits of the MR examination compared to those of other imaging procedures.

Figure 2: Increased motion robustness using radial VIBE.



Radial VIBE imaging under free breathing (2A) results in significantly higher image quality in patients with reduced compliance or shortness of breath compared to conventional breath-hold VIBE acquisitions (2B).

A further significant step for reducing MR scan times was the introduction of simultaneous multi-slice (SMS) imaging for EPI-based DWI. By simultaneous excitation of two or more slices, acquisition time can be reduced substantially maintaining high image quality [13].

Finally, fast imaging techniques for dynamic contrast-enhanced imaging including TWIST VIBE [14] and Compressed Sensing VIBE [15] sequences are being implemented for the *syngo* MR E11P software version on the Biograph mMR allowing for high spatial and temporal resolution in dynamic MR imaging. This development will likely enhance the potential for quantitative perfusion imaging in MR/PET.

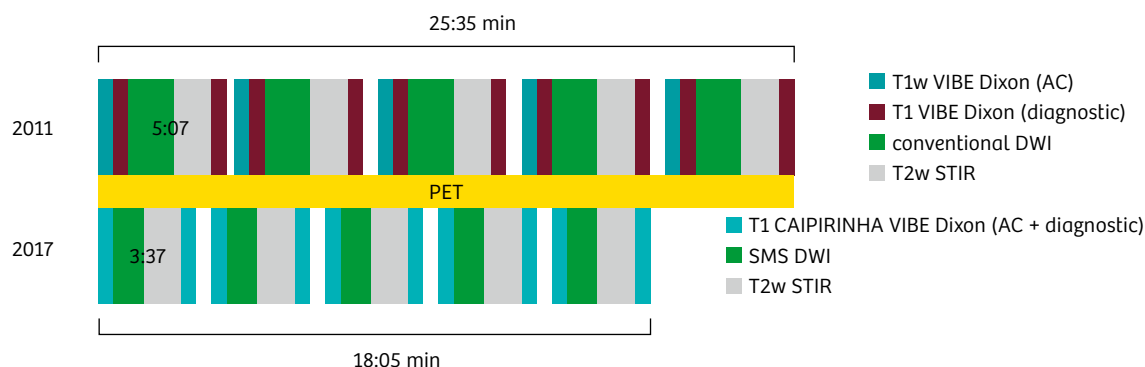
Improving diagnostic image quality

Advances in MR scanner and sequence technology have led to a rapid improvement in robustness and quality of MR studies in the recent past. These developments have also been transferred to the Biograph mMR allowing for MR imaging on a par with state-of-the-art MR-only scanners. Two developments are of special interest for hybrid MR/PET imaging: implementation of motion robust radial VIBE (Fig. 2) and ultrashort echo time spiral VIBE imaging as well as advanced EPI sequences for high quality diffusion-weighted imaging.

Motion artifacts are a challenge for MR imaging in general and can result in degraded image quality and corrupted diagnostic information. Especially in non-compliant patients and children¹, this can pose a diagnostic problem. In MR/PET in particular, a modality that promises com-

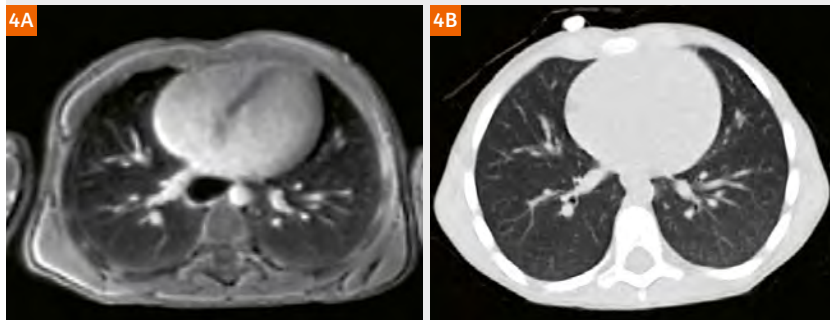
3

Figure 3: Acceleration of MR/PET imaging.



Using advanced MR sequence techniques (bottom row: CAIPIRINHA VIBE, SMS DWI²), acquisition time can be reduced substantially. Compared to the initial MR/PET protocol in the year 2011 (upper row), a reduction in measurement time by about 30% is feasible using the *syngo* MR E11P software version (bottom row) for an oncologic 5-bed whole-body protocol.

Figure 4: Improved lung imaging using ultra short echo time (UTE) spiral VIBE imaging².



The self-gated UTE VIBE sequence acquired under free breathing (4A) provides high pulmonary signal and robust image quality. Thus, an additional CT (4B) may be skipped in many patients.

¹ Siemens Healthineers Disclaimer does not represent the opinion of the authors: MR scanning has not been established as safe for imaging fetuses and infants less than two years of age. The responsible physician must evaluate the benefits of the MR examination compared to those of other imaging procedures.

² The product is under development and not commercially available yet. Its future availability cannot be ensured.

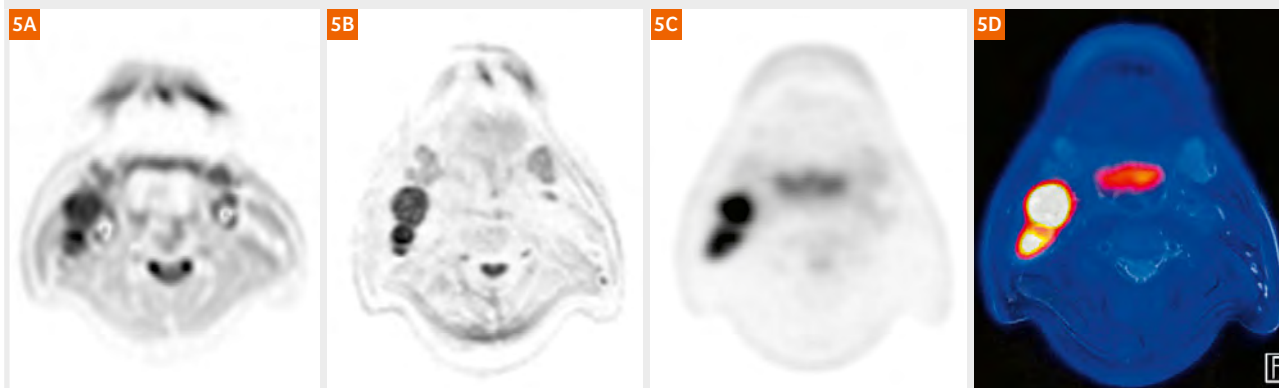
prehensive diagnostic information in a single session (one-stop-shop principle), high diagnostic quality is of utmost importance. The spiral VIBE sequence provides a convincing solution for this problem by offering motion robust MR imaging of the thorax and upper abdomen and allowing for T1-weighted acquisitions in free breathing [16].

Another related challenge for MR/PET is lung imaging. In this context, detection of pulmonary metastases has been discussed as a potential weakness of the modality [17]. Lung MRI however has evolved substantially and the use of ultrashort echo time sequences enables dedicated lung imaging with high tissue signal. The spiral UTE VIBE² that is being introduced also for the Biograph mMR offers additional respiratory self gating allowing for free-breathing acquisitions of the thorax promising significant improvement in lung imaging using combined MR/PET (Fig. 4) [18].

The second challenge with respect to MR image quality is EPI-based DWI especially in regions of inhomogeneous static field such as the neck area. As the majority of MR/PET examinations are performed in an oncological context, DWI is of special interest when using this modality. The implementation of advanced DWI sequence techniques including CoilShim² (integrated slice-specific shimming and frequency adjustment) also in combination with RESOLVE EPI (read-out segmented EPI) now enables EPI-based DWI with high spatial accuracy and significantly reduced artifacts [19, 20]. Thus, DWI has become a robust imaging tool and information of PET, DWI and further functional MR data can be analyzed down to a voxel-wise level (Fig. 5).

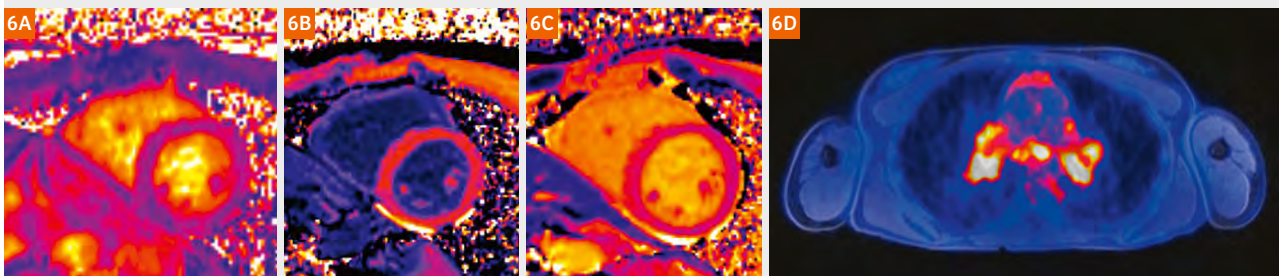
Finally, MR/PET has also caught up in the field of cardiac imaging by now offering the complete spectrum of quantitative myocardial mapping on the syngo MR E11P

Figure 5: Advanced EPI-based DWI techniques².



The application of CoilShim and RESOLVE EPI sequence techniques (5B) enable DWI also of the head and neck region with high spatial accuracy and significantly reduced artifacts compared to conventional single-shot EPI (5A). This allows for voxel-wise comparison with PET (5C). MR/PET fusion shown in 5D.

Figure 6: Quantitative cardiac MR/PET imaging.



Cardiac MR/PET in a patient with sarcoidosis in thoracic lymph node involvement (MR/PET Fusion, 6D). State-of-the-art T2 mapping (6A) and T1 mapping (6B non-enhanced, 6C contrast-enhanced image) as well as FDG-PET show no signs of cardiac involvement.

² The product is under development and not commercially available yet. Its future availability cannot be ensured.

software platform. In combination with PET information, ischemic and inflammatory cardiac disorders can be characterized in high detail and quantitative accuracy using T1/T2-mapping techniques, making MR/PET a comprehensive tool for anatomic and functional cardiac imaging (Fig. 6).

Conclusion and outlook

Combined MR/PET has gone through substantial steps of evolution since its introduction in 2010 and matured to a robust clinical modality. However, challenges remain for the future. Further reduction of scan times will be one main objective for further scientific and technological research. In this context, compressed sensing techniques may contribute soon.

New hardware equipment will certainly allow for further advances of this still relatively young technology that will hopefully be carried to a second generation regarding PET detector technology and MR system design.

References

- Delso, G., et al., Performance measurements of the Siemens mMR integrated whole-body PET/MR scanner. *J Nucl Med*, 2011. 52(12): p. 1914-22.
- Drzezga, A., et al., First clinical experience with integrated whole-body PET/MR: comparison to PET/CT in patients with oncologic diagnoses. *J Nucl Med*, 2012. 53(6): p. 845-55.
- Gatidis, S., et al., Defining optimal tracer activities in pediatric oncologic whole-body 18F-FDG-PET/MRI. *Eur J Nucl Med Mol Imaging*, 2016.
- Bailey, D.L., et al., Summary report of the First International Workshop on PET/MR imaging, March 19-23, 2012, Tübingen, Germany. *Mol Imaging Biol*, 2013. 15(4): p. 361-71.
- Bezrukov, I., et al., MR-Based PET attenuation correction for PET/MR imaging. *Semin Nucl Med*, 2013. 43(1): p. 45-59.
- Koesters, T., et al., Dixon Sequence with Superimposed Model-Based Bone Compartment Provides Highly Accurate PET/MR Attenuation Correction of the Brain. *J Nucl Med*, 2016. 57(6): p. 918-24.
- Paulus, D.H., et al., Whole-Body PET/MR Imaging: Quantitative Evaluation of a Novel Model-Based MR Attenuation Correction Method Including Bone. *J Nucl Med*, 2015. 56(7): p. 1061-6.
- Ladefoged et al. "A multi-centre evaluation of eleven clinically feasible brain PET/MRI attenuation correction techniques using a large cohort of patients", *NeuroImage Volume 147*, 15 February 2017, Pages 346-359
- Oehmigen, M., et al., Impact of improved attenuation correction featuring a bone atlas and truncation correction on PET quantification in whole-body PET/MR. *Eur J Nucl Med Mol Imaging*, 2017.
- Lindemann, M.E., et al., MR-based truncation and attenuation correction in integrated PET/MR hybrid imaging using HUGE with continuous table motion. *Med Phys*, 2017. 44(9): p. 4559-4572.
- Wurslin, C., et al., Respiratory motion correction in oncologic PET using T1-weighted MR imaging on a simultaneous whole-body PET/MR system. *J Nucl Med*, 2013. 54(3): p. 464-71.
- Breuer, F.A., et al., Controlled aliasing in parallel imaging results in higher acceleration (CAIPIRINHA) for multi-slice imaging. *Magn Reson Med*, 2005. 53(3): p. 684-91.
- Taron, J., et al., Scan time reduction in diffusion-weighted imaging of the pancreas using a simultaneous multislice technique with different acceleration factors: How fast can we go? *Eur Radiol*, 2017.
- Michaely, H.J., et al., CAIPIRINHA-Dixon-TWIST (CDT)-volume-interpolated breath-hold examination (VIBE): a new technique for fast time-resolved dynamic 3-dimensional imaging of the abdomen with high spatial resolution. *Invest Radiol*, 2013. 48(8): p. 590-7.
- Weiss, J., et al., Self-gated 4D-MRI of the liver: Initial clinical results of continuous multiphase imaging of hepatic enhancement. *J Magn Reson Imaging*, 2018. 47(2): p. 459-467.
- Chandarana, H., et al., Free-breathing radial 3D fat-suppressed T1-weighted gradient echo sequence: a viable alternative for contrast-enhanced liver imaging in patients unable to suspend respiration. *Invest Radiol*, 2011. 46(10): p. 648-53.
- Raad, R.A., et al., Outcome of small lung nodules missed on hybrid PET/MRI in patients with primary malignancy. *J Magn Reson Imaging*, 2016. 43(2): p. 504-11.
- Kumar, S., et al., Feasibility of free breathing Lung MRI for Radiotherapy using non-Cartesian *k*-space acquisition schemes. *Br J Radiol*, 2017. 90(1080): p. 20170037.
- Gatidis, S., et al., Diffusion-weighted echo planar MR imaging of the neck at 3T using integrated shimming: comparison of MR sequence techniques for reducing artifacts caused by magnetic-field inhomogeneities. *MAGMA*, 2017. 30(1): p. 57-63.
- Walter, S.S., et al., Combination of integrated dynamic shimming and readout-segmented echo planar imaging for diffusion weighted MRI of the head and neck region at 3Tesla. *Magn Reson Imaging*, 2017. 42: p. 32-36.

Contact

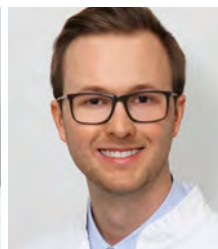
PD Dr. Sergios Gatidis
Department of Radiology
Diagnostic and Interventional Radiology
University of Tübingen
Hoppe-Seyler-Strasse 3
72076 Tübingen
Germany
+ 49 7071-29 68528
sergios.gatidis@med.uni-tuebingen.de



Sergios Gatidis



Regine M. Perl



Christian P. Reinert



Konstantin Nikolaou

HIGHLIGHTS OF PRESCRIBING INFORMATION

These highlights do not include all the information needed to use Fludeoxyglucose F 18 Injection safely and effectively. See full prescribing information for Fludeoxyglucose F 18 Injection. Fludeoxyglucose F 18 Injection, USP For intravenous use Initial U.S. Approval: 2005

RECENT MAJOR CHANGES

Warnings and Precautions	7/2010
(5.1, 5.2)	
Adverse Reactions (6)	7/2010

INDICATIONS AND USAGE

Fludeoxyglucose F18 Injection is indicated for positron emission tomography (PET) imaging in the following settings:

- Oncology: For assessment of abnormal glucose metabolism to assist in the evaluation of malignancy in patients with known or suspected abnormalities found by other testing modalities, or in patients with an existing diagnosis of cancer.
- Cardiology: For the identification of left ventricular myocardium with residual glucose metabolism and reversible loss of systolic function in patients with coronary artery disease and left ventricular dysfunction, when used together with myocardial perfusion imaging.
- Neurology: For the identification of regions of abnormal glucose metabolism associated with foci of epileptic seizures (1).

DOSAGE AND ADMINISTRATION

Fludeoxyglucose F 18 Injection emits radiation. Use procedures to minimize radiation exposure. Screen for blood glucose abnormalities.

- In the oncology and neurology settings, instruct patients to fast for 4 to 6 hours prior to the drug's injection. Consider medical therapy and laboratory testing to assure at least two days of normoglycemia prior to the drug's administration (5.2).
- In the cardiology setting, administration of glucose-containing food or liquids (e.g., 50 to 75 grams) prior to the drug's injection facilitates localization of cardiac ischemia (2.3).

Aseptically withdraw Fludeoxyglucose F 18 Injection from its container and administer by intravenous injection (2).

The recommended dose:

- for adults is 5 to 10 mCi (185 to 370 MBq), in all indicated clinical settings (2.1).
- for pediatric patients is 2.6 mCi in the neurology setting (2.2).

Initiate imaging within 40 minutes following drug injection; acquire static emission images 30 to 100 minutes from time of injection (2).

DOSAGE FORMS AND STRENGTHS

Multi-dose 30mL and 50mL glass vial containing 0.74 to 7.40 GBq/mL (20 to 200 mCi/mL) Fludeoxyglucose F 18 Injection and 4.5mg of sodium chloride with 0.1 to 0.5% w/w ethanol as a stabilizer (approximately 15 to 50 mL volume) for intravenous administration (3).

CONTRAINDICATIONS

None

WARNINGS AND PRECAUTIONS

- Radiation risks: use smallest dose necessary for imaging (5.1).
- Blood glucose abnormalities: may cause suboptimal imaging (5.2).

ADVERSE REACTIONS

Hypersensitivity reactions have occurred; have emergency resuscitation equipment and personnel immediately available (6).

To report SUSPECTED ADVERSE REACTIONS, contact PETNET Solutions, Inc. at 877-473-8638 or FDA at 1-800-FDA-1088 or www.fda.gov/medwatch.

USE IN SPECIFIC POPULATIONS

Pregnancy Category C: No human or animal data. Consider alternative diagnostics; use only if clearly needed (8.1).

- Nursing mothers: Use alternatives to breast feeding (e.g., stored breast milk or infant formula) for at least 10 half-lives of radioactive decay, if Fludeoxyglucose F 18 Injection is administered to a woman who is breast-feeding (8.3).
- Pediatric Use: Safety and effectiveness in pediatric patients have not been established in the oncology and cardiology settings (8.4).

See 17 for PATIENT COUNSELING INFORMATION

Revised: 1/2011

FULL PRESCRIBING INFORMATION: CONTENTS***1 INDICATIONS AND USAGE**

- 1.1 Oncology
- 1.2 Cardiology
- 1.3 Neurology

2 DOSAGE AND ADMINISTRATION

- 2.1 Recommended Dose for Adults
- 2.2 Recommended Dose for Pediatric Patients
- 2.3 Patient Preparation
- 2.4 Radiation Dosimetry
- 2.5 Radiation Safety – Drug Handling
- 2.6 Drug Preparation and Administration
- 2.7 Imaging Guidelines

3 DOSAGE FORMS AND STRENGTHS**4 CONTRAINDICATIONS****5 WARNINGS AND PRECAUTIONS**

- 5.1 Radiation Risks
- 5.2 Blood Glucose Abnormalities

6 ADVERSE REACTIONS**7 DRUG INTERACTIONS****8 USE IN SPECIFIC POPULATIONS**

- 8.1 Pregnancy
- 8.3 Nursing Mothers
- 8.4 Pediatric Use

11 DESCRIPTION

- 11.1 Chemical Characteristics
- 11.2 Physical Characteristics
- 12 CLINICAL PHARMACOLOGY
- 12.1 Mechanism of Action
- 12.2 Pharmacodynamics
- 12.3 Pharmacokinetics

13 NONCLINICAL TOXICOLOGY

- 13.1 Carcinogenesis, Muta-genesis, Impairment of Fertility

14 CLINICAL STUDIES

- 14.1 Oncology
- 14.2 Cardiology
- 14.3 Neurology

15 REFERENCES**16 HOW SUPPLIED/STORAGE AND DRUG HANDLING****17 PATIENT COUNSELING INFORMATION**

* Sections or subsections omitted from the full prescribing information are not listed.

FULL PRESCRIBING INFORMATION**1 INDICATIONS AND USAGE**

Fludeoxyglucose F 18 Injection is indicated for positron emission tomography (PET) imaging in the following settings:

1.1 Oncology

For assessment of abnormal glucose metabolism to assist in the evaluation of malignancy in patients with known or suspected abnormalities found by other testing modalities, or in patients with an existing diagnosis of cancer.

1.2 Cardiology

For the identification of left ventricular myocardium with residual glucose metabolism and reversible loss of systolic function in patients with coronary artery disease and left ventricular dysfunction, when used together with myocardial perfusion imaging.

1.3 Neurology

For the identification of regions of abnormal glucose metabolism associated with foci of epileptic seizures.

2 DOSAGE AND ADMINISTRATION

Fludeoxyglucose F 18 Injection emits radiation. Use procedures to minimize radiation exposure. Calculate the final dose from the end of synthesis (EOS) time using proper radioactive decay factors. Assay the final dose in a properly calibrated dose calibrator before administration to the patient [see Description (11.2)].

2.1 Recommended Dose for Adults

Within the oncology, cardiology and neurology settings, the recommended dose for adults is 5 to 10 mCi (185 to 370 MBq) as an intravenous injection.

2.2 Recommended Dose for Pediatric Patients

Within the neurology setting, the recommended dose for pediatric patients is 2.6 mCi, as an intravenous injection. The optimal dose adjustment on the basis of body size or weight has not been determined [see Use in Special Populations (8.4)].

2.3 Patient Preparation

- To minimize the radiation absorbed dose to the bladder, encourage adequate hydration. Encourage the patient to drink water or other fluids (as tolerated) in the 4 hours before their PET study.
- Encourage the patient to void as soon as the imaging study is completed and as often as possible thereafter for at least one hour.
- Screen patients for clinically significant blood glucose abnormalities by obtaining a history and/or laboratory tests [see Warnings and Precautions (5.2)]. Prior to Fludeoxyglucose F 18 PET imaging in the oncology and neurology settings, instruct patient to fast for 4 to 6 hours prior to the drug's injection.
- In the cardiology setting, administration of glucose-containing food or liquids (e.g., 50 to 75 grams) prior to Fludeoxyglucose F18 Injection facilitates localization of cardiac ischemia

2.4 Radiation Dosimetry

The estimated human absorbed radiation doses (rem/mCi) to a newborn (3.4 kg), 1-year old (9.8 kg), 5-year old (19 kg), 10-year old (32 kg), 15-year old (57 kg), and adult (70 kg) from intravenous administration of Fludeoxyglucose F 18 Injection are shown in Table 1. These estimates were calculated based on human² data and using the data published by the International Commission on Radiological Protection⁴ for Fludeoxyglucose¹⁸ F. The dosimetry data show that there are slight variations in absorbed radiation dose for various organs in each of the age groups. These dissimilarities in absorbed radiation dose are due to developmental age variations (e.g., organ size, location, and overall metabolic rate for each age group). The identified critical organs (in descending order) across all age groups evaluated are the urinary bladder, heart, pancreas, spleen, and lungs.

Table 1. Estimated Absorbed Radiation Doses (rem/mCi) After Intravenous Administration of Fludeoxyglucose F-18 Injection*

Organ	Newborn (3.4 kg)	1-year old (9.8 kg)	5-year old (19 kg)	10-year old (32 kg)	15-year old (57 kg)	Adult (70 kg)
Bladder wall b	4.3	1.7	0.93	0.60	0.40	0.32
Heart wall	2.4	1.2	0.70	0.44	0.29	0.22
Pancreas	2.2	0.68	0.33	0.25	0.13	0.096
Spleen	2.2	0.84	0.46	0.29	0.19	0.14
Lungs	0.96	0.38	0.20	0.13	0.092	0.064
Kidneys	0.81	0.34	0.19	0.13	0.089	0.074
Ovaries	0.80	0.8	0.19	0.11	0.058	0.053
Uterus	0.79	0.35	0.19	0.12	0.076	0.062
LLI wall *	0.69	0.28	0.15	0.097	0.060	0.051
Liver	0.69	0.31	0.17	0.11	0.076	0.058
Gallbladder wall	0.69	0.26	0.14	0.093	0.059	0.049
Small intestine	0.68	0.29	0.15	0.096	0.060	0.047
ULI wall **	0.67	0.27	0.15	0.090	0.057	0.046
Stomach wall	0.65	0.27	0.14	0.089	0.057	0.047
Adrenals	0.65	0.28	0.15	0.095	0.061	0.048
Testes	0.64	0.27	0.14	0.085	0.052	0.041
Red marrow	0.62	0.26	0.14	0.089	0.057	0.047
Thymus	0.61	0.26	0.14	0.086	0.056	0.044
Thyroid	0.61	0.26	0.13	0.080	0.049	0.039
Muscle	0.58	0.25	0.13	0.078	0.049	0.039
Bone surface	0.57	0.24	0.12	0.079	0.052	0.041
Breast	0.54	0.22	0.11	0.068	0.043	0.034
Skin	0.49	0.20	0.10	0.060	0.037	0.030
Brain	0.29	0.13	0.09	0.078	0.072	0.070
Other tissues	0.59	0.25	0.13	0.083	0.052	0.042

^a MIRDOSE 2 software was used to calculate the radiation absorbed dose. Assumptions on the biodistribution based on data from Gallagher et al.¹ and Jones et al.²

^b The dynamic bladder model with a uniform voiding frequency of 1.5 hours was used.

*LLI = lower large intestine; **ULI = upper large intestine

2.5 Radiation Safety – Drug Handling

- Use waterproof gloves, effective radiation shielding, and appropriate safety measures when handling Fludeoxyglucose F 18 Injection to avoid unnecessary radiation exposure to the patient, occupational workers, clinical personnel and other persons.
- Radiopharmaceuticals should be used by or under the control of physicians who are qualified by specific training and experience in the safe use and handling of radionuclides, and whose experience and training have been approved by the appropriate governmental agency authorized to license the use of radionuclides.
- Calculate the final dose from the end of synthesis (EOS) time using proper radioactive decay factors. Assay the final dose in a properly calibrated dose calibrator before administration to the patient [see Description (11.2)].
- The dose of Fludeoxyglucose F 18 used in a given patient should be minimized consistent with the objectives of the procedure, and the nature of the radiation detection devices employed.

2.6 Drug Preparation and Administration

Calculate the necessary volume to administer based on calibration time and dose. Aseptically withdraw Fludeoxyglucose F 18 Injection from its container. Inspect Fludeoxyglucose F 18 Injection visually for particulate matter and discoloration before administration, whenever solution and container permit. Do not administer the drug if it contains particulate matter or discoloration; dispose of these unacceptable or unused preparations in a safe manner, in compliance with applicable regulations. Use Fludeoxyglucose F 18 Injection within 12 hours from the EOS.

2.7 Imaging Guidelines

Initiate imaging within 40 minutes following Fludeoxyglucose F 18 Injection administration. Acquire static emission images 30 to 100 minutes from the time of injection.

3 DOSAGE FORMS AND STRENGTHS

Multiple-dose 30 mL and 50 mL glass vial containing 0.74 to 7.40 GBq/mL (20 to 200 mCi/mL) of Fludeoxyglucose F 18 Injection and 4.5 mg of sodium chloride with 0.1 to 0.5% w/w ethanol as a stabilizer (approximately 15 to 50 mL volume) for intravenous administration.

4 CONTRAINDICATIONS

None

5 WARNINGS AND PRECAUTIONS**5.1 Radiation Risks**

Radiation-emitting products, including Fludeoxyglucose F 18 Injection, may increase the risk for cancer, especially in pediatric patients. Use the smallest dose necessary for imaging and ensure safe handling to protect the patient and health care worker [see Dosage and Administration (2.5)].

5.2 Blood Glucose Abnormalities

In the oncology and neurology setting, suboptimal imaging may occur in patients with inadequately regulated blood glucose levels. In these patients, consider medical therapy and laboratory testing to assure at least two days of normoglycemia prior to Fludeoxyglucose F 18 Injection administration.

6 ADVERSE REACTIONS

Hypersensitivity reactions with pruritus, edema and rash have been reported in the post-marketing setting. Have emergency resuscitation equipment and personnel immediately available.

7 DRUG INTERACTIONS

The possibility of interactions of Fludeoxyglucose F 18 Injection with other drugs taken by patients undergoing PET imaging has not been studied.

8 USE IN SPECIFIC POPULATIONS**8.1 Pregnancy**

Pregnancy Category C

Animal reproduction studies have not been conducted with Fludeoxyglucose F 18 Injection. It is also not known whether Fludeoxyglucose F 18 Injection can cause fetal harm when administered to a pregnant woman or can affect reproduction capacity. Consider alternative diagnostic tests in a pregnant woman; administer Fludeoxyglucose F 18 Injection only if clearly needed.

8.3 Nursing Mothers

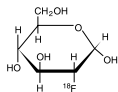
It is not known whether Fludeoxyglucose F 18 Injection is excreted in human milk. Consider alternative diagnostic tests in women who are breast-feeding. Use alternatives to breast feeding (e.g., stored breast milk or infant formula) for at least 10 half-lives of radioactive decay, if Fludeoxyglucose F 18 Injection is administered to a woman who is breast-feeding.

8.4 Pediatric Use

The safety and effectiveness of Fludeoxyglucose F 18 Injection in pediatric patients with epilepsy is established on the basis of studies in adult and pediatric patients. In pediatric patients with epilepsy, the recommended dose is 2.6 mCi. The optimal dose adjustment on the basis of body size or weight has not been determined. In the oncology or cardiology settings, the safety and effectiveness of Fludeoxyglucose F 18 Injection have not been established in pediatric patients.

11 DESCRIPTION**11.1 Chemical Characteristics**

Fludeoxyglucose F 18 Injection is a positron emitting radiopharmaceutical that is used for diagnostic purposes in conjunction with positron emission tomography (PET) imaging. The active ingredient 2-deoxy-2-[¹⁸F]fluoro-D-glucose has the molecular formula of C₆H₁₁¹⁸FO₅ with a molecular weight of 181.26, and has the following chemical structure:



Fludeoxyglucose F 18 Injection is provided as a ready to use sterile, pyrogen free, clear, colorless solution. Each mL contains between 0.740 to 7.40GBq (20.0 to 200 mCi) of 2-deoxy-2-[¹⁸F]fluoro-D-glucose at the EOS, 4.5 mg of sodium chloride and 0.1 to 0.5% w/w ethanol as a stabilizer. The pH of the solution is between 4.5 and 7.5. The solution is packaged in a multiple-dose glass vial and does not contain any preservative.

11.2 Physical Characteristics

Fluorine F 18 decays by emitting positron to Oxygen O 16 (stable) and has a physical half-life of 109.7 minutes. The principal photons useful for imaging are the dual 511 keV gamma photons, that are produced and emitted simultaneously in opposite direction when the positron interacts with an electron (Table 2).

Table 2. Principal Radiation Emission Data for Fluorine F18		
Radiation/Emission	% Per Disintegration	Mean Energy
Positron (b+)	96.73	249.8 keV
Gamma (γ)*	193.46	511.0 keV

*Produced by positron annihilation

From: Kocher, D.C. Radioactive Decay Tables DOE/TIC-1 1026, 89 (1981)

The specific gamma ray constant (point source air kerma coefficient) for fluorine F 18 is 5.7 R/hr/mCi (1.35 x 10⁻⁶ Gy/hr/kBq) at 1 cm. The half-value layer (HVL) for the 511 keV photons is 4 mm lead (Pb). The range of attenuation coefficients for this radionuclide as a function of lead shield thickness is shown in Table 3. For example, the interposition of an 8 mm thickness of Pb, with a coefficient of attenuation of 0.25, will decrease the external radiation by 75%.

Table 3. Radiation Attenuation of 511 keV Photons by Lead (Pb) shielding

Shield thickness (Pb) mm	Coefficient of attenuation
0	0.00
4	0.50
8	0.25
13	0.10
26	0.01
39	0.001
52	0.0001

For use in correcting for physical decay of this radionuclide, the fractions remaining at selected intervals after calibration are shown in Table 4.

Table 4. Physical Decay Chart for Fluorine F18	
Minutes	Fraction Remaining
0*	1.000
15	0.909
30	0.826
60	0.683
110	0.500
220	0.250

*calibration time

12 CLINICAL PHARMACOLOGY**12.1 Mechanism of Action**

Fludeoxyglucose F 18 is a glucose analog that concentrates in cells that rely upon glucose as an energy source, or in cells whose dependence on glucose increases under pathophysiological conditions. Fludeoxyglucose F 18 is transported through the cell membrane by facilitative glucose transporter proteins and is phosphorylated within the cell to [18F] FDG-6-phosphate by the enzyme hexokinase. Once phosphorylated it cannot exit until it is dephosphorylated by glucose-6-phosphatase. Therefore, within a given tissue or pathophysiological process, the retention and clearance of Fludeoxyglucose F 18 reflect a balance involving glucose transporter, hexokinase and glucose-6-phosphatase activities. When allowance is made for the kinetic differences between glucose and Fludeoxyglucose F 18 transport and phosphorylation (expressed as the 'lumped constant' ratio), Fludeoxyglucose F 18 is used to assess glucose metabolism. In comparison to background activity of the specific organ or tissue type, regions of decreased or absent uptake of Fludeoxyglucose F 18 reflect the decrease or absence of glucose metabolism. Regions of increased uptake of Fludeoxyglucose F 18 reflect greater than normal rates of glucose metabolism.

12.2 Pharmacodynamics

Fludeoxyglucose F 18 Injection is rapidly distributed to all organs of the body after intravenous administration. After background clearance of Fludeoxyglucose F 18 Injection, optimal PET imaging is generally achieved between 30 to 40 minutes after administration. In cancer, the cells are generally characterized by enhanced glucose metabolism partially due to (1) an increase in activity of glucose transporters, (2) an increased rate of phosphorylation activity, (3) a reduction of phosphatase activity or, (4) a dynamic alteration in the balance among all these processes. However, glucose metabolism of cancer as reflected by Fludeoxyglucose F 18 accumulation shows considerable variability. Depending on tumor type, stage, and location, Fludeoxyglucose F 18 accumulation may be increased, normal, or decreased. Also, inflammatory cells can have the same variability of uptake of Fludeoxyglucose F 18.

In the heart, under normal aerobic conditions, the myocardium meets the bulk of its energy requirements by oxidizing free fatty acids. Most of the exogenous glucose taken up by the myocyte is converted into glycogen. However, under ischemic conditions, the oxidation of free fatty acids decreases, exogenous glucose becomes the preferred myocardial substrate, glycolysis is stimulated, and glucose taken up by the myocyte is metabolized immediately instead of being converted into glycogen. Under these conditions, phosphorylated Fludeoxyglucose F 18 accumulates in the myocyte and can be detected with PET imaging. In the brain, cells normally rely on aerobic metabolism. In epilepsy, the glucose metabolism varies. Generally, during a seizure, glucose metabolism increases. Interictally, the seizure focus tends to be hypometabolic.

12.3 Pharmacokinetics

Distribution: In four healthy male volunteers, receiving an intravenous administration of 30 seconds in duration, the arterial blood level profile for Fludeoxyglucose F 18 decayed triexponentially. The effective half-life ranges of the three phases were 0.2 to 0.3 minutes, 10 to 13 minutes with a mean and standard deviation (STD) of 11.6 (±) 1.1 min, and 80 to 95 minutes with a mean and STD of 88 (±) 4 min. Plasma protein binding of Fludeoxyglucose F 18 has not been studied.

Metabolism: Fludeoxyglucose F 18 is transported into cells and phosphorylated to [18F]-FDG-6-phosphate at a rate proportional to the rate of glucose utilization within that tissue. [18F]-FDG-6-phosphate presumably is metabolized to 2-deoxy-2-[18F]fluoro-6-phospho-D-mannose([18F]FDM-6-phosphate).

Fludeoxyglucose F 18 Injection may contain several impurities (e.g., 2-deoxy-2-chloro-D-glucose (CLDG)). Biodistribution and metabolism of CLDG are presumed to be similar to Fludeoxyglucose F 18 and would be expected to result in intracellular formation of 2-deoxy-2-chloro-6-phospho-D-glucose (CLDG-6-phosphate) and 2-deoxy-2-chloro-6-phospho-D-mannose (CLDM-6-phosphate). The phosphorylated deoxyglucose compounds are dephosphorylated and the resulting compounds (FDG, FDM, CLDG, and CLDM) presumably leave cells by passive diffusion. Fludeoxyglucose F 18 and related compounds are cleared from non-cardiac tissues within 3 to 24 hours after administration. Clearance from the cardiac tissue may require more than 96 hours. Fludeoxyglucose F 18 that is not involved in glucose metabolism in any tissue is then excreted in the urine.

Elimination: Fludeoxyglucose F 18 is cleared from most tissues within 24 hours and can be eliminated from the body unchanged in the urine. Three elimination phases have been identified in the reviewed literature. Within 33 minutes, a mean of 3.9% of the administered radioactive dose was measured in the urine. The amount of radiation exposure of the urinary bladder at two hours post-administration suggests that 20.6% (mean) of the radioactive dose was present in the bladder.

Special Populations: The pharmacokinetics of Fludeoxyglucose F 18 Injection have not been studied in renally-impaired, hepatically impaired or pediatric patients. Fludeoxyglucose F 18 is eliminated through the renal system. Avoid excessive radiation exposure to this organ system and adjacent tissues. The effects of fasting, varying blood sugar levels, conditions of glucose intolerance, and diabetes mellitus on Fludeoxyglucose F 18 distribution in humans have not been ascertained [see Warnings and Precautions (5.2)].

13 NONCLINICAL TOXICOLOGY

13.1 Carcinogenesis, Mutagenesis, Impairment of Fertility

Animal studies have not been performed to evaluate the Fludeoxyglucose F 18 Injection carcinogenic potential, mutagenic potential or effects on fertility.

14 CLINICAL STUDIES

14.1 Oncology

The efficacy of Fludeoxyglucose F 18 Injection in positron emission tomography cancer imaging was demonstrated in 16 independent studies. These studies prospectively evaluated the use of Fludeoxyglucose F 18 in patients with suspected or known malignancies, including non-small cell lung cancer, colo-rectal, pancreatic, breast, thyroid, melanoma, Hodgkin's and non-Hodgkin's lymphoma, and various types of metastatic cancers to lung, liver, bone, and axillary nodes. All these studies had at least 50 patients and used pathology as a standard of truth. The Fludeoxyglucose F 18 Injection doses in the studies ranged from 200 MBq to 740 MBq with a median and mean dose of 370 MBq. In the studies, the diagnostic performance of Fludeoxyglucose F 18 Injection varied with the type of cancer, size of cancer, and other clinical conditions. False negative and false positive scans were observed. Negative Fludeoxyglucose F 18 Injection PET scans do not exclude the diagnosis of cancer. Positive Fludeoxyglucose F 18 Injection PET scans can not replace pathology to establish a diagnosis of cancer. Non-malignant conditions such as fungal infections, inflammatory processes and benign tumors have patterns of increased glucose metabolism that may give rise to false-positive scans. The efficacy of Fludeoxyglucose F 18 Injection PET imaging in cancer screening was not studied.

14.2 Cardiology

The efficacy of Fludeoxyglucose F 18 Injection for cardiac use was demonstrated in ten independent, prospective studies of patients with coronary artery disease and chronic left ventricular systolic dysfunction who were scheduled to undergo coronary revascularization. Before revascularization, patients underwent PET imaging with Fludeoxyglucose F 18 Injection (74 to 370 MBq, 2 to 10 mCi) and perfusion imaging with other diagnostic radiopharmaceuticals. Doses of Fludeoxyglucose F 18 Injection ranged from 74 to 370 MBq (2 to 10 mCi). Segmental, left ventricular, wall-motion assessments of asynergic areas made before revascularization were compared in a blinded manner to assessments made after successful revascularization to identify myocardial segments with functional recovery. Left ventricular myocardial segments were predicted to have reversible loss of systolic function if they showed Fludeoxyglucose F 18 accumulation and reduced perfusion (i.e., flow-metabolism mismatch). Conversely, myocardial segments were predicted to have irreversible loss of systolic function if they showed reductions in both Fludeoxyglucose F 18 accumulation and perfusion (i.e., matched defects). Findings of flow-metabolism mismatch in a myocardial segment may suggest that successful revascularization will restore myocardial function in that segment. However, false-positive tests occur regularly, and the decision to have a patient undergo

revascularization should not be based on PET findings alone. Similarly, findings of a matched defect in a myocardial segment may suggest that myocardial function will not recover in that segment, even if it is successfully revascularized. However, false-negative tests occur regularly, and the decision to recommend against coronary revascularization, or to recommend a cardiac transplant, should not be based on PET findings alone. The reversibility of segmental dysfunction as predicted with Fludeoxyglucose F 18 PET imaging depends on successful coronary revascularization. Therefore, in patients with a low likelihood of successful revascularization, the diagnostic usefulness of PET imaging with Fludeoxyglucose F 18 Injection is more limited.

14.3 Neurology

In a prospective, open label trial, Fludeoxyglucose F 18 Injection was evaluated in 86 patients with epilepsy. Each patient received a dose of Fludeoxyglucose F 18 Injection in the range of 185 to 370 MBq (5 to 10 mCi). The mean age was 16.4 years (range: 4 months to 58 years; of these, 42 patients were less than 12 years and 16 patients were less than 2 years old). Patients had a known diagnosis of complex partial epilepsy and were under evaluation for surgical treatment of their seizure disorder. Seizure foci had been previously identified on ictal EEGs and sphenoidal EEGs. Fludeoxyglucose F 18 Injection PET imaging confirmed previous diagnostic findings in 16% (14/87) of the patients; in 34% (30/87) of the patients, Fludeoxyglucose F 18 Injection PET images provided new findings. In 32% (27/87), imaging with Fludeoxyglucose F 18 Injection was inconclusive. The impact of these imaging findings on clinical outcomes is not known. Several other studies comparing imaging with Fludeoxyglucose F 18 Injection results to subspenoidal EEG, MRI and/or surgical findings supported the concept that the degree of hypometabolism corresponds to areas of confirmed epileptogenic foci. The safety and effectiveness of Fludeoxyglucose F 18 Injection to distinguish idiopathic epileptogenic foci from tumors or other brain lesions that may cause seizures have not been established.

15 REFERENCES

- Gallagher B.M., Ansari A., Atkins H., Casella V., Christman D.R., Fowler J.S., Ido T., MacGregor R.R., Som P., Wan C.N., Wolf A.P., Kuhl D.E., and Reivich M. "Radiopharmaceuticals XXVII. 18F-labeled 2-deoxy-2-fluoro-D-glucose as a radiopharmaceutical for measuring regional myocardial glucose metabolism in vivo: tissue distribution and imaging studies in animals," J Nucl Med, 1977; 18, 990-6.
- Jones S.C., Alavi, A., Christman D., Montanez, J., Wolf, A.P., and Reivich M. "The radiation dosimetry of 2 [F-18] fluoro-2-deoxy-D-glucose in man," J Nucl Med, 1982; 23, 613-617.
- Kocher, D.C. "Radioactive Decay Tables: A handbook of decay data for application to radiation dosimetry and radiological assessments," 1981, DOE/TIC-1 1026, 89.
- ICRP Publication 53, Volume 18, No. 1-4, 1987, pages 75-76.

16 HOW SUPPLIED/STORAGE AND DRUG HANDLING

Fludeoxyglucose F 18 Injection is supplied in a multi-dose, capped 30 mL and 50 mL glass vial containing between 0.740 to 7.40 GBq/mL (20 to 200 mCi/mL), of no carrier added 2-deoxy-2-[F 18] fluoro-D-glucose, at end of synthesis, in approximately 15 to 50 mL. The contents of each vial are sterile, pyrogen-free and preservative-free.

NDC 40028-511-30; 40028-511-50

Receipt, transfer, handling, possession, or use of this product is subject to the radioactive material regulations and licensing requirements of the U.S. Nuclear Regulatory Commission, Agreement States or Licensing States as appropriate.

Store the Fludeoxyglucose F 18 Injection vial upright in a lead shielded container at 25°C (77°F); excursions permitted to 15-30°C (59-86°F).

Store and dispose of Fludeoxyglucose F 18 Injection in accordance with the regulations and a general license, or its equivalent, of an Agreement State or a Licensing State.

The expiration date and time are provided on the container label. Use Fludeoxyglucose F 18 Injection within 12 hours from the EOS time.

17 PATIENT COUNSELING INFORMATION

Instruct patients in procedures that increase renal clearance of radioactivity.

Encourage patients to:

- drink water or other fluids (as tolerated) in the 4 hours before their PET study.
- void as soon as the imaging study is completed and as often as possible thereafter for at least one hour.

Manufactured by: PETNET Solutions Inc.
810 Innovation Drive
Knoxville, TN 37932

Distributed by: PETNET Solutions Inc.
810 Innovation Drive
Knoxville, TN 37932

PETNET Solutions

PN0002262 Rev. A

March 1, 2011

Fludeoxyglucose F¹⁸ 5-10mCi as an IV injection Indications and Usage

Fludeoxyglucose F¹⁸ Injection is indicated for positron emission tomography (PET) imaging in the following settings:

Oncology: For assessment of abnormal glucose metabolism to assist in the evaluation of malignancy in patients with known or suspected abnormalities found by other testing modalities, or in patients with an existing diagnosis of cancer.

Cardiology: For the identification of left ventricular myocardium with residual glucose metabolism and reversible loss of systolic function in patients with coronary artery disease and left ventricular dysfunction, when used together with myocardial perfusion imaging.

Neurology: For the identification of regions of abnormal glucose metabolism associated with foci of epileptic seizures.

Important Safety Information

Radiation Risks: Radiation-emitting products, including Fludeoxyglucose F¹⁸ Injection, may increase the risk for cancer, especially in pediatric patients. Use the smallest dose necessary for imaging and ensure safe handling to protect the patient and healthcare worker.

Blood Glucose Abnormalities: In the oncology and neurology setting, suboptimal imaging may occur in patients with inadequately regulated blood glucose levels. In these patients, consider medical therapy and laboratory testing to assure at least two days of normoglycemia prior to Fludeoxyglucose F¹⁸ Injection administration.

Adverse Reactions: Hypersensitivity reactions with pruritus, edema and rash have been reported; have emergency resuscitation equipment and personnel immediately available.

Dosage Forms and Strengths: Multiple-dose 30 mL and 50 mL glass vial containing 0.74 to 7.40 GBq/mL (20 to 200 mCi/mL) of Fludeoxyglucose F¹⁸ injection and 4.5 mg of sodium chloride with 0.1 to 0.5% w/w ethanol as a stabilizer (approximately 15 to 50 mL volume) for intravenous administration. Fludeoxyglucose F¹⁸ injection is manufactured by Siemens' PETNET Solutions, 810 Innovation Drive, Knoxville, TN 37932, USA.

Whole-body MR diffusion imaging in oncology: origins, practice, and outlook

Giuseppe Petralia, M.D.^{1,2,3}; Fabio Zugni, M.D.⁴; Marco Martinetti B.Sc.³; Paola Pricolo, M.D.¹; Massimo Bellomi, M.D.^{1,2,3}

¹ Department of Radiology, European Institute of Oncology (IEO), Milan, Italy

² Department of Oncology and Hematology, University of Milan, Milan, Italy

³ Scientific Committee, Advanced Screening Centers – ASC Italia, Castelli Calepio (Bergamo), Italy

⁴ Postgraduate School in Radiodiagnostics, University of Milan, Milan, Italy

Background

1905 was one of Albert Einstein's most productive years, his acclaimed *annus mirabilis* (from Latin meaning "extraordinary year"), in which he made a substantial contribution to the foundation of modern physics. In addition to other findings and innovations, Einstein extended Brown's theory about the random motion of particles [1]. Robert Brown, a Scottish botanist, was the first to notice the motion of particles in water; but he was not able to determine the underlying mechanisms of this motion. This was not the case for the German-born Nobel Prize winner. The first part of Einstein's theory was to determine how far a particle travels in a given time interval, and the second related the diffusion constant to physically measurable quantities, such as the mean squared displacement of a particle in a given time interval. Einstein observed, understood, and ultimately quantified water diffusion.

In 1974, R.V. Damadian patented the first magnetic resonance (MR) scanner as a "method for detecting cancer in tissue [2]." In this context, diffusion-weighted imaging played no significant role. This technical innovation was widely reported in the international media and had a significant impact on public opinion. In fact, with this new electronic device, Damadian claimed to be able to locate cancer across the whole body, raising expectations of the potential benefits of this innovation for oncology.

More than a decade later, a French physician named Denis Le Bihan came up with the intuitive idea of merging these two findings. Le Bihan showed that water diffusion could be displayed in the human brain through magnetic resonance imaging and, in 1985, produced the first diffusion-weighted image with MRI [3]. Since 1990, diffusion-weighted imaging (DWI) has become a standard neuroradiology tool for diagnosing ischemia. In 2004, Takahara et al. made a pioneering contribution to the development of DWI, by introducing a technology called diffusion-weighted whole-body imaging with background suppression (DWIBS), in which radiological images are acquired during free respiration, suppressing background

signals and allowing volumetric acquisitions and multiple section excitations of the whole body [4]. Thanks to these developments regarding the role of diffusion in magnetic resonance imaging, the scientific community finally had a method for quantifying the microscopic motion of water molecules in biological tissues over the entire body. Over the past decade, medical technology suppliers have launched incredible technological developments enabling whole-body MRI (WB-MRI), including morphological and diffusion-weighted images, to be performed in just 30–45 minutes. Moreover, clinicians have found many exciting uses for this radiation free technique for the management of malignancies and cancer screening.

Guidelines and key uses of WB-MRI by cancer histotype

Following growing evidence of its effectiveness in the management of cancer patients, the use of WB-MRI has increased exponentially over the last decade [5]. Encouraging results in the management of a variety of different cancer histotypes, in some cases substantiated

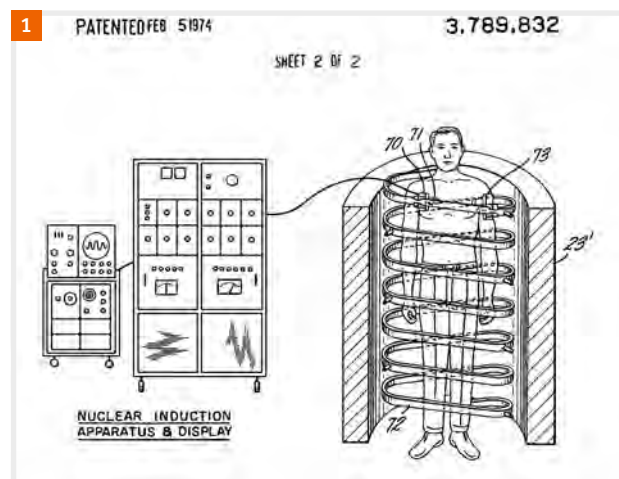


Figure 1:
Damadian's whole body MRI device, excerpt from the original U.S. Patent No. 3789832, Feb. 5, 1974.

by the highest level of scientific evidence [6], consolidated the role of WB-MRI in the management of several malignancies. In recent years, certain clinical guidelines have recommended the use of WB-MRI and important uses for this technique have been found in modern oncology.

Multiple myeloma

Multiple myeloma (MM) is a haematological cancer characterized by the accumulation of neoplastic plasma cells in the bone marrow. Bone disease, distinguished by the presence of bone fractures, osteolytic lesions, or osteoporosis, is a significant cause of morbidity and mortality in multiple myeloma [7]. Thus, according to the guidelines of the International Myeloma Working Group (IMWG), the presence of even asymptomatic bone disease on conventional radiography should be considered a criterion of symptomatic MM requiring treatment [8]. In a series of 611 MM patients, MRI detected more focal lesions than lytic lesions in whole-body X-rays of the spine (78% versus 16%; $P < 0.001$), pelvis (64% versus 28%; $P < 0.001$), and sternum (24% versus 3%; $P < 0.001$) [9], which are the most common areas of MM systemic spread. Moreover, in a study of 41 patients with newly-diagnosed multiple myeloma, WB-MRI proved superior to conventional whole-body CT screening in detecting lesions of the skeleton. WB-MRI should thus be used to detect regions with bone marrow infiltration for both diagnosis and monitoring of treatment response. According to the guidelines on the role of imaging in patients with MM, produced by the British Society for Haematology [10], WB-MRI is recommended for staging all forms of multiple myeloma (Grade of Recommendation A, GR A, reflecting the highest level of evidence-based medicine). It is also recommended for the monitoring of oligosecretory and non-secretory myelomas (Level of Evidence, LoE 1B [11]) as well as for extramedullary disease (LoE 1B [12]). The GR A recommendation also indicates that WB-MRI should be used for the staging of solitary bone plasmacytoma (SBP), an early stage malignancy with a clinical course between MGUS and multiple myeloma.

Prostate cancer

Prostate cancer is the most common histotype among men. While some types of prostate cancer grow slowly and may need only minimal or even no treatment, others may develop aggressive behavior, requiring accurate systemic staging and follow up.

In high-risk patients, guidelines developed by the European Association of Urology recommend cross-sectional abdominopelvic imaging and a bone-scan, as a minimum (GR A, LoE 2A [14]). However, the guidelines suggest that MRI is more sensitive (97%) than choline PET/CT (91%)

and bone scans (78%) for detecting bone metastasis. This was confirmed in a recent meta-analysis conducted by Shen et al. on 18 studies comparing the diagnostic accuracy of these three imaging techniques [15]. Moreover, the radiological assessment of metastasis also has prognostic value and changes treatment management protocols [16].

In advanced prostate cancer (APC) the management of metastasis is crucial: skeletal metastases are present in more than 90% of patients who die of the disease. In metastatic castrate-resistant prostate cancer (mCRPC) patients being treated with enzalutamide and abiraterone and radium-223, up to one disease progression in three is detected radiologically with no clinical symptom or PSA (prostate serum antigen) progression [17, 18]. Moreover, PSMA PET/CT may fail to provide information on tumor viability during androgen receptor inhibition. Two recent reviews identified the potential of WB-MRI to address the unmet need for robust imaging that allows us to monitor the response of bone metastases to treatment [19, 20]. The St Gallen Advanced Prostate Cancer Consensus Conference (APCCC) presented clear recommendations about castrate-resistant patients. The recommendations confirm that PSA alone is not reliable enough for monitoring disease activity in mCRPC (since metastases may develop without a rising PSA) and that imaging should be conducted before starting a new line of treatment [21]. Moreover, the APCCC recommendations affirm that “disease monitoring in the bone is especially difficult with well-described bone lesion are phenomena both on CT and bone scans, [...] and it is recognised that planar bone scintigraphy has short-comings and is less sensitive than other newer imaging technologies such as MRI of the whole body.” Finally, although it acknowledged the “limited availability of these newer imaging technologies,” the APC Consensus Conference confirmed that “advanced spinal/whole-body MRI techniques are also better able to identify and gauge the extent of bone disease than planar bone scans.”

Melanoma

Although we have seen significant developments in the clinical management of advanced melanoma in recent years, most patients with stage IV melanoma will still die of the disease. For this reason, guidelines for the treatment of malignant melanoma have been published since 2001, providing feasible practical recommendations for clinicians and surgeons. Several meta-analysis and systematic reviews have established WB-MRI as a valid alternative method to PET/CT in oncology [22, 23]. Further studies have confirmed that WB-MRI is highly sensitive in detecting extracranial metastases in melanoma patients [24]. Although MRI with hepatobiliary contrast agents is

considered the best imaging strategy for identifying hepatic secondary lesions, small liver metastases can also be confidently detected with diffusion-weighted imaging as the sole method, as briefly reported in the case study (Fig. 2).

Moreover, studies are investigating recent developments in non-standard ultra-short TE (UTE)¹ MRI sequences [25] as a viable radiation-free alternative to reference CT scans in detecting small metastatic lesions in the lungs from melanoma (Fig. 3). In a study conducted on behalf of the

¹ WIP, the product is currently under development and is not for sale in the US and in other countries. Its future availability cannot be ensured.

Figure 2: Hepatic metastases: do we really need contrast?



A patient with a stage III melanoma undergoes WB-MRI with hepatobiliary-specific contrast agent (gadolinium-ethoxybenzyl-diethylenetriamine penta-acetic acid, Gd-EOB-DTPA). The late hepatobiliary phase, 20 minutes after injection (2A), reveals the presence of a 9 mm metastasis in the fourth segment (white arrow). The same lesion is clearly detectable in the high b-value (900 s/mm²) diffusion-weighted image performed in the same session (2B).

German Dermatological Society and the Dermatologic Cooperative Oncology Group [26], Pflugfelder et al., strongly recommend WB-MRI for cross-sectional imaging of advanced melanoma (stage III or worse), asserting that the efficacy of this method is equivalent to whole-body CT and PET/CT. Moreover, WB-MRI is also recommended for the follow-up in patients with melanoma staged from IIC to IV [27].

Breast

Breast cancer is the second leading cause of death among women. An epidemiological study based on 25,336 women diagnosed with primary invasive breast cancer, confirmed bone as the most common site of metastasis [28]. The widely accepted RECIST criteria (Response Evaluation Criteria in Solid Tumors) should not be used for monitoring bone lesions, as they are considered non-measurable. Moreover, the revised RECIST 1.1 failed to fully address this point. According to the new criteria bone metastases are only measurable once they have spread to the surrounding soft tissue with a mass larger than at least 10 mm in diameter [29]. This does not occur in the majority of the cases.

Since being introduced in clinical practice, conventional MRI has proven capable of supplying extremely precise imaging of the bone marrow which, in some cases, would be unachievable using other imaging techniques [30]. In

Figure 3: Lung metastasis in CT and MRI



A patient with stage IV melanoma undergoes a follow-up examination with low-dose CT of the lung and WB-MRI. A subcentimetric metastasis in the left inferior lobe is identified on the axial CT image (arrow in 3A) as well as on the axial T1-weighted image (arrow in 3B).

a meta-analysis conducted by Yang et al. on 145 studies comprising 15,221 patients with bone metastasis, WB-MRI showed better sensitivity for lesion detection (97%) than FGD-PET (91%) and bone scan (79%) [31]. In some instances conventional MRI could have shortcomings, however. For instance, a phenomenon known as T1 pseudo-progression can occur. This is when a strong response to therapy results in a bone marrow edema, which is visible as a T1 hypo-intensity and can be misclassified as progression. In such cases, the addition of DWI to T1-weighted images allows both the presence of the bone marrow edema and an absence of restrictions for water molecules to be identified, thus avoiding misdiagnosis [32]. The sclerotic response occurs when, after treatment, bone metastases appear unchanged on morphologic T1 images, but a response is clearly visible on the ADC map. The response is identified by an increase in the ADC value to over $1,500 \mu\text{m}^2/\text{s}$, which is a well-documented threshold for response to therapy (Fig. 4).

Studies are underway to evaluate the impact of the superior diagnostic performance of WB-MRI compared to conventional imaging techniques on the management

of cancer patients and, ultimately, on their survival. In a recent study, Kosmin et al. [33] compared the findings of 210 paired WB-MRI scans and computed tomography of chest, abdomen, and pelvis (CT-CAP) performed at the same time (within 14 days) for follow-up in patients with metastatic breast cancer. They observed that therapy changes were made due to progressive disease (PD) detected in the imaging in 46 pairs of scans; in 16 of these pairs (34.7%), PD was only visible in the WB-MRI scans and was not diagnosed by CT examination. This observation emphasizes the additional value of performing WB-MRI scans as opposed to CT-CAP in actual clinical practice. There are several recognized breast cancer histotypes that have different gene expression profiles and thus need to be managed differently. In some cases, these types of breast cancer benefit from targeted therapies [34]. Clinical practice in treating invasive lobular breast cancer (ILC) has recently revealed an important use for WB-MRI scans in breast cancer patients. In ILC, the second most common histological subtype, the spread of metastases differs from invasive ductal breast cancer (IDC), the most common histological subtype. ILC is

Figure 4: Pseudo-progression of bone metastases



45-year-old woman with metastatic breast cancer. WB-MRI examinations before and after third-line systemic treatment with capecitabine and vinorelbine.

(4A) On T1-weighted sagittal images a diffuse reduction in signal intensity is identified in the whole spine following chemotherapy. However, it is impossible to assess whether this is consistent with progressive disease, stable disease, or response to therapy. This finding can sometimes be observed when bone metastases respond to cytotoxic chemotherapy. It is due to the increase in extracellular water in the bone marrow, which reduces signal intensity on T1-weighted images thus mimicking disease progression. Maximum intensity projection (MIP) in the high b-value (900 s/mm^2) diffusion-weighted images reveal a decrease in signal intensity after therapy, related to decreased cellularity that is in fact consistent with response to therapy.

(4B) WB-tumor load segmentation undertaken on syngo.via Frontier² MR Total Tumor Load software (Siemens Healthcare; released research prototype). The MIP images in the high b-value (900 s/mm^2) are overlaid with ADC value color classes using the thresholds indicated. The green voxels are values $\geq 1500 \mu\text{m}^2/\text{s}$ (representing voxels that are 'highly likely' to be responding). The yellow voxels are set to lie between the 95th centile ADC value of the pre-treatment histogram ($1390 \mu\text{m}^2/\text{s}$) and $1500 \mu\text{m}^2/\text{s}$ thus representing voxels 'likely' to be responding. Red voxels represent mostly untreated and still active disease. A reduction in the volume of the active disease is measured (418 mL before therapy and 255 mL after therapy), with an overall increase in ADC values ($946 \mu\text{m}^2/\text{s}$ and $1742 \mu\text{m}^2/\text{s}$) on the corresponding relative frequency histograms. Note: the decreased extent and volume of red voxels are consistent with disease response (94% before therapy and 56% after therapy). The residual red regions on the post-therapy scan are likely to represent residual active disease with low ADC value, in the spine, pelvis, and limbs.

² syngo.via Frontier is for research only, not a medical device.

statistically more likely than IDC to spread to gastrointestinal (GI) organs, the peritoneum and retroperitoneum, the gynecological system, and the pleura, which are anatomical sites that are notoriously challenging to explore using PET and CT techniques [35]. Moreover, metastases from ILC are less FDG avid than other breast cancer histotypes [36] and therefore less visible on FDG-PET scans. This is associated with the reduced (to absent) E-cadherin membrane expression, which provides cell-to-cell adhesion and facilitates permeation through tissue planes. In ILC cancer cells this feature is responsible for the characteristic spread of the disease. This is known as “Indian file” neoplastic growth and involves neoplastic cells infiltrating the parenchyma around non-neoplastic ducts of GI organs or spreading to the peritoneum or retroperitoneum [37]. In our experience, thanks to the superior contrast resolution in WB-MRI compared to CT scans and the ‘aspecific’ nature of diffusion-weighted imaging (hyper-cellular lesions are always visible irrespective of the glucose metabolism), they are often able to depict the presence of neoplastic spread of disease into GI organs or the peritoneum/retroperitoneum earlier and more effectively than CT and FDG/PET-CT scans (see Fig. 5). Lastly, WB-MRI has demonstrated extraordinary results in detecting and staging breast cancer during pregnancy. In 40% of these cases, breast cancer presents at an advanced stage, which is 2.5 times the rate of the general breast cancer population. This means that accurate staging of bone, liver, and chest malignancies is crucial. However, imaging techniques involving ionizing

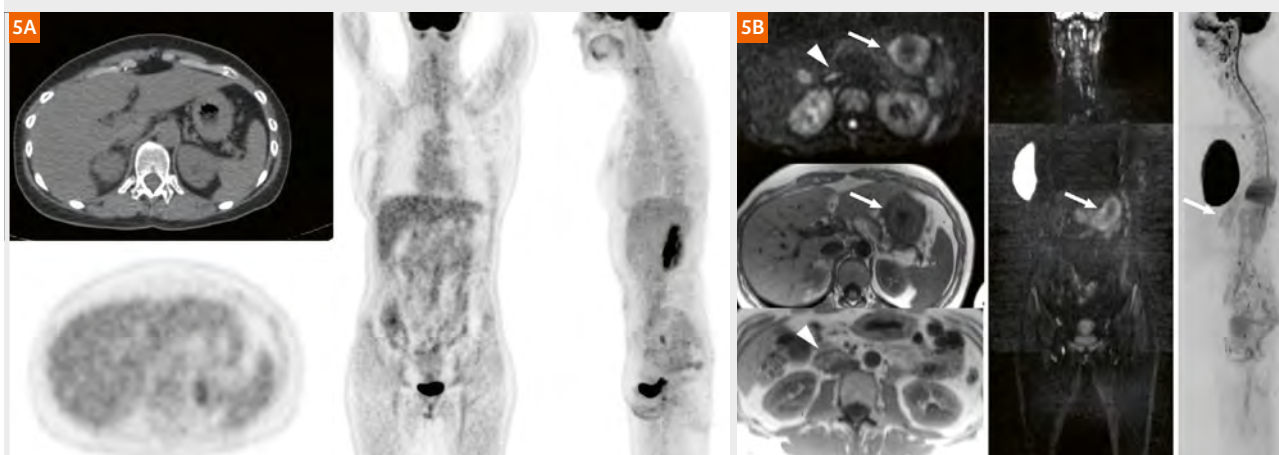
radiation and the administration of intravenous contrast agents should be limited during pregnancy making WB-MRI the imaging technique of choice for systemic staging in pregnant women with breast cancer [38].

Lymphoma

FDG-PET/CT is the recommended imaging technique for the most common lymphomas, including DLBCL, follicular lymphoma, and Hodgkin lymphoma [39]. However, its diagnostic performance depends on glucose metabolism and patients with severely altered glucose metabolism may not be ideal candidates for this imaging technique. The aim of WB-MRI, on the other hand, is to investigate hypercellularity across the whole body. This technique is thus likely to be less histology-dependent than FDG-PET and therefore more suitable for patients with lymphomas with poor or no FDG avidity. In a prospective study of 140 patients, WB-MRI demonstrated better diagnostic performance than both FDG-PET/CT and CE-CT in patients with lymphoma subtypes with variable FDG avidity (the majority were MALT lymphomas) [40].

Another important use that is on the rise for WB-MRI is in young (< 35-year-old) lymphoma patients. Over the last decade, there have been promising increases in the survival rates for lymphomas, particularly among young patients. Nevertheless, NCCN guidelines still recommend repeated CT or PET/CT examinations every year, including in the clinical management of low stage lymphomas [41]. WB-MRI has shown diagnostic performance comparable

Figure 5: Gastric and peritoneal metastases from lobular breast cancer



A 44-year-old woman with lobular breast cancer post-surgery undergoes several FDG PET/CT scans due to suspected disease recurrence based on a persistent and continuous rise in CA 15.3. No suspicious findings are visible on FDG PET/CT (5A). A WB-MRI performed 15 days later (5B) reveals a thickening of the gastric wall, with corresponding abnormally high signal intensity in the high b-value images b-900 DWI (white arrows), and suspicious solid tissue on the right anterior renal fascia (white arrowhead). A second WB-MRI examination performed two months later showed the same findings. Gastroscopy with multiple punch biopsies of the gastric wall has been performed, confirming the presence of malignant infiltration of lobular breast cancer cells.

to that of PET/CT both in staging and follow-up. Thus, following the introduction of a dose-saving criterion for the younger patients, WB-MRI could be considered as an alternative to PET/CT and CT in the young lymphoma patient subgroup.

Cancer screening and WB-MRI

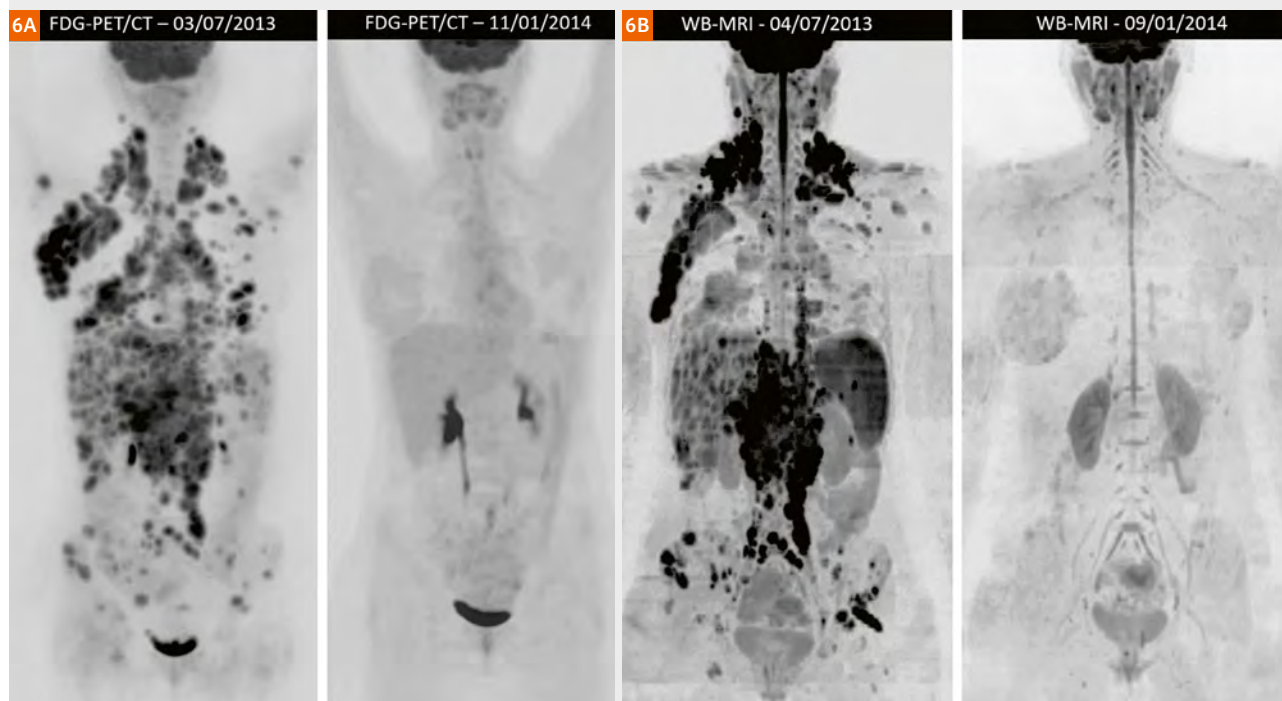
The aim of cancer screening is to detect cancer before symptoms appear. Several screening tests have proven to help detect cancer early and reduce the chance of dying from that disease [42]. Having saved thousands of lives, Pap tests, breast mammography for women, and FOBT for both women and men therefore became standard in many countries [43]. However, standard screening tests are not considered adequate for subjects genetically predisposed to cancer, such as those with Li-Fraumeni syndrome (LFS) and neurofibromatosis (NF). For patients with these conditions, advanced screening using WB-MRI is recommended. Moreover, there are high expectations of the benefits of advanced screening for the general population of asymptomatic subjects.

Li-Fraumeni syndrome

First described in 1969, Li-Fraumeni syndrome (LFS) is a highly penetrant cancer prone syndrome [44] caused by germline mutations of the TP53 tumor suppressor gene. Essentially, this rare, autosomal dominant, hereditary disorder, pre-disposes carriers to the development of a wide variety of cancer types. For this reason, it is also known as the sarcoma, breast, leukaemia, and adrenal gland (SBLA) syndrome. A recent meta-analysis validates the first statistically robust estimate of the clinical utility of WB-MRI in screening TP53 mutation carriers [45]. In addition, results from the UK SIGNIFY study on the cancer detection rate in this group of subjects argue for the adoption of at least a baseline whole body MRI scan [46]. Furthermore, the MD Anderson Cancer Center jointly with LFSA, the world largest LFS patients association, produced the first screening guidelines for the early detection of the syndrome. Guidelines developed by LEAD (Li-Fraumeni Syndrome Education and Early Detection) recommend WB-MRI for pediatric patients¹ between the age of 1 and

¹ Siemens Healthineers Disclaimer does not represent the opinion of the authors: MR scanning has not been established as safe for imaging fetuses and infants less than two years of age. The responsible physician must evaluate the benefits of the MR examination compared to those of other imaging procedures.

Figure 6: Assessment of post-treatment response



After multiple lines of systemic treatments, a 22-year-old woman with a relapse of non-Hodgkin lymphoma (Ann Arbor stage IVb) undergoes new chemotherapy combined with the ESHAP scheme and peripheral blood stem cell transplant. The patient undergoes FDG PET/CT and WB-MRI scans before treatment and six months post-treatment. Response assessment with PET/CT (**6A**) reveals a complete resolution of the abnormal FDG uptake across all body regions consistent with complete response (CR). Response assessment using WB-MRI at the same points in time (**6B**) is equally effective at showing CR.

10 years affected by sarcomas related to LFS, as well as for patients aged 10 or above, suffering from sarcomas, brain or adrenocortical tumors [47].

Lastly, according to a recent National Comprehensive Cancer Network (NCCN) recommendation, annual screening of LFS patients including WB-MRI should be a reference standard [48].

Neurofibromatosis

Neurofibromatosis is a genetic disorder causing tumors to form on nerve tissue. These tumors can develop anywhere across nervous system, including the brain, spinal cord, and nerves. Neurofibromatosis is usually diagnosed in childhood or early adulthood. Identifying pre-malignant and malignant tumors is essential for the clinical management of patients with NF, yet achieving this goal has remained challenging because of the heterogeneity of neurofibromas. Diffusion-weighted imaging is a particularly attractive technique for children¹ as most pediatric malignancies are small round cell tumors with impeded water diffusion. Moreover, WB-MRI has proven its efficacy in detecting and staging the three main clinical manifestations of NF: neurofibromatosis type 1 (NF1), neurofibromatosis type 2 (NF2), and schwannomatosis (SWN).

The National Cancer Institute has already recommended the development of practical guidelines to introduce WB-MRI for the detection of malignant peripheral nerve sheath tumors (MPNST) [49]. About half of all MPNST are diagnosed in people with neurofibromatosis and the lifetime risk of patients with NF1 developing this rare malignancy is between 8 and 13%. Moreover, a study conducted by Cashen et al. [50] showed an overall survival rate of 84% among treated patients emphasizing the key role of advanced imaging in early diagnosis and treatment management. The Response Evaluation in Neurofibromatosis and Schwannomatosis International Collaboration (REINS) is in the process of developing official recommendations for the use of WB-MRI in NF [51]. The Neuro Foundation, the largest NF patient foundation in the UK, already recommends MRI for investigating preliminary signs of neurofibromatosis across the whole body [52].

Asymptomatic subjects and screening

Although current paradigms and treatments for cancer have resulted in substantial progress, oncologic diseases frequently evade long-term monitoring and cure. Thus, early detection and diagnosis in asymptomatic patients, before the systemic spread of the primary neoplasm, are critical. Early detection of subclinical disease may enable

more efficient and effective initiation of preventive measures and treatment interventions at the early rather than later stages of disease. Imaging findings may thus result in the identification of early, and potentially curable, disease. Moreover, the role of the radiologist is crucial in deciding whether an image feature is normal or whether it potentially needs further examination.

The implementation of advanced imaging techniques in large cohort studies is an approach that has increasingly been used in epidemiologic research. The Framingham Heart study [53], the Multi-Ethnic Study of Atherosclerosis [54], and the Rotterdam study [55] have already demonstrated the invaluable scientific contribution of such techniques. In addition, advanced imaging has also improved our understanding of complex disease processes, as well as our ability to identify novel imaging biomarkers as precursors for subsequent disease states. The largest study using WB-MRI in asymptomatic subjects is the currently ongoing German National Cohort, a multicentric population-based study on 30,000 asymptomatic subjects. The study aims to identify risk and protective factors for population-relevant diseases and to provide new information that can be translated into primary prevention measures [56].

Several other studies regarding the use of WB-MRI for cancer screening have appeared in recent years. The first, published in 2008 by Gladys Lo et al. [57], described the incidental findings in a population of 132 doctors at Hong Kong Sanatorium and Hospital, who volunteered to undergo a WB-MRI for cancer screening. Various other studies have also been published over the last decade. The largest of these included 666 asymptomatic subjects in which a 1.05-percent rate of malignant cancers was determined [58].

Similar preliminary observations were made by the Advanced Screening Centers (ASC Italy), a recently founded social enterprise, originating from a collaborative partnership between a group of entrepreneurs and long-term supporters of cancer research, the European Institute of Oncology of Milan, and a panel of international experts in oncological WB-MRI, devoted exclusively to performing WB-MRI for cancer screening in asymptomatic subjects. From January 2017, when it was opened, to October 2017, ASC performed WB-MRI for cancer screening on 394 asymptomatic subjects.

The scans showed no abnormalities in just 12 of these subjects, which is actually consistent with the abnormality rates reported in the scientific literature. At least one abnormality was reported per 382 subjects (97% of the total).

However, for almost 80 percent of these subjects, no further investigation was requested, while 75 subjects were referred for follow-up. Further examinations were only requested for 9 subjects, and in 4 of these (1%) the presence of malignant cancer was confirmed histologically and the subject was informed.

However, the introduction of WB-MRI for screening the general population of asymptomatic subjects is still a long way off. First, it has to be proven that advanced cancer screening using WB-MRI, as opposed to screening that targets the most common malignancies (as per current standard practice) is scientifically relevant. Second, the diagnostic performance of WB-MRI in many cancer histotypes is well known, but it still needs validation for use in different populations (such as asymptomatic subjects). Third, there are practical issues associated with the relatively high cost of the equipment as well as the examination itself that present obstacles for the widespread use of WB-MRI. Lastly, but equally important, as with every practice in medicine, interpreting WB-MRI scans is heavily dependent on the experience of the reader. There is still inadequate standardization of image interpretation and reporting, as well as a lack of proper understanding of the learning curve required to be able to read an image effectively. Research to examine these issues is ongoing.

References

- Einstein A. On the motion of small particles suspended in liquids at rest required by the molecular-kinetic theory of heat. *Annalen der Physik*. 1905;17:549-60.
- Damadian RV. Apparatus and method for detecting cancer in tissue. US patent 3789832, filed 1972 March 17, issued 1974, February 5.
- Le Bihan D, Breton E. Imagerie de diffusion in-vivo par résonance magnétique nucléaire. *Comptes-Rendus de l'Académie des Sciences*. 1985;93(5):27-34.
- Takahara T, Imai Y, Yamashita T, Yasuda S, Nasu S, Van Cauteren M. Diffusion weighted whole body imaging with background-body signal suppression (DWIBS): technical improvement using free breathing, STIR and high-resolution 3D display. *Matrix*. 2004;160(160):160.
- Koh DM, Blackledge M, Padhani AR, Takahara T, Kwee TC, Leach, et al. Whole-body diffusion-weighted MRI: tips, tricks, and pitfalls. *American Journal of Roentgenology*. 2012;199(2):252-62.
- Wu LM, Gu HY, Zheng J, Xu X, Lin LH, Deng X, et al. Diagnostic value of whole-body magnetic resonance imaging for bone metastasis: a systematic review and meta-analysis. *Journal of Magnetic Resonance Imaging*. 2011;34(1):128-35.
- Kristinsson SY, Minter AR, Korde N, Tan E, Landgren O. Bone disease in multiple myeloma and precursor disease: novel diagnostic approaches and implications on clinical management. *Expert review of molecular diagnostics*. 2011;11(6):593-603.
- Kumar S, Paiva B, Anderson KC, Durie B, Landgren O, Moreau P, et al. International Myeloma Working Group consensus criteria for response and minimal residual disease assessment in multiple myeloma. *The Lancet Oncology*. 2016;17(8): e328-e346.
- Walker R, Barlogie B, Haessler J, Tricot G, Anaissie E, Shaughnessy Jr JD, et al. Magnetic resonance imaging in multiple myeloma: diagnostic and clinical implications. *Journal of Clinical Oncology*. 2007;25(9):1121-28.
- Dimopoulos MA, Hillengass J, Usmani S, Zamagni E, Lentzsch S, Davies FE, et al. Role of magnetic resonance imaging in the management of patients with multiple myeloma: a consensus statement. *Journal of Clinical Oncology*. 2015;33(6):657-664.
- Oxford Centre for Evidence-based Medicine - Levels of Evidence (March 2009). 2016 February 19. [Internet]. [Cited 2018 March 03]. Available from: <https://www.cebm.net/2009/06/oxford-centre-evidence-based-medicine-levels-evidence-march-2009/>
- Chantry A, Kazmi M, Barrington S, Goh V, Mulholland N, Streetly M, et al. Guidelines for the use of imaging in the management of patients with myeloma. *British Journal of Haematology*. 2017.
- Myeloma: diagnosis and management. [Internet]. [Cited 2018 March 03]. Available from: <https://www.nice.org.uk/guidance/ng35>
- Mottet N, Bellmunt J, Bolla M, Briers E, Cumberbatch MG, De Santis M, et al. EAU-ESTRO-SIOG guidelines on prostate cancer. Part 1: screening, diagnosis, and local treatment with curative intent. *European Urology*. 2017;71(4):618-29.
- Shen G, Deng H, Hu S, Jia Z. Comparison of choline-PET/CT, MRI, SPECT, and bone scintigraphy in the diagnosis of bone metastases in patients with prostate cancer: a meta-analysis. *Skeletal Radiology*. 2014;43(11):1503-13.
- Wang X, Pirasteh A, Brugarolas J, Rofsky NM, Lenkinski RE, Pedrosa I, et al. Whole-body MRI for metastatic cancer detection using T2-weighted imaging with fat and fluid suppression. *Magnetic Resonance in Medicine*. 2018.
- Morris MJ, Molina, A., Small, E. J., De Bono, J. S., Logothetis, C. J., Fizazi, K., et al. Radiographic progression-free survival as a response biomarker in metastatic castration-resistant prostate cancer: COU-AA-302 results. *Journal of Clinical Oncology*. 2015;33(12):1356-63.
- Bryce AH, Alumkal JJ, Armstrong A, Higano CS, Iversen P, Sternberg CN, et al. Radiographic progression with nonrising PSA in metastatic castration-resistant prostate cancer: post hoc analysis of PREVAIL. *Prostate Cancer and Prostatic Diseases*. 2017;20(2):221.
- Padhani AR, Lecouvet FE, Tunariu N, Koh DM, De Keyser F, Collins DJ, et al. Rationale for modernising imaging in advanced prostate cancer. *European Urology Focus*. 2017;3(2-3):223-239.
- Lecouvet FE, Talbot JN, Messiou C, Bourguet P, Liu Y, de Souza NM. Monitoring the response of bone metastases to treatment with Magnetic Resonance Imaging and nuclear medicine techniques: a review and position statement by the European Organisation for Research and Treatment of Cancer Imaging Group. *European Journal of Cancer*. 2014;50(15):2519-31.
- Gillesen S, Attard G, Beer TM, Beltran H, Bossi A, Bristow R, et al. Management of patients with advanced prostate cancer: the report of the Advanced Prostate Cancer Consensus Conference APCCC 2017. *European Urology*. 2018;73(2):178-211.
- Li B, Li Q, Nie W, Liu S. Diagnostic value of whole-body diffusion-weighted magnetic resonance imaging for detection of primary and metastatic malignancies: a meta-analysis. *European Journal of Radiology*. 2014;83(2):338-44.
- Ciliberto M, Maggi F, Treglia G, Padovano F, Calandriello L, Giordano A, et al. Comparison between whole-body MRI and Fluorine-18-Fluorodeoxyglucose PET or PET/CT in oncology: a systematic review. *Radiology and Oncology*. 2013;47(3):206-18.
- Petralia G, Padhani A, Summers P, Alessi S, Raimondi S, Testori A, et al. Whole-body diffusion-weighted imaging: is it all we need for detecting metastases in melanoma patients? *European Radiology*. 2013;23(12):3466-76.
- Grodzki DM, Jakob PM, Heismann B. Ultrashort echo time imaging using pointwise encoding time reduction with radial acquisition (PETRA). *Magnetic Resonance in Medicine*. 2012;67(2):510-18.
- Pflugfelder A, Kochs C, Blum A, Capellaro M, Czeschik C, Dettenborn T, et al. Malignant Melanoma S3-Guideline "Diagnosis, Therapy and Follow-up of Melanoma". JDDG: *Journal der Deutschen Dermatologischen Gesellschaft*. 2013;11(s6):1-116.

- 27 Dummer R, Siano M, Hunger R, Lindenblatt N, Braun R, Michielin O, et al. The updated Swiss guidelines 2016 for the treatment and follow-up of cutaneous melanoma. *Swiss Medical Weekly*. 2016;146:w14279.
- 28 Kwast AB, Groothuis-Oudshoorn KC, Grandjean I, Ho VK, Voogd AC, Menke-Pluymers MB, et al. Histological type is not an independent prognostic factor for the risk pattern of breast cancer recurrences. *Breast Cancer Research and Treatment*. 2012;135(1):271-80.
- 29 Eisenhauer EA, Therasse P, Bogaerts J, Schwartz LH, Sargent D, Ford R, et al. New response evaluation criteria in solid tumours: revised RECIST guideline (version 1.1). *European Journal of Cancer*. 2009;45(2):228-47.
- 30 Mehnati P, Tirtash MJ. Comparative efficacy of four imaging instruments for breast cancer screening. *Asian Pac J Cancer Prev*. 2015;16(15):6177-86.
- 31 Yang HL, Liu T, Wang XM, Xu Y, Deng SM. Diagnosis of bone metastases: a meta-analysis comparing 18FDG PET, CT, MRI and bone scintigraphy. *European Radiology*. 2011;21(12):2604-17.
- 32 Padhani AR, Makris A, Gall P, Collins DJ, Tunariu N, Bono JS. Therapy monitoring of skeletal metastases with whole-body diffusion MRI. *Journal of Magnetic Resonance Imaging*. 2014;39(5):1049-78.
- 33 Kosmin M, Makris A, Joshi PV, Ah-See ML, Woolf D, Padhani AR. The addition of whole-body magnetic resonance imaging to body computerised tomography alters treatment decisions in patients with metastatic breast cancer. *European Journal of Cancer*. 2017;77:109-16.
- 34 Romond EH, Perez EA, Bryant J, Suman VJ, Geyer Jr CE, Davidson NE, et al. Trastuzumab plus adjuvant chemotherapy for operable HER2-positive breast cancer. *New England Journal of Medicine*. 2005;353(16):1673-84.
- 35 Kwast AB, Groothuis-Oudshoorn KC, Grandjean I, Ho VK, Voogd AC, Menke-Pluymers MB, Siesling S. Histological type is not an independent prognostic factor for the risk pattern of breast cancer recurrences. *Breast Cancer Research and Treatment*. 2012;135(1):271-80.
- 36 Hogan MP, Goldman DA, Dashevsky B, Riedl CC, Gönen M, Osborne JR, et al. Comparison of 18F-FDG PET/CT for systemic staging of newly diagnosed invasive lobular carcinoma versus invasive ductal carcinoma. *Journal of Nuclear Medicine*. 2015;56(11):1674-80.
- 37 Goldstein NS. Does the level of E-cadherin expression correlate with the primary breast carcinoma infiltration pattern and type of systemic metastases? *American Journal of Clinical Pathology*. 2002;118(3):425-34.
- 38 Peccatori FA, Codacci-Pisanelli G, Del Grande M, Scarfone G, Zugni F, Petralia G. Whole body MRI for systemic staging of breast cancer in pregnant women. *The Breast*. 2017;35:177-81.
- 39 National Comprehensive Cancer Network Lymphoma. [Internet]. [Cited 2018 March 03]. Available from: <https://www.tri-kobe.org/nccn/guideline/hematologic/english/hodgkins.pdf>
- 40 Mayerhoefer ME, Karanikas G, Kletter K, Prosch H, Kiesewetter B, Skrabbs C, Hoffmann M. Evaluation of diffusion-weighted MRI for pretherapeutic assessment and staging of lymphoma: results of a prospective study in 140 patients. *Clinical Cancer Research*. 2014;20(11):2984-93.
- 41 Hoppe RT, Advani RH, Ai WZ, Ambinder RF, Aoun P, Bello CM, et al. Hodgkin lymphoma, version 2.2012 featured updates to the NCCN guidelines. *Journal of the National Comprehensive Cancer Network*. 2012;10(5):589-97.
- 42 Cancer Screening. (n.d.) [Internet]. [Cited 2018 March 03, 2018]. Available from: <https://www.cancer.gov/about-cancer/screening>
- 43 Kamangar F, Dores GM, Anderson WF. Patterns of cancer incidence, mortality, and prevalence across five continents: defining priorities to reduce cancer disparities in different geographic regions of the world. *Journal of Clinical Oncology*. 2006;24(14):2137-50.
- 44 Li FP, Fraumeni JF. Soft-tissue sarcomas, breast cancer, and other neoplasms: a familial syndrome? *Annals of internal medicine*. 1969;71(4):747-52.
- 45 Ballinger ML, Best A, Mai PL, Khincha PP, Loud JT, Peters JA, et al. Baseline surveillance in Li-Fraumeni syndrome using whole-body magnetic resonance imaging: a meta-analysis. *JAMA Oncology*. 2017;3(12):1634-9.
- 46 Saya S, Killick E, Thomas S, Taylor N, Bancroft EK, Rothwell J, et al. Baseline results from the UK SIGNIFY study: a whole-body MRI screening study in TP53 mutation carriers and matched controls. *Familial Cancer*. 2017;16(3):433-40.
- 47 MD Anderson Cancer Centre and LFSA [Internet]. [Cited 2018 March 03]. Available from: <http://www.livinglfs.org/wp-content/uploads/2016/03/LEAD-Pediatric-screening-program-2016.pdf>
- 48 National Comprehensive Cancer Network (n.d.) [Internet]. [Cited 2018 March 03]. Available from: <https://www.nccn.org/about/news/ebulletin/ebulletindetail.aspx?ebulletinid=535>
- 49 Reilly KM, Kim A, Blakely J, Ferner RE, Gutmann DH, Legius E, et al. Neurofibromatosis Type 1—Associated MPNST State of the Science: Outlining a Research Agenda for the Future. *JNCI: Journal of the National Cancer Institute*. 2017;109(8).
- 50 Cashen DV, Parisien RC, Raskin K, Hornicek FJ, Gebhardt MC, Mankin HJ. Survival data for patients with malignant schwannoma. *Clinical Orthopaedics and Related Research*. 2004;426:69-73.
- 51 Widemann BC, Blakeley JO, Dombi E, Fisher MJ, Hanemann CO, Walsh KS, et al. Conclusions and future directions for the REINS International Collaboration. *Neurology*. 2013;81(21 supplement 1):S41-4.
- 52 NF1 Facts. [Internet]. [Cited 2018 March 03]. Available from: <https://www.nfauk.org/what-is-neurofibromatosis/nf-type-1/nf1-facts/>
- 53 Splansky GL, Corey D, Yang Q, Atwood LD, Cupples LA, Benjamin EJ, et al. The third generation cohort of the National Heart, Lung, and Blood Institute's Framingham Heart Study: design, recruitment, and initial examination. *American Journal of Epidemiology*. 2007;165(11):1328-35.
- 54 Bild DE, Bluemke DA, Burke GL, Detrano R, Diez Roux AV, Folsom AR, et al. Multi-ethnic study of atherosclerosis: objectives and design. *American journal of epidemiology*. 2002;156(9):871-81.
- 55 Hofman A, Brusselle GG, Murad SD, van Duijn CM, Franco OH, Goedegebure A, et al. The Rotterdam Study: 2016 objectives and design update. *European Journal of Epidemiology*. 2015;30(8):661-708.
- 56 Bamberg F, Kauczor HU, Weckbach S, Schlett CL, Forsting M, Ladd SC, et al. Whole-body MR imaging in the German National Cohort: rationale, design, and technical background. *Radiology*. 2015;277(1):206-20.
- 57 Lo GG, Ai V, Au-Yeung KM, Chan JK, Li KW, Chien D. Magnetic resonance whole body imaging at 3 Tesla: feasibility and findings in a cohort of asymptomatic medical doctors. *Hong Kong Medical Journal*. 2008;14(2):90.
- 58 Cieszanowski A, Maj E, Kulisiewicz P, Grudzinski IP, Jakoniuk-Glodala K, Chlipala-Nitek I, et al. Non-contrast-enhanced whole-body magnetic resonance imaging in the general population: the incidence of abnormal findings in patients 50 years old and younger compared to older subjects. *PLOS One*. 2014;9(9):e107840.

Contact

Dr. Giuseppe Petralia, M.D.
Deputy Director Division of Radiology
IEO Istituto Europeo di Oncologia
Via Ripamonti, 435
20141 Milano
Italy
Phone +39 (0)257489915
giuseppe.petralia@ieo.it



Whole-body MRI at 1.5T – step-by-step

Will McGuire; Linda Culver; Anwar R. Padhani

Paul Strickland Scanner Centre, Mount Vernon Hospital, Northwood, Middlesex, UK

Whole-body MRI (WB-MRI) is a hot topic – you may have had enquiries from colleagues asking you if or when you might be able to offer the service. You may not know where to start or what is involved. The purpose of this article and the accompanying video tutorial is to introduce and guide you through the implementation for successful completion of a MET-RADS compliant WB-MRI protocol [1].

WB-MRI has been used as a clinical tool at Paul Strickland Scanner Centre for over 10 years. In that time over 6,500 patients have been examined using a protocol designed to enable the detection and surveillance of metastatic bone and soft tissue disease. Treatment regimens are routinely being altered based on serial qualitative and quantitative measurements produced by this technique [2].

To enable the serial analysis of quantitative ADC measurements we must reduce acquisition variables as far as practicable. Clearly it is not possible to fully control all patient variables between visits. The patient's condition may change, requiring a different coil set-up.

Adjusting scan parameters at a visit-by-visit basis adversely affects the reproducibility of both the qualitative and quantitative results. For the majority of sequences described below it is advised that the parameters are not adjusted by operators after initial protocol set-up. The sequences should be designed and saved to accommodate your largest (A>P and R>L) and tallest (H>F) patients by default, and ranges should not be reduced (e.g. phase FOV) even when this may normally prove advantageous. Those parameters which may be altered on a per-patient basis will be mentioned. Any changes made should remain constant between visits in the same patient where practicable.

Let's look at the equipment, preparation and steps required to successfully execute a WB-MRI protocol suitable for quantitative analysis.

You can find a video tutorial demonstrating the use of this protocol on the website at www.siemens.com/wb-mri. The video begins at the acquisition stage.

Sequence / stations	Core, comprehensive or both	TR (ms)	TE (ms)	FOV (mm)	Phase FOV (%)	Slices	Slices (mm)	Gap (%)	Matrix	Phase enc. direction	iPAT	b-values	Averages	TA (mins)
FastView	Both	3.31	2.19	480 x 1250	87.5	1	5	100	96	A>P	n/a		n/a	0:35
STIR spine sag (x2)	Both	5110	69	380	100	15	4	20	384	H>F (over-sampled)	2		2	2:30 (x2)
T1 spine sag (x2)	Both	200	9.6	380	100	15	4	20	256	H>F (over-sampled)	2		2	1:07 (x2)
T1 Dixon TimCT ax	Both	130	2.38 4.76	430 x 1015	81.3	12	5	0	256	A>P	2		1	3:45 + BHs
DWI (x4) ax	Core (Comprehensive)	7370	66	430	90.6	55	5	0	128	A>P	2	50, (600,) 900	2, (5,) 6	3:04 (4:55)
T1 Dixon CAIPI VIBE cor (x3)	Both	6.64	2.39 4.77	450	94.4	144	2	min	288	R>L (over-sampled)	5		1	0:19
T2 HASTE TimCT	Comprehensive	1000	81	430 x 1035	81.3	16	5	0	256	A>P	3		1	3:44
Total examination time														24:47
Comprehensive acquisition time														35:55

Table 1: Sequence parameters for MET-RADS compliant sequences for both core and comprehensive protocols at 1.5T [1].

Coil requirements

- Standard posterior spine coil
- Standard head & neck coil
- 2x anterior Body 18 coils (Fig. 1) as required for coverage to mid-thigh (3x recommended)

Number your Body coils and routinely positioning them in the same order will limit any sensitivity variability and also make coil troubleshooting much more straightforward.

It is important to note that the range required for MET-RADS compliant protocols is from vertex to mid-thigh (Fig. 2). Although not always required, access to 3x Body 18 coils is optimal and should accommodate even the tallest patients.

As such it's not necessary to use a peripheral coil for this protocol. If full imaging of the lower limbs is required it is advised to perform imaging separately and feet-first, allowing a bio-break for the patient.

As this technique will be used to generate quantitative ADC measurements it is especially important to ensure that the coils are working well. A coil QA program should be implemented with increased frequency of testing for the regularly used coils.

Product options and software compatibility

Product options used for this protocol are TimCT, Inline Composing and the Tim Planning Suite (set'n'go).

At www.siemens.com/wb-mri you can find a downloadable .exar1 file which was exported from an Avanto^{fit} running syngo MR E11C software.

If you are unable to import this file, please see the full protocol in Table 1 or the full protocol .pdf file which is available on the website.

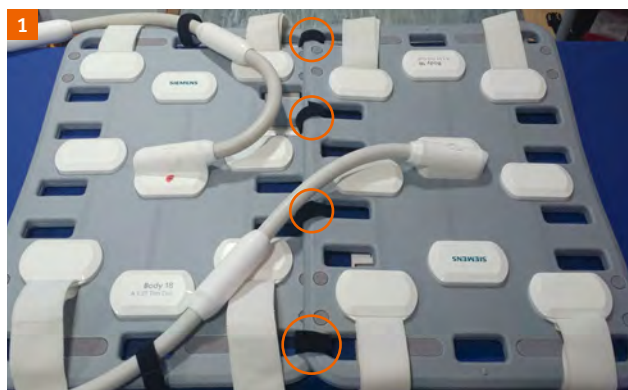


Figure 1: Improving workflow

Two Body 18 coils linked with Velcro loops (circled). This improves the reproducibility of positioning and reduces set-up time while remaining flexible.

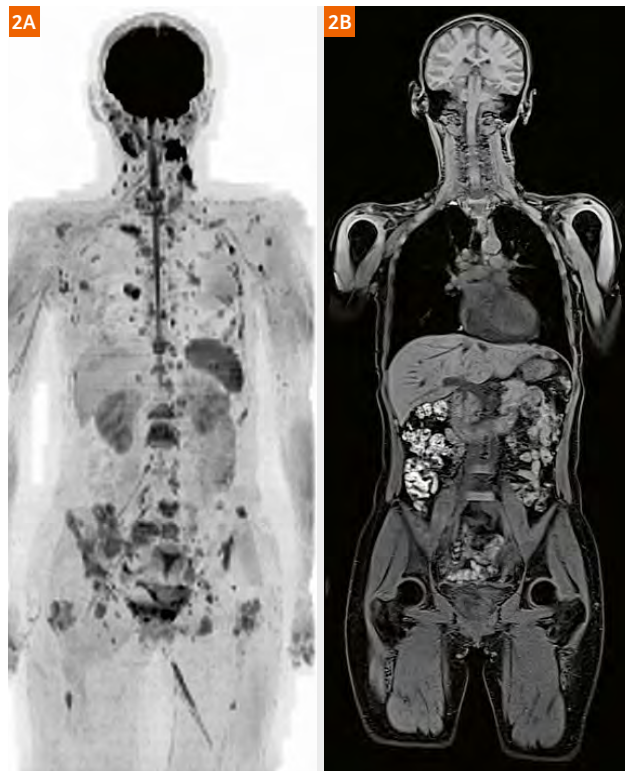


Figure 2: Range of imaging required

(2A) Coronal b900 MIP projection and (2B) composed coronal Dixon water images illustrating the vertex to mid-thigh range of coverage for this protocol.

Patient and equipment set-up

Patient comfort is absolutely critical to compliance with this protocol, so utilize any equipment required for comfort (e.g. extra padding, pillows, knee pad, etc.).

The patient should be advised to use the toilet where possible because the full protocol can take up to one hour.

Patients will warm up – particularly when scanning at 3T – and so the patient should wear a gown or entirely metal-free light clothing. Ensure adequate air flow to reduce the impact of heating.

Find out if the patient is able to hold their breath – if they can, use a breath-hold technique when scanning the chest and abdomen to reduce motion artifacts.

An optimal set-up includes the use of the anterior Head/Neck coil however this may not always be possible if the patient is kyphotic (Fig. 3).

Position the patient's head-first, with arms down by their side. The patient should be asked to move so that their shoulders are as close to the Head/Neck coil as possible, minimising any gap.

Place and secure anterior Body coils as required for coverage to mid-thigh. The superior margin of the first Body coil should be in line with SP1 as marked on the table-top.

As always, provide your patient with the call buzzer and adequate hearing protection.

Occasionally, due to patient body habitus, it may be necessary to place the first anterior Body coil overlapping the anterior part of the Head/Neck coil to ensure comfort.

Remember to make detailed notes of the patient set-up on their scanning record and ensure repeat visits use this set-up unless the patient's condition requires a change.

Use the positioning laser to set the start position to the inferior margin of the patient's chin – the FastView localizer will automatically move to begin acquiring at the vertex.

Form pads

Comfort and safety are key. Where possible, place foam padding between all contact points with coils, cables, the scanner and the table including elbows, sternum and knees.

Workstation

Before starting, make the following changes to the workstation options:

- Tim Planning UI active
- AutoCoilSelect ON
- Coupled graphics ON

Ready to go? It's time to scan.

Remember, you can follow along with the video from this point. Visit www.siemens.com/wb-mri to check it out.



Figure 3:

(3A) Optimal coil set-up. While it is important to keep the coils as close to the patient as possible, ensuring that anterior coils remain horizontal where possible, will maximize SNR.


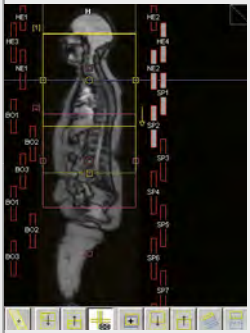
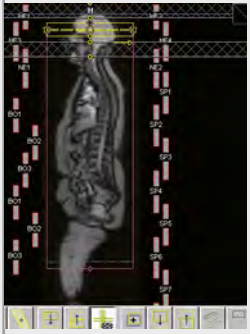
Position pads under the elbows and forearms.

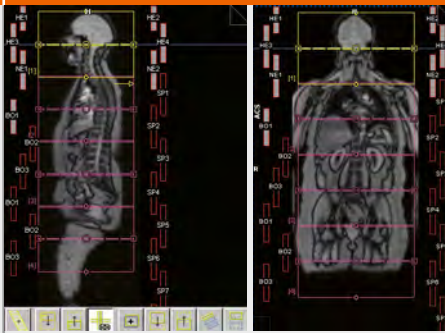
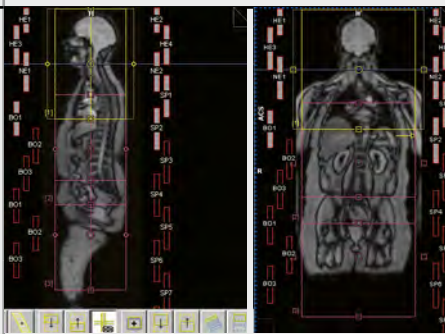
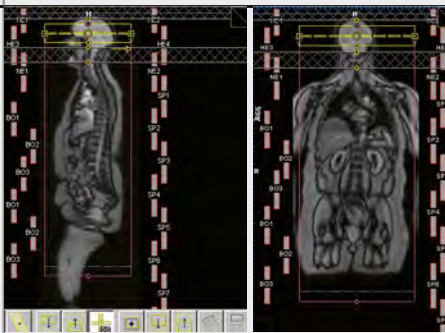
Ensure cables do not cross over or create loops.

Use a knee pad for patient comfort – use the same pad each time for reproducibility.

(3B) Comfort set-up. Patient comfort is increased at the cost of SNR in the head, neck and distal femurs.

Table 2: Step-by-step positioning examples and acquisition tips.

Sequence details	Positioning and ranges	Acquisition tips	Adjustable parameters	Notes
Step 1 FastView localizer Range: vertex to knees Plane: axial (MPRs will be generated) Method: TimCT		<p>On initial set-up, set the acquisition range to as far as your table movement range will allow</p> <p>TimCT adjustments are enabled: this sequence will perform imaging, 3D shim and TimCT adjustments (3x movements)</p> <p>Where not available: utilize a set'n'go multi-planar localizer covering head to knees</p> <p>Once the images have been reconstructed, begin planning the spine sequences</p>		<p>Until this sequence has fully completed the location of the anterior coils will not display on-screen</p> <p>Important: Don't proceed with planning beyond spinal imaging until the anterior coils are visible</p>
Step 2 STIR and T1 spine Range: whole spine Plane: sagittal to patient's anatomy Method: set'n'go		<p>Set'n'go with automatic composing enabled</p> <p>H>F coverage from skull base to at least S3</p> <p>Angle to cover the spine R>L – coupled graphics are ON so make this a best-fit</p> <p>To ensure anterior elements are not used during acquisition, at sequence set-up navigate to System: Misc: and set AutoCoilSelect OFF for both slice groups in both sequences once the required posterior elements are selected – save this into the protocol</p> <p>As all patients should always have their shoulders in the same position it is not usually necessary to change the active elements</p>	<p>Increase the number of slices to ensure full R>L coverage of the spine</p> <p>The TR may need to be increased to allow additional slices</p> <p>The FOV may be increased in order to include at least S3 for very tall patients</p>	<p>Ensure the same number of slices are used for each station AND each sequence type (both STIR and T1)</p> <p>Image contrast may be different between visits Record any changes</p> <p>Image resolution may be affected Usually this will not require matrix adjustments as long as the resolution remains constant between visits</p>
WAIT until FastView Localizer has fully completed before proceeding – this ensures anterior coils are visible and activate correctly with AutoCoilSelect ON				
Step 3 T1 Dixon TimCT Range: orbits to knees Plane: axial Method: TimCT Breath-holding where possible through the thorax and abdomen		<p>Where TimCT is not available: utilize an axial T1 Dixon set'n'go technique</p> <p>Adjust the position of the volume to ensure A>P coverage, equal R>L coverage using humeral heads as a guide, and ensure the blue isocenter line lies just inferior to the skull vertex (this allows the sequence to run – it may fail to start if not positioned in this manner)</p> <p>The volume will therefore not cover the entire brain – other sequences are included for this purpose</p> <p>If performing breath-holds: utilize the manual start-stop function to perform breath-holds while imaging the thorax and liver</p>	<p>Extend range as required to cover to mid-thigh</p>	<p>Detail the range selected on the patient's record to ensure reproducibility on future visits</p>

Sequence details	Positioning and ranges	Acquisition tips	Adjustable parameters	Notes
Step 4 Multi-b-value DWI Range: vertex to knees Plane: axial Method: set'n'go		<p>Adjust position of the set'n'go slice groups to ensure coverage from the skull vertex superiorly to at least mid-thigh inferiorly</p> <p>In the rare event that this range is insufficient, add another slice group (including overlap where required)</p> <p>Adjust position of slice groups to ensure A>P coverage, equal R>L coverage using humeral heads as a guide</p> <p>Manually activate the B01 element group on the first slice group – this will increase signal in the neck region</p>		<p>If using a fixed-frequency technique, ensure this value is copied or noted in order that it can be applied to the subsequent slice groups, however this should NOT be recorded on the patient's record as this value will necessarily change between visits</p> <p>A useful tip is to save this frequency as an image comment for the slice group</p>
Step 5 T1 Dixon CAIPIRINHA VIBE Range: vertex to knees Plane: coronal Method: set'n'go Breath-holding where possible		<p>Adjust position of slice groups to ensure A>P coverage, equal R>L coverage using humeral heads as a guide. In the H>F direction, ensure some air is included superior to the skull vertex to ensure full coverage of this structure</p> <p>If performing breath-holds: utilize manual or auto-matic breath-hold instructions as required</p>	<p>Slices per slab: increase to ensure full A>P coverage if this is insufficient by default</p> <p>Partial Fourier: use to decrease acquisition time for breath-holds where required</p>	<p>Your acquisition time will increase</p> <p>It may be necessary to introduce some partial fourier to control this</p> <p>Be conscious of the impact on SNR</p>
Step 6 T2 HASTE TimCT Range: orbits to knees Plane: axial Method: TimCT		<p>Where TimCT is not available: utilize an axial T2 HASTE set'n'go technique</p> <p>As this uses a copy reference from the T1 TimCT sequence it is not necessary to change the position of the volume, although care should be taken that the same range is acquired</p> <p>If the sequence fails to start, it is likely that a small 'footwards' change in the position of the slice group will allow it to run</p>	<p>Extend range as required to cover to mid-thigh</p>	<p>Detail the range selected on the patient's record to ensure reproducibility on future visits</p>

Sequence selection and discussion

If you are using the downloadable .exar1 protocol you will find sequences which have been included and optimized based upon the experience of scanning around 30 whole body examinations each week.

You should expect the protocol to take anywhere between 30 to 60 minutes depending on what is included.

Please see the MET-RADS document [1] for the clinical justification of sequences included, however it may be helpful to touch briefly upon how the sequences have been optimized and how they can be used clinically.

Spine sequences (STIR and T1-weighted):

Both sequences are used to detect and characterize bone lesions. High-resolution STIR imaging can also help to differentiate between active and inactive metastases. In our experience, T2 imaging without fat suppression does not provide significant additional diagnostic data.

Whole-body sequences (T1 Dixon and T2 HASTE):

The multiple contrasts generated by a T1 Dixon sequence can be used to calculate the signal fat fraction (F%). This can be used to quantitatively assess response to treatment or disease progression. Flip angles have been selected to

optimize T1 weighting; PD-weighted fat fractions may prove more accurate for F% estimates, but this comes at the expense of loss of the T1 contrast.

T2 HASTE imaging (in this case without fat suppression) facilitates the localization and characterization of pathologies. Asking patients to hold their breath during acquisition through the thorax and liver may improve detection of thoracic lesions or liver metastases; as such acquisition times have been kept to a minimum. The whole body axial T1 Dixon or T2 HASTE range can be acquired in under 4 minutes using TimCT where available.

Diffusion-weighted imaging:

Optimized for maximum signal generation, this sequence makes up the majority of the acquisition time. Depending on the capabilities of the scanner it is not unusual for each slice group to require over five minutes of acquisition time.

A **STIR technique** is used due to the improved fat suppression over a large FOV – although some centers have reported success using a SPAIR technique.

55 slices are acquired per slice group; any more and ADC values on end-of-group slices do tend to 'falsely' drift beyond acceptable margins [3]. An overlap can be introduced to counter this effect, although this is subject to optimization.

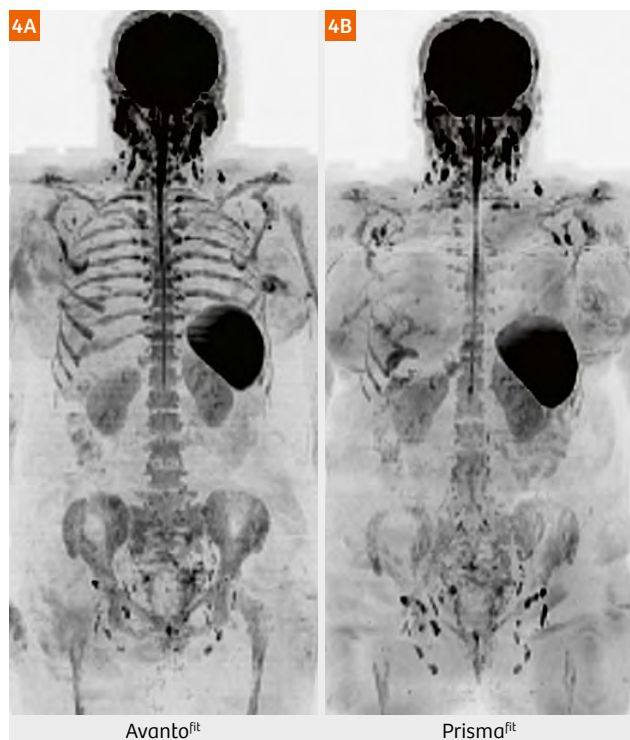


Figure 4: Coronal projections of b900 MIP with inverted greyscale
Images from a patient scanned at both (4A) 1.5T and (4B) 3T. Greater signal intensity of bone marrow is demonstrated at 1.5T due to the lower susceptibility effects of bone.

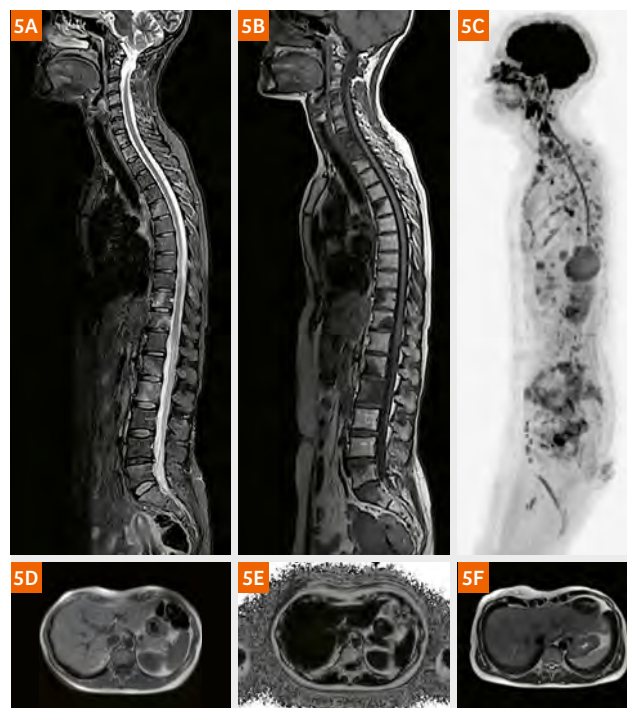


Figure 5: Example images from a completed dataset
(5A) Composed STIR and (5B) T1w spine images, (5C) sagittal projection of inverted b900 MIP, (5D) in-phase T1w Dixon and (5E) corresponding F%, (5F) T2w HASTE axial.

The optimal number of slices, and fat suppression technique, is entirely scanner-dependent and should be decided upon following rigorous testing and comparison (for example, acquiring fewer slices per station when using a shorter magnet).

Three b-values are used to optimize ADC calculation with the lowest set at $b = 50 \text{ mm}^2/\text{s}$. For the core protocol, two b-values are sufficient, thereby reducing the acquisition time (Table 1).

Asymmetric averaging is used to optimize acquisition time while ensuring sufficient SNR at higher b-values.

The **image scale correction** factor (**System: TxRx:**) is set at 3.5, optimizing the visual appearance of hypercellular lesions versus normal bone marrow on the high b-value images.

Diffusion schemes vary between imaging centers, however we have settled on a 3D diagonal, monopolar scheme for maximum signal generation with a minimal TE. Anisotropy-sensitive techniques are unnecessary.

Eddy currents and geometric distortions, while increased using this technique, are compensated for by using the newly-released SliceAdjust feature which allows for slice-specific shimming [4]. This technique is recommended where available.

Unfortunately, the downloadable .exar1 protocol does not feature this particular sequence due to licensing and compatibility issues. Manually apply the center frequency used for the first DWI station to all subsequent stations to avoid the so-called 'broken spine' artifact [5]. The .exar1 protocol has been set-up to allow frequency-fixing and features a 3-scan trace diffusion scheme to reduce the effect of geometric distortions where SliceAdjust is not available.

Scanning patients on different scanners is not recommended – especially at different field strengths (Fig. 4).

Post-processing

T1-weighted fat fractions (F%) should be generated from both the TimCT and coronal VIBE series. Add the FAT and WATER series together, and then divide the FAT by the ADD. Using a scaling factor of 1000 it is possible to window more finely. Using a ROI it is possible to read off the percentage of fat in an area which can be used to monitor response of bone metastases and liver fat condition.

Coronal MPRs and radial MIPs, generated from the highest b-value series, can be used during reporting but often serve as a very visual means of communicating findings to clinical colleagues. Generate coronal MPRs at 5 mm thickness and the radial MIPs every 3 degrees (120 images) displayed using an inverted grey-scale.

Conclusion

The tricky part with WB-MRI is the initial set-up – don't be surprised if your first efforts don't produce the results you expect. A typical completed data set (Fig. 5) can consist of over 6,000 images depending on the sequences chosen and reconstructions performed, but once the protocol is in place it's fairly straight-forward for operators to perform. In our experience, treating each examination as an experiment rather than a scan will lead to success.

Keep up to date at www.siemens.com/wb-mri for the latest news, case studies and the video tutorial.

Acknowledgements

Many thanks to everyone involved in the development of this protocol over the years including colleagues past and present from Paul Strickland Scanner Centre, The Institute of Cancer Research and Siemens Healthineers UK and Germany.

References

- 1 Padhani AR, Lecouvet FE, Tunariu N, et al. METastasis Reporting and Data System for Prostate Cancer : Practical Guidelines for Acquisition, Interpretation, and Reporting of Whole-body Magnetic Resonance Imaging-based Evaluations of Multiorgan Involvement in Advanced Prostate Cancer. *Eur Urol. European Association of Urology*; 2017;71:81–92.
- 2 Kosmin M, Makris A, Joshi PV, et al. The addition of whole-body magnetic resonance imaging to body computerised tomography alters treatment decisions in patients with metastatic breast cancer. *Eur J Cancer*; 2017;77:109–116
- 3 Winfield JM, Collins DJ, Priest AN, et al. A framework for optimization of diffusion-weighted MRI protocols for large field-of-view abdominal-pelvic imaging in multicenter studies. *Med. Phys*; 2016;43:95–110
- 4 Haibo Z, Huadan X, Stemmer A, et al. Slice Specific Shimming Improves the Image Quality of Whole-Body Diffusion-Weighted Examinations at 3T. *Magnetom Flash*; 2017: Magnetom Vida special issue;17–21
- 5 Koh DM, Blackledge M, Padhani AR, et al. Whole-Body Diffusion-Weighted MRI: Tips, Tricks, and Pitfalls. *AJR*; 2012;199:252–262

.....
Visit www.siemens.com/wb-mri to watch the video tutorial.



Contact

Will McGuire
 Deputy Superintendent Radiographer
 Paul Strickland Scanner Centre
 Northwood
 UK
will.mcguire@stricklandscanner.org.uk

MR-simulation for radiotherapy treatment planning of head and neck cancer using 3T MAGNETOM Vida

Daniela Thorwarth¹; Kerstin Zwirner²; René M. Winter¹; Stefan Welz²; Daniel Zips²; Sergios Gatidis³; Jakob Weiß³; Konstantin Nikolaou³

¹ Section for Biomedical Physics, Department of Radiation Oncology, University of Tübingen, Germany

² Department of Radiation Oncology, University of Tübingen, Germany

³ Department of Radiology, Diagnostic and Interventional Radiology, University of Tübingen, Germany

Abstract

Purpose

To explore the potential of the new 3T MAGNETOM Vida for magnetic resonance (MR)-based radiotherapy (RT) simulation and treatment planning in head and neck cancer (HNC) patients as well as for follow-up imaging during RT treatment.

Methods and materials

A set-up has been defined to position HNC patients in RT treatment position for MR examination using the MAGNETOM Vida system for anatomical and functional image data acquisition before and during RT. MR imaging was performed using a flexible 18-channel body coil (Body 18) to allow positioning of the patient using a thermoplastic mask for head and shoulder fixation as well as a flat table top. T1-weighted contrast-enhanced as well as T2-weighted images were acquired to assess anatomical information. Additionally, diffusion-weighted (DW) MR image sequences were used for assessing functional tissue information.

Results

Our first experience with the described setting showed that imaging with the MAGNETOM Vida system in RT treatment position using the flexible coil is possible. Anatomical and functional MR image data showed very high image quality. Furthermore, MR data could be easily fused to planning CTs of HNC patients and were used for more accurate target volume and organ at risk delineation.

Conclusion

MR imaging before and during RT in treatment position is possible in the MAGNETOM Vida system. With this set-up, high image quality can be achieved, which is essential for improved target volume delineation in MR-guided RT.

Introduction

Magnetic resonance (MR) guided radiotherapy (RT) approaches have gained a lot of attention in the last years [1]. MR offers high resolution imaging of anatomical and functional tissue properties. In contrast to computed tomography (CT), MR imaging provides high soft tissue contrast. Consequently, MR imaging data may be extremely valuable for target volume delineation in high precision RT and also for assessing anatomical and functional changes in the tumor region early during treatment [2, 3].



Figure 1: Patient examination in radiotherapy specific position using a flat table top, a thermoplastic mask and a flexible body coil in the MAGNETOM Vida.

The new generation of MR scanners, such as the 3T MAGNETOM Vida, offer extremely fast and accurate imaging sequences to assess anatomical and functional characteristics of tumors and may thus be ideal tools for MR-based RT simulation and response assessment during treatment.

The aim of this project was to develop an imaging set-up on the MAGNETOM Vida system allowing for MR imaging of head and neck cancer (HNC) patients in RT treatment position, i.e. using a thermoplastic mask and a flat table top for integration into RT target delineation and treatment planning [4, 5].

Methods and materials

Imaging set-up

To allow MR imaging of HNC patients in RT treatment position using the MAGNETOM Vida system, a flat table top overlay (Qfix, Avondale, PA, USA) is positioned on top of the regular patient table. Patients are positioned on this flat table top using a thermoplastic mask (ITV, Innsbruck, Austria) which is fixed at the table top using an MR-compatible mask holder system.

For MR imaging, the flexible 18-channel body coil (Body 18) is positioned around the RT mask with a distance of approximately 2 cm (cf. Fig. 1) in addition to the integrated 72-channel spine coil.

Using this set-up, MR imaging is performed before the start of RT treatment and after approximately two weeks of treatment to analyse early treatment response.

Imaging protocol

The MR imaging protocol consists of the following sequences:

1. T2w anatomical MRI:

A quiet T2w TSE anatomical sequence in transverse orientation is used for anatomical depiction of organ

structures and oncologic findings using the following parameters: matrix 192 x 192, resolution 1.3 x 1.3 mm², slice thickness 4 mm, TE = 53 ms, TR = 8180 ms, STIR fat sat.

2. Diffusion-weighted imaging (DWI):

DWI of the head/neck region is a challenge due to magnetic field inhomogeneities often resulting in image distortion, ghosting and signal loss which makes the use of DWI for RT planning difficult. The MAGNETOM Vida system offers technical solutions to overcome these limitations using readout-segmented (RESOLVE) echo-planar imaging (EPI) and slice specific shimming (SliceAdjust).

DWI was thus performed using a RESOLVE sequence with SliceAdjust and eight different b-values ($b = 0, 20, 40, 80, 120, 200, 500, 1000 \text{ s/mm}^2$) and the following parameters: matrix size 84 x 128, resolution 3 x 3 mm² (interpolated to 1.5 x 1.5 mm²), slice thickness 5 mm, TE = 44 ms, TR = 10800 ms, with water-specific excitation.

Subsequently, quantitative parameters are calculated including the apparent diffusion coefficient (ADC) but also perfusion parameters using multiple b-value images for intravoxel incoherent motion (IVIM) modeling. Thus detailed information about tissue perfusion and diffusion components can be obtained.

3. Dynamic contrast-enhanced imaging (DCE):

DCE of the neck poses a challenge due to the necessity for high temporal resolution and the occurrence of involuntary pharyngeal and laryngeal motion. In order to overcome these challenges, the MAGNETOM Vida offers time-resolved radial imaging with compressed sensing reconstruction (GRASP). We implemented GRASP DCE of the neck region for quantitative analysis of tumor perfusion after injection of 0.1 mmol Gadobutrol/kg using the following parameters: matrix

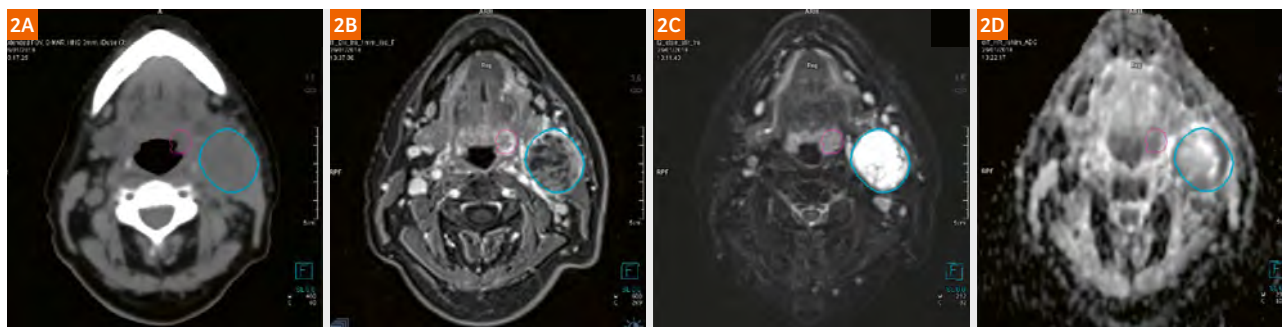


Figure 2:

CT and MR images for RT simulation in a patient with HNC. The primary tumor region is contoured in pink, a large lymph node metastasis in blue. Image data are shown in the following sequence: **(2A)** planning CT, **(2B)** T1w MR post contrast, **(2C)** T2w MR image (STIR) and **(2D)** ADC map.

size 224 x 224, resolution 1.1 x 1.1 mm², slice thickness 3 mm, TR = 4.14 ms, TE = 1.86 ms with spectral fat saturation. Dynamic frames were reconstructed with a time resolution of 4.3 s.

4. T1w post contrast:

After DCE, a highly resolved isotropic T1-weighted contrast-enhanced VIBE sequence is performed for detailed anatomical depiction of the structures of interest using the following parameters: matrix size 270 x 320, resolution 1 x 1 x 1 mm³, TR 6.56 ms, TEs 2.46 and 3.72 ms, with Dixon fat sat.

Axial, coronal and sagittal reformations are automatically performed within the *syngo* RT image suite.

Target volume delineation for radiotherapy treatment planning

After successful image acquisition, MR imaging data were transferred to the RT treatment planning system or a dedicated contouring system (RT image suite, Siemens Healthcare, Erlangen, Germany). Here, the MR data was registered to the RT planning computed tomography (CT) scan and used for target volume and organ at risk (OAR) delineation.

Results

First experience on five patients with this set-up showed MR images of high, diagnostic quality. In particular, we observed high image quality and anatomical accuracy of DWI using the RESOLVE sequence with slice adjust and of DCE using GRASP. An image example is provided in Figure 2.

Patients tolerated imaging in RT treatment position well, as the net imaging time for the RT simulation sequences was approximately 20 minutes. MR imaging data for each patient was transferred to the RT treatment planning system (Oncentra Masterplan, Elekta AB, Sweden) as well as to the *syngo.via* application RT image Suite for registration to the planning CT and tumor as well as OAR contouring. Rigid as well as deformable image registration with the planning CT worked very well due to the same patient positioning with flat table top and thermoplastic mask. Figure 2 presents an example of a patient examined with the 3T MAGNETOM Vida system for RT simulation.

In addition to anatomical information assessed from T1w and T2w MR sequences we aim for measuring functional properties of tumors using DW-MR imaging. IVIM data with eight different b-values were of very high quality in the first patients. Hence, quantitative ADC maps as well as information on perfusion and diffusion from a bi-exponential fit could be acquired.

Discussion

With the proposed set-up, consisting of a thermoplastic mask, a flat table top and a flexible body coil high quality anatomical and functional MR imaging in RT treatment position is possible for patients with HNC. Thus, this set-up constitutes an optimal tool for pre-treatment RT simulation in order to gain accuracy in target volume delineation as well as for the assessment of functional information in terms of ADC or IVIM data. Advanced MR sequence techniques such as RESOLVE DWI with slice adjust and GRASP together with the available hardware of the Vida System provide the necessary qualitative and quantitative image quality for precise RT planning.

Moreover, additional follow-up data can be acquired early during RT where this set-up may be beneficial to quantify radiation induced functional changes on a regional or even voxel level. Such quantitative and geometrically accurate data might be used in the future as a basis for individualized RT treatment interventions as e.g. dose painting.

References

- 1 Legendijk JJW, Raaymakers BW, Van den Berg CAT, Moerland MA, Philippens ME, van Vulpen M. MR guidance in radiotherapy. *Phys Med Biol* 2014;59:R349-69.
- 2 Van der Heide UA, Houweling AC, Groenendaal G, Beets-Tran RGH, Lambin P. Functional MRI for radiotherapy dose painting. *Magn Reson Imaging* 2012;30:1216-23.
- 3 Baumann M, Krause M, Overgaard J, et al. Radiation oncology in the era of precision medicine. *Nat Rev Cancer* 2016;16:234-9.
- 4 Harvey S, McJury M, Tho LM, et al. The influence of MRI scan position with oropharyngeal cancer undergoing radical radiotherapy. *Radiat Oncol* 2013;8:129.
- 5 Fortunati V, Verhaart RF, Verdujin GM, et al. MRI integration into treatment planning of head and neck tumors: Can patient immobilization be avoided? *Radiother Oncol* 2015;115:191-4.

Contact

Daniela Thorwarth
Section of Biomedical Physics
University Hospital for Radiation Oncology
University of Tübingen
Hoppe-Seyler-Strasse 3
72076 Tübingen
Germany
daniela.thorwarth@med.uni-tuebingen.de



Dynamic contrast-enhanced magnetic resonance imaging, diffusion kurtosis imaging, and intravoxel incoherent motion diffusion-weighted imaging: MRI functional parameters in the assessment of pancreatic cancer

Vincenza Granata¹; Roberta Fusco¹; Mario Sansone²; Roberto Grassi³; Francesca Maio¹; Raffaele Palaia⁴; Fabiana Tatangelo⁵; Gerardo Botti⁵; Robert Grimm⁷; Steven Curley⁶; Francesco Izzo⁴; Antonella Petrillo¹

¹ Radiology Unit, Istituto Nazionale Tumori IRCCS “Fondazione G. Pascale”, Naples, Italy

² Department of Information Technology and Electrical Engineering (DIETI), Naples, Italy

³ Radiology Unit, Second University of Naples, Italy

⁴ Hepatobiliary Surgical Oncology Unit, Istituto Nazionale Tumori IRCCS “Fondazione G. Pascale”, Naples, Italy

⁵ Diagnostic Pathology Unit, Istituto Nazionale Tumori IRCCS “Fondazione G. Pascale”, Naples, Italy

⁶ Department of Surgery, Baylor College of Medicine, Houston, TX, USA

⁷ Siemens Healthineers, Erlangen, Germany

Abstract

Purpose

To evaluate the diagnostic potential of perfusion parameters derived from dynamic contrast-enhanced MR imaging (DCE-MRI), diffusion kurtosis imaging (DKI), and parameters derived from the intravoxel incoherent motion model (IVIM)-based diffusion-weighted imaging (DWI) in differentiating between pancreatic tumors and normal pancreatic parenchyma.

Methods

We analyzed 24 patients with a histopathological pancreatic tumor diagnosis (median age: 71 years) and 24 patients without pancreatic lesions (median age: 56 years). For each voxel, DCE-MRI, IVIM, and DKI parameters were extracted. Accuracy was assessed using a non-parametric test and a receiver operating characteristic (ROC) curve.

Results

Based on a Kruskal-Wallis test, statistically significant differences were observed in the median values among the groups for the DKI mean diffusivity (MD), IVIM perfusion fraction (fp), and IVIM diffusion coefficient (Dt). In distinguishing between normal pancreatic parenchyma and pancreatic tumors, MD had an accuracy of 78%.

Conclusions

IVIM and DKI-derived parameters, as well as some of the DCE-MRI semi-quantitative parameters could be helpful in the differentiation of normal pancreatic parenchyma and pancreatic tumors.

Introduction

Pancreatic adenocarcinomas (PDACs) account for 90% of cancers of the pancreas and are the fourth most common cause of cancer-related death in the United States. In contrast to the steady improvement in survival for most cancers, advances in the field of pancreatic cancer have been slow. The five-year relative survival rate is currently just 8%. This low rate is partly because more than half of all cases are diagnosed at a distant stage, for which the five-year survival rate is 3% [1].

Despite significant technical advances in imaging, such as multidetector computed tomography (MDCT) and magnetic resonance imaging (MRI), the correct diagnosis of solid pancreatic lesions remains challenging. This is related to the overlapping imaging features with benign lesions [2]. Yet proper detection and characterization of pancreatic lesions is essential, since therapeutic approaches and the associated prognoses are considerably different, depending on the tumor type and grade [3]. Reliable, accurate imaging is critical for proper tumor staging: in fact, pancreatic adenocarcinoma infiltrates lymphatic vessels early and local infiltrative disease can be manifest as subtle infiltration of peripancreatic tissue. This local invasion can result in the true extent and stage of the tumor to be underestimated and can be a cause of aborted surgical resection if not identified preoperatively [4]. The best hope for patients is in earlier detection of pancreatic adenocarcinomas. Thus, a noninvasive imaging modality that provides higher tumor conspicuity would be invaluable in improving clinical outcomes [5, 6]. How to analyze organ-specific vascularity to differentiate between malignant and benign pancreatic lesions remains an unsolved problem. Quantitative analysis of enhancement patterns and perfusion parameters using dynamic contrast-enhanced MR imaging (DCE-MRI) has been shown to be both objective and helpful in the evaluation of pancreatic lesions [7, 8]. In recent years, we have seen unprecedented use of abdominal MR imaging in the evaluation of pancreatic lesions, with diffusion-weighted imaging (DWI) attracting much attention as a tool for detecting malignancies [9–12]. DWI can provide additional information on focal pancreatic lesions by demonstrating more restricted diffusion in solid malignant tumors than in benign inflammatory or cystic lesions. This can be indicated by a decreased apparent diffusion coefficient (ADC) [13–16]. However, the diffusion-weighted signal and ADC values may be influenced not only by molecular diffusion but also by microcirculation or blood perfusion, and ADC values may therefore be contaminated by perfusion effects. This limits the reliability of ADC in characterizing pancreatic lesions [17, 18]. Microcirculation

or perfusion effects can be distinguished from true tissue diffusion by using sufficient b-value sampling and a bi-exponential curve fit analysis with the intravoxel incoherent motion (IVIM) model [17–21].

Previous studies on IVIM in the pancreas have demonstrated that the reduced ADC in PDACs can be attributed to a difference in perfusion fraction (f_p), which is reduced in PDACs [20], and that f_p is a better DWI imaging-derived parameter for differentiating mass-forming pancreatitis and PDACs than ADC values [21]. To date, however, there has only been a small number of studies which have explored the value of IVIM in differentiating between malignant pancreatic tumors and benign lesions. Also, the conventional DWI model is based on the assumption that water diffusion within a voxel has a single component and exhibits Gaussian behavior where water molecules freely diffuse [18, 19]. However, due to the presence of microstructures (i.e., two tissue types or components within one voxel, organelles, and cell membranes), random motion or diffusion of thermally agitated water molecules within biological tissue exhibits non-Gaussian behavior [22]. In 2005, Jensen and colleagues proposed a non-Gaussian diffusion model called diffusion kurtosis imaging (DKI) [22]. This model includes the kurtosis coefficient (K), which measures the deviation of tissue diffusion from a Gaussian model, and the diffusion coefficient (D) with the non-Gaussian bias correction. DKI performed better than conventional ADC in tumor detection and staging [23–29].

The purpose of this study is to evaluate the diagnostic potential of perfusion parameters obtained by DCE-MRI, DKI and IVIM-derived parameters in DWI for the differentiation of pancreatic tumors and normal pancreatic parenchyma.

Materials and methods

Study population

The Scientific Institutional Review Board at the Istituto Nazionale Tumori approved this retrospective study, and the required informed consent was obtained for each patient. We conducted a search of the Institute's surgical database from January 2011 to October 2017 and selected 42 patients with pancreatic cancer who had undergone surgical resection. The inclusion criteria for the study population were as follows:

- A. Patients who had pathologically proven pancreatic cancer;
- B. Patients who had undergone both DCE-MRI and DWI;
- C. Patients who had an interval of less than one month between imaging and pathologic diagnosis;

D. Availability of diagnostic-quality pictures of the cut sections of the resected specimens in patients who had undergone surgical resection for the matching of imaging and pathology findings. The exclusion criteria were as follows:

1. Conflict between the imaging-based diagnosis and the pathologically confirmed diagnosis;
2. Limitations of pathologic imaging correlation owing to poor image quality;
3. No available DCE-MRI and DWI.

Based on these criteria the study group consisted of 24 patients (14 men and 10 women with a median age of 71 years; age range: 53–85 years). We also conducted a search of the Institute's radiological database during the study period and selected a control group of patients without pancreatic lesions that had undergone DCE-MRI and DWI upper abdomen studies to reduce spectrum bias. A total of 24 patients (13 men, 11 women with a median age of 56 years; age range: 33–78 years) who fitted these criteria were enrolled for the study.

MR protocol

The MR protocol consisted of morphological and functional imaging including DCE-MRI and DWI sequences. Imaging was performed with a 1.5T scanner (MAGNETOM Symphony, Siemens Healthcare, Erlangen, Germany) equipped with a phased-array body coil. Patients were placed in a supine, head-first position.

A morphological pre-contrast axial T2-weighted (T2w) 2D half-Fourier acquisition single-shot turbo spin-echo (HASTE) was performed with and without fat suppression. The acquisition parameters were: TR/TE = 1500/90 ms, slice thickness = 5 mm, gap between slice = 0 mm, flip angle = 180°, matrix = 320 x 320, field of view (FOV) = 380 x 380 mm². Morphological pre-contrast axial T1-weighted (T1w) fast low angle shot (FLASH) 2D in- and out-of-phase images were obtained with the following acquisition parameters: TR/TE = 160/4.87 ms, slice thickness = 5 mm, gap between slice = 0 mm, flip angle = 70°, matrix = 192 x 256, FOV = 285 x 380 mm². Morphological pre-contrast axial T1w fat-suppressed FLASH 2D out-of-phase imaging was completed with the following acquisition parameters: TR/TE = 178/2.3 ms, slice thickness = 3 mm, gap between slice = 0 mm, flip angle = 80°, matrix = 416 x 512, FOV = 325 x 400 mm². Morphological post-contrast axial and coronal fat-suppressed T1w volumetric interpolated breath-hold examination (VIBE) images were recorded with the following acquisition parameters: TR/TE = 4.89/2.38 ms, slice thickness = 3 mm, gap between slice = 0 mm, flip angle = 10°, matrix = 320 x 260, FOV = 325 x 400 mm².

A free breathing axial single-shot echoplanar DWI pulse sequence was performed with the parameters: TR/TE = 7500/91 ms; slice thickness = 3 mm; flip angle = 90°, matrix = 192 x 192, FOV = 340 x 340 mm²; tri-directional diffusion gradients with b-values of 0, 50, 100, 150, 400, and 800 s/mm².

As regards the DCE-MR imaging, we obtained one sequence before and 120 sequences (with no delay) after intravenous injection of 2 mL/kg of a positive, gadolinium-based paramagnetic contrast medium (Gadobutrol Gd-DTPA, Bayer Pharma AG, Berlin, Germany). The contrast medium was injected using a Spectris Solaris® EP MR pump (MEDRAD Inc., Indianola, PA), with a flow rate of 2 mL/s, followed by a 10 mL saline flush at the same rate. DCE-MRI T1w time-resolved angiography with stochastic trajectories (TWIST) 3D axial images were acquired in order to increase temporal resolution. Acquisition parameters were: TR/TE = 3.01/1.09 ms, flip angle = 25°, matrix = 256 x 256, slice thickness = 2 mm, gap = 0, FOV = 300 x 300 mm², temporal resolution = 3 seconds, pA: 0.20, pB: 0.20.

MR image analysis

Regions of interest (ROIs) were manually drawn by two expert radiologists in consensus, while simultaneously avoiding encircling any distortion artefacts. One radiologist with over 20 years of clinical experience and one with 8 years of clinical experience in interpreting abdominal MR imaging studies drew ROIs on DCE images with virtual fat suppression obtained by subtracting the pre-contrast from the post-contrast image and on the DWI image with the highest b-value. For patients with pancreatic cancer, the tumor was contoured slice by slice to obtain the neoplastic volume of interest. For patients without pancreatic cancer, we selected 4 regions of interest in the pancreas parenchyma (head, neck, body, and tail) to obtain the median value of pancreatic parenchyma tissue.

Features from DCE-MRI and DWI data were computed pixel by pixel to obtain the median value of the ROIs.

DCE-MRI features

For each voxel, 8 TIC shape descriptors were computed using an approach previously reported in [30]: maximum signal difference (MSD), the time to peak (TTP), the WI slope (WIS), the WO slope (WOS), the WI intercept (WII), the WO intercept (WOI), the WOS/WIS ratio, and the WOI/WII ratio.

DCE-MRI parameters were obtained using in-house prototype software developed within MATLAB R2007a (The MathWorks Inc., Natick, MA, USA)¹.

¹ The information shown herein refers to products of 3rd party manufacturers and thus are in their regulatory responsibility. Please contact the 3rd party manufacturer for further information.

DWI features

For each voxel, 6 features were extracted from DWI data using the mono-exponential model, the diffusion kurtosis imaging model, and the intra voxel incoherent motion model [17, 18; 31–39].

DWI signal decay is most commonly analyzed using the monoexponential model [17, 18]:

Equation 1

$$ADC = \frac{\ln \left(\frac{S_0}{S_b} \right)}{b}$$

where S_b is the MRI signal intensity with diffusion weighting b , S_0 is the non-diffusion-weighted signal intensity, and ADC is the apparent diffusion coefficient.

For a voxel with a large vascular fraction, the MRI data decay can deviate from a monoexponential form, in particular showing a rapid decay in the range of low b -values generated by the IVIM effect [17, 18, 33]. Thus, in addition to the monoexponential model, a biexponential model was used to estimate the IVIM-related parameters of pseudo-diffusivity (D_p indicated also with D^*), perfusion fraction (f_p), and tissue diffusivity (D_t):

Equation 2

$$\frac{S_0}{S_b} = f_p \cdot \exp(-b \cdot D_p) + (1 - f_p) \cdot \exp(-b \cdot D_t)$$

Moreover, diffusion kurtosis imaging was included in the analysis in order to obtain the final fitted images (mean of diffusion coefficient (MD) and mean of diffusional kurtosis (MK)).

Multi-b DW images were obtained through voxel-by-voxel fitting using the diffusion kurtosis signal decay equation (3) by applying a two-variable linear least squares algorithm as used in a previous study [22]:

Equation 3

$$S(b) = S_0 \exp \left(-b \cdot D + \frac{1}{6} b^2 \cdot D^2 \cdot K \right)$$

In this equation, D is a corrected diffusion coefficient; and K is the excess diffusion kurtosis coefficient. K describes the degree of deviation of molecular motion from the perfect Gaussian distribution. When K is equal to 0, equation (3) evolves into a conventional monoexponential equation (1):

The difference between D and ADC is that D is a corrected form of ADC for use in non-Gaussian circumstances.

The parameters of conventional DWI (ADC), IVIM (f_p , D_t , D_p), and DKI (MK and MD) were obtained from the multi-b DWI data with all measured b values using the prototype post-processing software Body Diffusion Toolbox² (Siemens Healthcare, Erlangen, Germany).

Statistical analysis

Continuous variables were presented as the median \pm standard deviation (SD). All parameters that had been subdivided into the three groups were compared using the nonparametric Kruskal-Wallis test. Receiver operating characteristic (ROC) curves were also calculated to determine each parameter value with the aim of assessing the ability to differentiate between pancreatic tumors and pancreatic parenchyma tissue. The optimal cut-off values (obtained according to the maximal Youden index = sensitivity + specificity - 1), the corresponding sensitivity, specificity, positive predictive value (PPV), negative predictive value (NPV), and accuracy were calculated.

A P value of < 0.05 was considered statistically significant. The Statistics Toolbox produced by MATLAB R2007a (The MathWorks Inc., Natick, MA, USA)¹ was used to perform statistical analysis.

Results

Table 1 shows the median value and standard deviation (SD) value for pancreatic tumor and pancreatic parenchyma tissue.

Based on a Kruskal-Wallis test, statistically significant differences were observed in median values among the groups for MD, f_p , and D_t , while there were no significant differences among these groups for dynamic parameters. Table 2 shows the diagnostic accuracy of MR-extracted parameters in distinguishing between normal pancreatic parenchyma and pancreatic tumors. WII , MD, f_p , and D_p showed an accuracy of $\geq 68\%$. MD had the best results with an accuracy of 78%.

Discussion

The purpose of this study is to evaluate the diagnostic potential of perfusion parameters obtained by DCE-MRI, DKI, and IVIM-derived parameters in DWI for the differentiation of pancreatic tumors and normal pancreatic parenchyma.

¹ The information shown herein refers to products of 3rd party manufacturers and thus are in their regulatory responsibility. Please contact the 3rd party manufacturer for further information.

² WIP, the product is currently under development and is not for sale in the US and in other countries. Its future availability cannot be ensured.

The accuracy of DCE-MRI in the assessment of pancreatic cancer remains unclear. One reason for this is that in pancreatic ductal adenocarcinoma the microvascular component is poorly represented. This can probably be explained by the functional impairment of vessels, often observed in tumors, as they are characteristically leaky, fragile, and incompletely formed, and also by the presence of a prominent stromal matrix embedding the vessels. Moreover, activated pancreatic stellate cells produce increasing fibrous stroma in the central areas of the tumor, which compresses the blood vessels, leading to changes in vascularity and perfusion [7, 8]. Several studies have evaluated the feasibility of DCE-MRI for the characterization of solid pancreatic diseases [7, 8, 11].

Kim et al. [7] evaluated 24 patients with pancreatic cancers, eight with pancreatic neuroendocrine tumors (PNETs), three with chronic pancreatitis, and 10 with a normal pancreas. For the different groups, they assessed K_{trans} , kep (flow of contrast agent to the plasma from the EES), and the initial area under the concentration curve (iAUC). They showed that K_{trans} , kep , and iAUC values in patients with pancreatic cancer ($0.042 \text{ min}^{-1} \pm 0.023$, $0.761 \text{ min}^{-1} \pm 0.529$, and

$2.841 \text{ mmol/sec} \pm 1.811$, respectively) were significantly lower than in patients with a normal pancreas ($0.387 \text{ min}^{-1} \pm 0.176$, $6.376 \text{ min}^{-1} \pm 2.529$, and $7.156 \text{ mmol/sec} \pm 3.414$, respectively) ($P < 0.05$ for all). In addition, the kep values of PNETs and normal pancreases also differed ($P < 0.0001$), and K_{trans} , kep , and iAUC values of pancreatic cancers and PNETs differed significantly ($P < 0.0001$, $P = .038$, and $P < 0.0001$, respectively).

Bali et al. [8] evaluated 28 patients with surgically resectable focal pancreatic lesions. DCE-MRI quantitative parameters derived from one-compartment (K_{trans} and distribution fraction [f]) and two-compartment (K_{trans} and tissue volume fraction occupied by vascular space [vp]) pharmacokinetic models were correlated with fibrosis content and microvascular density (MVD) counts in focal lesions and nontumoral tissue. The pharmacokinetic parameters were compared with tumoral and nontumoral tissue. The study also assessed the diagnostic performance of DCE-MRI fibrosis detection. It showed that K_{trans} values were significantly lower in primary malignant tumors compared with benign lesions ($P = .023$) and nontumoral pancreatic tissue downstream ($P < .001$) and upstream ($P = .006$); f and vp were also significantly higher in

	Normal pancreatic parenchyma tissue		Pancreatic cancer		P value from Kruskal-Wallis test
	Median	SD	Median	SD	
MSD [A.U.]	39.20	31.99	42.70	27.60	0.71
TTP [A.U.]	36.25	19.93	25.00	18.58	0.97
WOS [A.U.]	-0.42	17.81	-1.10	52.06	0.99
WOI [A.U.]	60.27	48.96	38.43	84.78	0.10
WIS [A.U.]	3.75	17.84	20.91	25.49	0.57
WII [A.U.]	35.95	58.94	15.47	97.71	0.15
WOS_WIS [A.U.]	-0.03	13.85	-0.01	3.31	0.82
WOI_WII [A.U.]	1.04	4.06	-0.94	10.40	0.21
ADC [$\text{mm}^2/\text{s} \times 10^{-6}$]	1397.50	309.75	1196.50	281.18	0.17
MK [$\times 10^{-3}$]	1193.85	1393.73	1399.30	384.69	0.33
MD [$\text{mm}^2/\text{s} \times 10^{-6}$]	2843.20	728.35	1849.50	603.95	0.00
f_p [$\% \times 10^{-1}$]	225.00	90.42	144.20	81.53	0.00
Dt [$\text{mm}^2/\text{s} \times 10^{-6}$]	1263.00	357.21	1018.60	328.62	0.75
Dp [$\text{mm}^2/\text{s} \times 10^{-5}$]	135.60	57.30	112.80	56.62	0.02

Table 1:

Median and standard deviation (SD) value for each MR-extracted parameter in two groups: normal pancreatic parenchyma and pancreatic tumor.

primary malignant tumors compared with nontumoral pancreatic tissue downstream ($P = .012$ and $.018$, respectively). Fibrosis was negatively correlated with K_{trans} and positively with f and vp . MVD was positively correlated with f and vp . Sensitivity and specificity in detecting fibrosis were 65% (24 of 37) and 83% (10 of 12) for K_{trans} one-compartment (cut-off value: 0.35 min^{-1}) and 76% (28 of 37) and 83% (10 of 12) for K_{trans} two-compartment (cut-off value: 0.29 min^{-1}), respectively.

We evaluated semi-quantitative descriptors of the contrast agent time course, such as MSD, TTP, WIS, WOS, WII, WOI, the WOS/WIS ratio, and the WOI/WII ratio. Our findings showed that there were no differences in the dynamic parameters among the groups with the exception of a statistically not significant difference between WIS and K_{trans} [30].

Diffusion parameters can be assessed using DWI [39]. The IVIM model provides a theoretical framework that allows for the separate extraction of a flowing blood volume fraction (perfusion) and microstructural information from DWI. Thus, IVIM is gaining interest in oncological applications of DWI as it allows a combined quantification

of a flowing blood volume fraction, a perfusion-free diffusion coefficient (microstructural parameter), and a pseudodiffusion coefficient. This is associated with the blood movement in the capillary network without a contrast agent [36, 37].

Several studies have reported that IVIM is a promising tool in identifying pancreatic cancer, since IVIM-derived parameters are useful in the characterization of solid focal lesions [22, 40, 41].

Kang et al. [40] evaluated the diagnostic performance of ADC and IVIM-derived parameters for distinguishing between common pancreatic tumors, chronic pancreatitis, and normal pancreases and for the characterization of the malignancy potential of intraductal papillary mucinous neoplasms. Ninety-three patients with surgically resected pancreatic tumors (39 PDACs, 17 NETs, and 37 IPMNs), seven patients with chronic pancreatitis, and 26 patients with a normal pancreas were included in their study. The ADC, slow component of diffusion (D_{slow}), incoherent microcirculation (D_{fast}), and perfusion fraction (fp) were calculated. They showed that the D_{fast} and fp values of PDACs were significantly lower than those of normal

	AUC	SEN	SPEC	PPV	NPV	ACC	CUT-OFF
MSD	0.47	0.14	0.96	0.75	0.54	0.56	92.21
TTP	0.54	0.59	0.61	0.59	0.61	0.60	31.02
WOS	0.51	0.64	0.48	0.54	0.58	0.56	-1.54
WOI	0.68	0.86	0.48	0.61	0.79	0.67	30.87
WIS	0.36	1.00	0.04	0.50	1.00	0.51	-44.80
WII	0.67	0.55	0.91	0.86	0.68	0.73	33.49
WOS_WIS	0.47	0.36	0.78	0.62	0.56	0.58	0.17
WOI_WII	0.59	0.77	0.52	0.61	0.71	0.64	-0.92
ADC	0.61	0.55	0.78	0.71	0.64	0.67	1330.99
MK	0.42	0.82	0.30	0.53	0.64	0.56	997.00
MD	0.82	0.86	0.70	0.73	0.84	0.78	2168.48
fp	0.79	0.82	0.70	0.72	0.80	0.76	167.81
Dt	0.59	0.55	0.74	0.67	0.63	0.64	1197.58
Dp	0.67	1.00	0.39	0.61	1.00	0.69	68.91

Table 2:

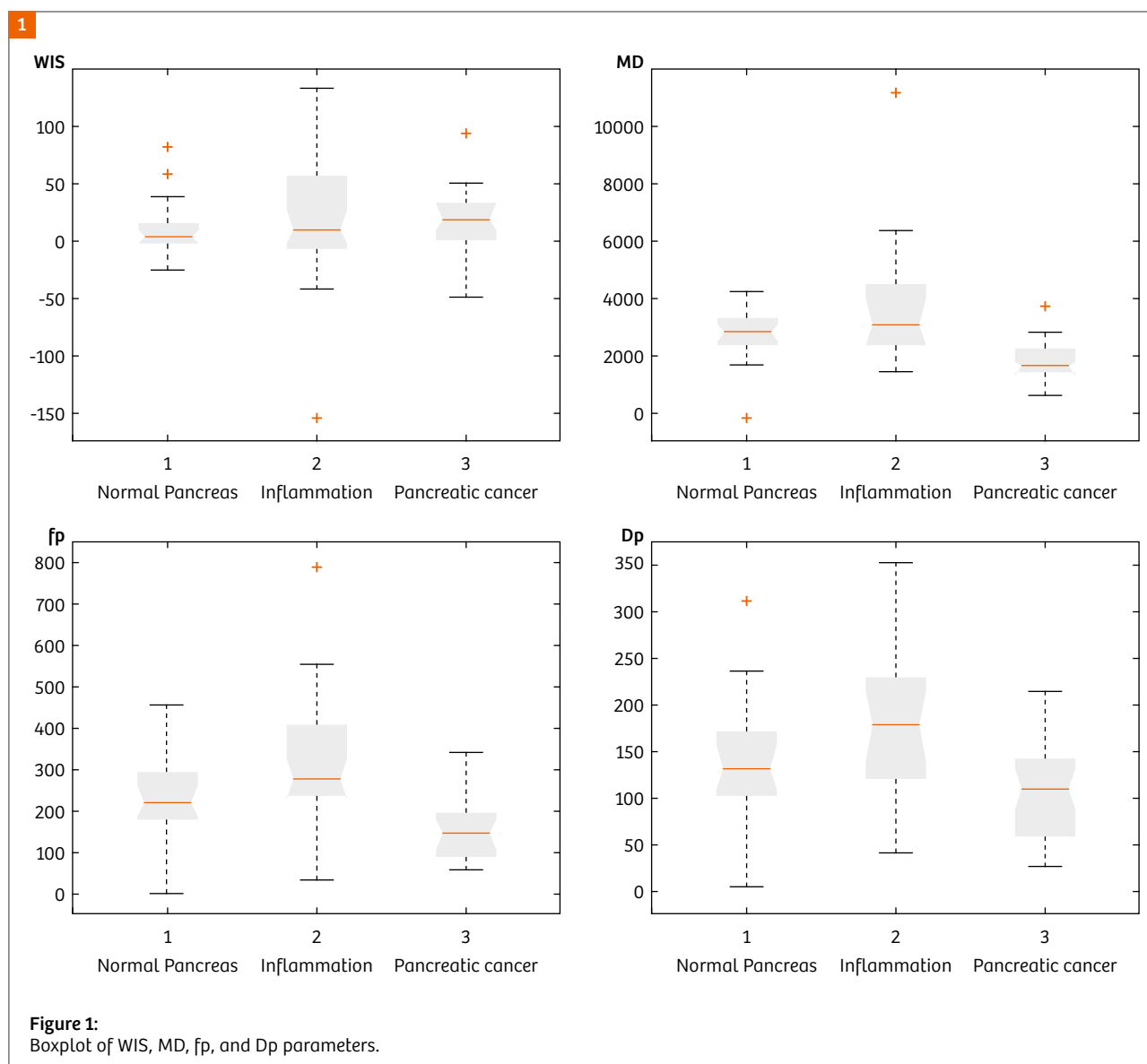
Diagnostic accuracy of MR-extracted parameters in distinguishing between normal pancreatic parenchyma and pancreatic tumors. Parameters with high accuracy and the area under the curve were underlined in bold.

Note: AUC = area under curve; SEN = sensitivity; SPEC = specificity; NPV = negative predictive value; ACC = accuracy

pancreases, chronic pancreatitis, and NETs (all $P < .05$). To differentiate between PDACs and NETs, f_p and D_{fast} showed a significant difference ($P < .0001$ for both) and were more useful parameters than ADC and D_{slow} in ROC analysis (all $P < .05$). Malignant IPMNs had significantly lower ADC and D_{slow} values and higher D_{fast} and f_p values compared to benign IPMNs (all $P < .05$). In ROC analysis, f_p showed the highest area under the ROC curve for distinguishing malignant from benign IPMNs [40]. They concluded that perfusion might be a more important factor than diffusion in differentiating between PDAC, normal pancreases, chronic pancreatitis, and NETs. In addition, f_p showed the highest area under the ROC curve for differentiating between malignant and benign IPMNs among ADC and IVIM-derived parameters. We therefore

believe that IVIM DWI is a valuable tool for characterizing the most common solid or cystic malignant tumors in the pancreas, owing to its ability to provide information not only on cellularity (D_{slow}) but also on perfusion (D_{fast} and f_p) [40].

Klauss et al. [41] investigated the correlation between parameters derived from the IVIM model and histologically determined microvasculature in pancreatic ductal adenocarcinomas (PDACs) and pancreatic neuroendocrine tumors (PNETs). In their study, intravoxel incoherent motion parameters were extracted from two types of volume of interest (VOIs), one VOI that encompassed the total tumor volume (TTV) and another VOI that corresponded to the histological regional tumor location



(RTV). They showed that blood volume fraction f_p was significantly lower in PDACs than in PNETs ($9.9\% \pm 5.4\%$ vs. $15.5\% \pm 5.2\%$; $P < 0.0001$) and the diffusion coefficient D_t was significantly higher ($1.2 \pm 0.18 \times 10^{-3}$ vs. $1.03 \pm 0.15 \times 10^{-3} \text{ mm}^2/\text{s}$; $P = 0.001$) in PDACs. There was no significant difference in the pseudodiffusion coefficient D_p ($44.9 \pm 52.9 \times 10^{-3}$ vs. $53.8 \pm 51.2 \times 10^{-3} \text{ mm}^2/\text{s}$). Microvessel density was significantly lower in PDACs ($36.8 \pm 25.9/\text{mm}^2$ vs. $80.0 \pm 26.1/\text{mm}^2$; $P = 0.0005$) than in PNETs. When derived from the RTV, the flowing blood volume fraction f_p and MVD of PDACs and PNETs showed excellent correlation ($r = 0.85$). The correlation using the TTV was moderate (0.64). The f_p (RTV and TTV) and microvessel area showed moderate correlation ($r = 0.54/0.47$).

In our study we evaluated the ADC and the IVIM-related parameters (D_p , f_p , and D_t), the kurtosis coefficient that signifies the deviation of tissue diffusion from a Gaussian model, and the diffusion coefficient with the correction of non-Gaussian bias by DKI. Recently, DKI has been used to assess therapy response in different kinds of tumors [42–44].

To the best of our knowledge there is no recent study analyzing perfusion and diffusion features (ADC, IVIM, and DKI-derived parameters) to differentiate between pancreas cancer tissue and normal tissue.

According to our findings, based on a Kruskal-Wallis test, there were statistically significant differences in the median values among the groups for MD, f_p , and D_t . In distinguishing between normal pancreatic parenchyma and pancreatic tumors, MD had the best results with an accuracy of 78%.

In our study, the perfusion-related factors of PDACs (f_p and D_p) and the MD of diffusion kurtosis imaging differed from those seen in patients with normal pancreatic parenchyma and showed better diagnostic performance than ADC. Although the differential diagnosis of PDACs and normal pancreatic parenchyma is usually easily assigned, there can be enough overlap in imaging features to cause occasional problems with differentiation. Therefore, the significantly different perfusion-related factors of PDACs and normal pancreatic parenchyma could help clinicians make the most accurate diagnosis. Moreover, these parameters should also help in assessing response to systemic and pancreatic-directed therapies by identifying responders and non-responders as quickly as possible.

Conclusion

An accurate diagnosis of pancreatic cancer is essential to facilitate accurate staging which, in turn, enables proper therapeutic management. Parameters derived from IVIM and diffusion kurtosis, as well as semi-quantitative parameters from DCE-MRI could be helpful in distinguishing between normal pancreatic parenchyma and pancreatic tumors. The parameters that allow the best classification of normal pancreatic parenchyma tissue and pancreatic tumors are MSD, WOI_WII, MD of diffusion kurtosis imaging, and f_p .

References

- 1 Siegel RL, Miller KD, Jemal A. Cancer statistic, 2017. *CA Cancer J Clin*. 2017 Jan;67(1):7–30.
- 2 Granata V, Fusco R, Catalano O, Setola SV, de Lutio di Castelguidone E, Piccirillo M, et al. Multidetector computer tomography in the pancreatic adenocarcinoma assessment: an update. *Infect Agent Cancer*. 2016 Nov 15;11:57. Li D, Xie K, Wolff R, Abbruzzese JL. Pancreatic cancer. *Lancet*. 2004;363(9414): 1049–57.
- 3 Brennan DD, Zamboni GA, Raptopoulos VD, Kruskal JB. Comprehensive preoperative assessment of pancreatic adenocarcinoma with 64-section volumetric CT. *Radiographics*. 2007 Nov–Dec;27(6):1653–66.
- 4 Fukukura Y, Shindo T, Hakamada H, Takumi K, Umanodan T, Nakajo M, et al. Diffusion-weighted MR imaging of the pancreas: optimizing b-value for visualization of pancreatic adenocarcinoma. *Eur Radiol*. 2016 Oct;26(10):3419–27.
- 5 Baek JH, Lee JM, Kim SH, et al. Small (< 3 cm) solid pseudopapillary tumors of the pancreas at multiphasic multidetector CT. *Radiology*. 2010;257(1):97–106.
- 6 Casneuf VF, Delrue L, Van Damme N, et al. Noninvasive monitoring of therapy-induced microvascular changes in a pancreatic cancer model using dynamic contrast-enhanced magnetic resonance imaging with P846, a new low-diffusible gadolinium-based contrast agent. *Radiat Res*. 2011;175(1):10–20.
- 7 Kim JH, Lee JM, Park JH, Kim SC, Joo I, Han JK, et al. Solid pancreatic lesions: characterization by using timing bolus dynamic contrast-enhanced MR imaging assessment—a preliminary study. *Radiology*. 2013 Jan;266(1):185–96.
- 8 Bali MA, Metens T, Denolin V, Delhaye M, Demetter P, Closset J, et al. Tumoral and nontumoral pancreas: correlation between quantitative dynamic contrast-enhanced MR imaging and histopathologic parameters. *Radiology*. 2011 Nov;261(2):456–66.
- 9 Kartalis N, Lindholm TL, Aspelin P, Permert J, Albiin N. Diffusion-weighted magnetic resonance imaging of pancreas tumors. *Eur Radiol*. 2009;19(8):1981–90.
- 10 Inan N, Arslan A, Akansel G, Anik Y, Demirci A. Diffusion-weighted imaging in the differential diagnosis of cystic lesions of the pancreas. *AJR Am J Roentgenol*. 2008;191(4):1115–21.
- 11 Choi SY, Kim SH, Kang TW, Song KD, Park HJ, Choi YH. Differentiating Mass-Forming Autoimmune Pancreatitis From Pancreatic Ductal Adenocarcinoma on the Basis of Contrast-Enhanced MRI and DWI Findings. *AJR Am J Roentgenol*. 2016 Feb;206(2):291–300.
- 12 Wang Y, Miller FH, Chen ZE, et al. Diffusion-weighted MR imaging of solid and cystic lesions of the pancreas. *RadioGraphics*. 2011;31(3):E47–E64.
- 13 Lee SS, Byun JH, Park BJ, et al. Quantitative analysis of diffusion-weighted magnetic resonance imaging of the pancreas: usefulness in characterizing solid pancreatic masses. *J Magn Reson Imaging*. 2008;28(4):928–36.

- 14 Ma C, Guo X, Liu L, Zhan Q, Li J, Zhu C, et al. Effect of region of interest size on ADC measurements in pancreatic adenocarcinoma. *Cancer Imaging*. 2017 May 2;17(1):13.
- 15 Muraoka N, Uematsu H, Kimura H, et al. Apparent diffusion coefficient in pancreatic cancer: characterization and histopathological correlations. *J Magn Reson Imaging*. 2008;27(6):1302–8.
- 16 Ma C, Liu L, Li J, Wang L, Chen LG, Zhang Y, et al. Apparent diffusion coefficient (ADC) measurements in pancreatic adenocarcinoma: A preliminary study of the effect of region of interest on ADC values and interobserver variability. *J Magn Reson Imaging*. 2016 Feb;43(2):407–13.
- 17 Le Bihan D, Breton E, Lallemand D, Aubin ML, Vignaud J, Laval-Jeantet M. Separation of diffusion and perfusion in intravoxel incoherent motion MR imaging. *Radiology*. 1988;168(2):497–505.
- 18 Le Bihan D, Breton E, Lallemand D, Grenier P, Cabanis E, Laval-Jeantet M. MR imaging of intravoxel incoherent motions: application to diffusion and perfusion in neurologic disorders. *Radiology*. 1986;161(2):401–7.
- 19 Koh DM, Collins DJ, Orton MR. Intravoxel incoherent motion in body diffusion-weighted MRI: reality and challenges. *AJR Am J Roentgenol*. 2011;196(6):1351–61.
- 20 Lemke A, Laun FB, Klauss M, et al. Differentiation of pancreas carcinoma from healthy pancreatic tissue using multiple b-values: comparison of apparent diffusion coefficient and intravoxel incoherent motion derived parameters. *Invest Radiol*. 2009;44(12):769–75.
- 21 Klauss M, Lemke A, Grünberg K, et al. Intravoxel incoherent motion MRI for the differentiation between mass forming chronic pancreatitis and pancreatic carcinoma. *Invest Radiol*. 2011;46(1):57–63.
- 22 Jensen JH, Helpert JA. MRI quantification of non-Gaussian water diffusion by kurtosis analysis. *NMR Biomed*. 2010;23:698–710.
- 23 Sun K, Chen X, Chai W, Fei X, Fu C, Yan X, et al. Breast Cancer: Diffusion Kurtosis MR Imaging-Diagnostic Accuracy and Correlation with Clinical-Pathologic Factors. *Radiology*. 2015;277:46–55.
- 24 Suo S, Chen X, Wu L, Zhang X, Yao Q, Fan Y, et al. Non-Gaussian water diffusion kurtosis imaging of prostate cancer. *Magn Reson Imaging*. 2014;32:421–7.
- 25 Nogueira L, Brandão S, Matos E, Nunes RG, Loureiro J, Ramos I, et al. Application of the diffusion kurtosis model for the study of breast lesions. *Eur Radiol*. 2014;24:1197–203.
- 26 Rosenkrantz AB, Sigmund EE, Winnick A, Niver BE, Spieler B, Morgan GR, et al. Assessment of hepatocellular carcinoma using apparent diffusion coefficient and diffusion kurtosis indices: preliminary experience in fresh liver explants. *Magn Reson Imaging*. 2012;30:1534–40.
- 27 Van Cauter S, Veraart J, Sijbers J, Peeters RR, Himmelreich U, De Keyser F, et al. Gliomas: diffusion kurtosis MR imaging in grading. *Radiology*. 2012;263:492–501.
- 28 Raab P, Hattingen E, Franz K, Zanella FE, Lanfermann H. Cerebral gliomas: diffusional kurtosis imaging analysis of microstructural differences. *Radiology*. 2010;254:876–81.
- 29 Rosenkrantz AB, Sigmund EE, Johnson G, Babb JS, Mussi TC, Melamed J, et al. Prostate cancer: feasibility and preliminary experience of a diffusional kurtosis model for detection and assessment of aggressiveness of peripheral zone cancer. *Radiology*. 2012;264:126–35.
- 30 Fusco R, Petrillo A, Petrillo M, Sansone M. Use of Tracer Kinetic Models for Selection of Semi-Quantitative Features for DCE-MRI Data Classification. *Applied Magnetic Resonance*. 2013;44(11):1311–24.
- 31 Deux J-F, Brugieres P, Rahmouni A. Liver cirrhosis: intravoxel incoherent motion MR imaging – pilot study. *Radiology*. 2008;249(3):891–9.
- 32 Wirestam R, Borg M, Brockstedt S, Lindgren A, Holtas S, Stahlberg F. Perfusion-related parameters in intravoxel incoherent motion MR imaging compared with CBV and CBF measured by dynamic susceptibility contrast MR technique. *Acta Radiol*. 2001;42(2):123–8.
- 33 Moteki T, Horikoshi H. Evaluation of hepatic lesions and hepatic parenchyma using diffusion-weighted echo-planar MR with three values of gradient b-factor. *J. Magn. Reson. Imaging* 2006;24(3):637–45.
- 34 Callot V, Bennett E, Decking UKM, Balaban RS, Wen H. In vivo study of microcirculation in canine myocardium using the IVIM method. *Magn. Reson. Med*. 2003;50(3):531–40.
- 35 Yao L, Sinha U. Imaging the microcirculatory proton fraction of muscle with diffusion-weighted echo-planar imaging. *Acad. Radiol*. 2000;7(1):27–32.
- 36 Granata V, Fusco R, Catalano O, Guarino B, Granata F, Tatangelo F, et al. Intravoxel incoherent motion (IVIM) in diffusion-weighted imaging (DWI) for Hepatocellular carcinoma: correlation with histologic grade. *Oncotarget*. 2016 Nov 29;7(48):79357–64.
- 37 Fusco R, Sansone M, Petrillo A. A comparison of fitting algorithms for diffusion-weighted MRI data analysis using an intravoxel incoherent motion model. *MAGMA*. 2017 Apr;30(2):113–20.
- 38 Granata V, Fusco R, Catalano O, Filice S, Amato DM, Nasti G, et al. Early Assessment of Colorectal Cancer Patients with Liver Metastases Treated with Antiangiogenic Drugs: The Role of Intravoxel Incoherent Motion in Diffusion-Weighted Imaging. *PLoS One*. 2015 Nov 13;10(11):e0142876.
- 39 Fusco R, Sansone M, Petrillo A. The Use of the Levenberg–Marquardt and Variable Projection Curve-Fitting Algorithm in Intravoxel Incoherent Motion Method for DW-MRI Data Analysis. *Applied Magnetic Resonance*. 2015;46(5):551–8.
- 40 Kang KM, Lee JM, Yoon JH, et al. Intravoxel incoherent motion diffusion weighted MR imaging for characterization of focal pancreatic lesions. *Radiology*. 2014;270:444–53.
- 41 Klauss M, Mayer P, Bergmann F, Maier-Hein K, Hase J, Hackert T, et al. Correlation of Histological Vessel Characteristics and Diffusion-Weighted Imaging Intravoxel Incoherent Motion-Derived Parameters in Pancreatic Ductal Adenocarcinomas and Pancreatic Neuroendocrine Tumors. *Invest Radiol*. 2015 Nov;50(11):792–7.
- 42 Chen Y, Ren W, Zheng D. Diffusion kurtosis imaging predicts neoadjuvant chemotherapy responses within 4 days in advanced nasopharyngeal carcinoma patients. 2015;42:1354–61.
- 43 Yu J, Xu Q, Song JC, Li Y, Dai X, Huang DY, et al. The value of diffusion kurtosis magnetic resonance imaging for assessing treatment response of neoadjuvant chemoradiotherapy in locally advanced rectal cancer. *Eur Radiol*. 2017;27:1848–57.
- 44 Goshima S, Kanematsu M, Noda Y, Kondo H, Watanabe H, Bae KT. Diffusion kurtosis imaging to assess response to treatment in hypervascular hepatocellular carcinoma. *AJR Am J Roentgenol*. 2015;204:W543–9.

Contact

Roberta Fusco
Department of Radiology
“Istituto Nazionale Tumori -
IRCCS Fondazione G. Pascale”
Via Mariano Semmola
80131 Naples
Italy Tel.: +3908 1590 3738
r.fusco@istitutotumori.na.it



A single-breath-hold magnetic resonance cholangiopancreatography using Compressed Sensing: A pilot study at 1.5T and 3T

Hélène Blaise¹; Khalid Ambarki Ph.D.²; Elisabeth Weiland, Ph.D.³; Valérie Laurent, M.D., Ph.D.¹

¹ Department of Radiology, Nancy University Hospital, Vandoeuvre-lès-Nancy, France

² Siemens Healthineers, Saint-Denis, France

³ Siemens Healthineers, Erlangen, Germany

Abstract

Background and purpose

Rapid imaging is essential in clinical MR imaging of the abdomen. Currently available high-resolution 3D magnetic resonance cholangiopancreatography (MRCP) techniques are typically respiratory triggered and time demanding.

The aim of the present study is to compare the image quality of a single-breath-hold Compressed Sensing (CS) 3D SPACE MRCP and the conventional respiratory-triggered (RT) 3D SPACE¹ MRCP sequence at both magnetic field strengths (1.5T and 3T).

Materials and methods

40 patients were enrolled for this retrospective study; 20 patients were scanned at 1.5T and 20 patients at 3T. The mean age was 54 years ranging from 22 to 85 years. Of those, 16 were male and 24 were female.

Results

No difference was found in the overall image quality and blurring between the conventional RT MRCP sequence and the prototype single-breath-hold CS MRCP sequence at 1.5T. At 3T, significantly better overall quality and sharpness was observed in the single-breath-hold CS MRCP images compared to the conventional method.

Conclusions

The single-breath-hold CS MRCP prototype provides a similar or superior overall quality and sharpness compared to the respective conventional sequence at 1.5T and 3T.

¹ WIP, the product is currently under development and is not for sale in the US and in other countries. Its future availability cannot be ensured.

Introduction

Magnetic resonance cholangiopancreatography (MRCP) is a non-invasive imaging technique that allows evaluation of the bile and pancreatic duct anatomy and provides highly relevant information in cases of stenosis of the gall bladder duct or occlusion of the pancreatic duct indicating related diseases. Currently, MRCP is either performed with breath-hold thick-slab two-dimensional acquisition or with respiratory-triggering (RT) using three-dimensional acquisition. MRCP can be performed using heavily T2-weighted fast-spin echo sequences such as sampling perfection with application-optimized contrast using different flip angle evolutions (SPACE) [1].

This technique is a three-dimensional acquisition typically providing images of isotropic and high spatial resolution

with good background suppression. In clinical routine, maximum-intensity-projection reconstructions can be done to provide a comprehensive overview of the biliary and the pancreatic systems. Due to breathing motion, the MRCP SPACE sequence uses a prospective RT technique to ensure that data is only acquired in a specific phase of the respiratory cycle. Thus, only a small amount of *k*-space data is acquired during each respiratory cycle. Consequently, the acquisition time is long, with an average of 6 minutes in our experience. Under unfavorable circumstances, it may even exceed 10 minutes when the patient has an irregularly respiratory rate. Furthermore, it is hard to breathe regularly over 6 minutes and patients with abdominal pain tend to have an irregular respiratory rate, significantly increasing blurring and motion artifacts. In MR imaging of the abdomen, MRCP is one of the longest

sequences and often longer acquisition time is associated with sub-optimal image quality [2, 3]. There is a clinical need for better techniques that shorten the scan time without comprising on image quality.

It is well known that MR images are compressible and contain redundant information. If only the main components of an MR image can be assessed, this will allow the measurement of fewer data and thus will accelerate the acquisition process. This challenge can be achieved using Compressed Sensing (CS) MR technique. The CS MR technique is based on three notions [4]:

1. Image sparsity
2. Incoherent sampling
3. Use of appropriated reconstruction method to enforce sparsity for image recovery.

An example of image sparsity is MR angiography where only few pixels (vessels) are bright and the majority of pixels are dark due to background tissue suppression. The information content of the image can thus be represented by a small amount of measurements. The second aspect is the incoherent sampling which is a requirement for subsequent optimization of image quality with iterative reconstruction. A well-established method for incoherent sampling is the random or pseudo-random fashion method where phase-encoded lines are omitted causing incoherent, 'noise-like' artifacts instead of discrete artifacts. Images with incoherent artifacts can't be used for clinical diagnosis. These incoherent artifacts need to be eliminated using appropriate iterative reconstruction methods in order to reconstruct images with quality comparable when incoherent k -space sampling is not applied.

CS was successfully applied in cerebral MR angiography imaging in different diseases [5, 6]. It is obvious that similarities exist between MR angiography and MRCP, therefore it is reasonable to assume that CS can be applied for MRCP. Recently, these three basic requirement concepts for CS were applied for MRCP application using a new compressed sensing 3D SPACE MRI sequence. This technique is based on a pseudo-random under-sampling with a variable density Poisson disc pattern. Previous studies have shown promising findings using a single-breath-hold 3D CS-MRCP sequence with comparable findings as the RT conventional MRCP sequence [2, 7]. To our knowledge, the breath-hold CS MRCP sequence has not been evaluated at 3T and 1.5T field strength. In the present study, we used a similar single-breath-hold (17 seconds) protocol of a non-product CS-SPACE MRCP sequence¹ and described our experience at both 1.5T and 3T field strengths on a 1.5T MAGNETOM

Avanto^{fit} system (using software version syngo MR E11C) and a 3T MAGNETOM Skyra system (using software version syngo MR E11C).

The purpose of the present study is to compare the image quality of a prototype single-breath-hold CS-SPACE MRCP sequence and the conventional RT SPACE MRCP.

Method

Patient group study

40 patients were recruited for this retrospective study, the MR examinations were performed during the period from January through April 2018. 20 patients were scanned at 1.5T and 20 at 3T. The mean age was 54 years ranging from 22 to 85 years. Of those, 16 patients were male and 24 were female.

Magnetic resonance imaging

The patients were scanned using a 1.5T MRI system (MAGNETOM Avanto^{fit}, Siemens Healthcare, Erlangen, Germany) or a 3T (MAGNETOM Skyra, Siemens Healthcare, Erlangen, Germany). Patients were scanned each time in supine position, feet-first. An 18-channel body-matrix coil and a 32-channel posterior spine coil were used. Only coil elements that covered the volume-of-interest were selected for all MRCP acquisitions.

All MRI investigations included the conventional RT SPACE MRCP sequence as well as the single-breath-hold CS-SPACE MRCP. The conventional MRCP sequence was always performed first. The main MRI parameters are described below:

Conventional RT SPACE MRCP: FOV = 400 x 400 mm²; TR = variable depending on respiratory rate; TE = 711 ms / 705 ms (1.5T/3T); FA = 140°/120°; number of averages = 1.4/2.0; parallel imaging factor = 2; 64 coronal sections were acquired. The acquired voxel size was 1.1 x 1.0 x 1.5 mm³ (reconstructed to 1 x 1 x 1.2 mm³) at 1.5T and 1.2 x 1.0 x 1.5 mm³ (reconstructed to 0.6 x 0.6 x 1.2 mm³) at 3T. The acquisition time was between 4 and 10 minutes.

Single-breath-hold CS-SPACE MRCP: FOV = 400 x 400 mm²; TR = 1700 ms; TE = 426 ms / 432 ms; FA = 120°/120°; number of excitation = 1.9/1.4; 64 coronal sections were acquired. The acquired size was 1.2 x 1.2 x 2.4 mm³ (reconstructed to 0.6 x 0.6 x 1.2 mm³) at 1.5T and 1 x 1 x 2.2 mm³ (reconstructed to 0.5 x 0.5 x 1.1 mm³) at 3T. The acquisition time was about 17 seconds for both magnetic field strengths. During the acquisition of this sequence an acceleration factor of 23 was achieved.

¹ WIP, the product is currently under development and is not for sale in the US and in other countries. Its future availability cannot be ensured.

CS reconstruction was done inline based on a SENSE optimization problem to enforce sparsity. Spatial regularization was performed using Haar wavelet transform [6]. 20 iterations were executed to reconstruct the images and the required time for reconstruction was about 6 minutes.

Image quality assessment

The native images of both MRCP sequences were independently analyzed by two raters. The image quality grading was based on the visualization of the main structures of the bile and pancreatic duct systems: Right and left intrahepatic ducts (IHDs), pancreatic duct and cystic duct. These structures are shown in Figure 1 on a reconstructed MIP data from both MRCP sequences in the same patient. The grading of the visualization of these structures as well as the overall image quality were based

on a 5-points scale. Background suppression and image blurring was evaluated using a 4-points scale as shown on Table 1. The average of both raters was used for statistical analysis to compare BH CS MRCP and RT MRCP sequences.

Statistical analysis

All measured variables (overall quality, blurring, background suppression and duct visualization) were expressed as mean ± standard deviation (SD). A two-tailed Wilcoxon signed-rank test was used to compare the mean values of the measured variables between the conventional RT-SPACE and the single-breath hold CS MRCP sequence. A non-parametric test (Wilcoxon test) was used because the small sample size (n = 20) of the present study. P-values < 0.05 were considered as statistically significant.

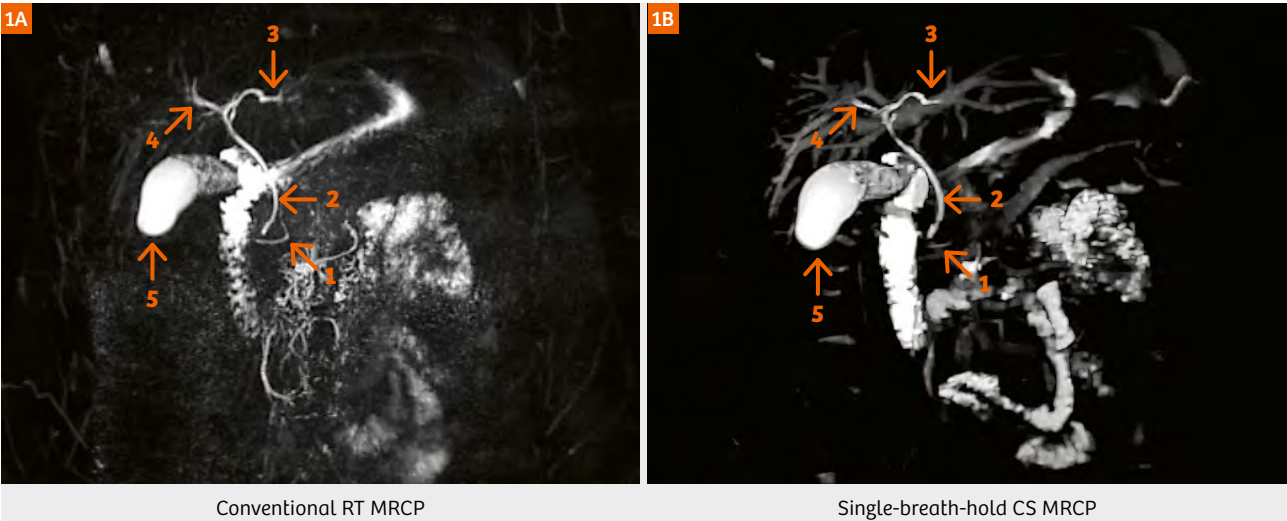


Figure 1: MIP of the conventional respiratory-triggering (RT) and the single-breath-hold Compressed Sensing (CS) MRCP sequence in the same patient at 1.5T. Numbers represent the main pancreatic and bile ducts: (1) Pancreatic; (2) bile; (3) left intrahepatic; (4) right intrahepatic and (5) gallbladder.

Image quality variables	Overall image quality	Image blurring	Background suppression	Duct visualization
Score 1	Not diagnostic	Not diagnostic	Significant background signal	No visualization
Score 2	Poor	Substantial blur	Substantial background signal	Poor visualization
Score 3	Fair	Mild blur	Noticeable background signal	Partial visualization
Score 4	Good	No or minimal blur	Sufficient background suppression	Clear and not complete
Score 5	Excellent	Not applicable	Not applicable	Clear and complete

Table 1: Measured variables and scores to compare the conventional respiratory-triggering and the single-breath-hold Compressed Sensing MRCP sequence.

Results

Table 2 shows the results of the evaluation of MRCP images at 1.5T.

At 1.5T, no difference was found in the overall image quality and image blurring between the conventional RT MRCP sequence and the prototype single-breath-hold CS MRCP sequence.

Furthermore, the main hepatic and bile ducts were equally visualized in the conventional MRCP and the single-breath-hold CS MRCP images. However, the background suppression was significantly better in the conventional sequence compared to the prototype sequence.

The evaluation of the MRCP images at 3T is shown in Table 3.

At 3T, the overall image quality was significantly improved and significantly less blurring was observed in the single-breath-hold CS MRCP images compared to the conventional RT MRCP images.

Interestingly, the cystic and the pancreatic ducts were better visualized in the prototype MRCP images. There was a tendency for a better visualization of the right and left intrahepatic ducts in the single-breath-hold CS MRCP images (Table 3). Background suppression was similar for both MRCP sequences.

Figures 2 and 3 show the comparison between the conventional respiratory-triggering MRCP and the respective single-breath-hold CS MRCP sequence at 1.5T and at 3T.

Continued on page 66

Measured variables	Conventional RT MRCP	Single-breath-hold CS MRCP	P-value
Overall image quality	3.23 ± 1.51	3.58 ± 1.17	0.34
Blurring	3.05 ± 1.00	3.13 ± 1.10	0.93
Background suppression	3.48 ± 0.73	2.00 ± 0.83	< 0.001
Cystic duct	3.20 ± 1.72	3.23 ± 1.70	0.95
Pancreatic duct	2.65 ± 1.52	2.58 ± 1.54	0.95
Right intrahepatic duct	3.48 ± 1.46	3.55 ± 1.49	0.95
Left intrahepatic duct	3.55 ± 1.28	3.75 ± 1.38	0.72

Table 2:

Values of the measured variables (mean ± SD) of MRCP images at 1.5T using the conventional respiratory triggering (RT) and the single-breath-hold compressed sensing (CS) sequence.

Measured variables	Conventional RT MRCP	Single-breath-hold CS MRCP	P-value
Overall image quality	3.25 ± 0.99	4.17 ± 0.71	< 0.001
Blurring	2.92 ± 0.92	3.60 ± 0.45	< 0.001
Background suppression	3.27 ± 0.82	3.57 ± 0.47	0.09
Cystic duct	2.55 ± 1.40	3.40 ± 1.34	0.005
Pancreatic duct	3.52 ± 1.14	4.27 ± 0.68	0.02
Right intrahepatic duct	3.55 ± 1.24	4.05 ± 0.97	0.06
Left intrahepatic duct	3.52 ± 1.16	3.95 ± 1.02	0.13

Table 3:

Values of the measured variables (mean ± SD) of MRCP images at 3T using the conventional respiratory triggering (RT) and the single-breath-hold compressed sensing (CS) sequence.

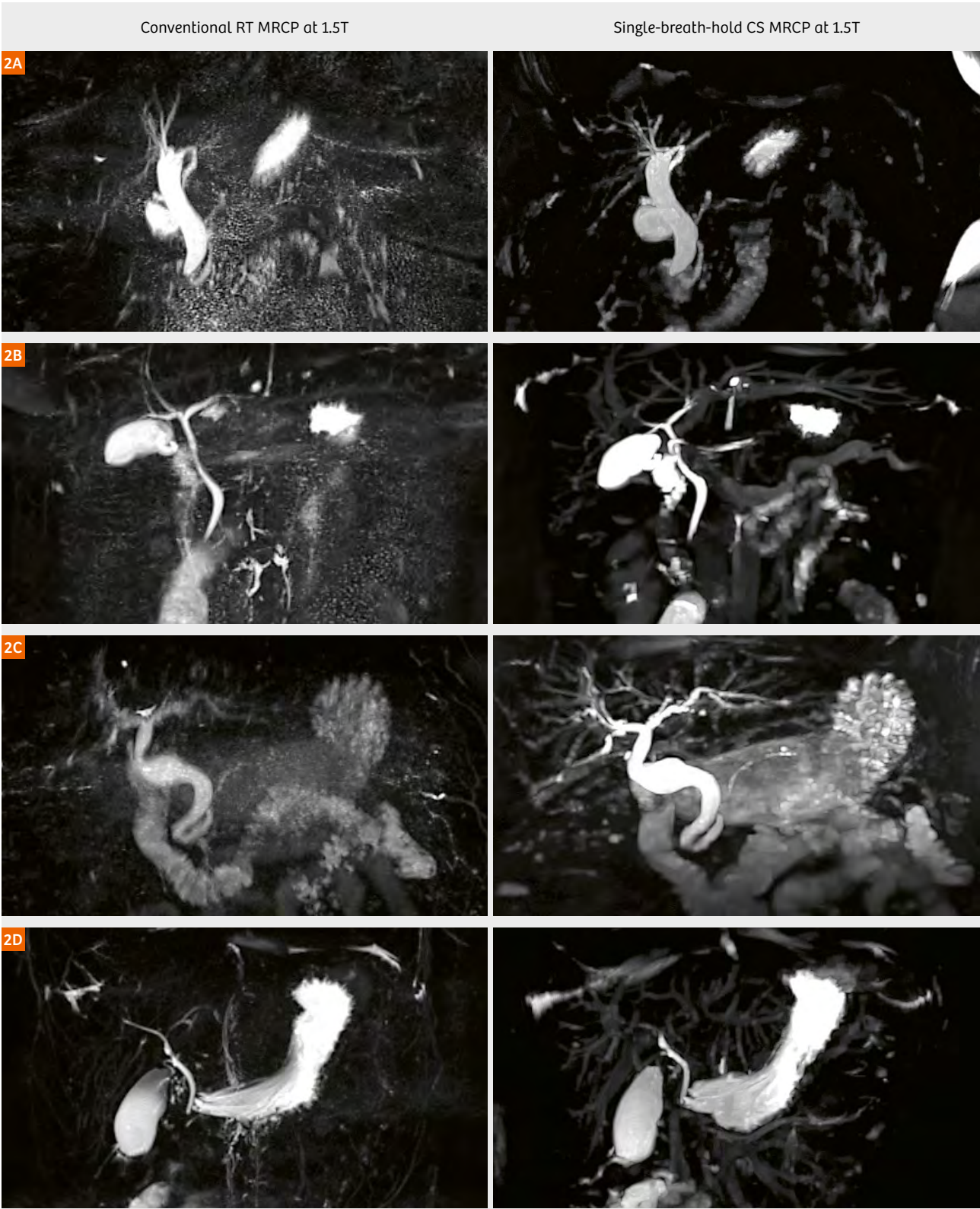


Figure 2:
MIP of the conventional respiratory-triggering (RT) and the single-breath-hold compressed sensing MRCP sequence in four different patients at 1.5T.

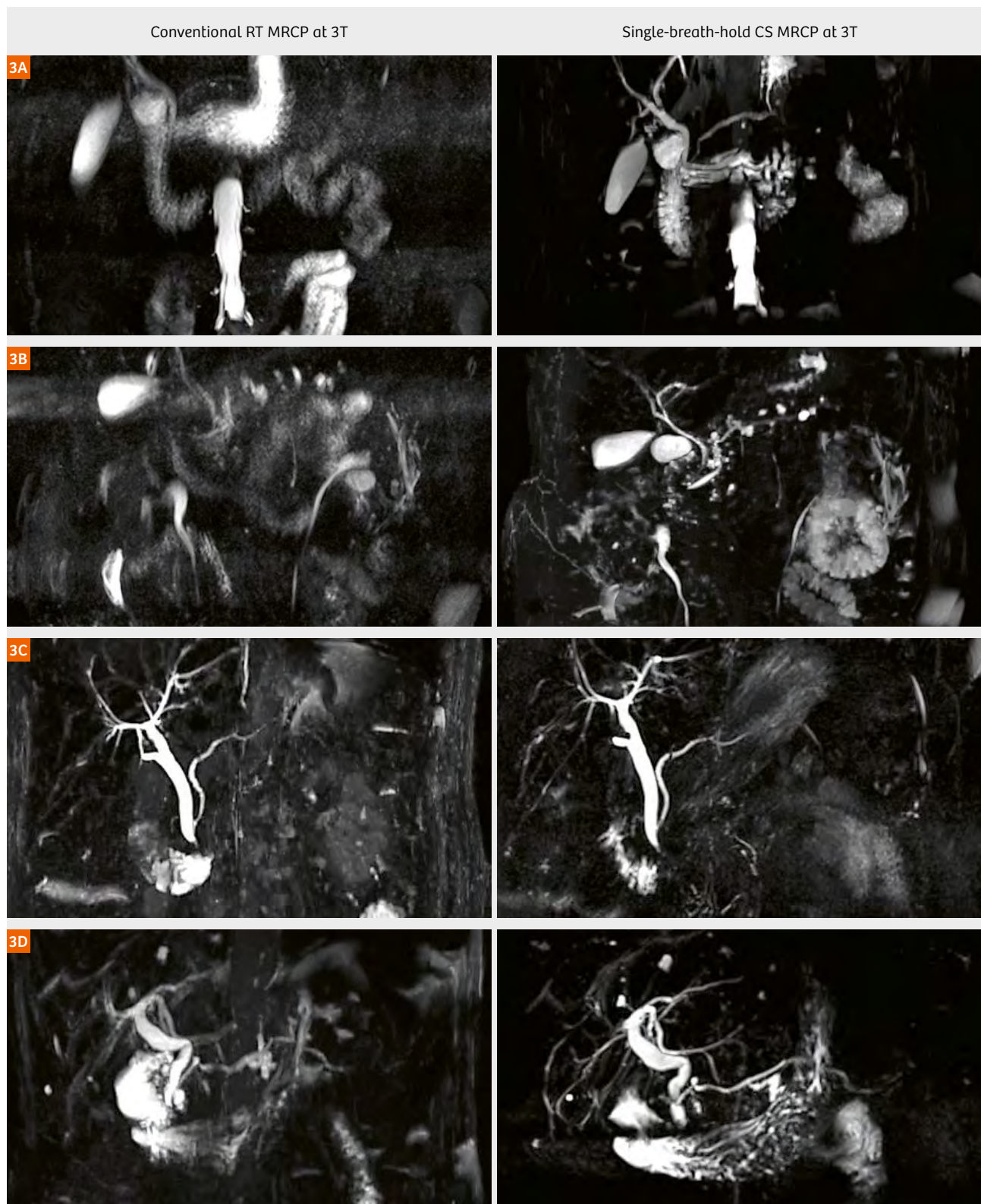


Figure 3: MIP of the conventional respiratory-triggering (RT) and the single-breath-hold compressed sensing MRCP sequence in four different patients at 3T.

Discussion and conclusion

Nowadays rapid MR imaging is of utmost importance for clinical decision making, whilst the comfort of the patient is crucial. Indeed, it is very important that the patient spends the shortest time in the magnet bore in order to get him/her back for a follow-up MR examination. To achieve this goal, development of rapid MR acquisition techniques is critical. One of the most promising techniques for rapid MR imaging is a highly undersampled acquisition in combination with compressed-sensing reconstruction method. The present study has demonstrated the clinical applicability of such a method for MRCP imaging.

At 3T, the quality of the breath-hold CS MRCP images was clearly superior and the main bile and pancreatic ducts were better visualized compared to the conventional MRCP images. Interestingly, at 1.5T the image quality and the visibility of the main ducts were comparable between the breath-hold CS MRCP and the conventional sequence. These findings are very promising since the acquisition time of the single-breath-hold was at least 17 times shorter than the conventional technique.

The main disadvantage of the conventional RT MRCP sequence is clearly the longer acquisition time. Indeed, for patients with irregular respiratory motion, the acquisition time can exceed 10 minutes and the resulting images suffer from motion artifacts and blurring as shown in Figure 2 (B and C) and in Figure 3 (A and B).

The overall quality and sharpness of the single-breath-hold CS MRCP images was good at 3T, this is in agreement with a study by Yoon et al. [2] where similar findings were reported: mean overall image quality: 4.17 vs. 4.10; mean image blurring: 3.60 vs. 3.80. It is interesting to note the better image quality and sharpness at 3T compared to 1.5T with the single-breath-hold CS MRCP sequence. However, this was not the case with the conventional MRCP sequence; there is a clear benefit to perform compressed-sensing reconstruction for MRCP imaging at higher magnetic field strength.

To our knowledge, this is the first 1.5T study showing similar image quality between the single-breath-hold CS and the conventional MRCP sequence. Furthermore, the visibility of the main ducts was also comparable between

both sequences. However, in the single-breath-hold CS MRCP images the background suppression was near to poor with substantial background. This was not observed at 3T, where sufficient background suppression was achieved. Therefore it would be beneficial to improve the background suppression of the single-breath-hold CS MRCP sequence at 1.5T.

An important issue with the evaluated single-breath-hold CS MRCP prototype implementation is the reconstruction time of the images. In the present study, the reconstruction time was about 6 minutes. This has to be addressed for a future product implementation e.g. by a GPU implementation, the reconstruction time needs to be as short as possible in order to facilitate the workflow of the MR protocol and also in case where the images need to be interpreted rapidly by the radiologist.

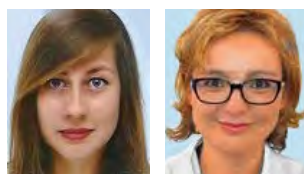
In conclusion, the single-breath-hold CS MRCP prototype provides a similar (at 1.5) or superior (at 3T) overall quality and sharpness compared to the conventional sequence.

References

- 1 Arizono S, Isoda H, Maetani YS, et al. High spatial resolution three-dimensional MR cholangiography using a high-sampling-efficiency technique (SPACE) at 3T: comparison with the conventional constant flip angle sequence in healthy volunteers. *J Magn Reson Imaging* 2008; 28:685–690.
- 2 Yoon JH, Lee SM, Kang HJ, et al. Clinical Feasibility of 3-Dimensional Magnetic Resonance Cholangiopancreatography Using Compressed Sensing: Comparison of Image Quality and Diagnostic Performance. *Invest Radiol*. 2017 Oct; 52(10):612-619.
- 3 Zhu L, Xue H, Sun Z, et al. Modified breath-hold compressed-sensing 3D MR cholangiopancreatography with a small field-of-view and high resolution acquisition: Clinical feasibility in biliary and pancreatic disorders. *J Magn Reson Imaging*. 2018 Apr 14. doi: 10.1002/jmri.26049. [Epub ahead of print]
- 4 Feng L, Benkert T, Block KT, et al. Compressed sensing for body MRI. *J Magn Reson Imaging*. 2017 Apr;45(4):966-987.
- 5 Yamamoto T, Okada T, Fushimi Y, et al. Magnetic resonance angiography with compressed sensing: An evaluation of moyamoya disease. *PLoS One*. 2018 Jan 19;13(1):e0189493.
- 6 Fushimi Y, Okada T, Kikuchi T, et al. Clinical evaluation of time-of-flight MR angiography with sparse undersampling and iterative reconstruction for cerebral aneurysms. *NMR Biomed*. 2017 Nov;30(11).
- 7 Chandarana H, Doshi AM, Shanbhogue A, et al. Three-dimensional MR cholangiopancreatography in a breath hold with sparsity-based reconstruction of highly undersampled data. *Radiology* 2016;280:585– 594.

Contact

Hélène Blaise
Hôpital universitaire Nancy
Rue du Morvan
54511 Vandœuvre-lès-Nancy
France



Hélène Blaise Valérie Laurent

Fast and efficient liver imaging with Primovist®/Eovist®

Thomas Lamprecht^{1,2}; Martin Rohrer, Ph.D.²; Gregor Thörmer, Ph.D.¹

¹ Siemens Healthineers, Erlangen, Germany

² Bayer AG, Radiology, Berlin, Germany

Introduction

Primovist¹ is a dedicated contrast agent for MR imaging of the liver. It combines the dynamic characteristics of an extracellular contrast agent with characteristics for liver-specific imaging during the hepatobiliary phase [1, 2]. Primovist contains an ionic, highly water-soluble Gd³⁺

chelate complex and therefore has magnetic properties comparable to other gadolinium-containing contrast media that are used to enhance dynamic T1-weighted imaging [3]. The addition of a lipophilic EOB group increases protein binding in plasma and maximizes

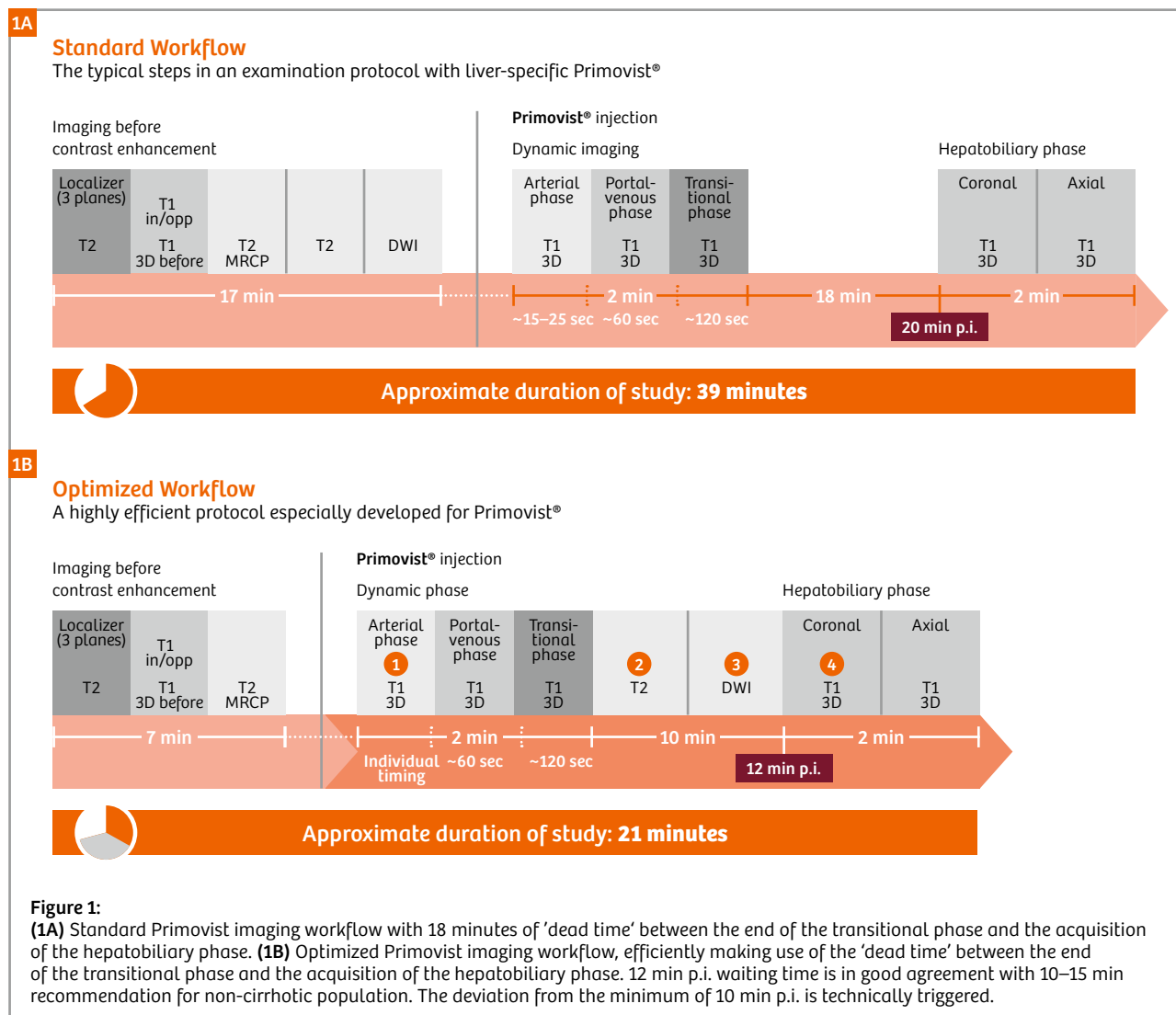


Figure 1 is courtesy of: Elmar M. Merkle, Department of Radiology, Basel University Medical Center, Basel, Switzerland.

contrast medium uptake by the hepatocytes. Once injected, Primovist is taken up by functional hepatocytes, which means that the contrast medium accumulates in the cells. After administration, the signal enhancement in healthy liver tissue is present for at least two hours. Since malignant tumors and non-hepatic tissues (e.g., metastases) possess very few functional hepatocytes, or none at all, they exhibit almost no Primovist uptake. This results in a pronounced contrast between malignancy (dark = hypointense) and adjacent healthy liver tissue (bright = hyperintense). Compared with healthy tissue, benign liver lesions may display an even more pronounced signal enhancement [4].

Since the recommended minimal waiting time of approximately 10 to 15 minutes (for non-cirrhotic population) between contrast media administration and the acquisition of hepatobiliary phase images is relatively short, examinations using Primovist make it possible to avoid taking the patient off the MR table, waiting until contrast accumulates in the hepatocytes, and rescheduling the patient for an additional late-phase scan. Nonetheless, the unused waiting time is still perceived as 'dead time', inevitably resulting in long exam slots (see Figure 1A).

A time-optimized workflow for Primovist liver MRI

In order to make better, effective use of the time between the dynamic and liver-specific phases, it is highly desirable to

- A. shift the time-intensive acquisition of high-resolution T2-weighted images and diffusion-weighted images to after the contrast injection, and
- B. shorten the delay between contrast dynamics and the acquisition of hepatobiliary phase images.

With this in mind, respective studies have been undertaken which show that Primovist does not have any significant impact on the signal of the liver parenchyma in T2-weighted [5] or diffusion-weighted sequences [6]. Furthermore, a fairly marked liver-specific contrast enhancement will already be present after 10 minutes in patients without liver cirrhosis. This will only increase slightly up to 20 minutes after contrast injection [7]. Accordingly, Bayer has suggested a shortened Primovist imaging protocol which allows performing a complete Primovist examination in a 30-minute exam slot (Fig. 1B).

In this article, we present three optimized workflows for efficient imaging with Primovist:

- Two standard strategies without additional license requirements
- One strategy using advanced Abdomen Dot Engine features such as automated slice positioning, auto coverage, and ABLE² for personalized timing of the arterial phase thanks to automated bolus detection, and automated adjustment of breath-hold times to individual patient capabilities.

Respective protocols for the 1.5T and 3T platforms are available to download on the MAGNETOM World website at www.siemens.com/magnetom-world > **Clinical Corner** > **Protocols**.

Primovist standard protocols

The standard protocol set for liver imaging with Primovist provides two different strategies: The default imaging strategy uses automated breath-hold commands during exhalation, while the alternative strategy uses breath-hold commands during inhalation. Before starting the actual examination, users can decide on the exam strategy (see Figure 2). Depending on this decision, respective protocols are automatically pulled into the exam queue. Figure 3 illustrates the flow of the two different strategies. The default strategy deliberately uses exhalation. Even though patients perceive breath-holding during exhalation to be more demanding, the literature shows that the stability and reproducibility is higher [8]. In addition, planning images can be used throughout the entire exam for both breath-hold and free-breathing acquisitions. The alternative strategy using inhalation includes additional planning images, since the free-breathing and triggered exams (T2-weighted and diffusion-weighted) should not be planned on images acquired during inhalation (see Figure 4).

The actual exam starts with the acquisition of localizer images. These are followed by fast overview scans with a single-shot T2 HASTE technique in coronal and axial orientation. If preferred, T2 BLADE scans may be used instead of a breath-hold T2 HASTE approach. Depending

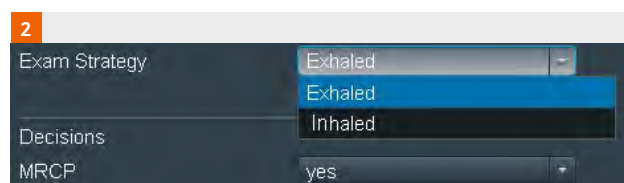


Figure 2: Prior to the exam, users can choose the strategy from the dialog box. In this step, they can also decide whether the individual clinical question requires a fast T2-weighted MRCP.

¹ The information shown herein refers to products of 3rd party manufacturers and thus are in their regulatory responsibility. Please contact the 3rd party manufacturer for further information.

² Automated Breath-hold Liver Exam

	Expiration	Inspiration
3A	✓ localizer_haste_multislice 00:18 t2_haste_cor_p2_mbh 00:48 t2_haste_tra_p2_mbh_320 01:08 t1_t2d_opp-in_tra_p2_mbh 00:45	localizer_haste_multislice 00:18 t2_haste_cor_p2_mbh 00:48 t2_haste_tra_p2_mbh_320 01:08 t1_t2d_opp-in_tra_p2_mbh 00:45
3B	MRCP t2_haste_fs_multislab_p2_384_mbh 00:47 t1_vibe_dixon_tra_p4_bh_pre 00:15 prepare injection t1_vibe_dixon_tra_p4_bh_arterial 00:15 t1_vibe_dixon_tra_p4_bh_portal-venous 00:15 t1_vibe_dixon_tra_p4_bh_delayed 00:15	MRCP t2_haste_fs_multislab_p2_384_mbh 00:47 t1_vibe_dixon_tra_p4_bh_pre 00:15 prepare injection t1_vibe_dixon_tra_p4_bh_arterial 00:15 t1_vibe_dixon_tra_p4_bh_portal-venous 00:15 t1_vibe_dixon_tra_p4_bh_delayed 00:15
3C	ep2d_diff_b50_400_800_tra_p3 03:35	loc_cor_Expiration_for_positioning 00:11 ep2d_diff_b50_400_800_tra_p3 03:35
3D	2d_T2_TSE t2_tse_tra_p2_trig_512 02:59 t2_space_fs_tra_p2_trig_512 05:11 t1_vibe_dixon_tra_p4_bh_12min_p1_higher FA 00:17 t1_vibe_dixon_cor_p6_bh_320_iso 00:21	2d_T2_TSE t2_tse_tra_p2_trig_512 04:02 t2_space_fs_tra_p2_trig_512 05:11 t1_vibe_dixon_tra_p4_bh_12min_p1_higher FA 00:17 t1_vibe_dixon_cor_p6_bh_320_iso 00:21
3E		

Figure 3:

Two standard strategies using exhalation and inhalation are provided. **(3A)** Fast planning images acquired with coronal HASTE and transversal HASTE FS scans provide an overview. **(3B)** Optional fast thick-slab HASTE FS scans for T2-weighted MRCP follow. **(3C)** Contrast dynamics; **(3D)** DWI and T2 (2D or 3D) post-contrast; **(3E)** delayed imaging in different planes.

(*) In the inhalation strategy, additional planning images are required to position the free-breathing scans correctly.

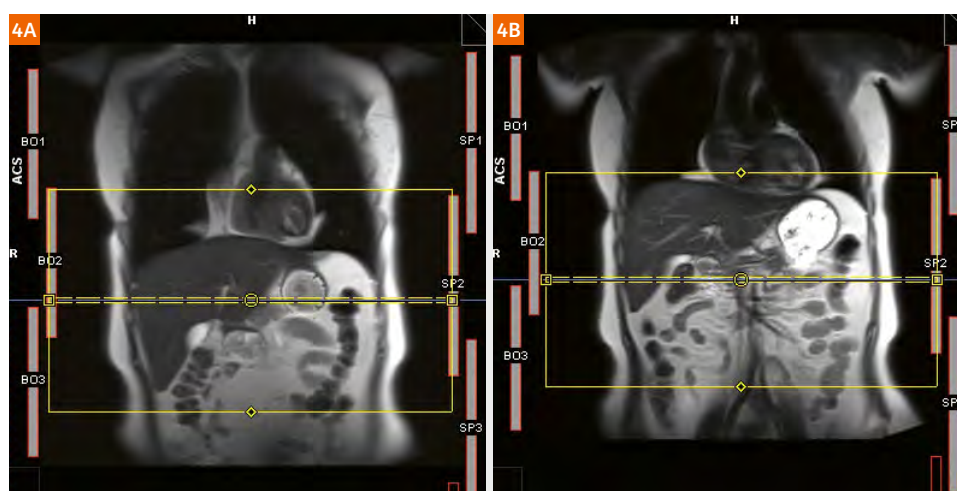


Figure 4:

Inhaled **(4A)** and exhaled **(4B)** coronal planning images illustrate how significantly the organ coverage is affected: While the liver is perfectly centered in the FOV in the inhaled exam, the liver dome risks being cut off in images acquired with triggering, which is typically performed in the exhaled phase. Therefore, an additional localizer is provided to ensure consistent planning of the free-breathing and triggered scans.

on individual preferences, *strongly* T1-weighted in-phase and opposed-phase scans can be acquired with a 2D FLASH technique. This information, however, is also included in the T1-weighted 3D VIBE scans prior to contrast administration and can therefore be skipped if acceptable in the specific clinical setting. Throughout the entire exam, users receive guidance on how to plan

and execute the subsequent scans, such as the optional multiple T2-weighted MRCP scans with a thick-slab 2D HASTE in rotating acquisition (see Figure 5).

For the contrast-enhanced scans, the protocols are prepared so that the system automatically issues breath-hold commands and adheres to typical delays between the different phases. The delay between the phases can



Figure 5:

Overview of the scanner's user interface. Planning images are displayed at the top of the screen, the scan queue is displayed in the lower left, and guidance on how to perform subsequent scans is provided in the "Guidance" window in the lower right of the screen. If "Coupled Graphics = On" is selected, users can intuitively plan five thick-slab MRCP scans with T2 HASTE by positioning the center of the slice stack in an image showing the common bile duct.

be adapted to the institution's individual needs. Important information regarding timing of the contrast-enhanced scans can be found in Figure 6. Depending on local availability and institutional preference, contrast can be delivered via an automated injector.

After starting the contrast injection and imaging countdown simultaneously, arterial, portal-venous and delayed phase imaging will be performed automatically with predefined pauses which can be adapted to the institution's own standards. If desired, subtraction images of the different phases can be automatically generated. As proposed by Bayer, the time between the delayed phase and the hepatobiliary phase can be effectively used to acquire high-resolution T2-weighted and diffusion-weighted images in free-breathing. Users can choose

between 2D or 3D acquisition for the T2-weighted scans. The 3D T2-weighted scans also include weak "diffusion" gradients to generate a dark-vessel contrast in the liver, which makes it easier to identify T2-intense lesions.

Approximately 10 to 15 minutes post contrast injection, the hepatobiliary phase scans can be started in non-cirrhotic patients. According to the recommendations in the literature, the flip angle is increased for higher contrast between enhancing normal liver parenchyma and non-enhancing lesions. At the end of the exam, an optional T1-weighted MR cholangiography with a high-resolution FLASH 3D protocol in one breath-hold can be acquired. This scan provides a nice functional overview of the biliary system (post-resection, for example), as Primovist is excreted by 50% via the hepatobiliary system).

**Figure 6:**

(6A) After acquisition of the pre-contrast T1-weighted scans (#6 in the queue), the examination is stopped to prepare the injector and to check the coverage and quality of the pre-contrast scans (#7). If everything is fine, users can proceed to the next step (#8) since the arterial phase imaging will not start yet ("play" symbol in the queue). A dialog box (6B) will open automatically and allow users to define the contrast media and contrast volume (1). In the "Timing" section, users set the delay (2) between contrast administration and start of arterial phase imaging. A typical value is 20 seconds. If "Auto continue" (3) is selected, users can start the countdown by pressing "Start" (4) and administer contrast agent at exactly the same time. In this case, the MR system will automatically count down to zero and will also issue the breath-hold commands in a good time to ensure that the scan starts when it reaches zero. When "Auto Continue" is selected, users should not press "Continue" or "Skip".

**Figure 7:**

Prior to the actual examination, users can tailor the exam to the individual patient characteristics and clinical question, e.g., by setting the maximum breath-hold duration and using Auto Bolus Detection for individualized arterial phase imaging, as recommended by Bayer for imaging with Primovist.

Primovist protocol using Abdomen Dot Engine features³

The Primovist Abdomen Dot Engine strategy follows exactly the same structure and logic as the standard protocols: Coronal and axial HASTE scans, 2D in-phase and opposed-phase FLASH, and optional fast T2-weighted MRCP scans prior to contrast are followed by dynamic contrast-enhanced scans and high-resolution T2-weighted, diffusion-weighted, and hepatobiliary phase imaging. The original, general Abdomen Dot Engine settings with breath-holds during inhalation remained unchanged. If desired, users can change this general approach. Additional features and related advantages of the Abdomen Dot Engine are as follows:

- The exam can be tailored to the patient's individual breath-hold capabilities by simply defining the maximum breath-hold duration at the beginning of the exam or by changing it during the exam. The software automatically adapts related imaging parameters in a consistent way.
- Automated landmark detection in the abdomen (organ box) allows automated adaptation of the field-of-view

³ A prerequisite for using this strategy is the local availability of the Abdomen Dot Engine license. TWIST-VIBE and GRASP-VIBE are licensed options and not available for all systems.

and number of slices, and correct positioning of the imaging volume in the individual anatomy (see Figure 7).

- Auto Bolus Detection with ABLE (see Figure 8) precisely adapts the start (respecting also TTC) of the arterial phase scans to the patient's physiology by releasing the scan when contrast agent arrives in the ROI in the descending aorta. The location of the ROI can either be defined by the user or automatically by the software (Auto ROI).
- Encapsulated acquisition is possible for double-echo T2-weighted scans with "normal" (TE = 70 ms) and "very strong" (TE = 430 ms) T2-weighting between venous and delayed scans.



Figure 8:
(8A) The progress of dynamic imaging is intuitively displayed, and it is easy to modify pauses between the different phases. (8B) To perfectly catch the early arterial enhancement in the liver, a ROI is automatically (or manually) placed above the descending aorta. As soon as a signal threshold in this region is exceeded, the subsequent T1-weighted VIBE is released and dynamic phase imaging starts without further user interaction. Automatic breath-hold commands are included. If preferred, the CareBolus scans can also be acquired in axial orientation.

- Automated subtraction of dynamic liver phases with a liver motion correction algorithm (DynaVIBE) ensures that slices from different breath-holds represent the same anatomical position.
- The system can seamlessly integrate multiple arterial phase images with TWIST-VIBE or free-breathing liver dynamics with GRASP-VIBE from the Abdomen Dot Library.

References

- 1 Bluemke DA, Sahani D, Amendola M, et al. Efficacy and safety of MR imaging with liver-specific contrast agent: U.S. multicenter phase III study. *Radiology*. 2005; 237(1):89–98.
- 2 Huppertz A, Balzer T, Blakeborough A, et al. Improved detection of focal liver lesions at MR imaging: multicenter comparison of gadoteric acid-enhanced MR images with intraoperative findings. *Radiology*. 2004; 230(1):266–275.
- 3 Rohrer M, Bauer H, Mintonovitch J, Requardt M, Weinmann H-J. Comparison of magnetic properties of MRI contrast media solutions at different magnetic field strengths. *Invest Radiol*. 2005;40:715–724.
- 4 Zech CJ, Grazioli L, Breuer J, et al. Diagnostic performance and description of morphological features of focal nodular hyperplasia in Gd-EOB-DTPA-enhanced liver magnetic resonance imaging: results of a multicenter trial. *Invest Radiol*. 2008;43(7):504–511.
- 5 Kim YK, Kwak HS, Kim CS, Han YM. Detection and characterization of focal hepatic tumors: a comparison of T2-weighted MR images before and after the administration of gadoteric acid. *J Magn Reson Imaging*. 2009;30(2):437–443.
- 6 Kinner S, Umutlu L, Blex S, et al. Diffusion weighted MR imaging in patients with HCC and liver cirrhosis after administration of different gadolinium contrast agents: is it still reliable? *Eur J Radiol*. 2012;81(4):e625–628.
- 7 van Kessel CS, Veldhuis WB, van den Bosch MA, van Leeuwen MS. MR liver imaging with Gd-EOB-DTPA: a delay time of 10 minutes is sufficient for lesion characterisation. *Eur Radiol*. 2012;22(10):2153–2160.
- 8 Lens E, Gurney-Champion OJ, Tekelenburg DR, et al. Abdominal organ motion during inhalation and exhalation breath-holds: pancreatic motion at different lung volumes compared. *Radiother Oncol*. 2016;121(2):268–275.

Contact

Gregor Thörmer, Ph.D.
Global Segment Manager MRI in Oncology
Siemens Healthineers
Phone: +49 (0)9131 84-7726
gregor.thoermer@siemens-healthineers.com



Now available: Optimized Primovist protocols

Download optimized Primovist protocols
for 1.5 and 3T systems at

www.siemens.com/magnetom-world



Cost-effectiveness of MR imaging-guided strategies for detection of prostate cancer in biopsy-naïve men

Shivani Pahwa, M.D.¹; Nicholas K. Schiltz, Ph.D.³; Lee E. Ponsky, M.D.²; Ziang Lu, BA⁵; Mark A. Griswold, Ph.D.^{1,4}; Vikas Gulani, M.D., Ph.D.^{1,4}

¹ Department of Radiology, University Hospitals Cleveland Medical Center, Cleveland, OH, USA

² Department of Urology, University Hospitals Cleveland Medical Center, Cleveland, OH, USA

³ Department of Epidemiology and Biostatistics, Case Western Reserve University, Cleveland, OH, USA

⁴ Department of Biomedical Engineering, Case Western Reserve University, Cleveland, OH, USA

⁵ Case Western Reserve University School of Medicine, Cleveland, OH, USA

The overdiagnosis and overtreatment of clinically indolent prostate cancer has been repeatedly criticized due to significant adverse effects on the quality of life for patients, and contribution to escalating health care costs [1, 2]. However, aggressive prostate cancer continues to cause significant morbidity and death. Hence, there is urgent need to develop better diagnostic pathways for detection of clinically significant cancer [3]. Magnetic resonance (MR) imaging and MR imaging-guided biopsy strategies are important technologies for the detection of clinically significant prostate cancer [4–7] but there is a reluctance to incorporate MR imaging into practice guidelines for prostate cancer detection because MR Imaging is perceived to be an expensive technology.

Escalating costs in the management of prostate cancer are related to inefficient diagnostic pathways that frequently place patients in incorrect treatment groups. Current estimates place prostate cancer care costs in the United States at over \$10 billion annually [8]. Rather than looking at imaging costs in isolation, the cost effectiveness of using imaging in outcome based paradigms for detection of clinically significant prostate cancer needs to be evaluated. If we can maximize the accuracy of identifying clinically significant lesions, the costs of overtreatment can be reduced while improving quality of life for the patients.

To test the assumption whether MRI is truly too expensive for routine insertion into prostate cancer diagnostic pathways prior to biopsy, we created a decision analysis model to compare the cost-effectiveness of different diagnostic strategies without and with the use of multi-parametric MRI in the detection of clinically significant

prostate cancer [9]. The base case in the model was a biopsy-naïve man for whom prostate biopsy has been recommended on the basis of abnormal digital rectal examination results or elevated prostate-specific antigen levels. The model was further tested in three age groups which are most affected by morbidity and mortality due to prostate cancer based on life expectancy: 41–50 years, 51–60 years, and 61–70 years. Strategies with and without contrast administration for diagnostic MRI exam were evaluated, each further evaluated for a diagnostic pathway using:

- a) cognitively guided biopsy;
- b) MRI-ultrasound fusion biopsy;
- c) in-gantry MRI guided biopsy.

These were compared with the standard clinical paradigm of a 12-quadrant transrectal ultrasound guided biopsy. An abbreviated model is depicted in Figure 1.

Model parameters as disease prevalence, sensitivity and specificity of each technique, were derived from literature. Costs of the techniques were derived from the physician fee schedule at www.CMS.gov; costs of patients losing a day of work were derived from the Bureau of Labor Statistics.

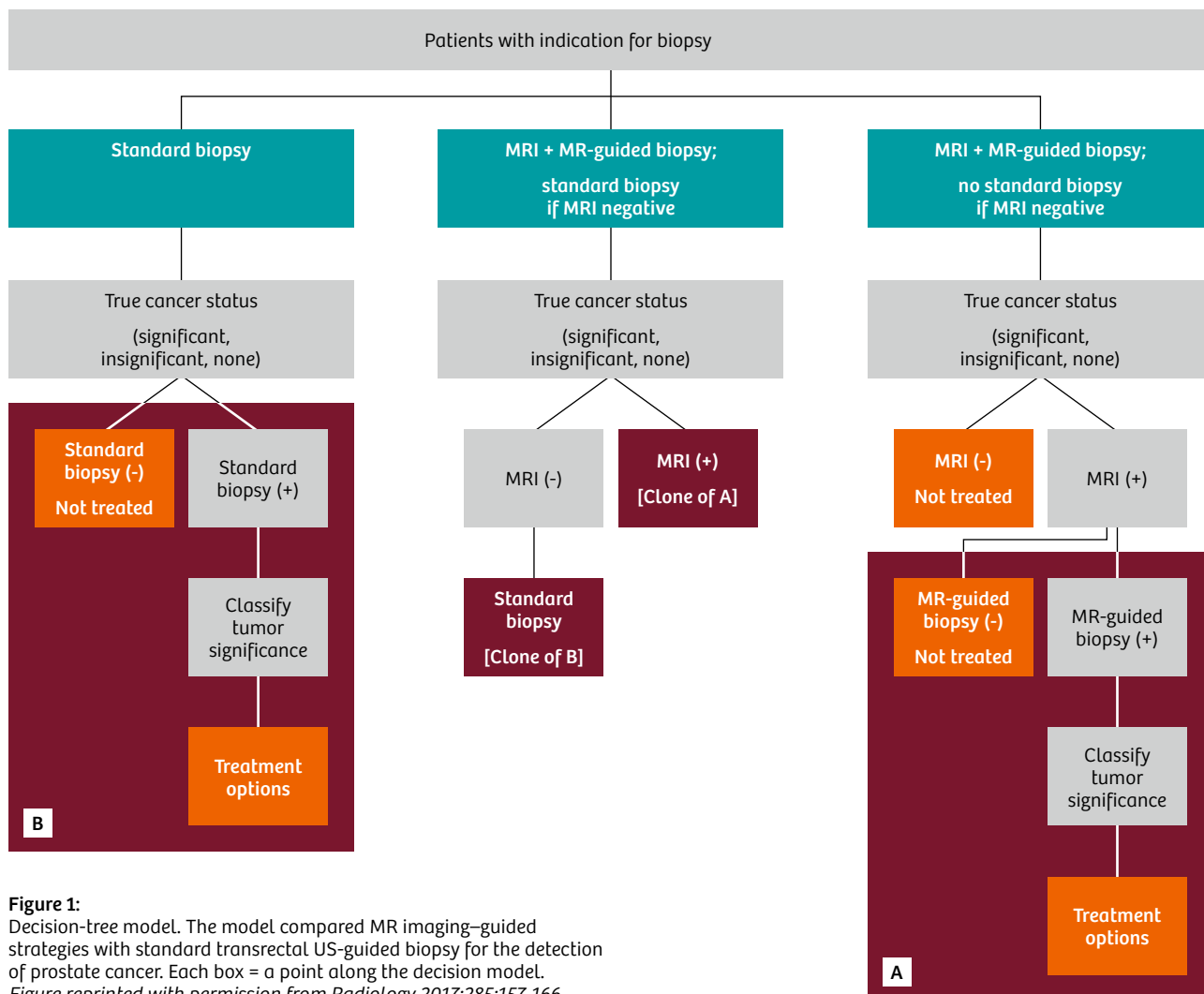
The primary outcome measure was net health benefit, which was measured as quality-adjusted life years gained or lost by investing resources in a new strategy compared with a standard strategy at a willingness-to-pay threshold of \$50,000 per quality adjusted life year gained. In other words, society is assumed to be willing to pay \$50,000 for each quality adjusted life year, and strategies meeting this threshold are considered cost effective. One way sensitivity

analysis was performed on the parameters input into the model. Probabilistic sensitivity analysis was performed by using Monte Carlo simulations, and the proportion of samples for each strategy that were cost-effective was then calculated.

We found that diagnostic MR imaging examinations followed by targeted MR-guided biopsy methods are cost-effective compared with the standard transrectal US-guided biopsy strategy for detection of clinically significant prostate cancer, in over 94% of the simulations. All strategies that employ diagnostic MR imaging followed by MR-guided biopsy of only suspicious lesions yielded additional net health benefits for all age groups, higher than the standard biopsy strategy. The analysis also revealed that, non-contrast diagnostic MR examinations followed by cognitively guided biopsy and foregoing standard biopsy in the case of a negative MR examination was the most cost-effective strategy. Maximal net health benefits were provided through in-Gantry biopsy, and the

additional QALY gained by this strategy over the cognitive biopsy strategy was also cost-effective.

MRI disproportionately misses low grade tumors, and microscopically (also less likely to be aggressive), both of which are often detected on an ultrasound guided biopsy, while yielding better performance for higher risk disease. These characteristics may result in avoiding unnecessary associated complications and overtreatment that may occur after diagnosis. MR imaging-guided pathways have been shown to reduce the detection of low risk cancers by 89.4% and reduced the overall need for biopsy by 51% [8]. A meta-analysis [10] revealed that the sensitivity of transrectal US biopsy in the detection of clinically insignificant cancers was approximately 83%, whereas that for MR imaging-guided methods was approximately 44% [10]. Furthermore, for intermediate/high-risk cancers, the negative predictive value of a negative MR imaging examination was 96.9% whereas that of a standard biopsy was 71.9% [8]. These are some



factors that likely accounted for the improved cost-effectiveness of MRI-guided strategies seen in the present study.

Thus we found in this study that contrary to the common assumptions (indeed contrary to our own assumptions prior to initiating the study), MRI guided strategies are cost effective for detection of clinically significant prostate cancer. This work may provide cost-effectiveness based impetus for exploring the incorporation of MRI guided strategies for the diagnosis of prostate cancer.

Please Note: The above is summarized from work presented in greater detail in our previous publication [9].

References

- 1 Moyer VA; U.S. Preventive Services Task Force. Screening for prostate cancer: U.S. Preventive Services Task Force recommendation statement. *Ann Intern Med* 2012;157(2):120–134
- 2 Non-Recommended PSA-Based Screening. Mathematica Policy Research. https://talkaboutprostatecancer.files.wordpress.com/2015/11/psa-screening_framing-document_measure-specification_hqmf-header3.pdf. Published 2016. Accessed January 4, 2016.
- 3 Cooperberg MR, Broering JM, Carroll PR. Time trends and local variation in primary treatment of localized prostate cancer. *J Clin Oncol* 2010;28(7):1117–1123.
- 4 Delongchamps NB, Peyromaure M, Schull A, et al. Prebiopsy magnetic resonance imaging and prostate cancer detection: comparison of random and targeted biopsies. *J Urol* 2013;189(2):493–499.
- 5 Ukimura O, Marien A, Palmer S, et al. Trans-rectal ultrasound visibility of prostate lesions identified by magnetic resonance imaging increases accuracy of image-fusion targeted biopsies. *World J Urol* 2015;33(11):1669–1676.
- 6 Rais-Bahrami S, Siddiqui MM, Turkbey B, et al. Utility of multiparametric magnetic resonance imaging suspicion levels for detecting prostate cancer. *J Urol* 2013;190(5):1721–1727.
- 7 Mariotto AB, Yabroff KR, Shao Y, Feuer EJ, Brown ML. Projections of the cost of cancer care in the United States: 2010–2020. *J Natl Cancer Inst* 2011;103(2):117–128.
- 8 Pokorny MR, de Rooij M, Duncan E, et al. Prospective study of diagnostic accuracy comparing prostate cancer detection by transrectal ultrasound-guided biopsy versus magnetic resonance (MR) imaging with subsequent MR-guided biopsy in men without previous prostate biopsies. *Eur Urol* 2014;66(1):22–29.
- 9 Pahwa S, Schiltz NK, Ponsky LE, Lu Z, Griswold MA, Gulani V. Cost-effectiveness of MR Imaging-guided Strategies for Detection of Prostate Cancer in Biopsy-Naive Men. *Radiology*. 2017;162181. Epub 2017/05/18. doi: 10.1148/radiol.2017162181. PubMed PMID: 28514203.
- 10 Schoots IG, Roobol MJ, Nieboer D, Bangma CH, Steyerberg EW, Hunink MG. Magnetic resonance imaging-targeted biopsy may enhance the diagnostic accuracy of significant prostate cancer detection compared to standard transrectal ultrasound-guided biopsy: a systematic review and meta-analysis. *Eur Urol* 2015;68(3):438–450. *World J Urol* 2015;33(11):1669–1676.



Contact

Vikas Gulani, M.D., Ph.D.
Department of Radiology
Case Western Reserve University
University Hospitals Case Medical Center
11100 Euclid Ave
Bolwell Building, Room B120
Cleveland, OH 44106
USA
vxg46@case.edu

Don't miss the talks from Leading experts given at the 10th MAGNETOM World Summit

Quality and consistency lead to efficiency. Application of automated workflows

Lawrence Tanenbaum
(RadNet, New York, NY, USA)

Creating an economic ecosystem for MRI

Stefan Schönberg
(University Hospital Mannheim, Germany)

www.siemens.com/magnetom-world
Clinical Corner > Clinical Talks



Impact of Compressed Sensing Cardiac Cine in a busy clinical practice

J  rome Garot, M.D., Ph.D.; Gilles Auvray

Institut Cardiovasculaire Paris Sud, Massy, France

Introduction

Since its foundation in 2008, the dedicated cardiovascular MRI facility at the Institut Cardiovasculaire Paris Sud (ICPS – Cardiovascular Institute Paris-Sud), has seen around 45,000 patients. Of these, ca. 70–75% underwent a stress MR perfusion examination. In 2017 alone, over 5,400 patients were scanned, with the MR examination duration averaging 20 minutes. This tempo has been achieved thanks to thorough planning and staffing of the reception and preparation areas, scanning and reading environment as well as to careful optimization of the entire examination process, from patient reception, preparation and coaching, to accessory selection, protocol tuning and workflow management.

Cardiovascular MRI at ICPS

The stress CMR perfusion examination at ICPS consists of localization, followed by long-axis cines, stress perfusion, short-axis cines and late-enhancement. Image viewing, quality control and interpretation are done in parallel on a dedicated reading console running *syngo.via* located in the MR control room. Reporting is performed alongside reading using a software package¹ (Clinigrid software, Hemolia Inc., Paris, France) written especially for the CMR practice at ICPS which, as well as combining audio, image and text input, also serves as a database, capable of providing statistical information about patient cohort, throughput etc.

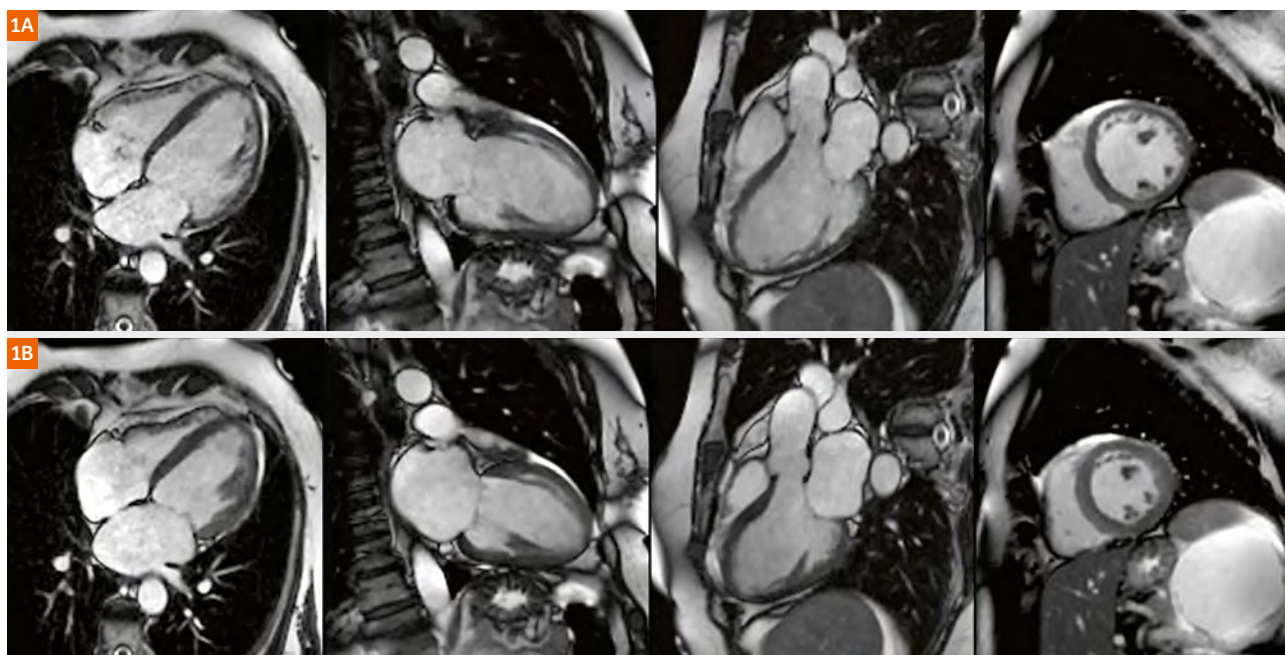


Figure 1:

Compressed Sensing Cine retrograded images obtained in diastole (1A) and systole (1B) using a two-shot imaging protocol in a patient with dilated cardiomyopathy.

¹ The information shown herein refers to products of 3rd party manufacturers and thus are in their regulatory responsibility. Please contact the 3rd party manufacturer for further information.

Ventricular function assessment

The assessment of left ventricular (LV) function is a core feature of every MR examination of the heart. Until September 2017, we typically performed LV function analysis using PAT-GRAPPA accelerated segmented retrogated cine TrueFISP with a PAT factor of 2. This approach is considered a gold standard in the MR imaging business, and in spite of lengthy and multiple breath-holds, it is generally well-accepted by patients and clinicians. In patients with breath-hold difficulties or arrhythmia, we resorted to prospectively triggered cine TrueFISP combined with TPAT imaging and a PAT factor of 3. The introduction of Compressed Sensing (CS) Cardiac Cine with *syngo* MR E11C-AP02 changed our examination workflow considerably. In particular, the prototype CS Cardiac Cine software², which allows for retrogated cine imaging across two heartbeats, has become our workhorse method for LV function assessment. Thus, following a brief investigative period including cross-comparisons with the current gold standard, we switched all our standard CMR imaging protocols to use CS Cine with retrogating. This has meant that we have been able to shorten the average stress perfusion CMR examination by 3 to 4 minutes, thereby increasing our patient throughput and improving patient comfort. As a direct consequence, we are now able to scan around 15 more patients per week.

Retrogated Compressed Sensing Cardiac Cine

The so-called “two-shot” CS Cine Retro method allows for a reduction in the total number of breath-holds required to assess left ventricular function both visually and quantitatively, as well as a shortening of the breath-hold duration itself. In general we employ an imaging protocol with a total acceleration factor of ~6.5, an in-plane spatial resolution of 1.5 mm x 1.5 mm and a temporal resolution of the order of 40 ms; slice thickness is usually 8 mm. The acquisition duration is three heartbeats per slice, the first heartbeat being a non-imaging “dummy” heartbeat, with application of gradients and RF pulses to ensure that the

magnetization has reached the steady state. Example images obtained in a patient with dilated cardiomyopathy are shown in Figure 1. Despite the high *k*-space under-sampling factor, endo- and epicardial boundaries are sharp, small trabecular structures and valves are clearly visible and, most importantly, the excellent temporal resolution ensures that wall-motion assessment and quantitative analysis are feasible. Figure 2 shows another representative example of a three-chamber cine obtained using CS Cine Retro.

In the case of patients with severe arrhythmia, or those who are unable to hold their breath, the real-time CS Cine sequence is now our alternative method of choice for the assessment of LV function. Albeit with a somewhat inferior spatial and temporal resolution compared with the two-shot CS Cine Retro method, real-time CS Cine nevertheless allows for a distinctly better image quality when evaluated against standard PAT-accelerated real-time imaging. With appropriate usage of adaptive triggering, or alternatively imaging across 1.5 cycles, it also allows for complete cycle cine imaging, necessary for accurate quantitative analysis. Figure 3 compares the two-shot CS Cine Retro method with real-time CS Cine obtained in a deaf patient in whom the conveyance of breath-hold commands was complicated. The images shown in Figure 4 illustrate the usage of the arrhythmia rejection option in CS Cine Retro to achieve clinically acceptable image quality.

The advantages of CS Cine Retro are not limited to scan time shortening alone. The method incorporates a means to trade scan time for extremely high temporal and/or spatial resolution in a single breath-hold. Thus, the so-called eight-shot protocol, which splits the acquisition over eight heartbeats, allows for the thus far inconceivable acquisition of single slice cine images with a temporal resolution of 10 ms and an in-plane spatial resolution of 1.2 mm x 1.2 mm in a total scan time of 9 heartbeats. An example of such an acquisition is shown in Figure 5.

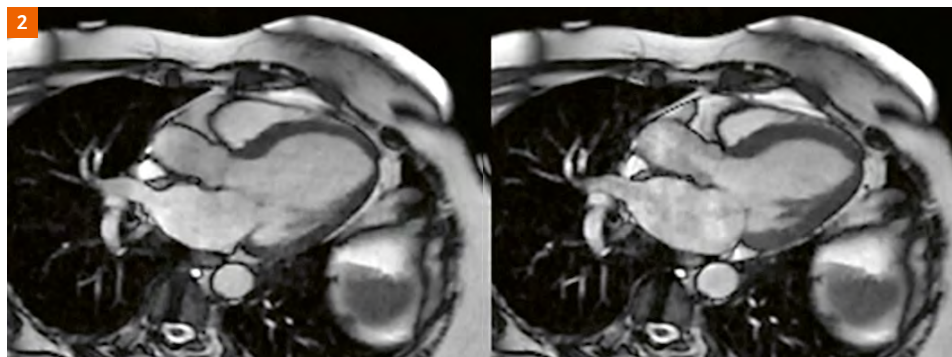


Figure 2:
Three-chamber CS Cine
retrogated images obtained at
end-diastole and end-systole.

² WIP, the product is currently under development and is not for sale in the US and in other countries. Its future availability cannot be ensured.



Figure 3:
Comparison of CS Cine Retro (3A) with CS Cine real-time (3B), obtained in a deaf patient and without breath-holding.

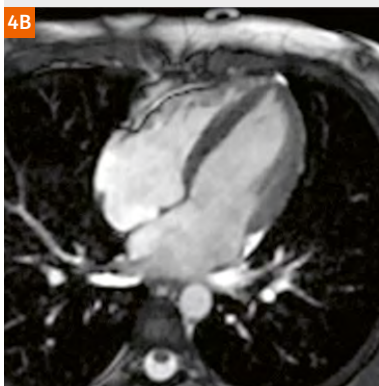
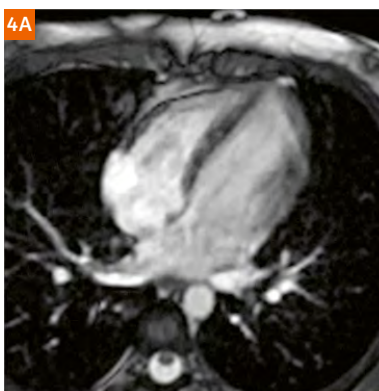


Figure 4:
CS Cine Retro images obtained without (4A) and with (4B) the arrhythmia rejection scanning option in a patient with heart rate irregularities.

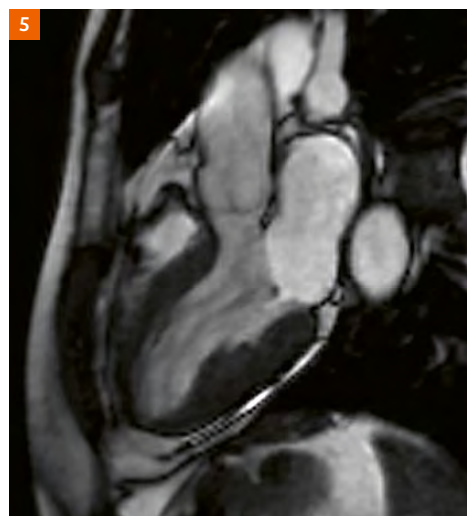


Figure 5:
Three-chamber cine obtained in a healthy volunteer using an eight-shot CS Cine Retro imaging protocol.

Conclusion

Compressed Sensing Cardiac Cine is proving to be a game-changer in the field of cardiovascular MRI. The prototype retrograded CS Cine package allows for significantly shorter scan times without loss of diagnostic information. This in turn is beneficial not only for patients, but also in further improving workflow and in expanding the usage of MRI in the assessment of cardiovascular diseases.

Acknowledgements

The authors would like to thank their colleagues at the Institut Cardiovasculaire Paris Sud, as well as their collaborators at Siemens Healthineers, in particular Carmel Hayes, Christoph Forman, Michaela Schmidt, Solenn Toupin and Matthieu Lepetit-Coiffé, for their valuable contributions to the development and testing of the prototype CS Cine Retro package in a busy clinical practice.

Contact

Professor Jérôme Garot
Head of Cardiovascular MR
Cardiovascular Institute Paris-Sud (ICPS)
6 Avenue du Noyer Lambert
91300 Massy
France
jgarot@angio-icps.com



Learn more about Compressed Sensing at
[siemens.com/magnetom-world](https://www.siemens.com/magnetom-world) > Hot Topics

MyoMap quantification of myocardial toxicity following concurrent chemoradiotherapy for esophageal carcinoma

Simon Tang^{1,2,3}; Eng-Siew Koh^{1,2,3}; Robba Rai^{1,2,3}; James Otton⁴; Mark Lee^{2,3}; David Tran⁴; Lois Holloway^{1,2,3,5}; Liza Thomas^{3,5}; Benjamin Schmitt⁶; Gary Liney^{1,2,3}

¹ Ingham Institute of Applied Medical Research, Liverpool, NSW, Australia

² Cancer Therapy Centre, Liverpool Hospital, NSW, Australia

³ University of New South Wales, NSW, Australia

⁴ Department of Cardiology, Liverpool Hospital, NSW, Australia

⁵ University of Sydney, NSW, Australia

⁶ Siemens Healthineers, Sydney, Australia

Introduction

Crude rates of symptomatic cardiac toxicity in esophageal carcinoma are reportedly 10.8% [1]. Cardiac manifestations including clinical findings such as pericardial effusion, arrhythmia, ischemia and cardiomyopathy, typically occur between 4 to 24 months following thoracic radiation [2, 3]. Subclinical manifestations including declines in mean ejection fraction [4] and perfusion abnormalities and wall ischemia [5] have also been noted at shorter time scales between 1–3 months. Hatakenaka *et al.* [6], using cardiac MRI, have demonstrated focal wall motion abnormalities in conjunction with changes in heart rate, stroke volume and left ventricular (LV) end-diastolic volume index following concurrent chemoradiation.

In-house quantification of longitudinal and cross sectional reproducibility *in vivo* has shown variation of 3.9% for T1 measurements, and a 15.2% variation in T2 measurements [7].

This paper presents the case of a patient treated with concurrent chemoradiation for esophageal cancer, where cardiac tissue properties were assessed by cardiac mapping (MyoMaps) longitudinally prior to, 6 weeks following, and 12 months following treatment.

Patient case

This 67-year-old male patient was diagnosed with a Stage IB T2N0M0 squamous cell carcinoma of the lower esophagus, following investigations for unexplained dysphagia and weight loss. He was otherwise fit and well, with the cardiac risk factors of hypercholesterolaemia and a smoking history.

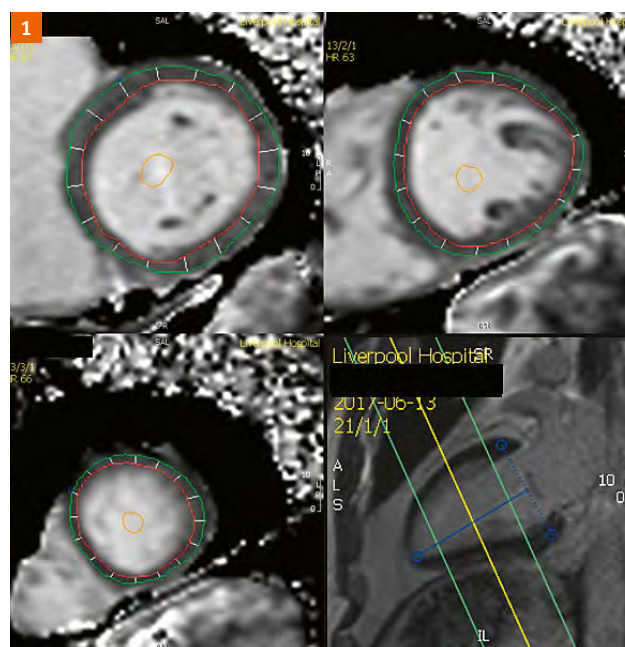


Figure 1: Native T1 MyoMap with myocardium contoured at the basal, mid, and apical levels.

T1 Relaxation: Measure of longitudinal signal recovery. This is elevated in the presence of edema or fibrosis.

T2 Relaxation: Measure of transverse signal decay. This is elevated in the presence of edema.

ECV: Is a measure of myocardial extracellular volume. It is elevated in myocardial fibrosis.

Table 1: Definitions.

The concepts and information presented in this paper are based on research and are not commercially available.

He subsequently underwent chemoradiation 50 Gy / 25 fractions using a 3D conformal technique, with concurrent carboplatin/paclitaxel chemotherapy. He experienced no cardiac symptoms during or following his treatment.

Image acquisition

The patient underwent three separate cardiac MRI scans, one prior to, 6 weeks, and 12 months following completion of his chemoradiation. A clinical modified look locker inversion (MOLLI) sequence¹ was used to generate myocardial short axis T1 maps (MyoMaps, Siemens Healthcare, Erlangen, Germany), pre- and 15 minutes post-administration of a gadolinium-based contrast agent, as well as T2 maps (MyoMaps) at 3 Tesla. T1, T1 post-contrast and T2 relaxation times of the LV were acquired with MRI mapping software (cvi42, v4.5, Circle Software). Extracellular volume (ECV) was derived from the myocardial portioning coefficient (λ), adjusting for hematocrit. Values were recorded in the American Heart Association (AHA) 17 segment model [8]. Figure 1 illustrates the delineation of the left ventricle on a native T1 map. Definitions and possible significance of various MRI sequences are outlined in Table 1.

Radiotherapy dose calculations

Corresponding RT doses to the AHA LV segments were determined from contours outlined in the cardiac axes

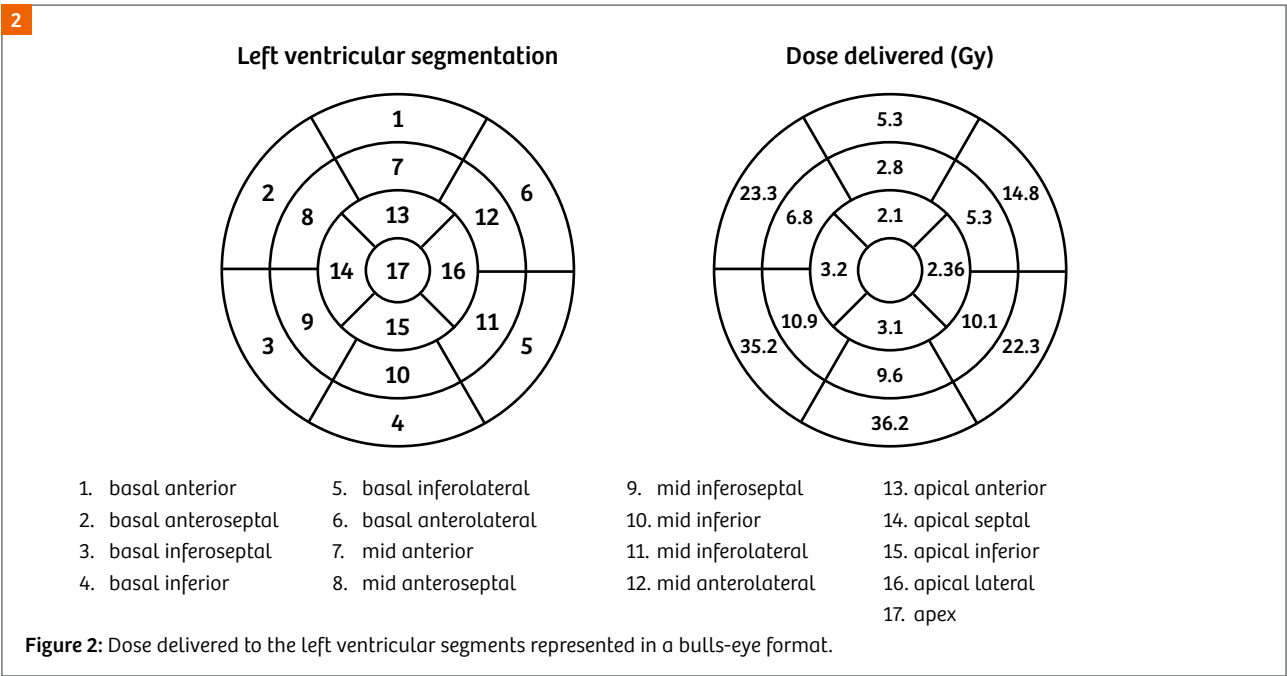
on reformatted planning CT images in Oncentra Brach Treatment Planning v4.5.2 (Elekta AB, Stockholm, Sweden), before being imported into Mim v6.77 (Mim Software, Beachwood, OH, USA) for dosimetric readout. Mean heart dose, mean LV dose, and mean segmental doses were reported, with mean heart doses having known associations with radiation induced cardiac toxicity [9].

Results

The mean heart dose was 28.82 Gy. The mean LV dose was 14.16 Gy. Mean dose delivered to the left ventricular segments was heterogeneous, with segments 3 and 4 receiving 30 Gy or more, segments 2 and 5 receiving 20 Gy or more, and segments 6, 10, and 11 receiving 10 Gy or more. Figure 2 reports the dose delivered in a bulls-eye format.

Changes in the T1, T2, and ECV values are as illustrated in Figures 3–5, with the changes depicted on the MyoMaps represented in Figures 6 and 7. Visually there appears to be an increase in native T1 values post chemoradiation, most prominently 12 months following treatment, which is occurring most prominently in segments 3, 4, and 5, which correspondingly received the highest radiation doses. A 12 month increase in T2 relaxation time values was also seen, although occurring more globally throughout the left ventricle. The ECV percentage transiently increased 6 weeks following chemoradiation.

¹ WIP, the product is currently under development and is not for sale in the US and in other countries. Its future availability cannot be ensured.



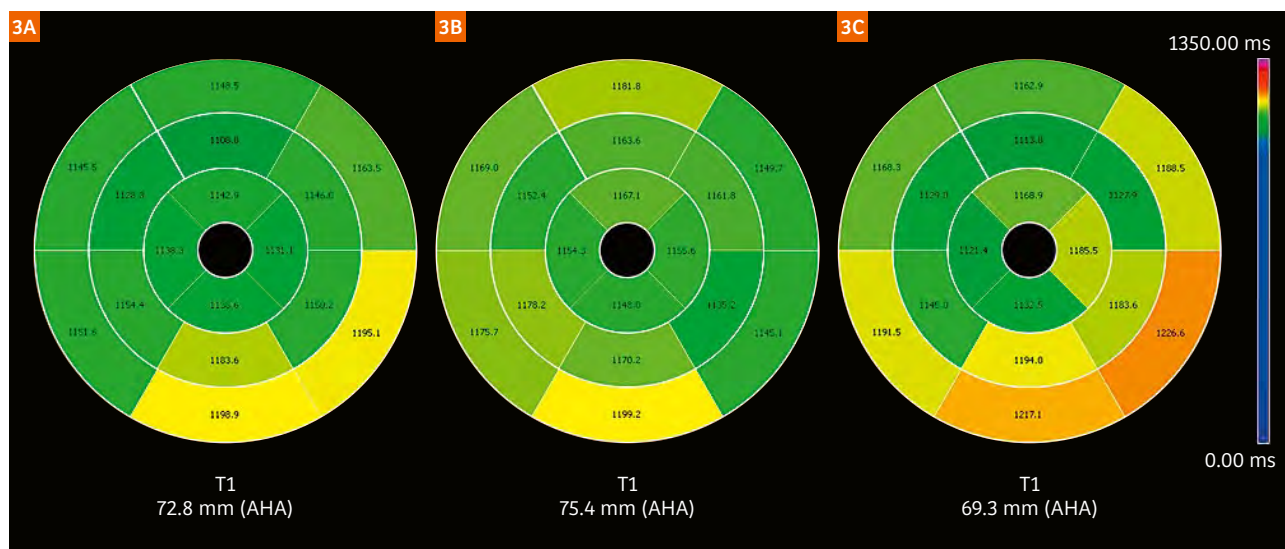


Figure 3: T1 values

(3A) Pre-treatment

(3B) 6 week post-treatment

(3C) 12 months post treatment time points respectively

Elevation of T1 values were most pronounced at 12 months in the basal segments.

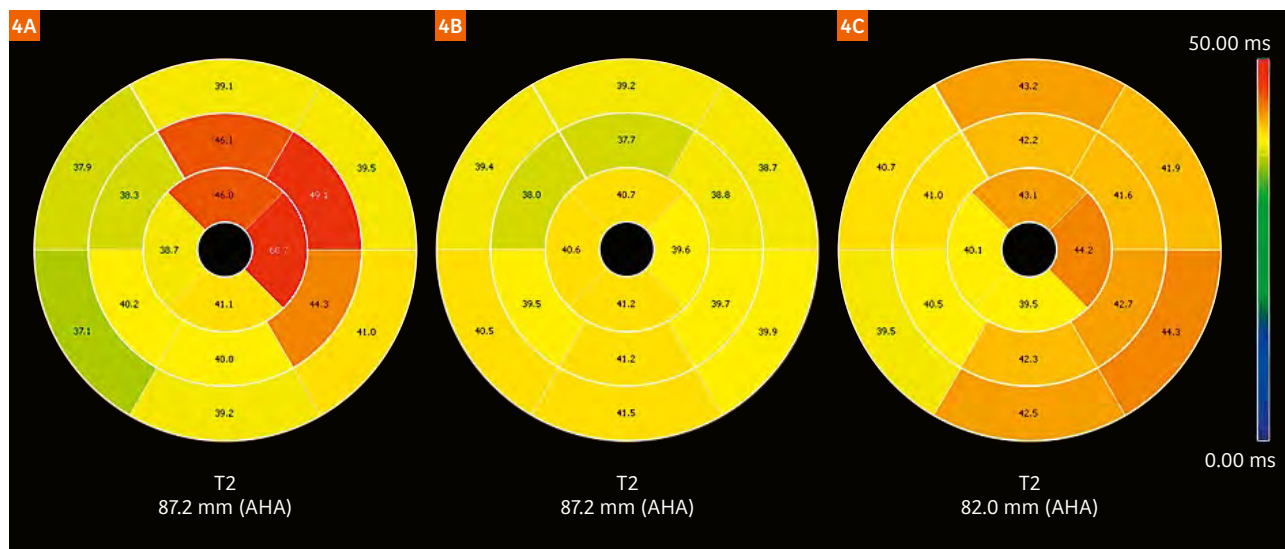


Figure 4: T2 values

(4A) Pre-treatment

(4B) 6 week post-treatment

(4C) 12 months post treatment time points respectively

Elevation of the segments 7, 11, 12, 13, and 16 in 4A are artefactual from errors in motion correction. An increase in T2 values in predominantly the basal segments was seen after 12 months.

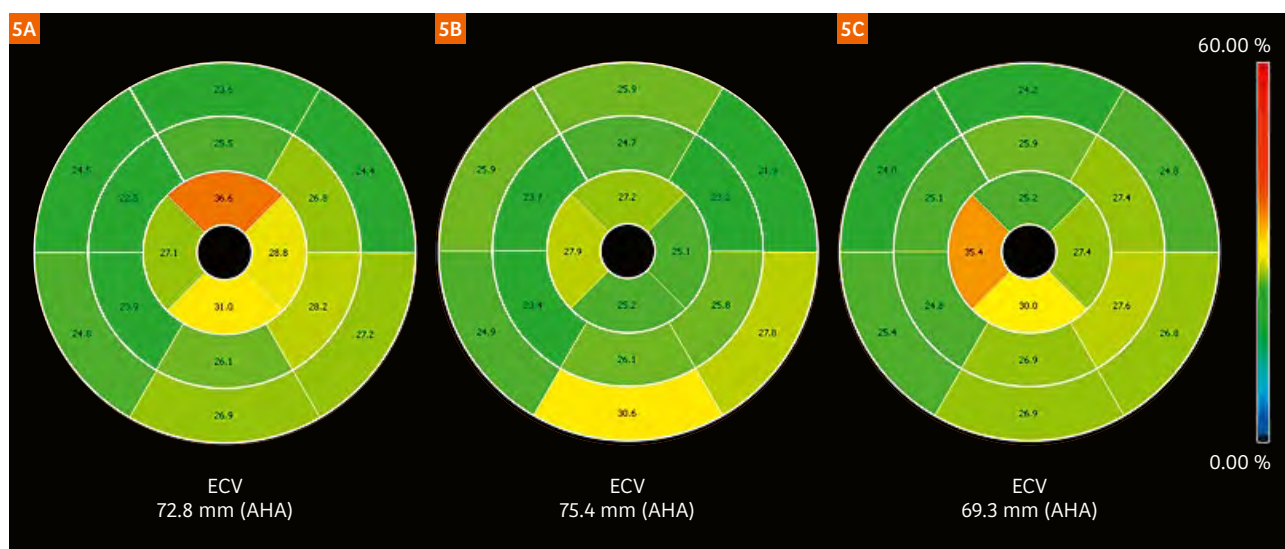


Figure 5: ECV values

(5A) Pre-treatment

(5B) 6 week post-treatment

(5C) 12 months post treatment time points respectively

A subtle increase in ECV is seen the basal segments following treatment, however returns to baseline at 12 months.

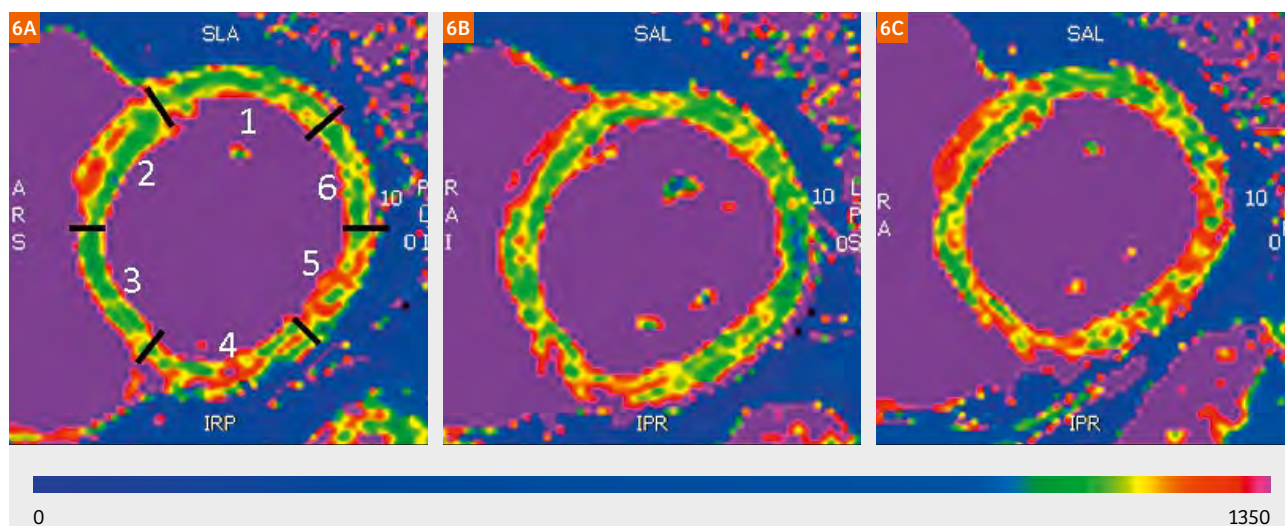


Figure 6: Basal slice through left ventricle – T1 maps

(6A) MyoMaps through the basal segments pre-treatment, individual segments being labelled from one to six

(6B) 6 weeks post

(6C) 12 months post treatment respectively

A qualitative change (increase in relaxation time) can be seen affecting the myocardium in segments 3, 4, 5, and 6 which may indicate myocardial inflammation or fibrosis.

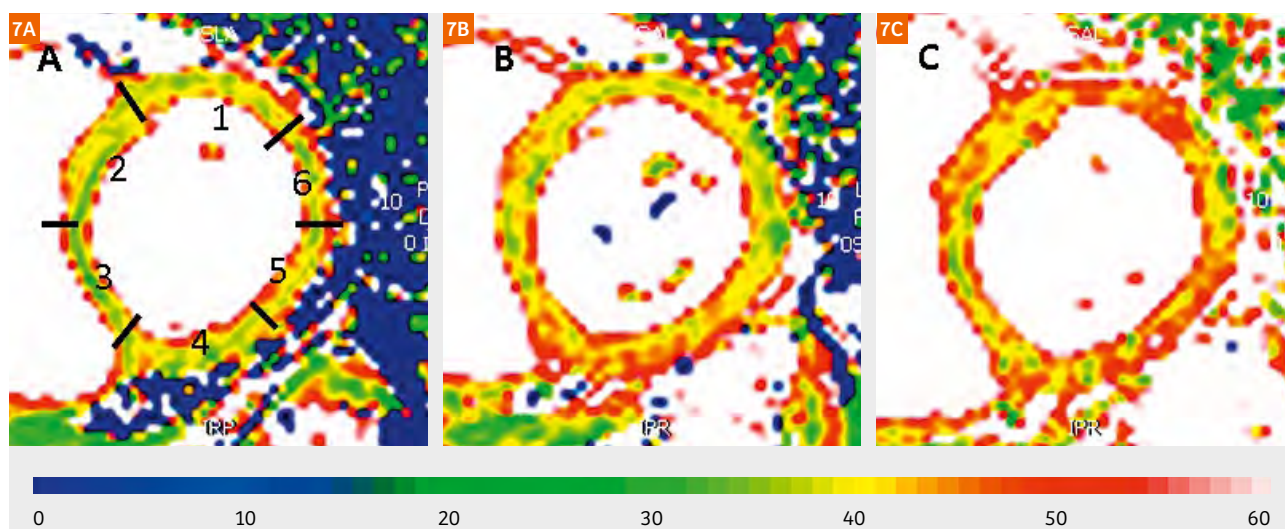


Figure 7: Basal slice through left ventricle – T2 maps

(7A) MyoMaps through the basal segments pre-treatment, individual segments being labelled from one to six

(7B) 6 weeks post

(7C) 12 months post treatment respectively

A qualitative change (increase in relaxation time) can be seen affecting the myocardium in segments 1, 4, 5, and 6 which may indicate myocardial edema.

Conclusion

The use of MyoMaps for quantitative assessment of the myocardium following cancer therapy treatment shows promise, and experience with this patient has demonstrated feasibility. In this single case study, there was an elevation of T1 and T2 relaxation times occurring 12 months following treatment, which is preceded by an increase in ECV percentage immediately following chemoradiation. These results must be placed in the context of inherent variability in T1/T2 measurements. Further studies will be required in order to determine if the findings reported in this case are significant.

The use of cardiac MRI mapping however may provide novel information regarding acute to sub-acute myocardial changes following radiation therapy.

References

- 1 Beukema, J.C., et al., Is cardiac toxicity a relevant issue in the radiation treatment of esophageal cancer? *Radiotherapy and Oncology*, 2015. 114(1): p. 85–90.
- 2 Shirai, K., et al., Volume Histogram Parameters and Clinical Factors Associated With Pleural Effusion After Chemoradiotherapy in Esophageal Cancer Patients. *International Journal of Radiation Oncology • Biology • Physics*. 80(4): p. 1002–1007.
- 3 Kumekawa, Y., et al., Late toxicity in complete response cases after definitive chemoradiotherapy for esophageal squamous cell carcinoma. *Journal of Gastroenterology*, 2006. 41(5): p. 425–432.
- 4 Mukherjee, S., et al., The significance of cardiac doses received during chemoradiation of oesophageal and gastro-oesophageal

junctional cancers. *Clin Oncol (R Coll Radiol)*, 2003. 15(3): p. 115–20.

- 5 Gayed, I., et al., The clinical implications of myocardial perfusion abnormalities in patients with esophageal or lung cancer after chemoradiation therapy. *The International Journal of Cardiovascular Imaging*, 2009. 25(5): p. 487–495.
- 6 Hatakenaka, M., et al., Acute cardiac impairment associated with concurrent chemoradiotherapy for esophageal cancer: magnetic resonance evaluation. *Int J Radiat Oncol Biol Phys*, 2012. 83(1): p. e67–73.
- 7 Wijesekera, D., et al., Longitudinal Accuracy and Reproducibility of Quantitative Cardiac MRI Mapping. *Journal of Medical Imaging and Radiation Oncology*, 2016. 60: p. 41–95.
- 8 Cerqueira, M.D., et al., Standardized Myocardial Segmentation and Nomenclature for Tomographic Imaging of the Heart. A Statement for Healthcare Professionals From the Cardiac Imaging Committee of the Council on Clinical Cardiology of the American Heart Association, 2002. 105(4): p. 539–542.
- 9 Taylor, C.W., et al., Exposure of the Heart in Breast Cancer Radiation Therapy: A Systematic Review of Heart Doses Published During 2003 to 2013. *Int J Radiat Oncol Biol Phys*, 2015. 93(4): p. 845–53.



Contact

Associate Professor Gary Liney (UNSW)
Hon. Principal Fellow, University of
Wollongong Ingham Institute for Applied
Medical Research & Radiation Oncology
Liverpool Hospital
1 Campbell Street
Liverpool NSW 2170
Australia
Tel.: +61 2 8738 9221
gary.liney@sswhs.nsw.gov.au

4-dimensional phase contrast imaging in congenital heart disease: How we do it

Timothy C. Slesnick, M.D.; Sassan Hashemi, M.D.

Emory University School of Medicine, Children's Healthcare of Atlanta, Atlanta, GA, USA

Introduction

The field of phase contrast (PC) imaging has expanded greatly in the last 30 years. The fundamental principle that a moving nuclei will experience a phase shift when subjected to a magnetic field gradient that is proportional to the flow velocity, and thus measurement of this phase shift can allow measurement of the velocity of the nuclei [1, 2], has transformed our approach to flow quantification. Today, cardiac magnetic resonance (CMR) is the gold standard for quantification of vascular flows [3, 4]. Though initially confined to 2-dimensional (2D) measurements of either through plane or in-plane flow, the development of 4-dimensional phase contrast imaging (4D flow) was first applied to central nervous system vasculature in the late 1980's [5] and subsequently to cardiovascular blood flow in the late 1990's [6] and has opened new avenues and insights.

Two-dimensional phase contrast imaging is now a routine part of most CMR studies in pediatric and adult patients with congenital heart disease (CHD). Though options exist for both breath held and free breathing 2D PC sequences, our lab, like most, prefer to use free breathing techniques with multiple signal averages (NSA). Assessment of flow in the aorta (Ao) and main pulmonary artery (MPA) allows for quantification of systemic (Qs) and pulmonary blood flow (Qp). Flow in the right pulmonary artery (RPA) and left pulmonary artery (LPA) allows quantification of differential pulmonary blood flow, as well as validation of the MPA flow.

In the present work, we delineate our current practices with 4D flow imaging in children¹ and young adults with CHD, with a focus on practical tips for users to bring this technology to their programs and their patients. Illustrative cases are given with some of the ever-expanding array of applications for this technology. Finally, several recent advances are highlighted which promise to continue to evolve this new technique.

Works in progress 4D Flow

The fundamental tenants of 4D flow are flow encoding in all three directions (x, y, z-axes). True 4D flow sequences obtain a 3D volume, with the fourth dimension representing time. The works in progress (WIP) 4D flow pulse sequence² we currently utilize is WIP 785A, first released in January of 2016 (Figures 1A and 1B, Clip 1 – to access the .avi's please visit www.siemens.com/4Dflow). The sequence utilizes 3D Cartesian sampling with flow encoding and generalized auto-calibrating partially parallel acquisition (GRAPPA) acceleration where the reference lines are acquired separately (aka ePAT). Acceleration can be applied in both phase encoding and the partition encoding directions since the dataset is a true 3D volume, with the expected decrease in signal to noise (SNR) of square root of each of the acceleration factors. When acceleration is applied in both phase encoding and partition encoding directions, SNR is decreased by

¹ Siemens Healthineers Disclaimer does not represent the opinion of the authors: MR scanning has not been established as safe for imaging fetuses and infants less than two years of age. The responsible physician must evaluate the benefits of the MR examination compared to those of other imaging procedures.

² WIP, the product is currently under development and is not for sale in the US and in other countries. Its future availability cannot be ensured.

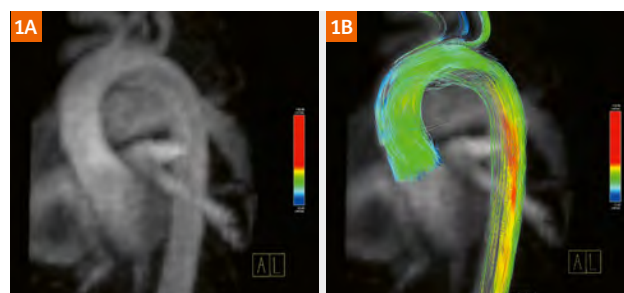


Figure 1: 4D flow magnitude (1A) image of an aortic arch obtained using WIP 785A, as well as particle trace image (1B).

the product of those factors, but the resultant change in the geometry factor, which also influences signal to noise loss, is less pronounced than if all acceleration is performed in one direction, so acceleration of 2×2 does result in less signal loss than 4×1 . One final point on acceleration is that running 4D flow sequences post-contrast will obviously result in more signal, and thus more acceleration can be applied without loss of data integrity. On our 1.5 Tesla scanner, we typically run our 4D flow sequences post contrast (if contrast is given during the routine exam), and apply ePAT in either the phase encoding direction alone with a factor of 3 or in both the phase and partition encoding directions with factors of 2 for each (2×2). If no contrast is given to the patients during routine exam, we typically run the 4D flow sequence applying parallel imaging with a factor of 2 in the phase encoding direction alone.

In order to obtain this quantity of data, even for a small slab of coverage, requires substantial k -space sampling, far longer than is possible in a breath held study. In order to minimize respiratory motion, a respiratory navigator is typically employed (though as delineated below in the product section free breathing techniques with multiple signal averages can also be used). A cross-beam respiratory navigator is positioned on the dome of the diaphragm, and an acceptance window of ± 3 –5 mm is typically used (± 3 mm for smaller children, ± 4 –5 mm for larger children and young adults). Some users have reported using larger respiratory navigator windows, up to ± 8 mm, with acceptable degree of motion artifacts, but we do not have

personal experience with this broad a range of respiratory navigated acceptance.

The WIP sequence can be run with either prospective or retrospective gating. In patients with an irregular heart rate, it is possible to use prospective ECG gating with a reduced acquisition window to avoid data acquisition spanning into the early systolic phase of the following heartbeat. In our experience, however, we find that even with optimal modifications to the 4D flow sequences, the validity of the data due to the inherent fluctuations in the hemodynamics of patients with significant arrhythmias continues to be challenging, and typically we choose not to perform 4D Flow imaging in these patients.

Using retrospective gating, the number of reconstructed phases ("Calculated phases") can be set by the user (Figure 2). Caution should be employed, however, that the reconstructed phases will be interpolated from the true number of cardiac phases acquired, which is determined by the heart rate and the repetition time. For example, we typically acquire 3 segments per heart beat per cardiac phase, which results in a TR of 58.2 msec. In a patient with a heart rate of 75 beats per minute (bpm), and a resultant cardiac cycle of 800 msec, this would yield 13 true cardiac phases. Though the interface allows the user to set the number of reconstructed phases to any desired value, our experience has shown that using slightly less than double the number of true phases produces values which correlate well with 2D PC data. We therefore typically calculate the actual number of phases for a given patient and sequence prescription, double the value, and then

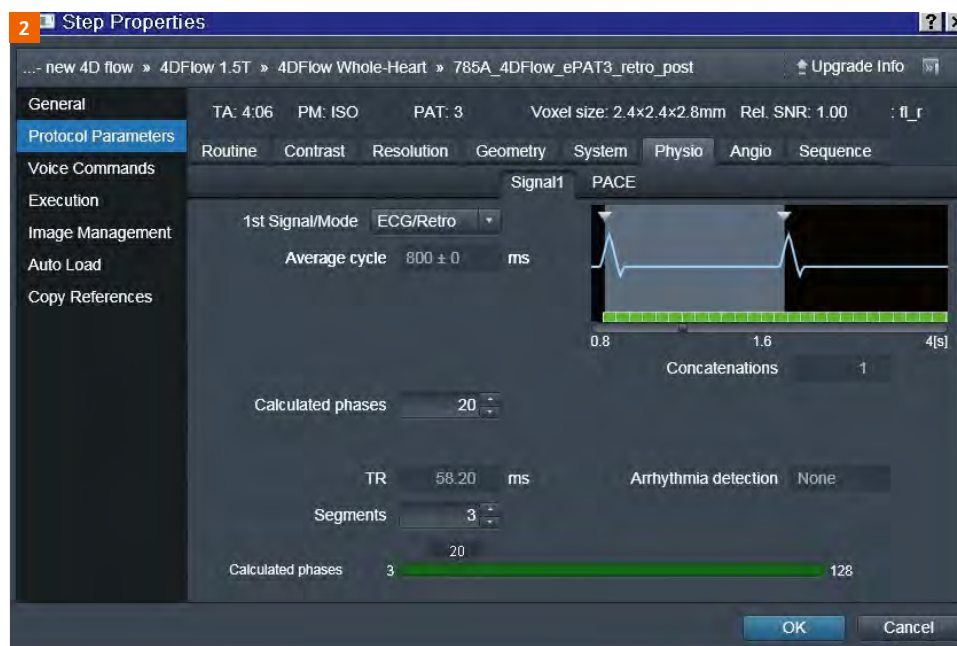


Figure 2: Screen shot demonstrating the Physio tab on the user interface where the number of "Calculated Phases" can be adjusted and the number of true phases can be calculated (cardiac cycle length divided by the TR).

decrease slightly to allow all reconstructed phases to have some component of unique data.

Though this manipulation may seem a bit cumbersome, it allows the user to tailor the sequence and results to the individual patient. For smaller children with faster heart rates, it may be necessary to decrease the number of segments to 2 to allow a shorter TR and thus more reconstructed phases. Conversely, in older patients with slower heart rates (< 50–55 bpm) we will often increase segments to 4 to speed up the acquisition without compromising the number of reconstructed phases. Since each change to the number of segments has a direct correlation to the scan length, these manipulations must be made very thoughtfully. Increasing from 3 to 4 segments will cut acquisition time by 25%, while decreasing from 3 to 2 segments will require 50% longer. For most of our scans, we aim to reconstruct 16–25 phases, adjusting the parameters as needed.

As with any 3D dataset, obtaining isotropic voxels is advantageous as it allows the user to reformat/slice the data in any plane without loss of resolution. With the 4D Flow WIP, we typically decrease the phase and slice encoding direction percentages, so the actual obtained voxels are not quite isotropic, but the reconstructed voxels are. The user must remember that the voxel size is determined by the field of view (FOV), matrix (base resolution), and the slice thickness. FOV and matrix can be changed, but this does affect the in plane resolution and the SNR. The sequence will allow decreasing slice thickness to 1.5 mm, though in our lab we typically run the sequence at 2 mm isotropic.

Slice coverage is prescribed based on the anatomy of interest. For aortic pathology, simply covering the aortic arch (with care taken that the entirety of the aortic root, which is typically the largest portion of the thoracic aorta, is fully covered) is often sufficient. Aligning the plane in a sagittal oblique geometry along the long axis of the arch allows maximal coverage in a minimum number of slices. Depending on the child's (and aorta's) size, this can often be accomplished in as few as 12–14 slices, though with more dilated aortas 16–20 slices may be necessary. For alternative underlying pathologies, coverage may be needed for the entire ventricular volumes (when heart failure or inflow/outflow assessment is desired), branch pulmonary arteries (for TOF and single ventricle [SV] patients), or systemic or pulmonary veins (particularly in patients with anomalous returns). These cases often require wider coverage and thus more slices, so the balance between voxel size and acquisition time is paramount when planning these scans. For most 4D Flow datasets, we prescribe a straight or oblique sagittal plane of some type. Axial geometries can be used if only branch

PA flow is desired, but coverage in the z-direction with axial slices is often quite limited unless large slabs are obtained. Coronal orientations are also possible, but will require phase encoding in the left-right direction (as opposed to anterior-posterior in sagittal or axial oblique geometries), so FOV and acquisition duration will be increased. Additionally, some analysis platforms have difficulties processing coronal 4D Flow datasets, though this can be overcome with manipulation on the user interface.

The final component we prescribe is our velocity encoding upper limits (VENC). As explained in the case examples below, we routinely set the VENC at the highest velocity value within the imaging prescription of interest to avoid aliasing. For most aortic and pulmonary artery studies we use either 150 or 200 cm/sec, unless there is known stenosis of a valve or great artery. For single ventricle studies where the bidirectional Glenn (BDG) or Fontan circuit are the primary area of interest, either 100 or 120 cm/sec is used, with the knowledge that aliasing may occur in the aorta but that is outside the primary vessels of interest (if quantification in the aorta is desired in an SV patient, then 150 or 200 cm/sec is used).

Product 4D Flow options

True 3D datasets

The current software platforms for Siemens Healthineers magnets allow the user to prescribe a 4D Flow dataset with a true 3D volume and flow encoding in all three directions using the product sequences alone (Figures 3A and 3B, Clip 2). This derivation must start with a base product sequence which utilizes prospective ECG triggering (more on this in a moment). On our magnet (MAGNETOM AvantoFit on software platform *syngo* MR E11B), we have built this option from the underlying, "BEAT_FQ" sequence, though other options are possible. On *syngo* MR E11B, the current product sequence will not support a 3D acquisition



Figure 3: 4D flow magnitude (3A) image of an aortic arch obtained using the product 4D flow derivative, as well as particle trace image (3B).

when parallel imaging with GRAPPA and reference lines obtained using “GRE/separate” (aka ePAT) is employed, so under the Resolution tab, iPAT subtab, “Integrated” must be selected to change to iPAT parallel imaging (Figure 4). On the *syngo* MR E11C and subsequent platforms 3D acquisitions are possible with ePAT image acceleration. For the product 3D acquisition, parallel imaging can only be used in the phase encoding direction. We typically run the sequence with 3 fold acceleration and perform it post-contrast to ensure adequate signal. Next, under the Sequence card, Part 1 subtab, the Dimension can be

changed from 2D to 3D (for *syngo* MR E11B this option will not be available until the parallel imaging is changed from ePAT to iPAT) (Figure 5). This change will automatically convert the flow direction from “Single dir” to “Single vel” (which results in flow encoding in all three directions, represented as F>>H, Throughplane, and A>>P in a sagittal geometry) (Figure 6).

Product phase contrast sequences do not have an option for a respiratory navigator, and since data acquisition is far too long for an individual breath-hold, free breathing

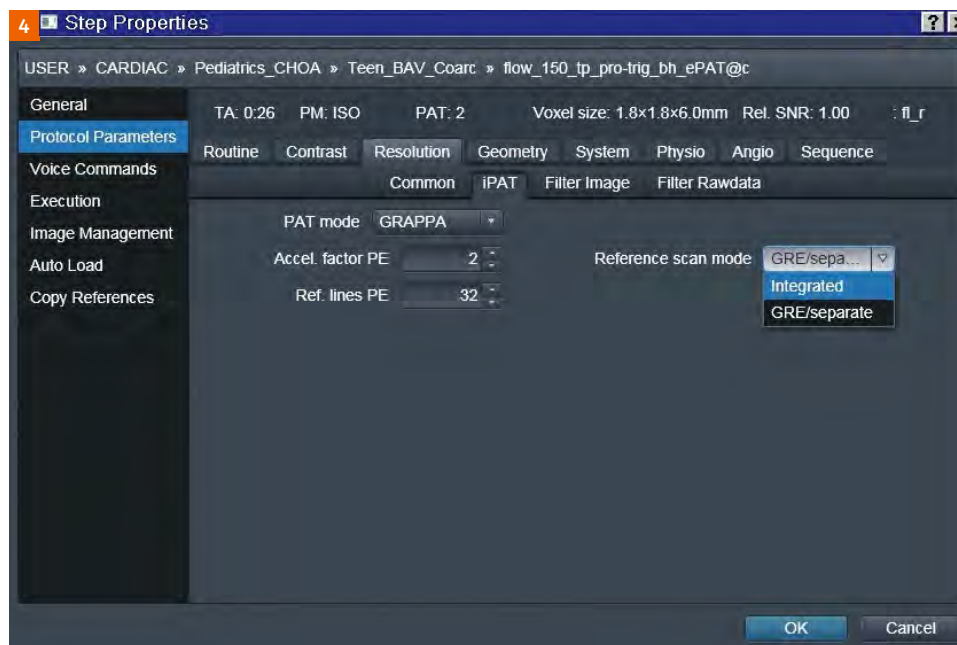


Figure 4: Screen shot illustrating how the reference line acquisition must be changed from “GRE/separate” to “Integrated” (aka ePAT to iPAT) in order to convert the sequence as described in the text.

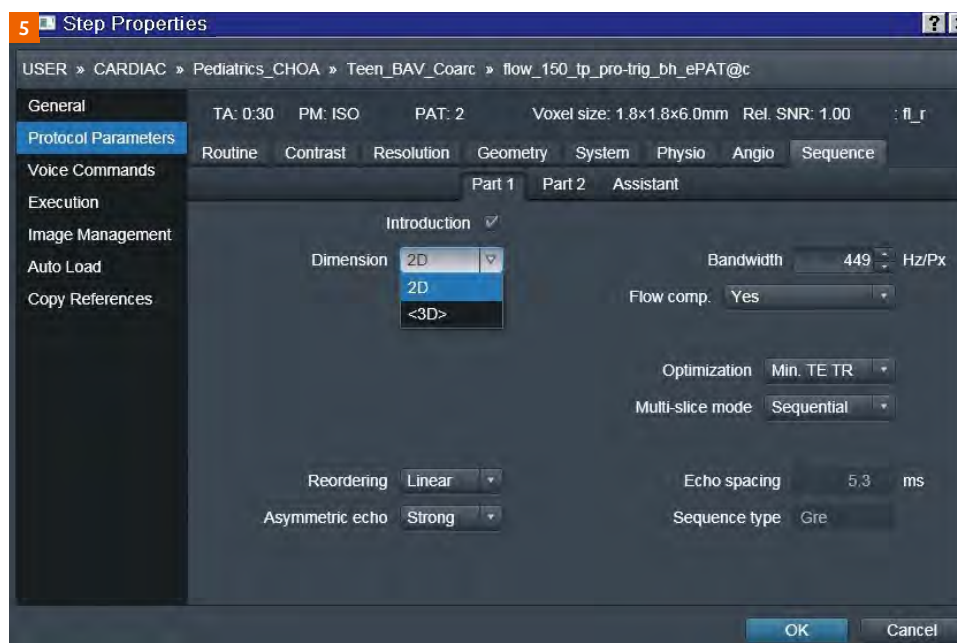


Figure 5: Screen shot illustrating how the 2D product phase contrast sequence can be changed to a 3D volume under the Sequence tab, Part 1.

techniques with multiple signal averages are needed. Since this variant does produce a true 3D volume, it is less respiratory motion sensitive, so we typically acquire 2 NSA.

Slice thickness can be as thin as 1 mm, though again we typically run this variant at 2–2.5 mm in the interest of acquisition time. FOV and matrix are adjusted to ensure isotropic voxels. Slice orientation and number are set to cover the regions of interest. The VENC is set as described above.

The largest difference in this variant of 4D Flow is that the Siemens Healthineers current product sequence does not support retrospective gating for 3D volumes. This fact has three important consequences. First, the end of diastole cannot be captured, and thus the sequence represents only a large portion (not the entirety) of the cardiac cycle. Second, unexpected pronounced heart rate variability result in challenges with data sampling both in mistiming at the end of the cardiac cycle and missed acquisition on the beats following shorter cardiac intervals. Finally, with prospective gating, the number of phases is fixed

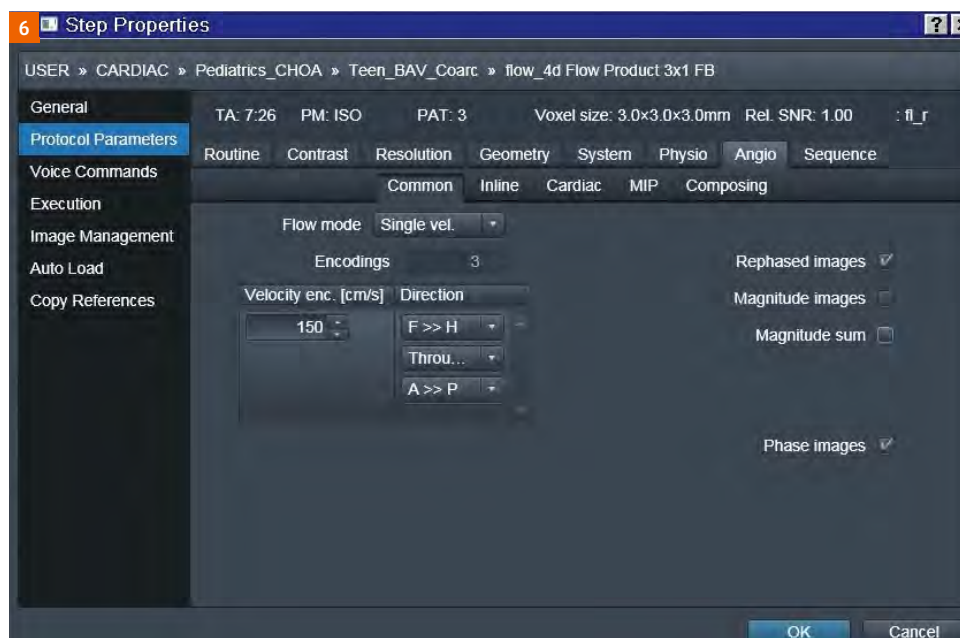


Figure 6: Screen shot illustrating the change to the “Single vel” option with velocity encoding in all three directions (F>>H, Throughplane, and A>>P) under the Angio tab.

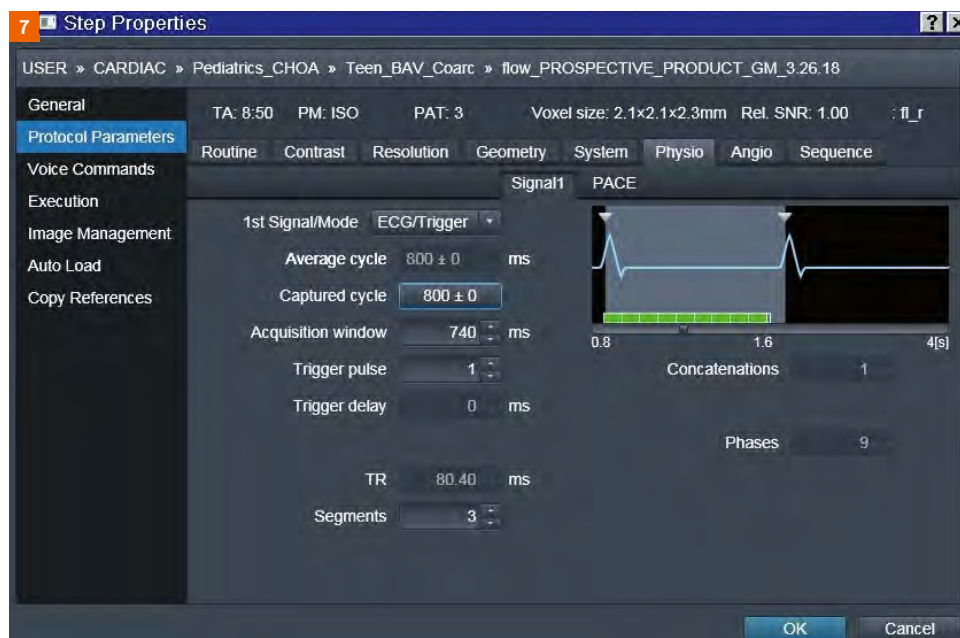


Figure 7: Screen shot demonstrating the Physio tab on the user interface where the number of phases is displayed on the right hand side. Note, that compared to the WIP version, there is no input for “Calculated Phases” since this sequence is prospectively gated.

at the true number of acquired phases and cannot be interpolated to yield more reconstructed phases. Thus for this product 4D Flow sequence on a patient with an average heart rate of 75 bpm, a resultant cardiac cycle of 800 msec, the repetition time would be 80.4 msec (assuming 3 segments are selected) and there will only be 9 phases produced (Figure 7). If the user desires more phases, the number of segments must be reduced (with resultant increased acquisition time).

“Pseudo 4D Flow”: Contiguous stack of 2D slices

An additional alternative to the product 4D Flow described above is acquisition of a contiguous stack of 2D slices, each with flow encoding in all three directions, which in summation represent a 3D volume (Figures 8A and 8B, Clip 3). The sequence can again be built starting with the base “BEAT_FQ” sequence. It is important when setting up the multiple 2D slices to utilize no slice gap



Figure 8:
4D flow magnitude (8A) image of an aortic arch obtained using the product “pseudo 4D flow” stack of 2D slices derivative, as well as particle trace image (8B).

(aka “Distance factor”) (Figure 9). Parallel imaging can remain with “GRE/separate”, and similar to the true 3D product sequence, acceleration is only possible in the phase encoding direction. We typically run the sequence post-contrast with 3 fold acceleration.

Since there is no option for respiratory navigator on the product flow sequences, again multiple signal averages are employed. As opposed to the variant described above, 2D slices are more motion sensitive, so we typically utilize 3 NSA with the patient free breathing (though with small patients and very shallow respirations, we have utilized 2 NSA with this variant).

With a contiguous stack of 2D slices, minimum slice thickness is 2.8 mm, which means that even with FOV and matrix optimization, the isotropic voxel size is larger than on other 4D flow variants. Typically, we run this variant with 3 mm isotropic voxels, which does result in decreased resolution which is readily apparent on the magnitude images (Figures 10A and 10B), but as explained below, still produces reasonable data for flow visualization and hemodynamic analysis.

Under the Angio tab, “Flow mode” can be manually changed from the standard “Single dir” to the “Single vel” (Figure 6). The VENC is set to an appropriate value. The contiguous stack of 2D slices variant does have the advantage that it, like the WIP, can be run with retrospective gating, and thus the number of reconstructed phases can be set by the user (Figure 11). As described above, we do not recommend setting the total phases greater than twice the number of actual phases as



Figure 9:
Screen shot of the Routine tab where the stack of slices are composed with no gap (“Distance Factor”).

determined by the repetition time and the heart rate, but you can achieve improved temporal resolution compared to the other product variant (where prospective gating is the only option).

In our experience, for similar patient's conditions and imaging data size, the continuous stack of 2D slices technique requires a shorter acquisition time than the true 3D volume product variant. This time savings does come at a price of worse spatial resolution, but offers the user improved temporal resolution compared to the other product option and also does allow retrospective gating. As described below, for flow visualization and simple quantification, we have found the resolution of this technique to be sufficient.

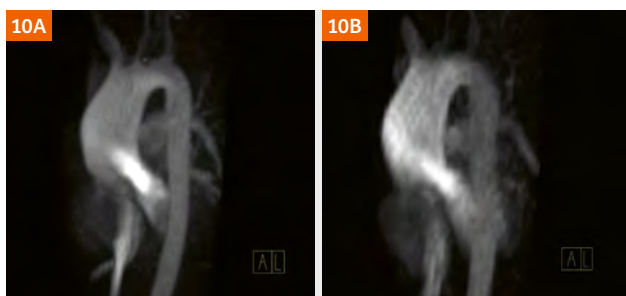


Figure 10: Comparison of imaging on the same patient with both WIP (10A) and product pseudo 4D flow images (10B). Note that the spatial resolution is not as good with the latter technique.

Analysis of data

Currently, we use prototype Siemens Healthineers "4Dflow v2.4" software for the majority of our 4D flow post-processing. In its current form, it is a work-in-progress software intended only for research which is equipped with good visualization and analytic options. User interface is simple and familiar since it uses the same format as in other MRI software packages in the Siemens Healthineers syngo ecosystem. It is divided into six consecutive tabs which guide the user from loading the data to visualization of 4D flow.

There is no PACS integration available at this time and 4D flow data should be loaded from a local disk. After loading the study ("Study Load" tab), the user can navigate between different phases and slices to find the desired structure and check for gross aliasing in different velocity encoding directions. You can also crop the dataset in phase and frequency encoding directions retrospectively (Crop Box). This helps to minimize the use of processing resources by the software, provides more accurate background phase correction and also reduces noise during visualization.

The second tab, "Corrections", provides background phase correction, anti-aliasing and motion tracking. Background phase correction extracts the stationary tissue by looking at the variance of velocities in each voxel which is deemed to be the lowest for stationary tissue. The resultant velocities in each slice are corrected so that the stationary tissue has zero velocity. As mentioned previously, cropping

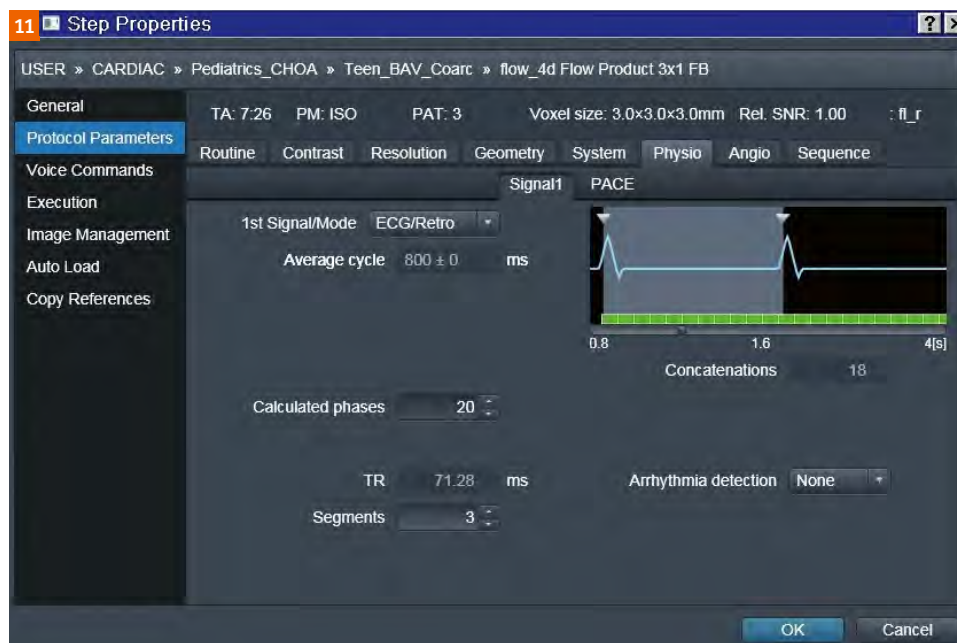


Figure 11: Similar to Image 2, the Physio tab on the user interface with the stack of 2D slices technique gives the user the ability to input the number of "Calculated Phases".

the dataset in the previous tab helps to eliminate wrap and ghosting artifacts which may interfere with stationary tissue extraction. The anti-aliasing algorithm looks for very large opposite jumps in the velocity-time curve for each voxel and removes the wrap introduced by insufficient velocity range. Finally, motion tracking uses a symmetric deformable registration technique to track the segmented anatomy, analysis planes and particle seeds over time. Note that motion tracking requires at a minimum of 16 slices to function properly, per the Siemens Healthineers user manual. We recommend utilizing all three correction techniques to provide the most robust data.

Before proceeding to the next tab, we adjust the “segmentation threshold” from the tools tab in the bottom toolbox. This slider controls the threshold-based segmentation according to the signal intensity. The goal is to find the balance between including the desired anatomy without going beyond vessel boundary (Figure 12). After adjusting the threshold, the mesh transparency can be adjusted or turned off from the display tab if desired.

Since the majority of our 4D flow patients have complex and abnormal flow patterns (e.g. eccentric and helical

flow in ascending aorta in stenotic bicuspid aortic valve or low velocity and opposing flow directions in Fontan circuit), we have opted not to use centerline and vessel model extraction available in “Segmentation” tab and skip to “Flow evaluation”. These are options within the software platform and can streamline the workflow for patients with laminar flow, but for the majority of our cases this aspect of the software often produces unreliable results (Figure 13).

Next, under the “Flow evaluation” tab, there are different functions located under sub-tabs: “Planes” and “Calc”. Under Planes, the user can draw contours along the vessel(s) of interest for flow quantification and particle seeding for visualization. We recommend setting the overlay to “none” for easier recognition of the anatomy (Figure 14). One can then navigate through the vessel in the 3D viewer on the left hand side of the screen. Note that contours can only be drawn in the left upper window, marked by a red border. Therefore, the red orthogonal line should always be perpendicular to the flow at the desired location. Once a contour is drawn, the flow-time curve will be automatically shown in the lower section of the screen. After all contours are added, user can switch

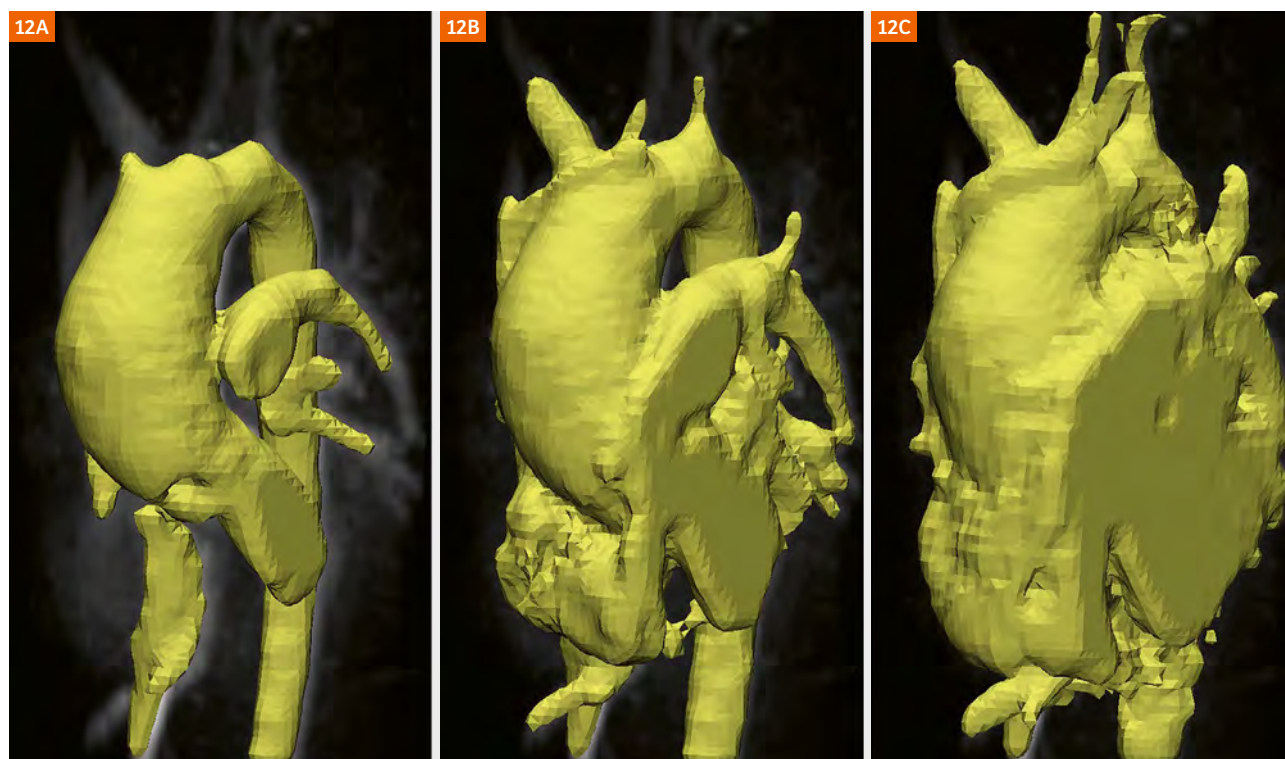


Figure 12: Segmentation with the Threshold slider: inadequate (12A), adequate (12B), excessive (12C) threshold.

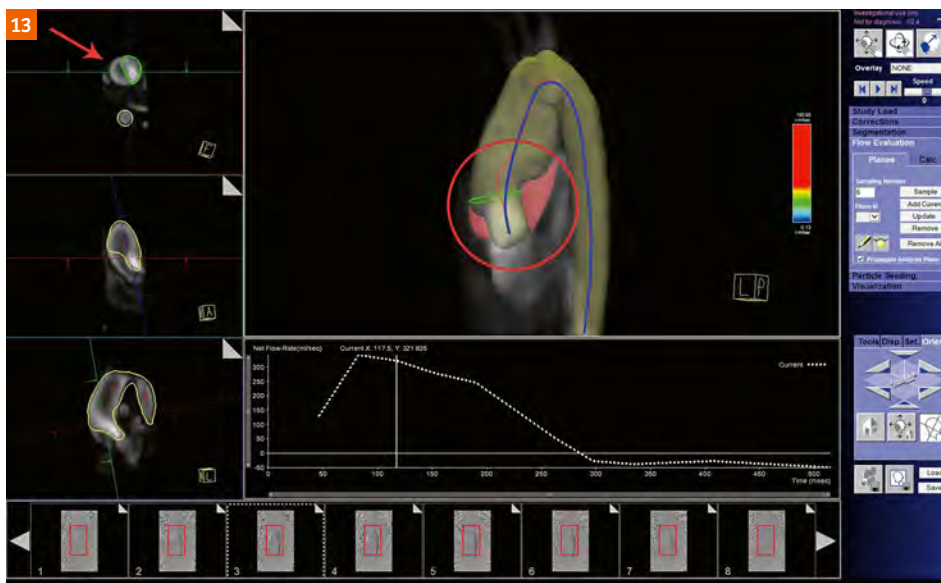


Figure 13: Unsuccessful centerline extraction and volume segmentation in a patient with bicuspid aortic valve. The true centerline (blue) and unsegmented aortic volume (bright red) are shown. Arrow points to the unsegmented ascending aortic lumen in axial plane.



Figure 14: Switching the overlay preset to "none" makes for easier navigation of the anatomy in the left panel (arrow).

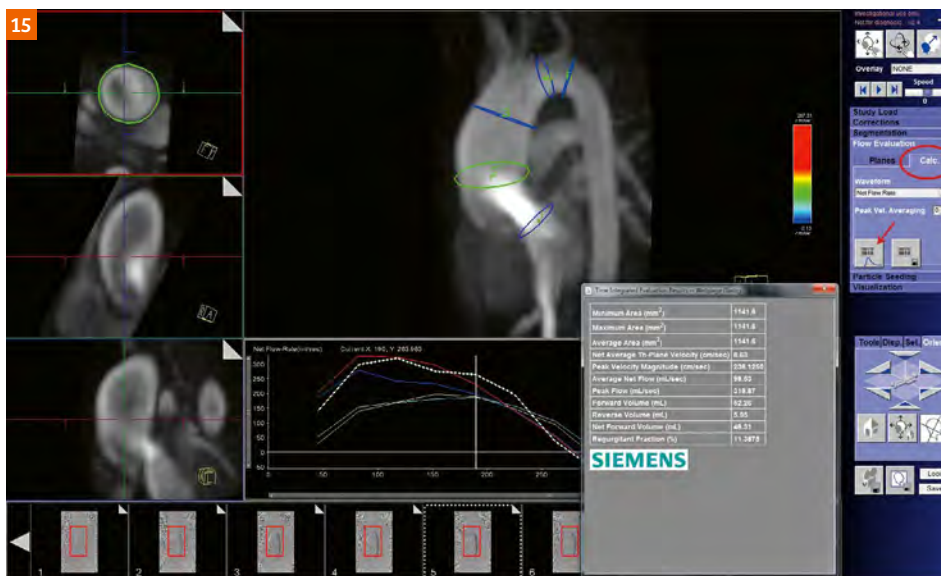


Figure 15: Flow quantification through the desired contour by switching to the "Calc" tab in flow evaluation.

to calculation tab to get detailed flow quantification (e.g. net flow, velocities, regurgitation fraction) through each contour. This is a valuable option to cross-examine 2D phase contrast flow data with 4D flow, especially in cases when 2D flow data quality is suboptimal (Figure 15).

The focus of the last two tabs is visualization of 4D flow. The “Particle seeding” tab allows the user to seed each contour drawn in the previous step with either the same or different colors (up to 4 colors). In cases where there are multiple inflows, the user can assign different colors to better visualize flow contribution and behavior during mixing (e.g. color coding SVC and IVC in Fontan circuit or pulmonary veins and mitral regurgitation jet in mitral valve disease). The user can also choose between seeding the drawn contours or the entire segmented volume by switching between volume and planes in the drop down menu. There are options to control the density of particle seeds, intervals in which they are emitted and the number of cardiac cycles they are visualized throughout. In our lab, we typically only change particle density for better visualization. In general, we use higher density in cases with larger voxel size (50–60% for 2–2.5 mm voxels and 70–80% for 2.6–3 mm voxels).

The final tab offers three visualization options. “Vector Field” illustrates the velocity vectors summation in the segmented planes or volume for each voxel over the cardiac cycle. “Particle Traces” continuously creates time-resolved pathlines originating from the seed planes to visualize the dynamic change in trajectory and velocity. “Streamlines” captures the instantaneous 3D velocity vector field in each cardiac phase. Unlike “Particle Traces”, it does not represent temporal evolution of flow in the

vessel (Figure 16). We prefer to visualize our 4D flow data with “Particle Traces” since subjectively it is more easily understood (and has good agreement with “Streamline” visualization). Finally, the user can export desired images or movie clips or save the workflow (segmentation, centerline and contours) for future use.

Case examples

Our most common patient population in which we utilize 4D flow imaging is those with various forms of Aortopathies. Bicuspid aortic valve patients frequently have abnormal flow jets in the ascending aorta, and in extreme examples can have a left hand helix pattern (Figure 17, Clip 4). Those with genetic syndromes, such as Turner syndrome, may have vortex formations in atypical locations, such as at the base of the left subclavian artery at the terminal end of an elongated transverse arch (Figure 18, Clip 5). There is work underway to assess these abnormal flow patterns and the resultant effect on wall integrity, rate of vascular dilation, and propensity to dissection [7–9]. Using the tools we have described above, flow dynamics can be visualized and basic assessment of hemodynamics can be obtained. Calculation of wall shear stress can also be performed. In our lab, when patients are found to have altered flow patterns in various forms of Aortopathy, the frequency of their follow up is often increased, and consideration is given for how these insights help predict their risk of cardiovascular events in the scope of surgical timing and planning.

The next most common patient population is those with repaired tetralogy of Fallot (TOF). Regardless of whether a transannular patch is used at the time of TOF repair, the

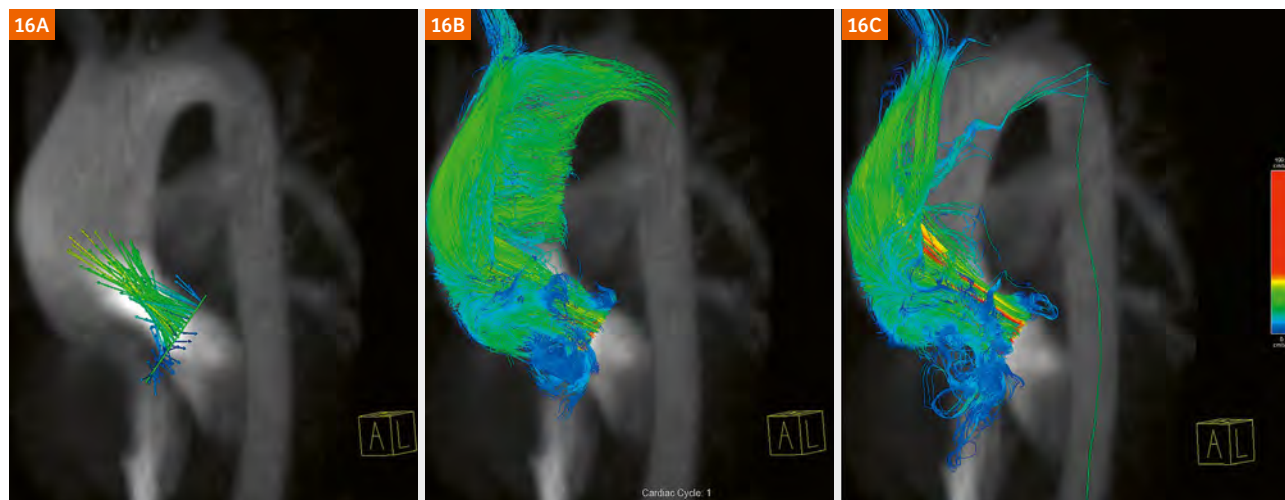


Figure 16:
Visualization options: vector field (16A), particle traces (16B) and Steamlines (16C).

pulmonary valve is virtually always non-functional by the time patients reach adolescence, and severe pulmonary insufficiency (coupled often with some degree of residual obstruction) is nearly universal. Visualization of the flow in the RVOT, both stenotic and regurgitant, is very helpful to understand the progression of the disease (Figure 19, Clip 6). Flow within the main and branch PA's, with

quantification of vortices, can be studied and correlated with presence and rate of RV dilation [10–12]. In those with irregular main and branch pulmonary artery architecture, such as those with pseudoaneurysm formation, these abnormal flow patterns are even more pronounced (Figure 20, Clip 6).

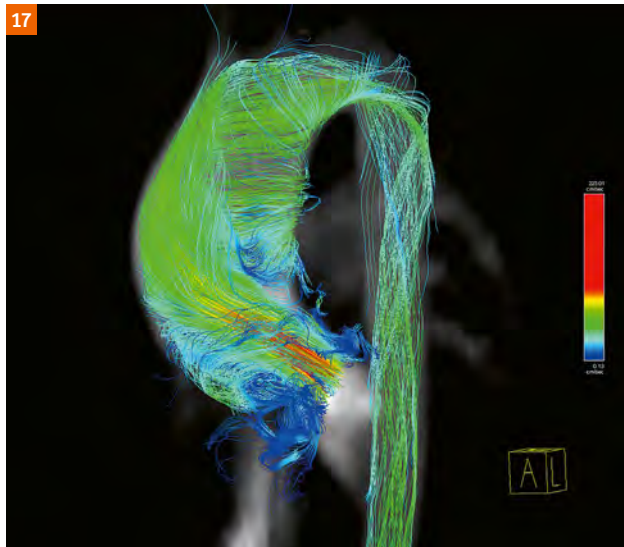


Figure 17:
Patient with a bicuspid aortic valve and a left hand helical pattern in the ascending aorta.

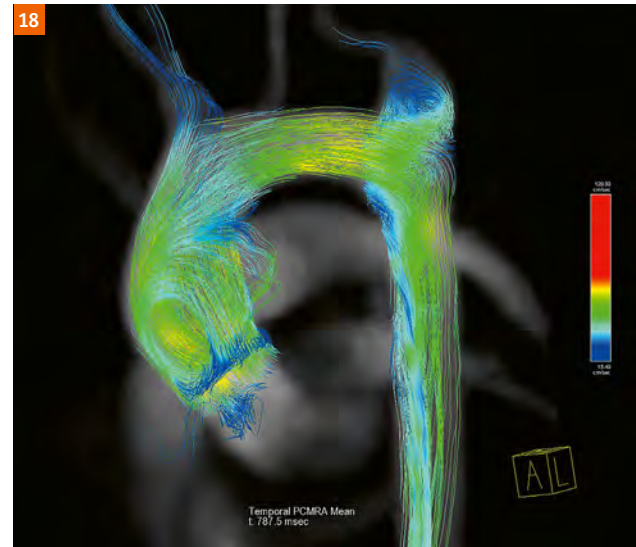


Figure 18:
Patient with Turner syndrome, no evidence of coarctation of the aorta, but with a prominent vortex formation at the base of the left subclavian artery.

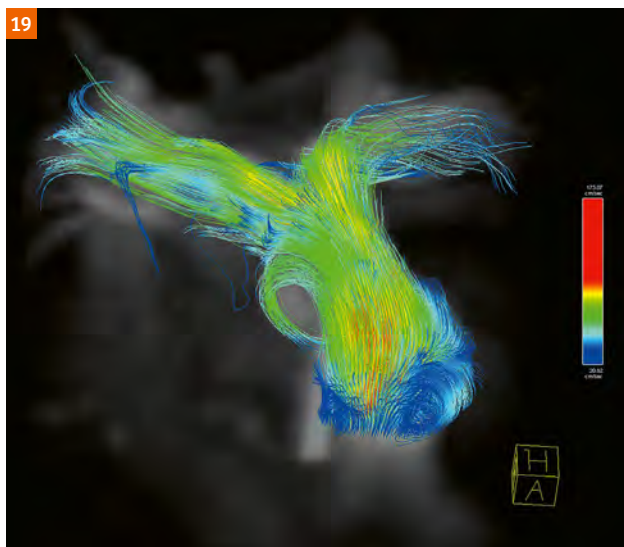


Figure 19:
Patient with repaired tetralogy of Fallot and turbulent flow noted in the main and branch pulmonary arteries.

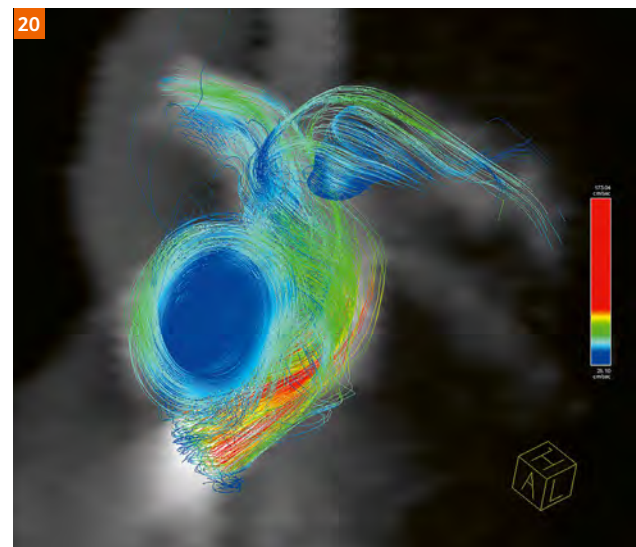


Figure 20:
Different patient with repaired tetralogy of Fallot and a pseudoaneurysm on the anterior surface of the main pulmonary artery. Note the prominent vortex within the pseudoaneurysm.

In our opinion, one of the most helpful patient subgroups for 4D flow imaging are those with single ventricle anatomies. A heterogeneous group, ranging from variants such as tricuspid atresia with a single left ventricle, to those with hypoplastic left heart syndrome with a single right ventricle, to those with heterotaxy syndrome with a myriad of systemic and pulmonary venous anomalies on top of

their intracardiac defects, these patients truly represent the extreme end of complexity in the field of congenital heart disease. The unifying feature for these patients is the series of staged palliations they undergo, culminating in a Fontan procedure. With only a single functional ventricle which must be used to pump blood to the body, the Fontan circulation relies on passive systemic venous return into the pulmonary arteries by anastomosing the superior vena cava (SVC) (Figure 21, Clip 7) directly to the PA and connecting the inferior vena cava (IVC) to the PA as well (Figure 22, Clip 8), via either an intracardiac tunnel or a separate conduit.

In patients whom have undergone a Fontan completion, altered flow hemodynamics within their circuit can lead to several clinical issues. One of the most difficult to assess is formation of pulmonary arteriovenous malformations (PAVM), thought to be due to lack of a component of hepatic blood flow (termed “hepatic factor”) to reach the pulmonary capillary bed in affected lung segments. Knowledge of the streaming of the inferior systemic venous return, therefore, is of paramount importance in assessing these patients’ risk for development of PAVM’s [13]. Traditional 2D flow imaging can assess total volumes of flow into the RPA and LPA, but cannot quantify how much of each lung’s arterial supply comes from the IVC versus the SVC. While the Siemens Healthineers software mentioned above does not have specific features to

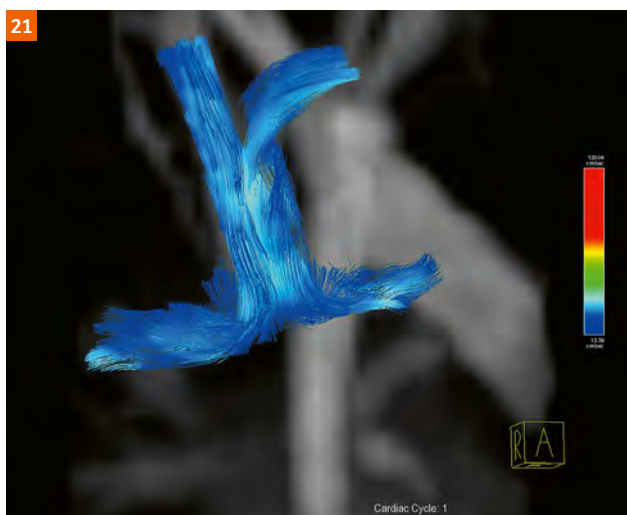


Figure 21: Flow from the superior vena cava into the branch pulmonary arteries in a patient with single ventricle anatomy who has undergone a bidirectional Glenn anastomosis.

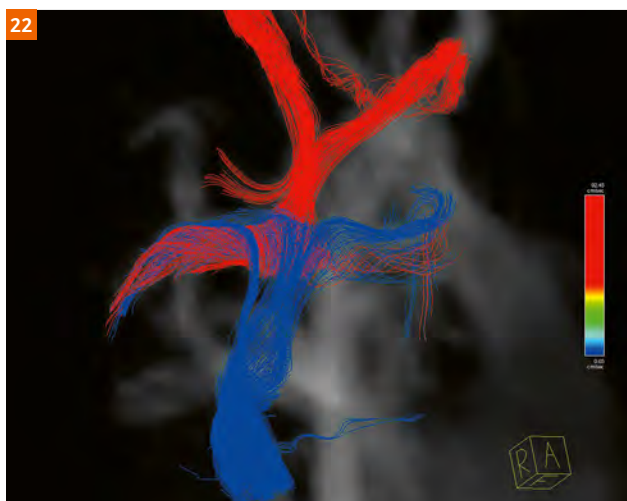


Figure 22: Flow from the superior vena cava (colored red) and inferior vena cava (labeled blue) into the branch pulmonary arteries in a patient with single ventricle anatomy who has undergone a bidirectional Glenn anastomosis and subsequent Fontan completion. In this patient’s case, there was a small fenestration placed in the Fontan baffle, seen by the blue streamlines heading rightward on the image near the lower margin of the Fontan.

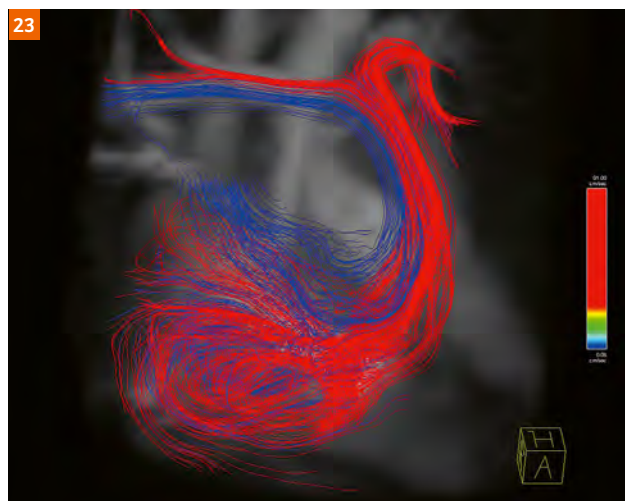


Figure 23: Patient with Ebstein’s anomaly of the tricuspid valve, with flow across the superior aspect of the tricuspid valve labeled blue and across the inferior aspect labeled red, so that the abnormal flow in the right ventricle based on portion of tricuspid inflow can be visualized.

quantify flow volumes produced only from select vessels, we have developed an in-house MATLAB code which allows us to perform these calculations.

One final application that we are increasingly using 4D flow to assess is intraventricular flow dynamics in patients with heart failure or abnormal ventricular loading. While in adult patients, this topic is much more common in those with a structurally normal heart and heart failure from ischemic cardiac disease [14], in pediatric patients many forms of native and palliated congenital heart disease lead to long-term heart failure. Labs have looked at both left and right ventricular mechanics, including in patients with repaired TOF [15] and single ventricle patients [16, 17]. An additional, less studied disease type is patients with Ebstein's anomaly, where marked tricuspid insufficiency results in very abnormal flow patterns in the right ventricle (Figure 23, Clip 9). Performing 4D flow allows visualization of these hemodynamics, which may lead to better understanding of the mechanism of ventricular dilation and dysfunction for many of these patients.

Future directions

One limitation of 4D flow is the long acquisition times required. With the addition of compressed sensing and other image acceleration techniques, data acquisition times continue to shrink, allowing increases in spatial and temporal resolution in the datasets. Many vendors and labs are now working towards a vision of having 4D flow represent a "one stop shop" for congenital cardiac magnetic resonance imaging. One can imagine that if the spatial resolution can be decreased to roughly one millimeter voxels, then full anatomic reconstructions including short axis cine stacks can be extracted from the 4D datasets for analysis. If the temporal resolution can be improved to match current 2D flow methodologies (typically 30 phases per cardiac cycle), and retrospective gating acquisitions are used, then the 4D flow data would obviate the need for additional 2D phase contrast imaging. Thus, a high spatial and temporal resolution 4D flow dataset would provide all of the anatomic, functional, and flow data on a given patient, without need for acquiring separate double oblique 2D planes. This approach also has the advantage of being much easier for a technologist to acquire, as it is not patient specific / anatomy dependent for accurate image plane set up.

There are, however, several existing challenges to such an approach. Full chest coverage with millimeter voxels requires a large quantity of data, and this is amplified by the desire for high temporal resolution increasing the number of phases. For example, in many adolescent size patients, in order to cover the whole chest in a sagittal

geometry with 1 mm slices, 100–150 slices are needed. If temporal resolution of 30 phases per cycle is desired, this will produce between 12,000 and 18,000 images. This vast array of data takes substantial time for reconstruction, made even more computationally demanding when iterative reconstruction is used with compressed sensing. Computational power and processors continue to improve, but most labs that are currently taking this type of approach to 4D flow imaging the reconstruction is done off-line and takes several hours before the data is ready.

Another challenge to this approach to 4D flow imaging is ensuring consistent, uniform signal throughout the study. As discussed above, while 4D flow sequences can be obtained with or without contrast, performing these sequences post-contrast allows increased SNR and CNR as well as higher degrees of parallel imaging acceleration. In the past, blood-pool gadolinium contrast agents such as Gadofosveset trisodium were used in several pediatric labs for performance of contrast enhanced MR angiography and 4D flow imaging [18], but this agent is no longer commercially available in the United States. Another option is non-gadolinium based contrast agents, such as ferumoxytol, which has been used for neonatal and pediatric CMR studies, though our lab does not have personal experience with this approach. Ferumoxytol has a different risk profile than gadolinium based agents, but there is data that for select patient groups these techniques can decrease the need for sedation/anesthesia (which also carries its own inherent risks) [19].

Conclusions

Application of 4D flow imaging to patients with congenital heart disease is an exciting new avenue for greater understanding of patient specific hemodynamics. Both prototype sequences as well as derivations of product pulse sequences allow acquisition of 4D flow datasets, with strengths and weaknesses in each technique. In our lab, we utilize a combination of these sequences, tailored to the individual patient anatomy, size, heart rate, and time limitations on the study. While several third party analysis platforms are available, at the current time the majority of our experience is with the Siemens 4D flow software, and we find that both the 3D visualization and quantification potential on this platform allows comprehensive use of these 4D flow data for our patients.

To access the .avi clips please visit

www.siemens.com/4Dflow

Abbreviations

2D	2-dimensional	GRAPPA	Generalized auto-calibrating partially parallel acquisition	Qp	Pulmonary blood flow
4D flow	4-dimensional phase contrast imaging	IVC	Inferior vena cava	RPA	Right pulmonary artery
Ao	Aorta	LPA	Left pulmonary artery	PC	Phase contrast
bpm	Beats per minute	MPA	Main pulmonary artery	TR	Repetition time
BAV	Bicuspid aortic valve	NSA	Number of signal averages	SNR	Signal to noise ratio
BDG	Bidirectional Glenn	PAVM	Pulmonary arterio-venous malformations	SV	Single ventricle
CMR	Cardiac magnetic resonance imaging	PA	Pulmonary artery	SVC	Superior vena cava
CHD	Congenital heart disease			Qs	Systemic blood flow
FOV	Field of view			TOF	Tetralogy of fallot
				VENC	Velocity encoding
				TOF	Tetralogy of fallot
				VENC	Velocity encoding

References

- 1 P. R. Moran. "A flow velocity zeugmatographic interlace for NMR imaging in humans". *Magn Reson Imaging*, 1, 197-203, 1982.
- 2 M. O'Donnell. "NMR blood flow imaging using multiecho, phase contrast sequences". *Med Phys*, 12, 59-64, 1985.
- 3 A. J. Powell and T. Geva. "Blood flow measurement by magnetic resonance imaging in congenital heart disease". *Pediatr Cardiol*, 21, 47-58, 2000.
- 4 K. K. Whitehead, K. S. Sundareswaran, W. J. Parks, M. A. Harris, A. P. Yoganathan and M. A. Fogel. "Blood flow distribution in a large series of patients having the Fontan operation: a cardiac magnetic resonance velocity mapping study". *J Thorac Cardiovasc Surg*, 138, 96-102, 2009.
- 5 C. L. Dumoulin, S. P. Souza, M. F. Walker and W. Wagle. "Three-dimensional phase contrast angiography". *Magn Reson Med*, 9, 139-149, 1989.
- 6 H. G. Bogren and M. H. Buonocore. "4D magnetic resonance velocity mapping of blood flow patterns in the aorta in young vs. elderly normal subjects". *J Magn Reson Imaging*, 10, 861-869, 1999.
- 7 L. Mirabella, A. J. Barker, N. Saikrishnan, E. R. Coco, D. J. Mangiameli, M. Markl and A. P. Yoganathan. "MRI-based Protocol to Characterize the Relationship Between Bicuspid Aortic Valve Morphology and Hemodynamics". *Ann Biomed Eng*, 43, 1815-1827, 2015.
- 8 N. Saikrishnan, L. Mirabella and A. P. Yoganathan. "Bicuspid aortic valves are associated with increased wall and turbulence shear stress levels compared to trileaflet aortic valves". *Biomech Model Mechanobiol*, 14, 577-588, 2015.
- 9 Y. Shan, J. Li, Y. Wang, B. Wu, A. J. Barker, M. Markl, C. Wang, X. Wang and X. Shu. "Aortic shear stress in patients with bicuspid aortic valve with stenosis and insufficiency". *J Thorac Cardiovasc Surg*, 153, 1263-1272 e1261, 2017.
- 10 J. Geiger, M. Markl, B. Jung, J. Grohmann, B. Stiller, M. Langer and R. Arnold. "4D-MR flow analysis in patients after repair for tetralogy of Fallot". *Eur Radiol*, 21, 1651-1657, 2011.
- 11 C. J. Francois, S. Srinivasan, M. L. Schiebler, S. B. Reeder, E. Niespodzany, B. R. Landgraf, O. Wieben and A. Frydrychowicz. "4D cardiovascular magnetic resonance velocity mapping of alterations of right heart flow patterns and main pulmonary artery hemodynamics in tetralogy of Fallot". *J Cardiovasc Magn Reson*, 14, 16, 2012.
- 12 D. Hirtler, J. Garcia, A. J. Barker and J. Geiger. "Assessment of intracardiac flow and vorticity in the right heart of patients after repair of tetralogy of Fallot by flow-sensitive 4D MRI". *Eur Radiol*, 26, 3598-3607, 2016.
- 13 P. Bachler, I. Valverde, N. Pinochet, S. Nordmeyer, T. Kuehne, G. Crelier, C. Tejos, P. Irrazaval, P. Beerbaum and S. Uribe. "Caval blood flow distribution in patients with Fontan circulation: quantification by using particle traces from 4D flow MR imaging". *Radiology*, 267, 67-75, 2013.
- 14 J. Zajac, J. Eriksson, P. Dyverfeldt, A. F. Bolger, T. Ebbers and C. J. Carlhall. "Turbulent kinetic energy in normal and myopathic left ventricles". *J Magn Reson Imaging*, 41, 1021-1029, 2015.
- 15 P. Sjöberg, S. Bidhult, J. Bock, E. Heiberg, H. Arheden, R. Gustafsson, S. Nozohoor and M. Carlsson. "Disturbed left and right ventricular kinetic energy in patients with repaired tetralogy of Fallot: pathophysiological insights using 4D-flow MRI". *Eur Radiol*, 2018.
- 16 V. P. Kamphuis, A. A. W. Roest, J. J. M. Westenberg and M. S. M. Elbaz. "Biventricular vortex ring formation corresponds to regions of highest intraventricular viscous energy loss in a Fontan patient: analysis by 4D Flow MRI". *Int J Cardiovasc Imaging*, 34, 441-442, 2018.
- 17 J. Wong, R. Chabiniok, S. M. Tibby, K. Pushparajah, E. Sammut, D. S. Celermajer, D. Giese, T. Hussain, G. F. Greil, T. Schaeffter and R. Razavi. "Exploring kinetic energy as a new marker of cardiac function in the single ventricle circulation". *J Appl Physiol* (1985), 2018.
- 18 A. Tandon, S. Hashemi, W. J. Parks, M. S. Kelleman, D. Saltee and T. C. Slesnick. "Improved high-resolution pediatric vascular cardiovascular magnetic resonance with gadofosveset-enhanced 3D respiratory navigated, inversion recovery prepared gradient echo readout imaging compared to 3D balanced steady-state free precession readout imaging". *J Cardiovasc Magn Reson*, 18, 74, 2016.
- 19 L. M. Lai, J. Y. Cheng, M. T. Alley, T. Zhang, M. Lustig and S. S. Vasanawala. "Feasibility of ferumoxytol-enhanced neonatal and young infant cardiac MRI without general anesthesia". *J Magn Reson Imaging*, 45, 1407-1418, 2017.



Contact

Timothy C. Slesnick, M.D.
 Director, Cardiac MRI
 Children's Healthcare of Atlanta
 Associate Professor
 Department of Pediatrics
 Emory University School of Medicine
 1405 Clifton Road North East
 Atlanta, GA 30322
 USA
 Tel: +1 404-256-2593
 SlesnickT@kidsheart.com

Advanced neuroimaging and pediatric epilepsy surgery

Sarah Barton^{1,2,3}; Michael Kean^{1,2,3}; Simon Harvey^{1,2,3}; Joseph Yang^{1,2}

¹ Murdoch Children's Research Institute, Parkville, VIC, Australia

² Royal Children's Hospital, Melbourne, VIC, Australia

³ Department of Paediatrics, University of Melbourne, VIC, Australia

Neuroimaging in epilepsy surgery

Epilepsy, a common chronic brain disorder characterized by recurrent unprovoked seizures, usually has onset during childhood. Worldwide, epilepsy affects 10.5 million children and represents about a quarter of the global epilepsy population [1]. At least 50% of epilepsy during childhood is of focal onset, and up to 30% of children with focal epilepsy have seizures that are incompletely controlled on medications [2]. Epilepsy surgery offers some of these children the opportunity for seizure freedom, improvements in development and overall better quality of life for them and their family [3].

Advanced multi-modal magnetic resonance imaging (MRI) techniques are pivotal to comprehensive presurgical evaluation in children¹ with drug-resistant focal epilepsy [4].

These advanced imaging techniques contribute to lesion identification; localization of the seizure focus, with concordant clinical and electrophysiological information; lateralisation of the language dominant cerebral hemisphere [5]; and localization of functional cortical and subcortical brain regions subserving movement, memory, language and visual function. Advanced multi-modal MRI has the potential to simplify the patient's presurgical workup, obviate the need for intracranial EEG monitoring and electrical stimulation, improve postoperative seizure outcome, and avoid or minimize postoperative neurological deficits.

¹ Siemens Healthineers disclaimer does not represent the opinion of the authors: MR scanning has not been established as safe for imaging fetuses and infants less than two years of age. The responsible physician must evaluate the benefits of the MR examination compared to those of other imaging procedures.

TR	TE	FOV	Matrix	Slice	Grappa	SMS	B ₀ Shim	Ref Scan	RF Mode Gradient	ESP	BW
Multi-Shell DWI MAGNETOM Prisma syngo MR E11C 32-channel Head Coil											
4000	78 ms	244	122 100%	2 mm	2	2	Adv	Gre/Sep	Normal Performance	0.58 ms	2276 Hz/Px
fMRI Language Task MAGNETOM Prisma MB Acquisition syngo MR E11C 32-channel Head Coil											
1500	30 ms	255	104 100%	2.5 mm	2	3	Adv	FLEET	Normal Performance	0.5 ms	2404 Hz/Px
Resting State MAGNETOM Prisma MB Acquisition syngo MR E11C 32-channel Head Coil											
1500	30 ms	255	104 100%	2.5mm	2	3	Adv	FLEET	Normal Performance	0.5 ms	2404 Hz/Px

Table 1: MR acquisition parameters for DWI, fMRI, and fMRI sequences.

Diffusion MRI tractography – limitations of Diffusion Tensor Imaging (DTI)

Diffusion MRI tractography is a post-processing imaging technique that generates virtual reconstructions of the anatomy of brain nerve fibre tracts, also known as white matter tracts (WMTs) [6, 7]. Accuracy of the tractography reconstruction is paramount in neurosurgery because surgical injury to the WMTs or their blood supply can lead to permanent neurological deficits [8–10]. MRI data can be coregistered and overlaid on a live view of the patient's brain during surgery, using image-guided navigation software. Preoperative tractography combined with the intraoperative live view of the patient, provide important information to the neurosurgeon to plan the optimal surgical approach to minimize injury to surrounding healthy brain structures.

The tractography techniques adopted in neurosurgery traditionally involve diffusion tensor imaging (DTI) data acquisition and a deterministic tractography algorithm, but this approach is unable to accurately model diffusion over crossing fibre regions [11, 12], present in up to 90% of the cerebral white matter (WM) [13]. State-of-the-art methods are available that improve WMT modelling, with advances in diffusion MRI data acquisition, improved tracking algorithms, and better methods for image-based tract reconstructions. Modern tractography techniques incorporate high angular resolution diffusion imaging (HARDI) data acquisition and probabilistic fibre tracking [14] based on the constrained spherical deconvolution (CSD) crossing fibre models [15, 16], improving tractography results in ways that have a significant impact on surgical planning and intraoperative image-guidance.

More recent advances in tractography include multi-shell and multi-band diffusion acquisitions. Multi-shell diffusion imaging acquires low, intermediate and high b-value diffusion data in one sitting, producing diffusion propagation maps that are more specific to the WM tissue domain [17]. This is termed the multi-shell multi-tissue-CSD (MSMT-CSD) technique. MSMT-CSD improves the accuracy of fibre-orientation distribution (FOD) estimation in WM regions over the grey-white matter tissue interface and removes noisy isotropic voxels that belong to the cerebrospinal fluid space, thereby improving further the anatomical accuracy of the tractography reconstruction (Fig. 1). Multi-band or simultaneous multi-slice acquisition schemes reduce the time needed to acquire multi-shell diffusion data within a clinically acceptable timeframe [18, 19].

Diffusion MRI tractography at the Royal Children's Hospital, Melbourne

Since 2012, advanced tractography reconstructions using HARDI data acquisition and based on CSD crossing-fibre modelling and probabilistic tracking have been used for preoperative planning for epilepsy surgery at the Royal Children's Hospital, Melbourne, Australia. The introduction of multi-band, multi-shell DWI acquisition in 2016 further improved the anatomical accuracy of our tractography reconstructions. Combined with clinical expertise and other imaging and electrophysiological modalities, we believe our clinical tractography program has contributed to improved seizure and functional outcomes in children undergoing epilepsy surgery. In this article we present the neuroimaging data for three children in whom tractography played a role in pre-surgical planning for their epilepsy surgery.

MR protocol at the Royal Children's Hospital, Melbourne

Our early implementation of multi-band diffusion sequences and SMS TSE into our comprehensive epilepsy protocol utilized MAGNETOM Trio / MAGNETOM Verio syngo MR B17 software and resulted in a significant improvement in our diagnostic imaging protocols (spatial resolution, reduction in scan times and integration of advanced image analysis). Prior to implementing these sequences into clinical practice we undertook comprehensive comparative studies in volunteers using conventional and multi-band acquisitions plus analysis pipeline verification. The comparative studies looked at the optimization of protocols for 3T [20–22], variations in tSNR that could affect analysis of resting state data [23], interslice artefacts [24, 25], effects of patient movement during the ACS acquisition [26, 27] and how far we could push the multi-band factor on our systems [28–30]. Our initial protocols (DWI, fMRI and rfMRI) have been transitioned through to our current systems (MAGNETOM Prisma syngo MR E11C and Biograph mMR syngo MR E11P) with modifications to the imaging parameters, notably multi-band factors and spatial resolution (Table 1). Multi-shell acquisitions are acquired using 3 separate scans (Monopolar diffusion scheme; $b = 3000 \text{ s/mm}^2$, 69 dir including 5 $b = 0$, $b = 2000 \text{ s/mm}^2$, 50 dir including 5 $b = 0$ and $b = 1000 \text{ s/mm}^2$, 30 dir including 5 $b = 0$) using a custom vector file.

WIP, the product is currently under development and is not for sale in the US and in other countries. Its future availability cannot be ensured.

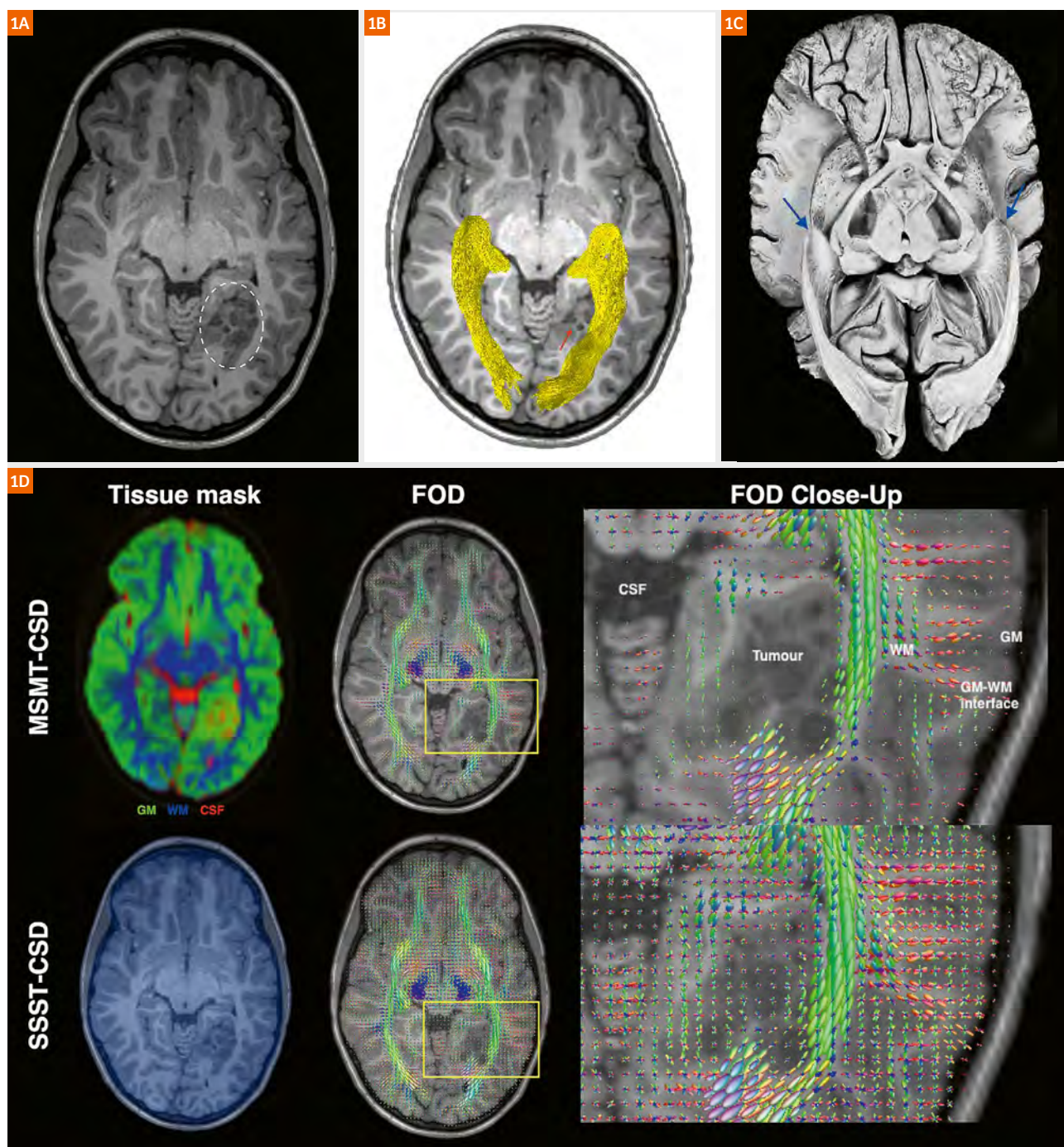


Figure 1:

(1A–C) Advanced diffusion MRI white matter modelling and tractography reconstruction in a patient with focal drug refractory epilepsy referable to a developmental brain tumor located in the left fusiform gyrus (white dashed circle, **(1A)** T1-weighted image). Multi-band, multi-shell diffusion data acquired using a 3T MAGNETOM Prisma Siemens scanner, was used to reconstruct the optic radiation tractography (yellow color in **(1B)**) closely abutting the tumor. The reconstructed tractography closely resemble cadaveric fibre dissection (blue arrows in **(1C)**); taken from Ludwig & Klinger's atlas, 1956.

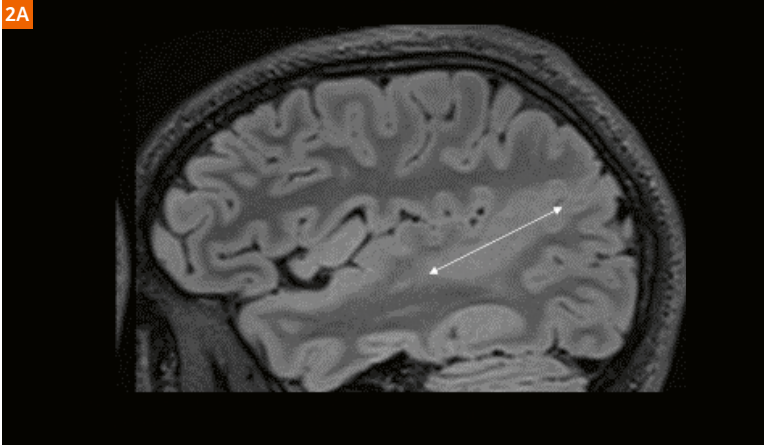
(1D) shows the multi-shell multi-tissue-constrain spherical deconvolution (MSMT-CSD) framework improves tissue specificity of the diffusion mask, and the accuracy of corresponding fibre orientation distribution (FOD) estimations, than the traditional approach of using single-shell single-tissue-CSD (SSST-CSD). Combinations of these features improved anatomical accuracy of the tractography output. CSF = cerebrospinal fluid; GM = gray matter; WM = white matter.

Case 1

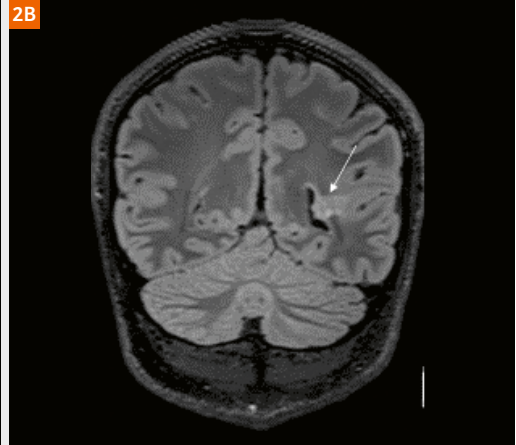
In this case, we present neuroimaging data from an adolescent with temporal lobe epilepsy. Seizure onset was at two years of age, with seizures from wake and sleep characterized by staring, confusion, speech difficulties and sometimes convulsing. The seizures were refractory to numerous antiepileptic medications. MRI showed a long bottom-of-sulcus focal cortical dysplasia

in the left superior temporal sulcus, which merged into the sylvian fissure at the lateral convexity. The dysplasia was characterized by cortical thickening and grey-white blurring on T1-weighted MPR images, subcortical signal hyperintensity on FLAIR and T2-weighted images, and hypometabolism on FDG-PET images. Also associated with the dysplasia was an unusual transmantle band leading to a periventricular nodule in the left trigone.

2A



2B



3

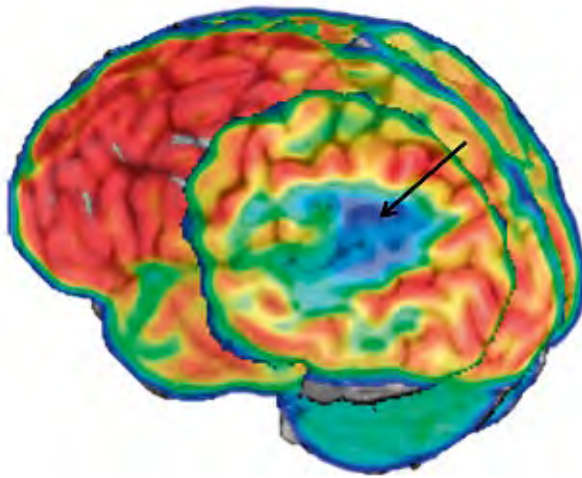


Figure 2:

FLAIR image showing an extensive focal cortical dysplasia in the left superior temporal sulcus (2A) with a transmantle band and periventricular nodule at the trigone (2B).

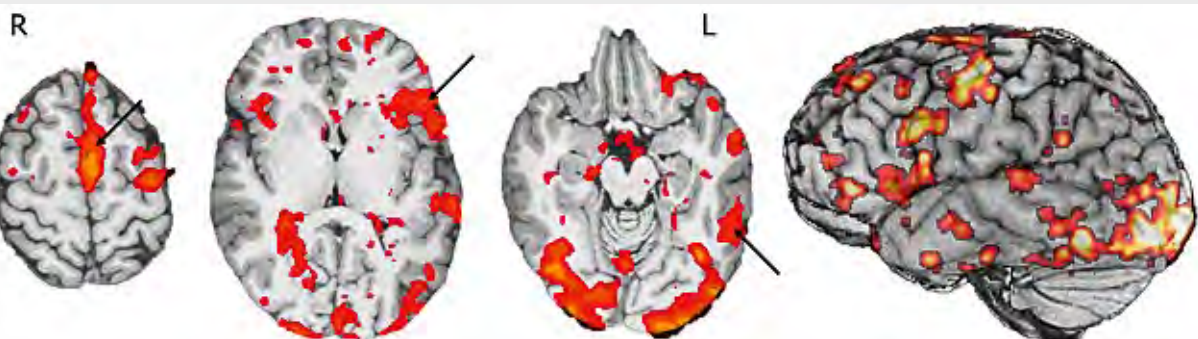
Figure 3:

3D surface-rendered, co-registered T1-weighted MRI and FDG-PET with oblique slice showing focal hypometabolism in the depth of the cortical dysplasia which involved the left superior temporal sulcus at the depth and the sylvian fissure at the lateral convexity superior temporal sulcus.

Figure 4:

Axial slices from language fMRI with a verb generation task showing left medial frontal, inferior frontal and inferior temporal BOLD activation. The surface-rendered 3D image shows the atypical localization of temporal activation in the inferior temporal gyrus.

4



Functional MRI with a visually-presented verb generation paradigm [31] showed left lateralization of language activation. Typical distribution of frontal activation was observed in the posterior-medial frontal region and frontal operculum; however, temporal activation was somewhat atypical, with the greatest activation in the inferior (as opposed to superior) temporal gyrus. No BOLD activation was seen in the dysplasia.

Probabilistic tractography was performed on HARDI data [15, 16, 32] to localize the superior longitudinal fasciculus (SLF) and the optic radiations (OR), in particular their relationship to the deeper components of the dysplasia. The temporal projections of the left SLF travelled immediately medial to the depth of the dysplastic superior temporal sulcus. The majority of the

cortical terminations of the left SLF were in the inferior temporal gyrus, which corresponded with location of the temporal BOLD activation. The left OR travelled through and around the transmantle band in the WM between the depth of the dysplasia and the periventricular nodule.

The functional and structural imaging therefore showed the extent of the dysplasia, the likely absence of function in the dysplasia, the proximity of language cortex and WM pathways to the superficial and deeper components of the dysplasia, and the passage of the transmantle component of the dysplasia through the visual pathways. The epilepsy surgery team could conceivably proceed with knowledge of the operative risks and without need for additional electrical stimulation mapping.

5

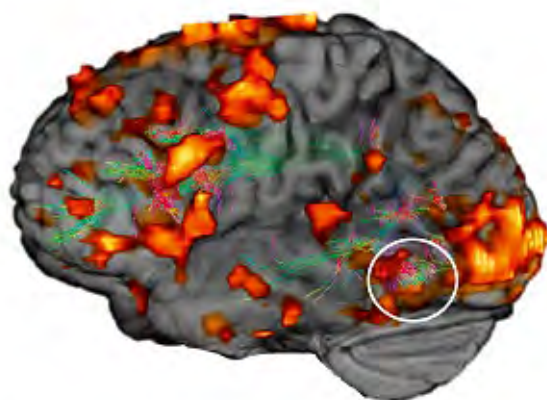
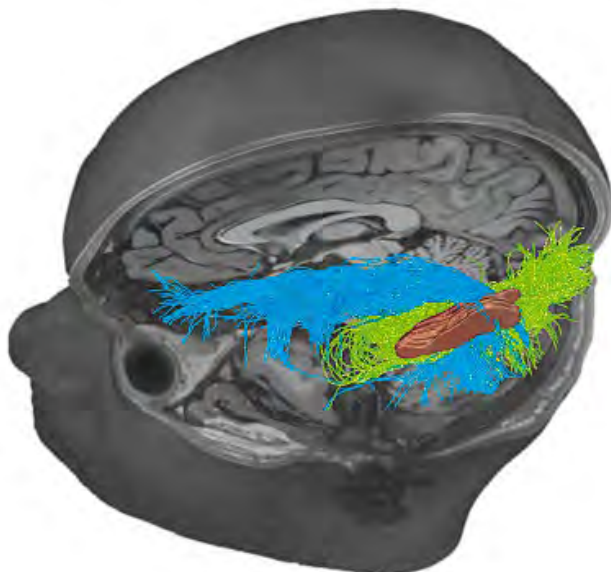


Figure 5:
3D projection of the left SLF showing the correspondence with language BOLD activation in the inferior temporal gyrus.

Figure 6:
Location of the SLF (blue) and OR (green) in relation to the dysplastic superior temporal sulcus (brown) in 3D (**6A**) and relative to periventricular nodule on axial FLAIR (**6B**).

6A



6B



Case 2

This patient was a primary school aged child with a brief history of focal seizures with prominent confusion and aphasia. They occurred at weekly frequency, despite several antiepileptic medications being trialled. MRI revealed a lesion in the left temporal lobe laterally and posteriorly, involving grey and white matter and filling a gyrus. The lesion was believed to be a low-grade glioma, rather than a focal cortical dysplasia or developmental tumor. Minor growth was seen on serial imaging over six months.

On functional MRI using a visually-presented verb generation task [31], language was left lateralized. There was language activation in cortex medial to and surrounding the lesion. Probabilistic tractography was performed on HARDI data [15, 16, 32] to localize the superior longitudinal fasciculus (SLF). The terminations of the SLF tracts were in the cortex and WM abutting the lesion, where BOLD activation was seen on fMRI. Optic radiation (OR) tractography showed visual pathways travelled deeper to the SLF. The functional imaging indicated that surgery would need to be a conservative lesionectomy, sparing superficial and deep language cortex and pathways.



Figure 7: Appearance of left temporal lesion on T2-weighted coronal image.

Figure 8: Language BOLD activation in left hemisphere relative to temporal lesion (crosshair).



Figure 9: 3D renders of the left hemisphere showing language BOLD activation (9A) and SLF terminations (9B) relative to the temporal lesion.



Figure 10: 3D tractography showing the location of the SLF (blue) and OR (green) in relation to the lesion (yellow).

Case 3

Here we present neuroimaging data from a child with recent-onset of seizures secondary to a left medial temporal-occipital tumour. Seizures were characterized by behavioural arrest, head and eye deviation and repetitive hand movements, followed by brief nonsensical speech. MRI showed a multi-cystic, cortically-based and contrast-enhancing tumor in the left fusiform gyrus, abutting the parahippocampal gyrus and calcarine fissure. The tumor had mixed MRI features of a DNET and PCA and showed slight change in enhancement and size on serial imaging. Left language dominance was established with functional MRI utilizing verb generation and verbal fluency

paradigms [31]. Additionally, it revealed prominent BOLD activation in the posterior-basal temporal lobe, just lateral to the tumor.

Probabilistic tractography was performed on HARDI data [15, 16, 32] to localize the SLF and OR pathways. It revealed that the tumor was encircled by visual and language pathways, indicating significant risk of deficits in cognition, language, verbal memory and peripheral vision with attempted resection. However, with the aid of neuronavigation, preoperative simulated surgery using the detailed tractography data, and intraoperative MRI (IMRIS), surgery was performed with the impression of complete resection and no neurological deficits. Post-operative imaging and assessments are pending.

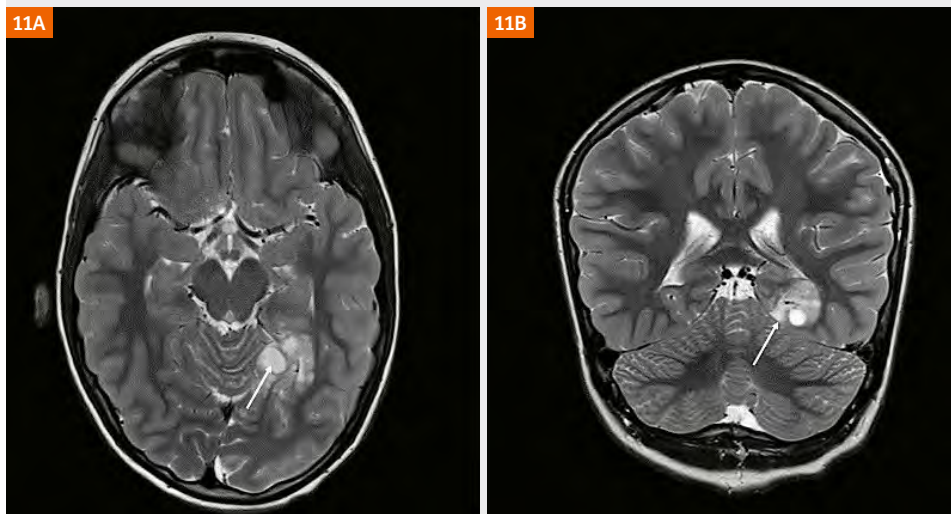
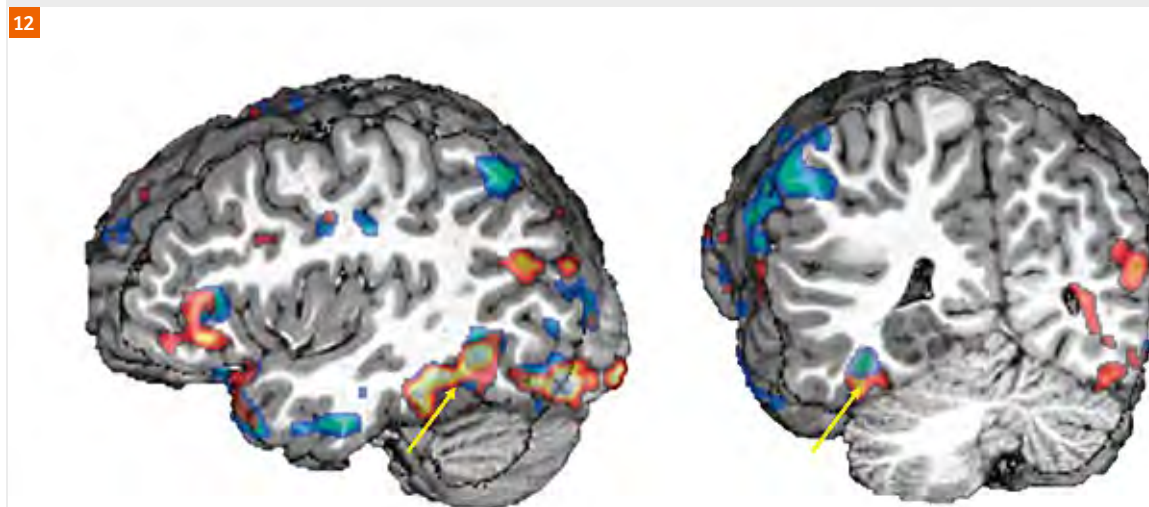


Figure 11: Appearance of left medial temporal-occipital tumour on T2-weighted axial (**11A**) and coronal (**11B**) image.

Figure 12: Lateral and oblique cut-aways showing the basal temporal language BOLD (noun verb = orange; verbal fluency = blue) overlying the tumor.



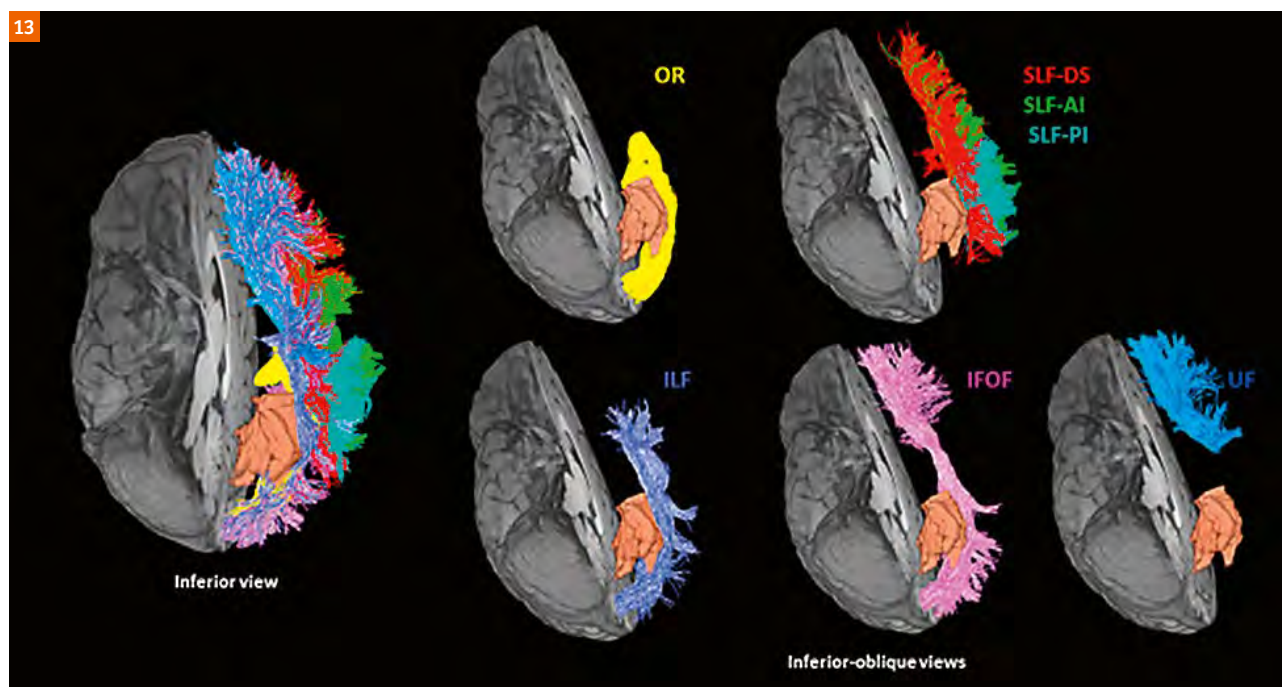


Figure 13: Tractography in relation to the tumor (brown). OR = optic radiation, SLF-AI = anterior indirect segment of superior longitudinal fasciculus, SLF-DS = direct segment of superior longitudinal fasciculus, SLF-PI = posterior indirect segment of superior longitudinal fasciculus, ILF = inferior longitudinal fasciculus, IFOF = inferior fronto-occipital fasciculus; UF = uncinate fasciculus.

Acknowledgements

This work was conducted within the Department of Neurology and Neurosurgery, Royal Children's Hospital, and the Developmental Imaging and Neuroscience Research groups, Murdoch Children's Research Institute at the Melbourne Children's MRI and PET centre, Melbourne, Victoria, Australia. It was supported by the Royal Children's Hospital Foundation, Murdoch Children's Research Institute, The University of Melbourne Department of Paediatrics, and the Victorian Government's Operational Infrastructure Support Program.

The authors acknowledge the assistance of Siemens Healthineers for ongoing support with works in progress sequences (WIPs) plus scientific support and the Centre for Magnetic Resonance Research Minnesota for access to multiband sequences through a C2P agreement. The authors also acknowledge the staff of the Melbourne Children's MRI and PET centre for their efforts in scanning our patients.

The authors and author's institutions did not receive any incentive or inducement, financial or otherwise, from Siemens Healthineers for the preparation of this article. The data in this article was generated by the authors on institutional infrastructure and was not edited by Siemens Healthineers.

References

- Guerrini, R. Epilepsy in children. *Lancet* 367, 499-524, doi:10.1016/S0140-6736(06)68182-8 (2006).
- Berg, A. T. et al. How long does it take for epilepsy to become intractable? A prospective investigation. *Ann Neurol* 60, 73-79, doi:10.1002/ana.20852 (2006).
- Snead, O. C., 3rd. Surgical treatment of medically refractory epilepsy in childhood. *Brain Dev* 23, 199-207 (2001).
- Rastogi, S., Lee, C. & Salamon, N. Neuroimaging in pediatric epilepsy: a multimodality approach. *Radiographics* 28, 1079-1095, doi:10.1148/rq.284075114 (2008).
- Binder, J. R. Functional MRI is a valid noninvasive alternative to Wada testing. *Epilepsy & behavior* 20, 214-222 (2011).
- Basser, P. J., Mattiello, J. & LeBihan, D. Estimation of the effective self-diffusion tensor from the NMR spin echo. *J Magn Reson B* 103, 247-254 (1994).
- Basser, P. J., Pajevic, S., Pierpaoli, C., Duda, J. & Aldroubi, A. In vivo fiber tractography using DT-MRI data. *Magnetic resonance in medicine : official journal of the Society of Magnetic Resonance in Medicine / Society of Magnetic Resonance in Medicine* 44, 625-632 (2000).
- Duffau, H. The dangers of magnetic resonance imaging diffusion tensor tractography in brain surgery. *World Neurosurg* 81, 56-58, doi:10.1016/j.wneu.2013.01.116 (2014).
- Farquharson, S. et al. White matter fiber tractography: why we need to move beyond DTI. *Journal of neurosurgery* 118, 1367-1377, doi:10.3171/2013.2.JNS121294 (2013).
- Kinoshita, M. et al. Fiber-tracking does not accurately estimate size of fiber bundle in pathological condition: initial neurosurgical experience using neuronavigation and subcortical white matter stimulation. *Neuroimage* 25, 424-429, doi:10.1016/j.neuroimage.2004.07.076 (2005).
- Tournier, J. D., Calamante, F. & Connelly, A. MRtrix: diffusion tractography in crossing fiber regions. *International Journal of*

- Imaging Systems and Technology 22, 53-66, doi:10.1002/ima.22005 (2012).
- 12 Tournier, J. D., Mori, S. & Leemans, A. Diffusion tensor imaging and beyond. *Magnetic resonance in medicine : official journal of the Society of Magnetic Resonance in Medicine / Society of Magnetic Resonance in Medicine* 65, 1532-1556, doi:10.1002/mrm.22924 (2011).
 - 13 Jeurissen, B., Leemans, A., Tournier, J. D., Jones, D. K. & Sijbers, J. Investigating the prevalence of complex fiber configurations in white matter tissue with diffusion magnetic resonance imaging. *Hum Brain Mapp* 34, 2747-2766, doi:10.1002/hbm.22099 (2013).
 - 14 Tuch, D. S. Q-ball imaging. *Magnetic resonance in medicine : official journal of the Society of Magnetic Resonance in Medicine / Society of Magnetic Resonance in Medicine* 52, 1358-1372, doi:10.1002/mrm.20279 (2004).
 - 15 Tournier, J. D., Calamante, F. & Connelly, A. Robust determination of the fibre orientation distribution in diffusion MRI: non-negativity constrained super-resolved spherical deconvolution. *Neuroimage* 35, 1459-1472, doi:S1053-8119(07)00124-3 [pii] 10.1016/j.neuroimage.2007.02.016 (2007).
 - 16 Tournier, J. D., Calamante, F., Gadian, D. G. & Connelly, A. Direct estimation of the fiber orientation density function from diffusion-weighted MRI data using spherical deconvolution. *Neuroimage* 23, 1176-1185, doi:S1053-8119(04)00410-0 [pii] 10.1016/j.neuroimage.2004.07.037 (2004).
 - 17 Jeurissen, B., Tournier, J. D., Dhollander, T., Connelly, A. & Sijbers, J. Multi-tissue constrained spherical deconvolution for improved analysis of multi-shell diffusion MRI data. *Neuroimage* 103, 411-426, doi:10.1016/j.neuroimage.2014.07.061 (2014).
 - 18 Feinberg, D. A. & Setsompop, K. Ultra-fast MRI of the human brain with simultaneous multi-slice imaging. *J Magn Reson* 229, 90-100, doi:10.1016/j.jmr.2013.02.002 (2013).
 - 19 Moeller, S. et al. Multiband multislice GE-EPI at 7 tesla, with 16-fold acceleration using partial parallel imaging with application to high spatial and temporal whole-brain fMRI. *Magnetic resonance in medicine : official journal of the Society of Magnetic Resonance in Medicine / Society of Magnetic Resonance in Medicine* 63, 1144-1153, doi:10.1002/mrm.22361 (2010).
 - 20 Barth, M., Breuer, F., Koopmans, P.J., Norris, D.G. and Poser, B.A., 2016. Simultaneous multislice (SMS) imaging techniques. *Magnetic resonance in medicine*, 75(1), pp.63-81.
 - 21 Todd, N., Moeller, S., Auerbach, E.J., Yacoub, E., Flandin, G. and Weiskopf, N., 2016. Evaluation of 2D multiband EPI imaging for high-resolution, whole-brain, task-based fMRI studies at 3T: sensitivity and slice leakage artifacts. *Neuroimage*, 124, pp.32-42.
 - 22 Xu, J., Moeller, S., Auerbach, E.J., Strupp, J., Smith, S.M., Feinberg, D.A., Yacoub, E. and Ugurbil, K., 2013. Evaluation of slice accelerations using multiband echo planar imaging at 3 T. *Neuroimage*, 83, pp.991-1001.
 - 23 Preibisch, C., Bührer, M. and Riedl, V., 2015. Evaluation of multiband EPI acquisitions for resting state fMRI. *PLoS one*, 10(9), p.e0136961.
 - 24 Cauley, S.F., Setsompop, K., Polimeni, J.R. and Wald, L.L., 2012. Inter-slice artifact reduction for slice-GRAPPA reconstruction of simultaneous multi-slice (SMS) acquisitions. In *Proceedings of the 20th Annual Meeting of ISMRM, Melbourne, Australia* (p. 2543).
 - 25 Cauley, S.F., Polimeni, J.R., Bhat, H., Wald, L.L. and Setsompop, K., 2014. Interslice leakage artifact reduction technique for simultaneous multislice acquisitions. *Magnetic resonance in medicine*, 72(1), pp.93-102.
 - 26 Bhat, H., Polimeni, J.R., Cauley, S.J., Setsompop, K., Wald, L., Heberlein, K., 2014. Motion Insensitive ACS Acquisition Method for in-plane Simultaneous Multi-Slice Accelerated EPI. In *Proceedings of the ISMRM, Abstract (Vol. 0644)*
 - 27 Kelly, M.E., Duff, E.P., Bijsterbosch, J.D., Voets, N.L., Filippini, N., Moeller, S., Xu, J., Yacoub, E.S., Auerbach, E.J., Ugurbil, K. and Smith, S.M., 2013. An assessment of motion artefacts in multi band EPI for high spatial and temporal resolution resting state fMRI. In *Proceedings of the ISMRM, Abstract (Vol. 3275)*
 - 28 Golestani, A. M., Faraji-Dana, Z., Kayvanrad, M., Setsompop, K., Graham, S. J., & Chen, J. J. (2018). Simultaneous Multislice Resting-State Functional Magnetic Resonance Imaging at 3 Tesla: Slice-Acceleration-Related Biases in Physiological Effects. *Brain connectivity*, 8(2), 82-93.
 - 29 Demetriou, L., Kowalczyk, O.S., Tyson, G., Bello, T., Newbould, R.D. and Wall, M.B., 2018. A comprehensive evaluation of increasing temporal resolution with multiband-accelerated protocols and effects on statistical outcome measures in fMRI. *NeuroImage*.
 - 30 Setsompop, K., Cohen-Adad, J., McNab, J., Gagoski, B.A., Wedeen, V.J. and Wald, L.L., 2010. Improving SNR per unit time in diffusion imaging using a blipped-CAPIRINHA simultaneous multi-slice EPI acquisition. In *Proceedings of the 18th Annual Meeting of ISMRM* (p. 187).
 - 31 Wood, A. G. et al. Language cortex activation in normal children. *Neurology* 63, 1035-1044 (2004).
 - 32 Yang, J. Y.-M. et al. A systematic evaluation of intraoperative white matter tract shift in pediatric epilepsy surgery using high-field MRI and probabilistic high angular resolution diffusion imaging tractography. *Journal of Neurosurgery: Pediatrics* 19, 592-605 (2017).

Contact

Michael Kean, FSMRT
Chief MR Technologist
Children's MRI and PET Centre
Department of Medical Imaging
Honorary Fellow, Developmental Imaging,
Murdoch Children's Research Institute
Honorary Senior Research Fellow,
Department of Paediatrics,
The University of Melbourne
Royal Children's Hospital,
Flemington Road
Parkville
Australia
Tel.: +61 411681198
Michael.Kean@rch.org.au



Learn more!

Advanced pediatric neuro imaging. Application of new sequences

Michael Kean
(The Royal Children's Hospital, Melbourne, Australia)

www.siemens.com/magnetom-world
Clinical Corner > Clinical Talks

Our Protocols – Prisma VE11C

- When do we use SMS TSE – subject to patient compliance
 - Epilepsy
 - Stroke
 - Tumour
 - Headaches
 - Encephalitis
- When do we use SMS RESOLVE
 - All tumours
 - Presence of Blood or Calcium
 - Replaced RESOLVE in Brain

Dot for productivity

Kevin Dirlam

Halifax Health, New Smyrna Beach, Florida, USA

Breaking the status quo is not an optimal strategy for any viable, fast paced institution. However, developing and implementing a robust Dot platform can overcome any of the anxiety and disruption that typically characterize change. The Dot platform has not always been the highlight of protocol building, but with the advances introduced by the *syngo* MR E platform, creating and using protocols far surpasses the expectations that came with the earlier *syngo* MR D platform. We began our Dot journey by stumbling through the early iterations of Dot development, and now find ourselves equipped with an efficient and user-friendly software that streamlines processes and increases functionality, but only as far as we allow the platform to go.

The *syngo* MR D line was the jumping off point for our Dot journey – and it really was a matter of jumping off. This new software was meant to ease the workload for the user, but adopting the design elements took some acclimatization. The D line allowed the user, or rather the application specialist, to build site protocols into a multilevel user platform that organized the workflow into strategies that achieved efficiency by making it possible to

quickly switch scanning patterns for different patients. To better explain this, I will use an everyday example of a typical MRI patient: The exam begins with the patient asking what MRI is and how MRI differs from CT scans. After listening to a brief explanation of how MRI uses a large magnet to make detailed pictures from the protons inside the body, the technologist makes the patient as comfortable as possible and begins the exam. Some of the streamlined efficiencies start at this point. In the case of basic brain or abdomen scans, the MRI system knows the common centering points for certain body regions and automatically positions the patient at the center of the magnet. Technologists do not have to turn on the laser light to initiate location of isocenter. Instead, they simply press and hold the toggle wheel on the front of the scanner to center the patient directly at isocenter. By handling simple tasks like this, the scanner allows technicians to concentrate on the patient and the exam. Dot was created to relieve users of some monotonous tasks by having the system perform them without demanding too much expertise. At the console equipped with the D level software, technologists can choose the

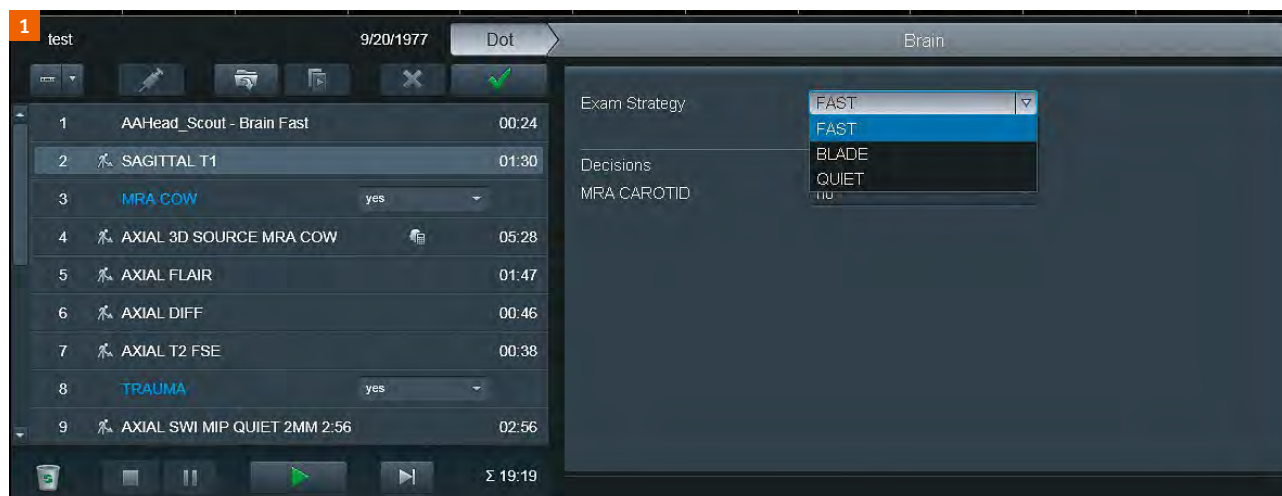


Figure 1:

The window on the right shows the Dot exam strategy chosen from a simple dropdown menu. The three strategies that we built are FAST, BLADE, and QUIET.

exam strategy that best fits their assessment of what the patient can tolerate. Dot allows users to determine if the patient is compliant enough for the routine exam or if a fast strategy is needed to accommodate the patient's needs. With Dot, users can simply choose a strategy from the Dot menu and start the exam. It is also possible to change the exam strategy along the way.

Back in our example patient scenario, the patient in the scanner begins to wonder where the loud noise is coming from and starts to look around. The diligent technologist asks the patient to stop moving and to remain still for the exam. After a few more minutes, the patient starts to move again, but this time the technologist decides to employ a different strategy. By simply clicking on the Dot menu again, the technologist can switch the pulse sequence strategy to BLADE sequences. The Dot menu makes it possible to change the manner in which the exam is delivered with four mouse clicks. For busy technologists managing patients who need extra attention, this ease of altering the exam strategy is key. The D platform changes the routine series into a BLADE series without the technologist having to enter the user tree and locate the sequences manually – as demonstrated in this Dot Cockpit screenshot.

For a fast-paced, patient-centered facility, the efficiency gains here are monumental. The speed at which technologists can alter the scan to accommodate the patient reduces scan times and improves exam quality.

The Dot platform added another ingenious option that streamlines throughput: AutoAlign is a user-preference feature that allows the scanner to attempt to align the slices as set out in the protocol. To illustrate this, think of the basic axial brain. The scanner has built-in options that tell the software to align the slices in an axial fashion with the base of the brain, orbits, temporal lobe, etc.

With the slice set-up fixed in the protocol, the scanner will attempt to align the slices as programmed, which means users can simply accept the scanner's decision or adjust the slices as they see fit. This may seem like the scanner is taking over the job of the technologist, but it is simply a tool that helps technologists achieve the efficient throughput that today's busy MRI departments require. As mentioned above, this option is entirely user-induced, and the creator of the protocol can choose the extent to which the scanner operates on behalf of the technologist. This feature also allows for reproducibility across different users in a single facility, which benefits the patient and the radiologist.

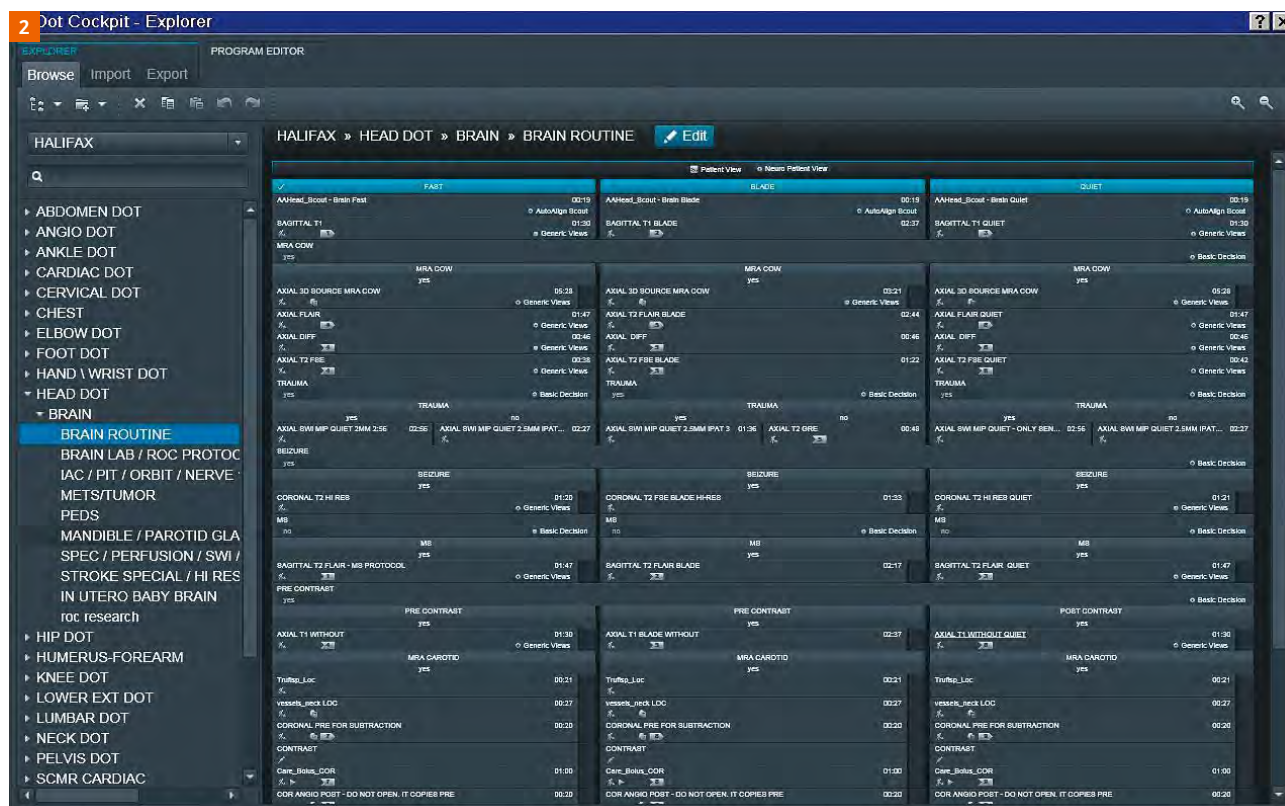


Figure 2: The Dot Cockpit with all the brain strategies tailored for our facility.

Advances to the D platform came with some limitations. The software would occasionally freeze when attempting to mix pulse sequences that were not in Dot protocols with

Dot scans. This sometimes left users with only one option: Restarting the software. In addition to this shortcoming, my earlier comment about an application specialist



Figure 3: Screenshot illustrating the different AutoAlign features that are preprogrammed for brain imaging.

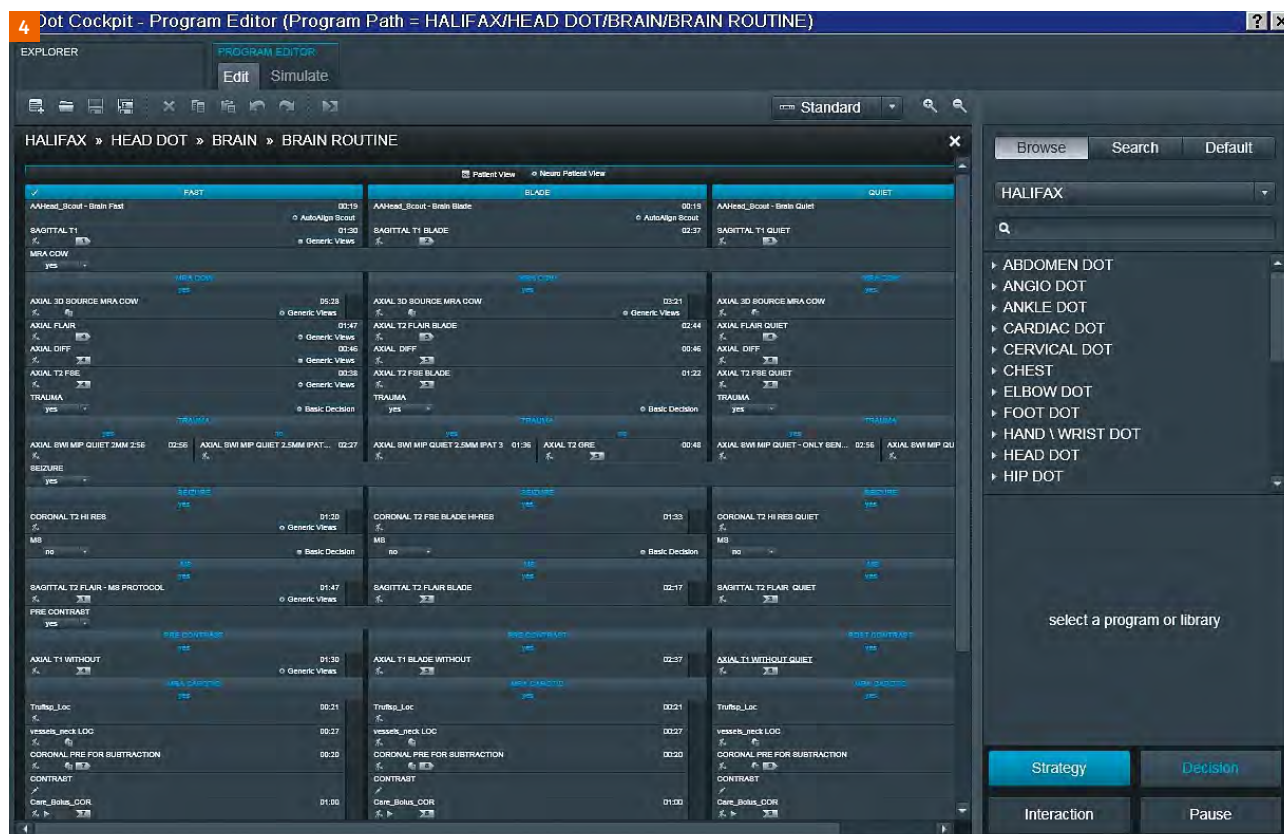


Figure 4: The bottom-right corner of this screenshot shows the Strategy option, which can be dragged directly into the exam series list for ease of protocol building.

building the Dot tree for users was not lightly made. The Dot building in the D platform did not make it easy for authors to navigate the string of pulse strategies. This statement is not characterizing the platform as a useless toy, but as a sophisticated tool that can enhance a department's productivity once the software has been implemented in a logical and user-friendly fashion.

After working with the D line for two years, we acquired the E line with Evolve. The benefits of this version exceptionally enhanced our workflows both in terms of daily throughput and protocol management. The E line is what the D line needed. To start with, the protocol-building portion of this upgrade is fast and user-friendly. After a day of application training, users can build a Dot protocol with multiple strategies from scratch. Some of the best

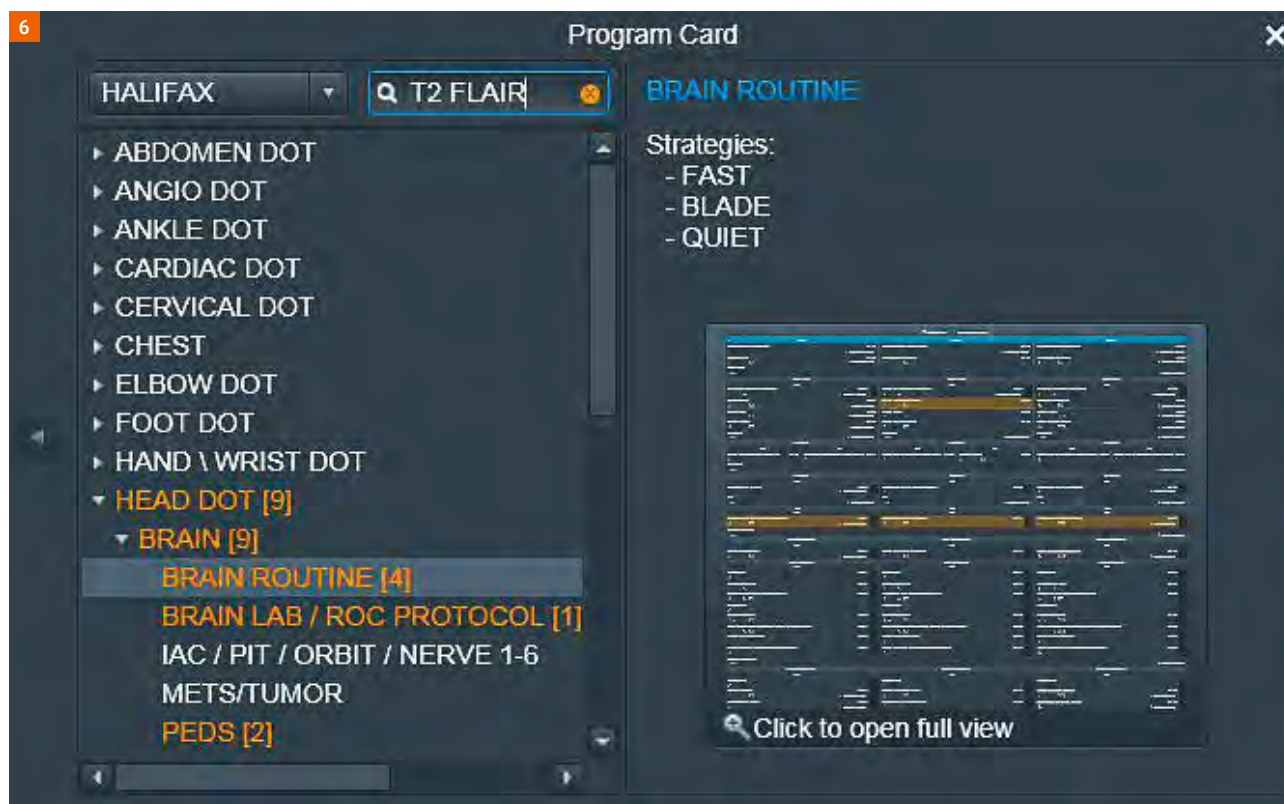


Figure 6: Screenshot showing the ease of finding a sequence using the search function.



Figure 7: Copy series options

additions are the drag-and-drop AddIns that appear directly on the protocol screen.

Users can decide whether a decision such as giving contrast should be built into the protocol or added to the options in the Dot screen so that technologists can choose it at the same time as the strategy. Adding images and text for guidance is simple. It can be done for any sequence so that all technologists can reproduce difficult or rare exams accurately and easily.

This is also a good feature for new technologists who might need assistance in achieving proper characterization of an exam. Another excellent workflow improvement is the ability to intertwine Dot and non-Dot sequences without overwhelming the scanner. Sequences can be easily added to an exam by simply opening the Dot Cockpit to the desired protocol and using the drag-and-drop function. In addition to locating sequences by protocol, Dot also offers an ingenious search feature. If a sagittal T2w FLAIR is needed for an MS patient but is not already built into the protocol, users can simply open the Dot Cockpit and type 'T2 FLAIR' (or the name of any

other pulse sequence). The scanner will search all the sequences in the active user tree and highlight relevant protocols in yellow.

This allows the user to see all the protocols containing T2 FLAIR, and to choose one that will fit the needs of the patient. Although this might not sound like much, the feature can help alleviate the anxiety that a technologist might feel when a radiologist stops by and asks to have a special pulse added to an exam.

Another excellent Dot feature is the speed at which it can preset copy references. Again, this sounds basic, but the ability to build the exact slice copy into a sequence allows the technologist to set the orthogonal slices as desired and have the scanner copy options such as slices and saturation bands, or indeed everything about the sequence.

This function makes it possible to set the basic axial brain and have the following axials copy the slice locations. Technologists might therefore only have to set up one sagittal, one axial, and one coronal for the entire exam. For the remainder of the time, they are free to complete other tasks involved in the exam or workflow. In a high-volume facility, every minute counts, and relieving staff of some monotonous tasks improves patient care and increases efficiency.

MRI scans can still be performed without Dot. However, to effectively accommodate the needs of today's patients and fulfil clerical expectations, using Dot to streamline repetitive or mundane tasks is the far superior option. By allowing the scanner to handle basic user tasks without removing the autonomy of the technologist, a well-developed Dot system can simplify workflows and enhance efficiency. Entrusting the scanner with these tasks does take a leap of faith, but once users see the consistency and reliability that is available through the Dot system, the benefits will greatly outweigh the concerns. The one thing to remember is that Dot is a tool and not a replacement. Working with the system to improve patient outcomes and efficiency is paramount in modern healthcare, so embrace the technology, but rest assured that you are always in control.



Contact

Kevin Dirlam
MRI Coordinator
Halifax Health
401 Palmetto St
New Smyrna Beach, Florida 32168
USA

MR imaging of the cervical spinal cord at 7T: a multiparametric portfolio

Aurélien Massire, Ph.D.¹; Thorsten Feiweier, Ph.D.²; Tobias Kober, Ph.D.³; Thomas Troalen, Ph.D.⁴;
Jean-Philippe Ranjeva, Ph.D.¹; Maxime Guye, M.D., Ph.D.¹; Virginie Callot, Ph.D.¹

¹ Aix-Marseille University, CNRS, AP-HM, CRMBM, Hôpital de la Timone, CEMEREM, Marseille, France

² Siemens Healthineers, Erlangen, Germany

³ Advanced Clinical Imaging Technology, Siemens Medical Solutions-CIBM, Lausanne, Switzerland

⁴ Siemens Healthineers, Saint-Denis, France

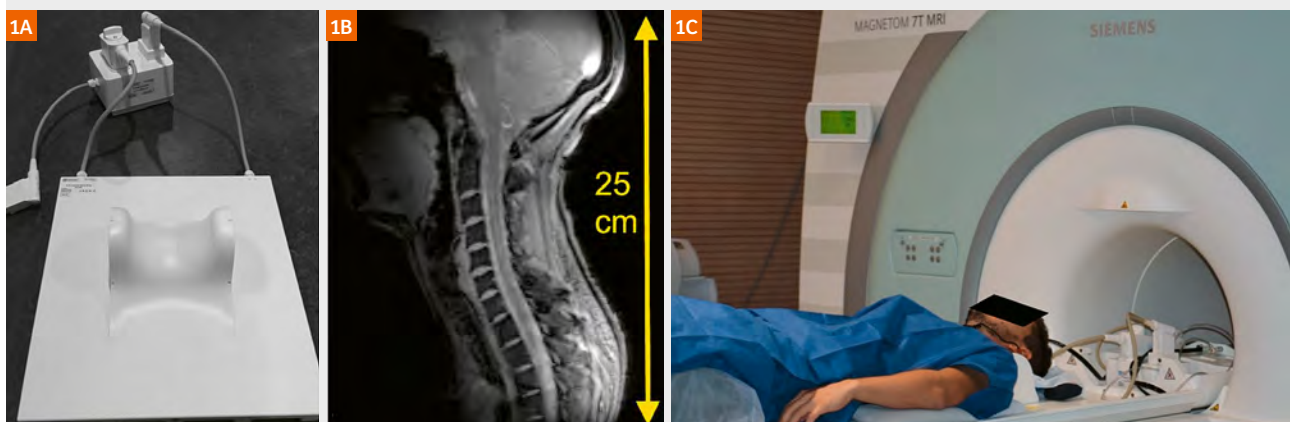
Introduction

The increased signal-to-noise ratio (SNR) provided by ultra-high field (UHF) MR systems (7T and above) used to enhance spatial resolution has strong potential to image tiny structures, such as in the spinal cord (SC) [1]. In addition, increased sensitivity to magnetic susceptibility and modifications of tissue relaxation times at UHF could result in an improved ability to detect small lesions [2]. As a result, 7T MR systems bear great potential for providing high-quality high-resolution anatomical images that may improve pathological cervical SC characterization. Nevertheless, SC applications have been able to benefit from the higher sensitivity provided by UHF only within

recent years [1–5]. In addition to many challenges related to SC imaging [6] such as partial volume effect (PVE) contamination or physiological motion, the lack of SC-dedicated 7T MR coils has greatly delayed investigations until recently [1]. Last but not least, static and radio-frequency magnetic fields (ΔB_0 and B_1^+) inhomogeneities are exacerbated at UHF, resulting in additional technical challenges for imaging [1].

On the other hand, quantitative MRI (qMRI), which is now largely used on 1.5T and 3T MR systems to characterize SC pathologies [6, 7], has been recognized as a valuable tool to strengthen diagnosis and prognosis, and it usually correlates well with clinical disabilities in a wide range

Figure 1: MAGNETOM 7T MR system in CRMBM-CEMEREM, Marseille, France



(1A) Customized 8-channel transceiver coil-array. The coil elements are spread on a curved saddle surface cradling the subject's neck. In transmit mode, an identical RF waveform is delivered to each of the elements after dividing the supplied power through a power splitter. The coil operates with pre-fixed phase polarization, and fixed tuning and matching at 297 MHz / 50 Ω . The central element (#8) is typically centered at the C3–C4 vertebral level location. **(1B)** Sagittal scout localizer MR image showing typical spatial coil coverage (from cerebellum to T1 vertebra). **(1C)** Picture of coil and volunteer set-up.

syngo B17 MR sequences	GRE ΔB_0 field mapping	MP-TFL B_1 mapping (#543B)	TSE	SPACE (#692)	Multi-echo GRE	MP2RAGE (#900B)	SS-SE-EPI adv. diff. (#511F)
Dimension	2D	2D	2D	3D	2D	3D	2D
Orientation	sag	sag	sag	cor	tra	cor	tra
TA (min)	1.17	1.10 ¹	2.20 ¹	6.00	15.37	9.00	7.00 ¹
TR (s)	0.2	5 ¹	4 ¹	4	0.5	5	4 ¹
TE (ms)	3.06/4.08	3.05	34	289	5.2/9.4/13.7/17.9	2.15	55.2
FA (°)	32	8	Hyperechoes	T ₂ var	50	4/5	90
FOV (mm ²)	192 x 192	256 x 256	192 x 192	224 x 190	180 x 146	260 x 177	103 x 103
Matrix size	192 x 192	256 x 256	320 x 320	320 x 272	1024 x 832	368 x 250	128 x 128
Resolution (mm) ³	1 x 1 x 2	1 x 1 x 5	0.6 x 0.6 x 2.2	0.35 x 0.35 x 0.35 ²	0.18 x 0.18 x 2	0.7 x 0.7 x 0.7	0.8 x 0.8 x 3
Number of slices	7	7	7	384	7	192	7
GRAPPA factor	–	–	2	3	–	2	3
Partial Fourier	–	–	–	enabled	6/8	6/8	6/8
Number of averages	1	1	1	1	3	1	3

Table 1: Main sequence parameters used at CRMBM-CEMEREM

¹ The sequence was triggered using a peripheral pulse-oximeter placed on the finger.

² The sequence resolution was interpolated (native in-plane resolution of 0.7 mm).

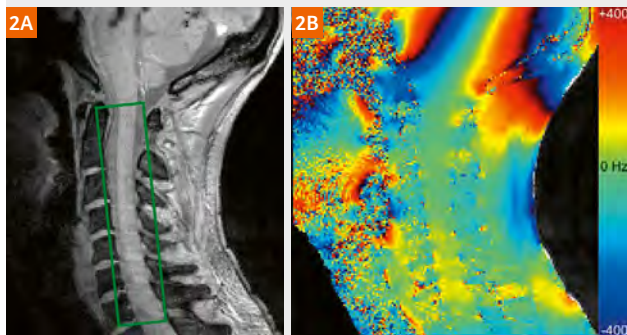
of degenerative SC diseases [8]. In order to also benefit from multi-parametric quantitative MR techniques for SC studies at 7T, setting appropriate strategies to tackle the aforementioned challenges is mandatory. In this work, we therefore propose a multi-parametric MR investigation of the healthy cervical SC at 7T³ that could be further used to characterize structural impairments in various SC pathologies.

To drastically reduce PVE and explore SC substructures while taking advantage of the increased SNR conferred at UHF, transverse imaging of the SC was performed using a multiple-echo gradient echo (GRE) sequence and T2* mapping with an ultra-high in-plane resolution as high as (180 μ m)².

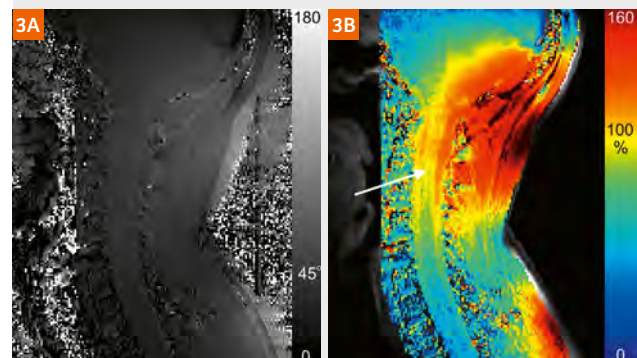
To quantitatively investigate diffuse SC tissue alterations along the cord and allow robust T1 mapping at all cervical levels with a 0.7 mm isotropic resolution, the magnetization-prepared two rapid acquisition GRE sequence (MP2RAGE) used for brain imaging [9] has been adapted for SC imaging. This included offline B_1^+ -inhomogeneity correction [4] to compensate for imperfect radiofrequency excitations encountered at UHF, which could bias T1 estimation and was not taken into account by the original sequence.

Diffusion tensor imaging (DTI), which is used in clinical research to characterize the underlying microstructural impairments in many SC diseases [7] was also adapted for 7T SC applications [10]. The increased magnetic susceptibility differences between vertebrae and the spinal cord require dedicated approaches, such as the reversed phase-encoding method [11], to correct for the increased image distortions. In addition, the natural curvature of the SC also makes it prone to PVE along the cord axis when dealing with contiguous transverse slab acquisition. Regarding this issue, the single-shot spin-echo echo-planar imaging (SS-SE-EPI) sequence has been modified to support multiple individual slice-group acquisitions with different orientations. Whereas the majority of the studies reported so far [6, 7] focused for DTI on one transverse slab centered at a given cervical level (usually C3–C4), this multi-slice-multi-angle (MSMA) strategy allows measurements at all cervical levels while ensuring minimum PVE contamination.

³ MAGNETOM 7T and higher field strengths is ongoing research. All data shown are acquired using a non-commercial system under institutional review board permission. MAGNETOM 7T and higher field strengths are still under development and not commercially available yet. Its future availability cannot be ensured.

Figure 2: Gradient Echo (GRE) field (ΔB_0) mapping sequence

(2A) Magnitude image of the central sagittal slice (first echo time). The green box illustrates the region of interest selected to perform 2nd order B_0 shimming prior to imaging (3 iterations). Additional manual B_0 shimming could be performed when needed in order to reach a full-width at half-maximum (FWHM) of the water peak of typically 100 Hz. (2B) Overlaid color-coded ΔB_0 field map (in Hz). After compensating for magnetic field inhomogeneities within the SC induced by spinous processes and vertebra, the ΔB_0 field map still contains residual quasi-periodic high-frequency field distortions at the level of the intervertebral junctions. Overall, B_0 shimming is a crucial step which inherently drives subsequent imaging performance. For further details, the reader is directed to the B_0 shimming section in [1].

Figure 3: Magnetization-prepared turbo-FLASH B_1^+ mapping sequence

(3A) Absolute flip angle map (in degrees) measured on the central sagittal slice (prescribed pre-saturation flip angle: 45°). (3B) Corresponding color-coded relative B_1^+ field map (in % with respect to the nominal flip angle) superimposed to anatomical TSE image. Coil voltage calibration was achieved targeting the nominal flip angle between C2 and C3 levels (see white arrow). Unlike clinical systems using transmit body coils, the voltage calibration has to be performed manually. Just like B_0 shimming, this step is crucial to ensure subsequent imaging performance.

Figure 4: Turbo Spin Echo (TSE) sequence



A sagittal T2-weighted Turbo Spin Echo (TSE) sequence is used as a precise localizer for positioning the transverse slices perpendicular to the cord, in order to minimize PVE contamination. The Hyperechoes [13] option is enabled to refocus the MR signal while reducing overall Specific Absorption Rate (SAR).

The protocol proposed in the following paragraph is intended to further describe the 'how to' of each of the mentioned MR sequences, reported altogether for the first time at 7T³. The whole setup aims to provide relevant quantitative parameters and high-resolution anatomical images within a scan-time acceptable for clinical research (one hour in total, including all system adjustments and calibrations). This brief review will outline our imaging methods and post-processing strategy, and present initial results obtained on healthy volunteers, as well as future outlooks.

MR imaging

The 7T MR system³ (Siemens Healthcare, Erlangen, Germany) used at CRMRM-CEMEREM in Marseille (France) is a whole-body actively-shielded research magnet equipped with a body gradient coil (SC72, amplitude 70 mT/m, slew rate 200 T/m/s). Cervical spinal cord MRI is performed using a customized eight-channel transceiver coil array (Rapid Biomedical GmbH, Rimpf, Germany) designed to cover levels from C1 to C7 (see details in Figure 1). The MR protocol, which consisted in 2D and 3D anatomical and quantitative sequences (*syngo* MR B17

³ MAGNETOM 7T and higher field strengths is ongoing research. All data shown are acquired using a non-commercial system under institutional review board permission. MAGNETOM 7T and higher field strengths are still under development and not commercially available yet. Its future availability cannot be ensured.

Figure 5: Sampling Perfection with Application optimized Contrasts using different flip angle Evolution (SPACE) sequence



The 3D SPACE sequence generates one T2-weighted volume. The refocusing train option chosen was T2 var. The signal from the mobile CSF fades out during the acquisition readout, facilitating nerve root and pia matter visualization (see white arrows).

version, see details in Figures 2 to 8), was approved by the local Ethics Committee. Informed consents were obtained for each subject prior to the MR examination. Exclusion criteria were chosen conservative and included: pivot teeth's, stents, intrauterine devices and orthopedic implants⁴.

The main sequence parameters used at CRMBM-CEMEREM are summarized in Table 1. Additional information is provided along with typical images acquired on different healthy volunteers (Figures 2 to 8). The total acquisition time, including all system adjustments, was about one hour. Sequences used were: GRE ΔB_0 field mapping, B_1^+ mapping magnetization-prepared turbo-FLASH (MP-TFL), Turbo-Spin-Echo (TSE), MP2RAGE, multi-echo GRE, Sampling Perfection with Application optimized Contrasts using different flip angle Evolution (SPACE) [12] as well as DTI using SS-SE-EPI.

Data post-processing

To perform studies within reproducible ROIs free from manual delineation bias, SC images are usually co-registered for potential motion and normalized in common reference spaces [19, 20] using semi-automated processing pipelines. Data registration to templates also enables automated segmentation of SC substructures (WM/GM, WM tracts...) and group analysis.

⁴ The MRI restrictions (if any) of the metal implant must be considered prior to patient undergoing MRI exam. MR imaging of patients with metallic implants brings specific risks. However, certain implants are approved by the governing regulatory bodies to be MR conditionally safe. For such implants, the previously mentioned warning may not be applicable. Please contact the implant manufacturer for the specific conditional information. The conditions for MR safety are the responsibility of the implant manufacturer, not of Siemens.

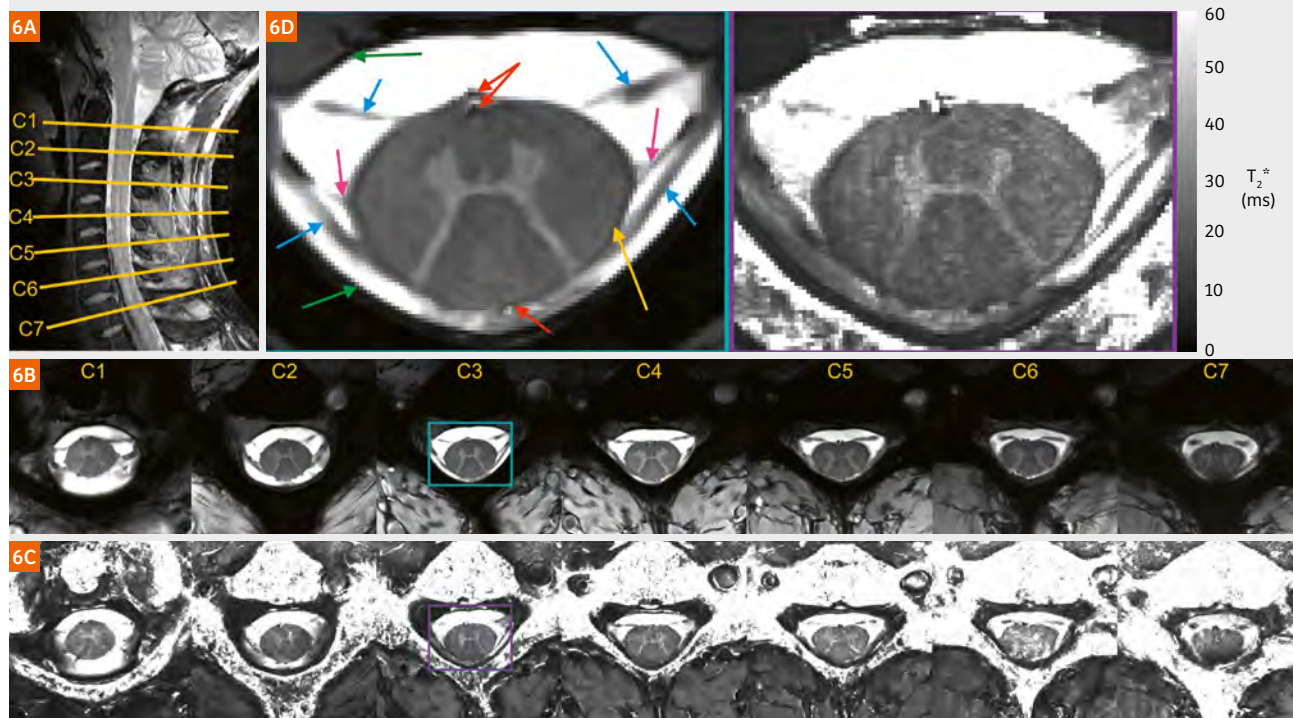
For illustration (Fig. 9), affine and non-linear registrations of FA maps to the AMU_{40} template [20] were performed slice by slice using *FSL FLIRT* and *ANTs SyN* [21] respectively. Automated GM/WM segmentation was possible after binarization of the AMU_{40} [20] GM/WM probabilistic atlases (orange/blue, threshold: 0.5, i.e. $\geq 50\%$ probability to belong to the region of interest (ROI)). Three ROIs were also selected: anterior GM horns (red), lateral WM (green) and posterior WM (yellow), which were extracted from the probabilistic WM tract atlas [22]. For more details, the reader is directed to references [4] and [10].

Discussion

In this work, a multi-parametric quantitative MRI protocol has been proposed for cervical SC 7T imaging. The whole protocol required one hour to collect high-resolution anatomical, morphological and microstructural data, making it compatible with clinical research.

Acquisitions have been performed using a commercial customized coil, which exhibited satisfactory coverage and signal homogeneity within the cervical SC, but would presumably benefit from further developments to improve parallel imaging performances and SNR for large necks. The B_1^+ distribution along the SC was similar between subjects, with homogeneous values around the nominal flip angle for C1–C3 levels and a linear decrease down to 70% in average of the nominal value at C7 level. This situation is not optimal, as B_1^+ could likely drop further in subjects with large necks and hence lead to reduced SNR level, contrast-to-noise ratio dropouts or inefficient fat saturation. A further improved coil geometry, advanced

Figure 6: Gradient Echo (GRE) sequence



(6A) Ultra high-resolution axial imaging was performed using an axial 2D T2*-weighted GRE sequence with multiple echo times ($n=4$), with one slice positioned mid-vertebra at each cervical level (from C1 to C7), perpendicular to the SC axis. Flow compensation in the slice direction, bipolar gradients and phase stabilization options were enabled. The multiple TEs (5.1, 9.4, 13.8 and 17.7 ms) were chosen as short as possible to limit magnetic susceptibility artifacts. **(6B)** The GRE echoes were combined to generate high SNR contrast-enhanced MEDIC (Multi-echo data image combination) images [14]. **(6C)** Mono-exponential fitting of the signal intensity TE-decay with a Gauss-Newton non-linear least-squares algorithm enables T2* mapping. Typical T2* values for both WM and GM were in the order of 20 ms and 30 ms, respectively (see [4] for more details). **(6D)** When zooming, refined anatomical details could be visualized (nerve roots: blue, ligaments: purple, blood vessels: red, *dura mater*: green and *pia mater*: yellow).

Remark: 3 mm slice thickness and 2 averages could also be selected as an alternative in order to reduce the acquisition time to 10 minutes.

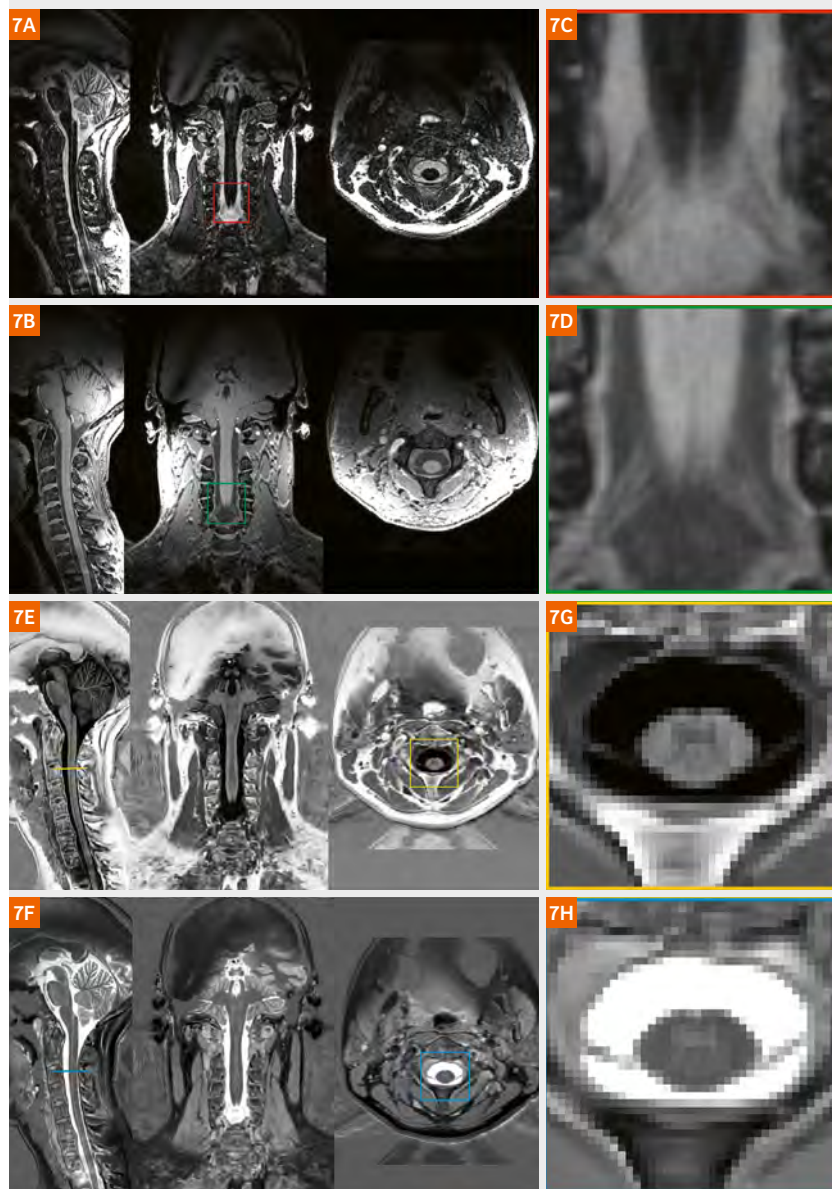
RF pulse design, or the use of parallel transmission [23] technology would be necessary to mitigate these imperfections.

A crucial consideration when working at 7T is B_0 shimming, especially for T2* mapping and DTI. Based on our experience, 2nd order global automated adjustments do not always seem sufficient to ensure reliable DTI quality, with ghosting artifacts sometimes observed, especially at C7 [10]. Manual shimming refinements with physiological triggering in a reduced volume covering approximately only the cervical canal, appeared mandatory to obtain better results. Still, these adjustments could be time-consuming and were not always efficient. Slice-wise dynamic (or integrated) shimming [24] therefore holds great potential to improve lower cervical levels B_0 shimming at 7T.

T1 mapping derived from the MP2RAGE sequence was only marginally affected by B_1^+ , B_1^- , proton density and T2* dependence, and demonstrated strong robustness and accuracy. Based on these optimizations, WM, as well as GM T1 values were measured in the SC. The T1 of SC GM was observed to be lower than GM in the brain. The reader is directed to reference [4] for further discussion on T1 mapping.

Transverse SC DTI covering from C1 to C7 has been reported only recently at 7T [10]. DTI is indeed not straightforward at 7T, as it directly suffers from T2 shortening, B_1 and B_0 inhomogeneities, and SAR increase [25]. MSMA capabilities enabled to report DTI metrics covering the whole cervical SC in one single acquisition, saving a considerable amount of time as compared to conventional strategies (stack of slices). DTI metrics were

Figure 7: Magnetization Prepared 2 Rapid Acquisition GRE (MP2RAGE) sequence



The 3D MP2RAGE sequence generates two volumes, acquired at two different inversion times: **(7A)** T_1 (0.7 s) and **(7B)** T_2 (2.4 s). These weightings allow a fine visualization of the nerve roots **(7C)** and **(7D)**, here at C5–C6 levels. The two volumes can be combined to obtain **(7E)** a volume with uniform T_1 contrast (UNI) and devoid of T_2^* , proton density and B_1 influences. Sequence parameters were chosen to maximize the SC GM/WM T_1 contrast. **(7F)** Using the UNI signal intensities and the integration of Bloch equations, a 3D T_1 map can be generated [9]. Incorrect estimation of T_1 values due to B_1^+ inhomogeneities are corrected offline with a look-up table [4] built in MATLAB (R2015b, The Mathworks, Natick, MA, USA). WM and GM along the whole cervical SC can be clearly depicted on both T_1 -weighted image **(7G)** and quantitative T_1 map **(7H)**, here at C3 level. Typical T_1 values for both WM and GM were in the order of 1180 ms and 1330 ms, respectively (see [4] for more details). T_1 map denoising was performed with the *BM4D* function [15].

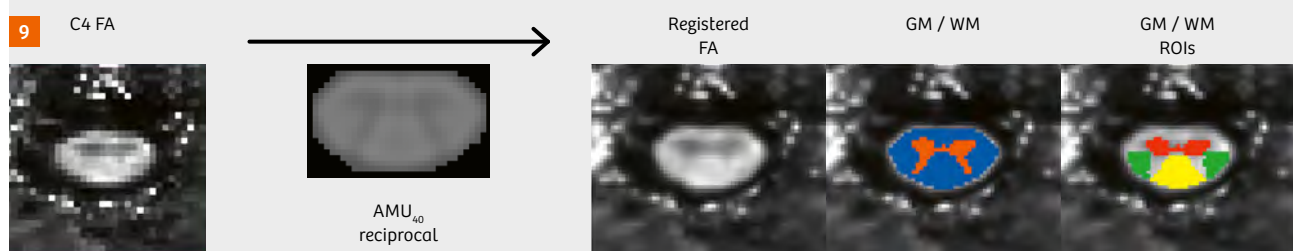
found in agreement with corresponding literature [26, 27] obtained at 3T. The reader is directed to reference [10] for further discussion on DTI.

As a conclusion, a high-resolution multi-parametric MRI protocol dedicated to cervical SC investigation at 7T was proposed. Obtained images and maps, with unmatched resolutions compared to lower field investigations, provided exquisite anatomical details and clear delineation of the SC substructures within an acquisition time compatible with clinical research. Nevertheless, clinical

applications of SC UHF imaging are still at an early stage [1]. By relying on the assets of 7T imaging, such high resolution multi-parametric quantitative SC investigations could legitimately go further than purely descriptive clinical reports based on anatomical imaging by studying specific sub-regions impairments, such as grey matter horn atrophy or anterior white matter tract degeneration, hence paving the way for new understandings of pathological processes.

Figure 8: Diffusion-weighted single-shot spin-echo echo-planar-imaging (SS-SE-EPI) sequence⁵

Figure 9: Example of data registration to template



Registrations of FA maps to the reciprocal (i.e. Inverted contrast) AMU₄₀ template. Automated, robust and reproducible substructure segmentation and group studies are further enabled. GM binarization mask is shown in orange, while WM mask is in blue. The three additional considered ROIs are: anterior GM horns (red), lateral 'motor' WM (green) and posterior 'sensory' WM (yellow).

Acknowledgments and grant supports

The authors would like to thank Robin Heidemann, Christina Triantafyllou, Florian Odoj and Tobias Wichmann for their support, as well as Véronique Gimenez and Lauriane Pini for the study logistics. This work was supported by the following funding sources: Investissements d'Avenir 7T-AMI-ANR-11-EQPX-0001, A*MIDEX-EI-13-07-130115-08.38-7T-AMISTART, A*MIDEXANR-11-IDEX-0001-02, Aix-Marseille Université, AP-HM and CNRS (Centre National de la Recherche Scientifique).

Bibliography

- 1 Barry RL, Vannesjo SJ, By S, Gore JC, Smith SA: Spinal cord MRI at 7T. *NeuroImage* 2017;10.1016/j.neuroimage.2017.07.003.
- 2 Dula AN, Pawate S, Dortch RD, et al.: Magnetic resonance imaging of the cervical spinal cord in multiple sclerosis at 7T. *Mult Scler* 2015;10.1177/1352458515591070.
- 3 Sigmund EE, Suero GA, Hu C, et al.: High-resolution human cervical spinal cord imaging at 7 T. *NMR Biomed* 2012; 25:891–899.
- 4 Massire A, Taso M, Besson P, Guye M, Ranjeva J-P, Callot V: High-resolution multi-parametric quantitative magnetic resonance imaging of the human cervical spinal cord at 7T. *NeuroImage* 2016; 143:58–69.
- 5 Kogan F, Singh A, Debrosse C, et al.: Imaging of glutamate in the spinal cord using GluCEST. *NeuroImage* 2013; 77:262–267.
- 6 Stroman PW, Wheeler-Kingshott C, Bacon M, et al.: The current state-of-the-art of spinal cord imaging: Methods. *NeuroImage* 2014; 84:1070–1081.
- 7 Wheeler-Kingshott CA, Stroman PW, Schwab JM, et al.: The current state-of-the-art of spinal cord imaging: Applications. *NeuroImage* 2014; 84:1082–1093.
- 8 Abdel-Aziz K, Ciccarelli O: Rationale for quantitative MRI of the human spinal cord and clinical applications. In *Quant MRI Spinal Cord* Ed J Cohen-Adad C Wheel-Kingshott. San Diego, Calif.: Academic Press.; 2014.
- 9 Marques JP, Kober T, Krueger G, van der Zwaag W, Van de Moortele P-F, Gruetter R: MP2RAGE, a self bias-field corrected sequence for improved segmentation and T1-mapping at high field. *NeuroImage* 2010; 49:1271–1281.
- 10 Massire A, Rasoanandrianina H, Taso M, et al.: Feasibility of single-shot multi-level multi-angle diffusion tensor imaging of the human cervical spinal cord at 7T. *Magn Reson Med* 2018;10.1002/mrm.27087.
- 11 Andersson JLR, Skare S, Ashburner J: How to correct susceptibility distortions in spin-echo echo-planar images: application to diffusion tensor imaging. *NeuroImage* 2003; 20:870–888.
- 12 Mugler JP 3rd: Three-dimensional T2-weighted imaging of the brain using very long spin-echo trains. In *Proceedings of the 8th Annual Meeting of ISMRM*, Denver, Colorado, USA; 2000:687.
- 13 Hennig J, Scheffler K: Hyperechoes. *Magn Reson Med* 2001; 46:6–12.
- 14 Held P, Dorenbeck U, Seitz J, Fründ R, Albrich H: MRI of the abnormal cervical spinal cord using 2D spoiled gradient echo multiecho sequence (MEDIC) with magnetization transfer saturation pulse. A T2* weighted feasibility study. *J Neuroradiol J Neuroradiol* 2003; 30:83–90.
- 15 Smith SM, Jenkinson M, Woolrich MW, et al.: Advances in functional and structural MR image analysis and implementation as FSL. *NeuroImage* 2004; 23 Suppl 1:S208–219.
- 16 Andersson JLR, Sotiropoulos SN: An integrated approach to correction for off-resonance effects and subject movement in diffusion MR imaging. *NeuroImage* 2016; 125:1063–1078.
- 17 Kellner E, Dhital B, Kiselev VG, Reiser M: Gibbs-ringing artifact removal based on local subvoxel-shifts. *Magn Reson Med* 2016; 76:1574–1581.
- 18 Manjón JV, Coupé P, Concha L, Buades A, Collins DL, Robles M: Diffusion Weighted Image Denoising Using Overcomplete Local PCA. *PLOS ONE* 2013; 8:e73021.
- 19 Fonov VS, Le Troter A, Taso M, et al.: Framework for integrated MRI average of the spinal cord white and gray matter: The MNI–Poly–AMU template. *NeuroImage* 2014; 102, Part 2:817–827.
- 20 Taso M, Le Troter A, Sdika M, et al.: A reliable spatially normalized template of the human spinal cord — Applications to automated white matter/gray matter segmentation and tensor-based morphometry (TBM) mapping of gray matter alterations occurring with age. *NeuroImage* 2015; 117:20–28.
- 21 Avants BB, Epstein CL, Grossman M, Gee JC: Symmetric diffeomorphic image registration with cross-correlation: Evaluating automated labeling of elderly and neurodegenerative brain. *Med Image Anal* 2008; 12:26–41.
- 22 Lévy S, Benhamou M, Naaman C, Rainville P, Callot V, Cohen-Adad J: White matter atlas of the human spinal cord with estimation of partial volume effect. *NeuroImage* 2015; 119:262–271.
- 23 Padormo F, Beqiri A, Hajnal JV, Malik SJ: Parallel transmission for ultrahigh-field imaging. *NMR Biomed* 2016; 29:1145–1161.
- 24 Gatidis S, Graf H, Weiß J, et al.: Diffusion-weighted echo planar MR imaging of the neck at 3 T using integrated shimming: comparison of MR sequence techniques for reducing artifacts caused by magnetic-field inhomogeneities. *Magn Reson Mater Phys Biol Med* 2017; 30:57–63.
- 25 Gallichan D: Diffusion MRI of the human brain at ultra-high field (UHF): A review. *NeuroImage* 2017;10.1016/j.neuroimage.
- 26 Xu J, Shimony JS, Klawiter EC, et al.: Improved in vivo diffusion tensor imaging of human cervical spinal cord. *NeuroImage* 2013; 67:64–76.
- 27 Taso M, Girard OM, Duhamel G, et al.: Tract-specific and age-related variations of the spinal cord microstructure: a multi-parametric MRI study using diffusion tensor imaging (DTI) and inhomogeneous magnetization transfer (ihMT). *NMR Biomed* 2016;10.1002/nbm.3530.



Contact

Aurélien Massire, Ph.D.
Post-doctoral fellow
Centre de Résonance Magnétique Biologique et Médicale (CRMBM-CEMEREM, UMR 7339, CNRS, Aix-Marseille Université)
27 boulevard Jean Moulin,
13385 Marseille cedex 05,
France
aurelien.massire@univ-amu.fr
<http://crmbm.univ-amu.fr/>



Virginie Callot, Ph.D.
CNRS Research Director
Centre de Résonance Magnétique Biologique et Médicale (CRMBM-CEMEREM, UMR 7339, CNRS, Aix-Marseille Université)
27 boulevard Jean Moulin,
13385 Marseille cedex 05,
France
Phone: +33 (0) 491 388 465
virginie.callot@univ-amu.fr
<http://crmbm.univ-amu.fr/>

Magnetic Resonance Field Fingerprinting (MRF²)

Gregor Kördörfer^{1,2}; Yun Jiang³; Jianing Pang⁴; Peter Speier¹; Vikas Gulani^{3,5}; Mark Griswold^{3,5}; Mathias Nittka¹

¹ Siemens Healthineers, Erlangen, Germany

² Friedrich-Alexander-Universität Erlangen-Nürnberg, Erlangen, Germany

³ Radiology, Case Western Reserve University, Cleveland, OH, USA

⁴ Siemens Medical Solutions USA, Inc., Chicago, IL, USA

⁵ Biomedical Engineering, Case Western Reserve University, Cleveland, OH, USA

Magnetic Resonance Fingerprinting

Magnetic resonance fingerprinting (MRF)¹ [1] is a recently introduced technique that promises multiparametric quantitative MRI. In essence, MRF aims to identify multiple tissue properties simultaneously in a single acquisition. To do so, a measured signal is compared to a set (or “dictionary”) of pre-simulated signals. Each signal is unique, and can therefore be considered a kind of fingerprint. By comparing a measured fingerprint with the

dictionary entries, the most similar simulated fingerprint is identified. This reveals the measured fingerprint’s properties, which are the parameters that were used for the simulation.

The interaction of two main characteristics of MRF plays an important role. First, MRF encoding patterns aim to generate highly variable signal responses from tissues with different properties. This is different from conventional imaging, which aims for highly specific tissue contrasts. Second, a pattern-matching process is used to identify the parameters of the measured signals. This makes MRF independent of analytical models and means that signals

¹ WIP. The product is still under development and is not commercially available yet. Its future availability cannot be ensured.

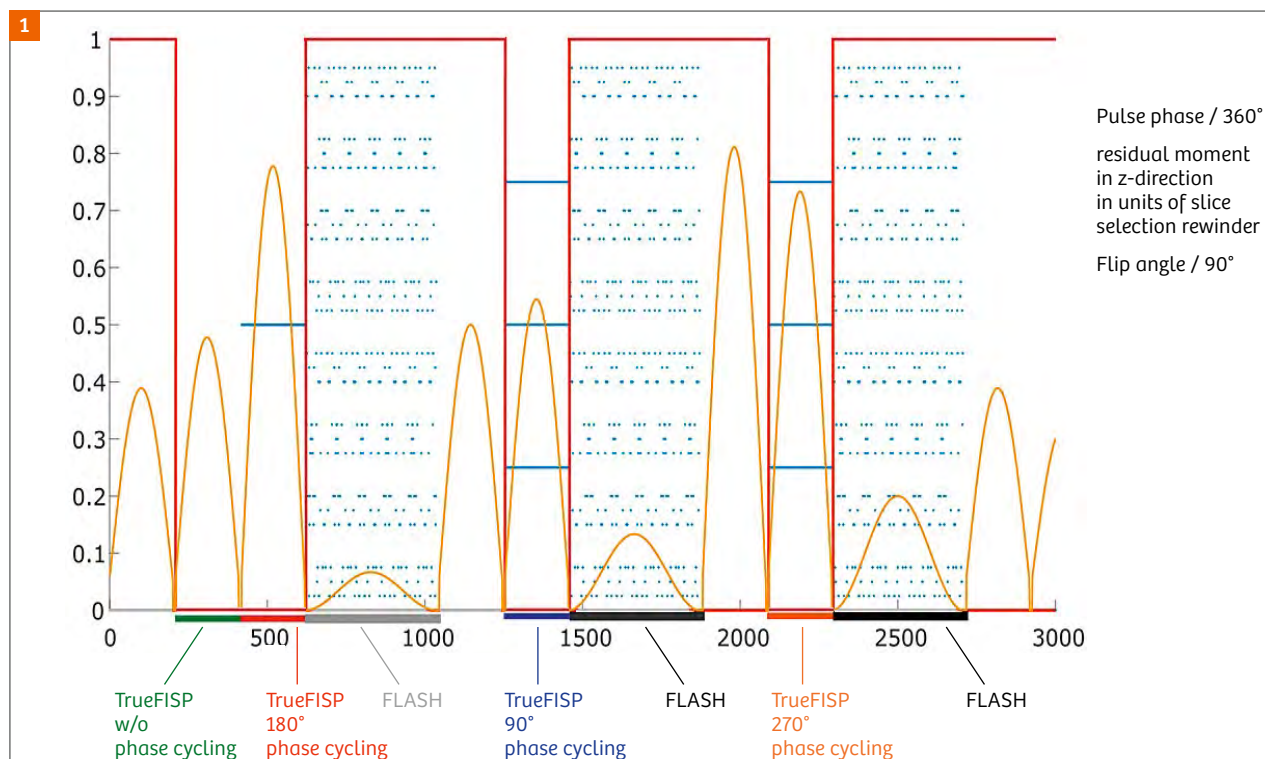


Figure 1:

Sequence configuration used for MRF² showing flip angle, z-gradient moment at the end of the TR, and the pulse phase. The TrueFISP segments are also described by their phase cycling pattern.

are designed by exploiting many more degrees of freedom. Highly distinguishable, complex signal responses can be generated with a series of RF pulses – in contrast to conventional sequences, which require a steady-state signal. The combination of high distinguishability and the pattern-matching approach opens up the possibility of strong undersampling during data acquisition. While all k -space data would have to be acquired to generate artifact-free images of each time point, MRF only acquires a small fraction of the data. The k -space sampling patterns can be so sparse that a single image barely shows the underlying object. By varying the k -space sampling pattern in a reasonable manner from time point to time point, the resulting artifacts that overlie the signal also vary and do not affect the pattern match. Even though the measured signals are heavily affected by artifacts, the algorithm can still find the best fingerprint match in each voxel. This is mostly performed by a voxel-wise pattern match, but can also be achieved with more sophisticated techniques [e.g., 2–4].

In general, any sequence in combination with any k -space sampling scheme (Cartesian, radial, spiral, etc.) could be applied for MRF. When choosing a suitable sequence, one has to keep in mind that specific sequence properties are also present in MRF. Ma et al. showed a first working implementation based on a TrueFISP sequence with spiral sampling yielding B_0 , T1, and T2 parameter maps [1]. TrueFISP has high signal efficiency but suffers from problems linked to B_0 inhomogeneities, which result in banding artifacts. Although the signal can be simulated accurately under such conditions, a low signal-to-noise ratio can severely affect the MRF results with systematic biases or higher standard deviation in the parameter maps. The original method was therefore followed by the FISP-based approach devised by Jiang et al. [5]. This method does not incorporate B_0 in the signal model, as FISP has negligible B_0 dependency. Several works [6, 7] identified a dependency of the parameter maps on the RF transmit field B_1+ that probably also exists in the TrueFISP MRF method. This can be addressed with a B_1+ prescan [7–9] as a brute-force approach. A more elegant solution would be to also incorporate B_1+ in the encoding and matching, which can be done by integrating dedicated B_1+ dependent signal segments in an encoding pattern [6, 10]. Instead of fighting artifacts that are related to magnetic field inhomogeneities, MRF can embrace them. B_0 and B_1+ can also be simultaneously identified in addition to parameters associated with the underlying tissues, such as T1 and T2. This is necessary in cases where the signal behavior is influenced by variations in one or both of the magnetic fields. Mismatches can appear when the signal is affected in a way that makes it more closely resemble a signal with different tissue parameters. By simultaneously mapping spatial magnetic field distributions, such

mismatches can be resolved, and MRF can generate parameter maps that are free of influences from the underlying magnetic fields.

Magnetic Resonance Field Fingerprinting (MRF²)

Magnetic resonance field fingerprinting (MRF²)¹ follows the MRF idea and attempts to generate B_0 , B_1+ , T1, and T2 maps from a single continuous acquisition. As MRF does not rely on a steady-state, there is theoretically no need to use a single sequence framework throughout an acquisition. MRF² uses different sequence types and thus benefits from exploiting more degrees of freedom. By varying flip angles, pulse phases, and gradient moments, a sequence is designed that integrates FLASH, FISP, and TrueFISP segments into one continuous acquisition (Fig. 1). Each sequence differs in its sensitivity to tissue parameters and magnetic fields. FISP is mainly sensitive to T1, T2, and B_1+ , while FLASH is sensitive to T1 and B_1+ , and TrueFISP is sensitive to T1, T2, B_0 , and B_1 . In MRF², the TrueFISP related limitations are being dealt with by also using sequences that are less B_0 -dependent and complementing it by varying the phase cycling pattern in the TrueFISP segments. Low signal levels in one TrueFISP segment are offset by other TrueFISP segments, and by FISP and FLASH segments. Figure 2 shows examples of MRF² parameter maps in a healthy volunteers' brain.

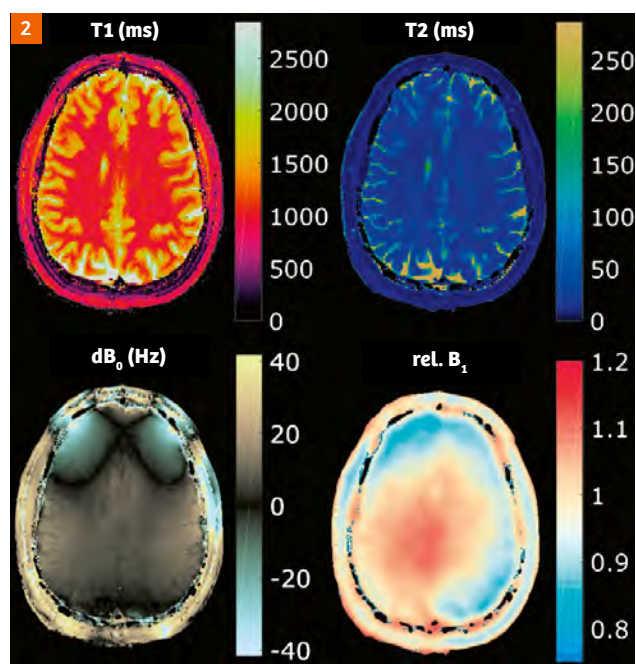


Figure 2: T1, T2, B_0 and B_1+ maps obtained using MRF² in a healthy volunteer brain (FOV: 230 mm; undersampling factor: 48; in-plane resolution: 0.9 mm; slice thickness: 5 mm).

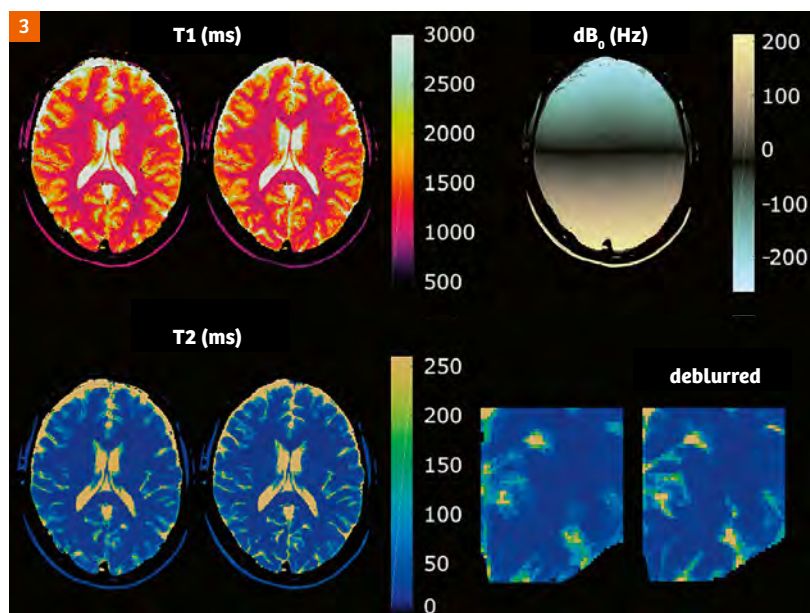


Figure 3:

A human brain acquired using MRF² with an additional B_0 shim in y-direction, as shown in the top right (FOV: 230 mm; undersampling factor: 48; in-plane resolution: 0.9 mm; slice thickness: 5 mm). The image in the bottom right compares the resulting MRF² T1 and T2 maps with and without deblurring using the B_0 map with zoomed-in T2 maps.

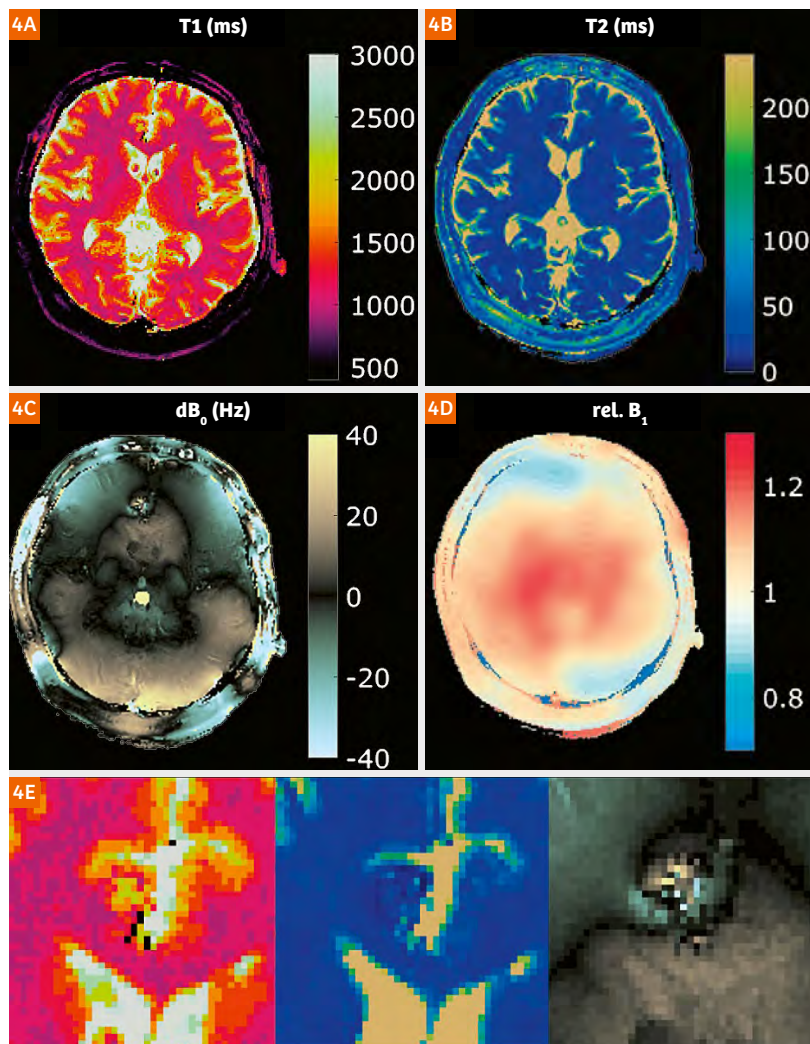


Figure 4:

MRF² parameter maps (undersampling factor: 48; in-plane resolution: 1.2 mm; slice thickness: 5 mm) in a volunteer with a diagnosed cavernoma. The images show T1/T2 changes in the cavernoma compared to the surrounding white matter, and abrupt changes in B_0 . A zoomed excerpt of the cavernoma is shown in 4E.

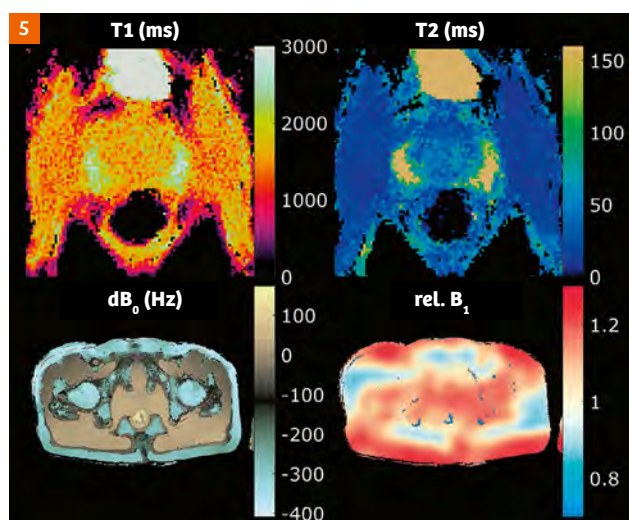


Figure 5: Parameter maps (undersampling factor: 60; in-plane resolution: 1 mm; slice thickness: 3.5 mm) in a volunteer's prostate. Zoomed-in versions of the T1 and T2 maps are shown, as well as B_0 and B_1+ in the whole abdomen.

Another important factor in MRF is the dictionary size. Adding dimension exponentially increases the number of fingerprints. Since the simulation tries to accurately resemble MR physics on a macroscopic level, this is a time-consuming task. Although investing this time is bearable because the dictionary must only be computed once for a given sequence, having more fingerprints means that it takes more memory and time to match each acquired dataset. The four orthogonal dimensions in MRF² result in a very large dictionary. To minimize the size, the TR is kept constant to limit the extent of the B_0 dimension: Keeping the TR constant means that two spin ensembles with a frequency difference of an integer multiple of $1/TR$ will experience almost the same evolution. Therefore, the dictionary size can be substantially limited to the range of $\pm 2/TR$ Hz. The downside of limiting the B_0 dimension is that wraparounds appear in the B_0 dimension. Although the parameter maps are free of influences from B_0 , the full scale B_0 cannot be identified. In order to assess higher off-resonances, the echo time in two of the FISP segments is slightly different but constant throughout one segment. The resulting phase differences serve to compute a coarse B_0 map for unwrapping.

High overall signal levels and good distinguishability of fingerprints with MRF² enable high resolutions. Derived B_0 maps can be used for spiral deblurring (Fig. 3) and, as a measure of susceptibility, for diagnostic information. Figure 4 shows a volunteer's brain with a diagnosed cavernoma. Besides higher T1 and lower T2 signals inside the cavernoma compared to the surrounding white matter, abrupt changes in the B_0 are visible. Figure 5 displays

MRF² results from another body region. B_0 and B_1+ maps in the abdomen are shown as well as zoomed-in T1 and T2 maps in the prostate only. Pixels containing fat were removed based on the off-resonance map.

Summary

MRF² extends the concept of MRF by simultaneously identifying both magnetic fields and relaxation parameter maps. It is therefore highly robust against field variations, and yields additional information to relaxation parameter maps. Signal changes related to B_0 and B_1+ are intrinsically accounted for by adding a B_1+ and B_0 dimension to the dictionary with subsequent matching of these field parameters. Higher signal levels, better distinguishability between fingerprints, and integrated spiral deblurring help achieve higher resolutions. The high-resolution B_0 information that is related to susceptibility can also be used for diagnosis.

References

- 1 Ma D, Gulani V, Seiberlich N, et al. Magnetic resonance fingerprinting. *Nature* 2013;495(7440):187-192. doi: 10.1038/nature11971.
- 2 Cline CC, Chen X, Mailhe B, et al. AIR-MRF: Accelerated iterative reconstruction for magnetic resonance fingerprinting. *Magn Reson Imaging* 2017;41:29-40. doi: 10.1016/j.mri.2017.07.007.
- 3 Zhao B, Lu W, Hitchens TK, et al. Accelerated MR parameter mapping with low-rank and sparsity constraints. *Magn Reson Med*. 2015;74(2):489-98. doi: 10.1002/mrm.25421.
- 4 Assländer J, Cloos MA, Knoll F, et al. Low rank alternating direction method of multipliers reconstruction for MR fingerprinting. *Magn Reson Med*. 2017;79(1):83-96. doi: 10.1002/mrm.26639.
- 5 Jiang Y, Ma D, Seiberlich N, et al. MR fingerprinting using fast imaging with steady state precession (FISP) with spiral readout. *Magn Reson Med*. 2015;74(6):1621-31. doi: 10.1002/mrm.26048.
- 6 Buonincontri G, Sawiak SJ. MR fingerprinting with simultaneous B1 estimation. *Magn Reson Med*. 2016;76(4):1127-1135. doi: 10.1002/mrm.26009.
- 7 Chen Y, Jiang Y, Pahwa S, et al. MR Fingerprinting for Rapid Quantitative Abdominal Imaging. *Radiology* 2016;279(1):278-286. doi: 10.1148/radiol.2016152037.
- 8 Ma D, Jiang Y, Chen Y, et al. Fast 3D magnetic resonance fingerprinting for a whole-brain coverage. *Magn Reson Med*. 2017;79(4):2190-2197. doi: 10.1002/mrm.26886.
- 9 Ma D, Coppo S, Chen Y, et al. Slice profile and B1 corrections in 2D magnetic resonance fingerprinting. *Magn Reson Med*. 2017;78(5):1781-1789. doi: 10.1002/mrm.26580.
- 10 Cloos MA, Knoll F, Zhao T, et al. Multiparametric imaging with heterogeneous radiofrequency fields. *Nat Commun*. 2016;7:12445. doi: 10.1038/ncomms12445.



Contact

Mathias Nittka, Ph.D.
Siemens Healthcare GmbH
DI MR DL ORTH
Erlangen
Germany
Phone: +49 9131 84 4460
mathias.nittka@siemens-healthineers.com

Definitions of RF receiver channels and coil density

Mathias Blasche, MSc.

Siemens Healthineers, Erlangen, Germany

Introduction

The number of RF receiver channels is one of the key purchasing criteria. Multi-channel RF systems offer clear clinical benefits with regard to coverage, image quality, and speed. Multi-channel RF technology started in the early 1990s with typically 4 RF channels. Nowadays, systems with 16 to 32 independent channels are seen as “standard mid-class”, while even 128 independent channels are available for high-end research scanners.

In the past, there used to be a common understanding about the definition of a “receiver channel”. Unfortunately, this is no longer the case. There are numerous different definitions from different vendors, and many of them are not comparable. For example, the number of ADCs (analog-to-digital converters) is not a relevant definition for “channels” if many of the digitized signals are discarded and are not used for the reconstruction of the final image. As another example, the broadband capabilities of fiber optic cables are not relevant if there are limitations in the number of channels that can be processed in the given architecture and especially if there are limitations in the number of available coil connectors.

We therefore want to propose two definitions for RF receiver channels that should be considered relevant in this context. The definitions are relevant because they are clearly connected to relevant clinical benefits. These definitions will be explained in chapters 1) and 2).

From a clinical perspective, the RF system is only as good as the coils that utilize the available receiver channels. Also for coils, we are seeing different definitions for the “channel count” from different vendors. In the third chapter, we will therefore look at meaningful definitions of “coil density” that are linked to the relevant clinical benefits.

1. Channels that can be connected simultaneously

Definition 1:

Number of channels¹ that can be connected simultaneously.

This definition mainly depends on the available coil connectors:

- How many coil connectors are available?
- How many coil channels can be plugged into each coil connector?

The number of channels that can be connected simultaneously via the available coil connectors is important for the clinical benefits of coverage and flexibility.

¹ A coil consists of coil elements. If the signal from each coil element is processed via a separate channel, i.e. if there is a 1-to-1 relationship between elements and channels, one can also call it “channels”. Note that it is in principle possible to combine several coil elements to fewer channels, but then most clinical benefits are lost.

² This definition of independent receiver channels was inspired by a definition by Allen D. Elster: “Channels are independent, complete electronic chains required for processing information received from a coil segment. Channels include amplifiers, filters, analog-to-digital conversion circuitry, demodulation/mixer devices, and image processing capability. The output of each channel is generally a partial view of the entire anatomy being imaged, subsequently combined with output from the other channels to produce the final MR image.” (<http://mriquestions.com/array-coils.html>)

³ SNR = signal-to-noise ratio. A higher number of independent channels (i.e. partial images) will increase the average SNR of the image, due to higher SNR in the image periphery close to the coil windings. When using parallel imaging, the SNR gain will be even more pronounced, as the g-factors (also in the center of the coil) will be better. Coil geometry will also play a major role for the SNR but is independent of channel count and therefore not discussed here.

⁴ This includes the possibility to achieve higher acceleration factors in SMS (Simultaneous Multi-Slice) scanning.

⁵ Note: There is no need for a separate reconstructor for each signal, but the designated reconstructor must be scaled with the available number of channels to be able to handle the image reconstruction load of the multiple receive channels in an acceptable time.

Clinical benefits:

- **Coverage:** Multiple coils can be connected for large anatomical coverage, for multi-station imaging with an extended field of view (e.g. thorax-abdomen-pelvis), up to whole-body imaging
- **Flexibility** in the choice of coils. Multiple coils can be connected also when using high-density coils.

2. Channels that can be used simultaneously**Definition 2:**

Number of independent receiver channels that can be used simultaneously in one single scan and in one single FOV, each generating an independent partial image².

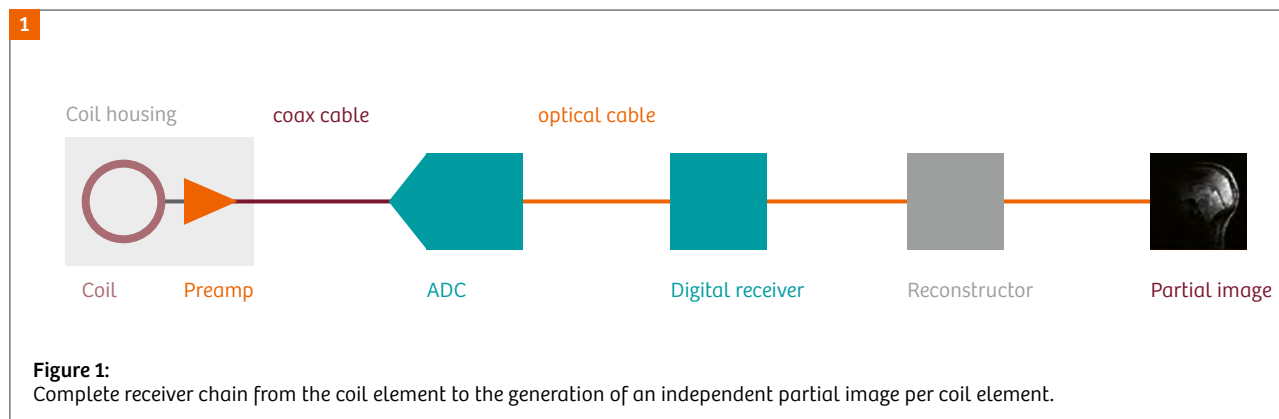
The important aspect of this definition is that the whole receiver chain is taken into account, from the coil element to the “partial image”. Only this definition is tied to the relevant clinical benefits.

Clinical benefits:

- **Higher image quality**, i.e. higher SNR³ due to the simultaneous (!) use of multiple independent channels in one single FOV and in one single scan
- **Higher speed** due to higher possible PAT factors (higher acceleration factors⁴) – the g-factors are better when multiple independent channels are used simultaneously

Figure 1 shows a coil with one element (and integrated preamplifier) connected to the whole receiver chain of one individual receive channel. The complete receiver chain consists of:

- the ADC (analog-to-digital converter) for the digitization of the signal that comes from the coil
- a digital receiver for further processing of the signal in the digital domain
- the reconstructor⁵, i.e. the computer that calculates the final image
- the resulting partial image for each independent channel



All the partial images from a multi-channel coil are combined to produce the final image as illustrated in Figure 2 for the example of a Head/Neck 64 coil with 64 independent channels.

It should be noted that the ADC is only a part of the whole receiver chain. If many digitized signals (from coils outside the FOV) are discarded after digitization and do not result in partial images, they do not provide any clinical benefit.

The higher the number of independent receiver channels (according to definition 2), i.e. the higher the number of partial images, the higher the clinical benefits (image quality and speed) will be.

Both channel definitions, by the way, are covered in the “Tim nomenclature” that we have been using since 2003 to describe our RF system configurations. Tim [204x48], for example, means that we can connect up to 204 coil elements/channels⁶ simultaneously (according to definition 1), and that up to 48 independent receiver channels can be used simultaneously (according to definition 2).

⁶ With most Tim 4G systems, there is a clear 1-to-1 relationship between coil elements and independent receiver channels; each coil element is processed via a separate independent channel. For these systems, the terms “coil elements” and “coil channels” can be used interchangeably. For Tim systems with a Mode Matrix, the highest mode also results in an identical number of coil elements and independent receiver channels.

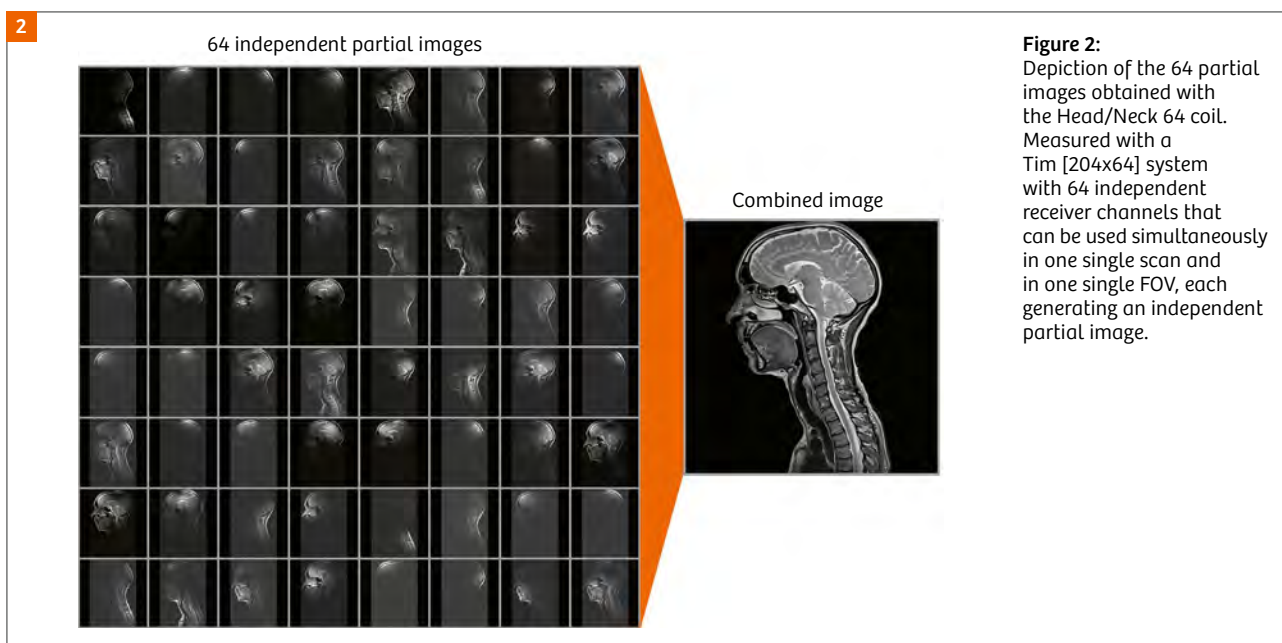


Figure 3 shows the two channel definitions and the respective clinical benefits in a summary.

An additional benefit which is often seen in a high number of independent receiver channels (right side in Figure 3) is **future security** – having no limitations by the number of independent channels for purchasing (future) high-density coils. This is a valid point. However, some additional aspects are relevant in the context of future security:

- In the past, RF channels used to be extremely expensive, while low-density coils were relatively cheap in comparison. This has changed: An ultra-high-density

coil (such as a 64-channel coil) can actually be more expensive than a channel upgrade. Therefore, the coils themselves (and their respective coil densities, see chapter 3) should not be neglected in comparison to the channel count of the system.

- The coil connectors (see chapter 1) present a natural limitation for the maximum coil density. Only the connectors on one side of the patient table can be used for a single coil, otherwise the coil would require long cables to both ends of the patient table. This is not feasible for clinical use due to patient safety and workflow requirements. If there is not a sufficient

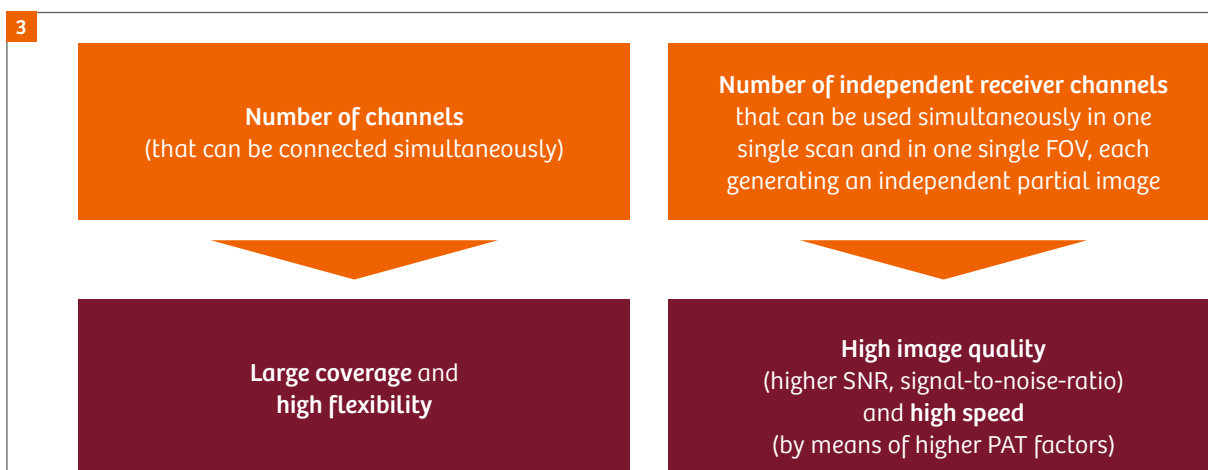


Figure 3:
Summary of the clinical benefits of the two channel definitions.

number of coil connectors, a high-density coil will block too many connectors and will prohibit the use of additional coils for extended coverage.

It should be noted that an exchange of coil connectors will most probably require a change of the whole patient table, besides changes in the overall RF architecture. This would most probably be much more expensive than a channel upgrade. Therefore, the number of connectable channels, as defined in chapter 1, also plays a significant role regarding future security.

3. Coil density

The number of independent receiver channels, as defined in chapter 2, is the upper limit of channels that can be used simultaneously. However, the actual usage of the receiver channels depends on the coils/coil combinations that are available for the diversity of clinical applications.

Therefore, the channel number of the available coils (and coil combinations) is also an important specification for the MR system.

As previously mentioned for the definition of “channels”, also the channel count of the coils is defined differently among the vendors, making a fair comparison virtually impossible. Various definitions are used, for example

- A. the number of channels of the coil alone, as a hardware entity (“box”)
- B. the number of channels of the coil in combination with other coils
- C. the number of channels of the coil in combination with other coils, adding up multi-station examinations

These different definitions are often non-transparent and can vary by factors, for coils that are actually comparable in clinical use. The clinically most relevant specification is the **coil density** which is closely related to the definition of independent RF channels in chapter 2:

Definition of coil density:

Number of independent channels of a coil (or coil combination) that can be used simultaneously in one single scan for imaging a particular anatomy of interest, each generating an independent partial image.

Only relevant coil channels that contribute significant signal for the anatomy of interest should be counted. Examples for anatomies of interest would be:

- Brain only (without counting channels from a spine coil)
- Head-neck imaging with a specified FOV (up to max. FOV)
- Abdominal imaging with a specified FOV (up to max. FOV)
- Knee imaging (with a knee coil)
- etc.

As an example⁷ for the different definitions for the channel count, let's have a look at the Body 18 coil, see Figure 4.

- A. The coil alone, as a hardware entity (“box”), has 18 elements = 18 channels.

⁷ Example for MAGNETOM Vida with Tim [204x64]. Other systems with a different max. FOV and/or different coil portfolio may result in different numbers.

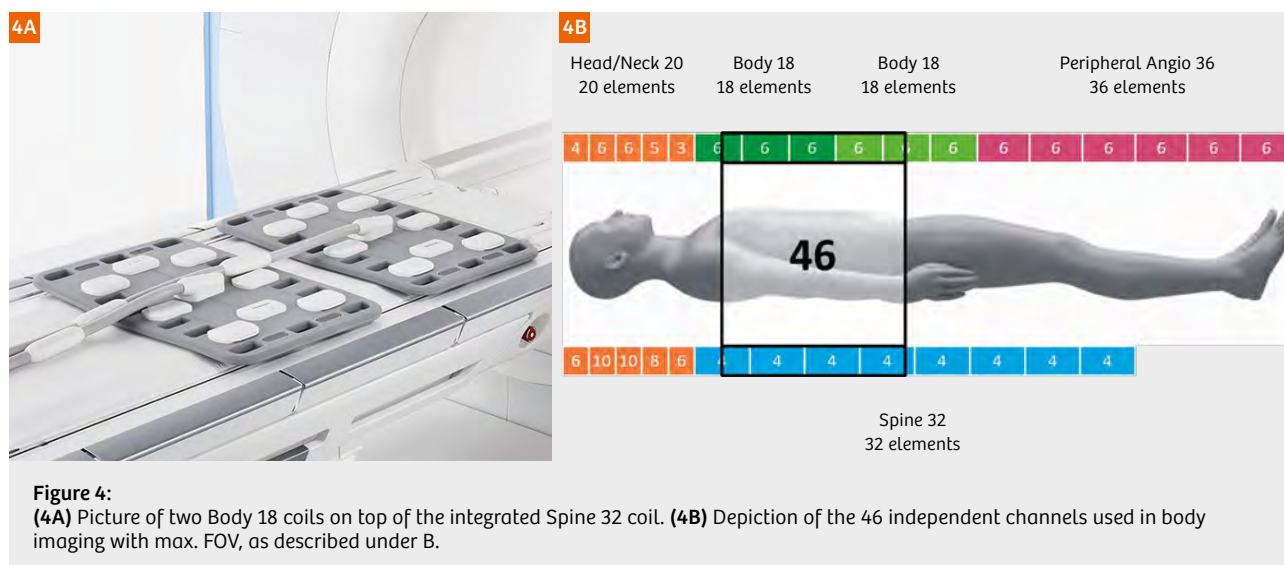


Figure 4:
(4A) Picture of two Body 18 coils on top of the integrated Spine 32 coil. (4B) Depiction of the 46 independent channels used in body imaging with max. FOV, as described under B.

- B.** The Body 18 coil is typically used in combination with the Spine 32 coil: One Body 18 coil in combination with 12 channels from the Spine 32 coil result in 30 channels for a FOV of approx. 35 cm. For the max. FOV of the scanner, 1 ½ Body 18 coils and 16 channels from the Spine 32 coil can be used simultaneously in one single scan, resulting in a total of 46 channels.
- C.** For multi-station examinations, the Body 18 coil can be combined with various other coils, e.g. the Spine 32 coil, the Head/Neck 20 coil or Head/Neck 64 coil, and the Peripheral Angio 36 coil. A multi-step whole-body examination will use up to 168 channels in total (without counting overlaps).

As a second example⁸ for the different definitions for the channel count, we show the Head/Neck 20 coil, see Figure 5.

- A.** The coil alone, as a hardware entity ("box"), has 20 elements = 20 channels, 16 in the head region and 4 in the C-spine/neck region.
- B.** The Head/Neck 20 coil can be used in combination with the Body 18 coil and the Spine 32 coil: For the max. FOV of the scanner, the Head/Neck 20 coil, 6 channels from the Body 18 coil and 4 channels from the Spine 32 coil can be used simultaneously in one single scan, resulting in a total of 30 channels.

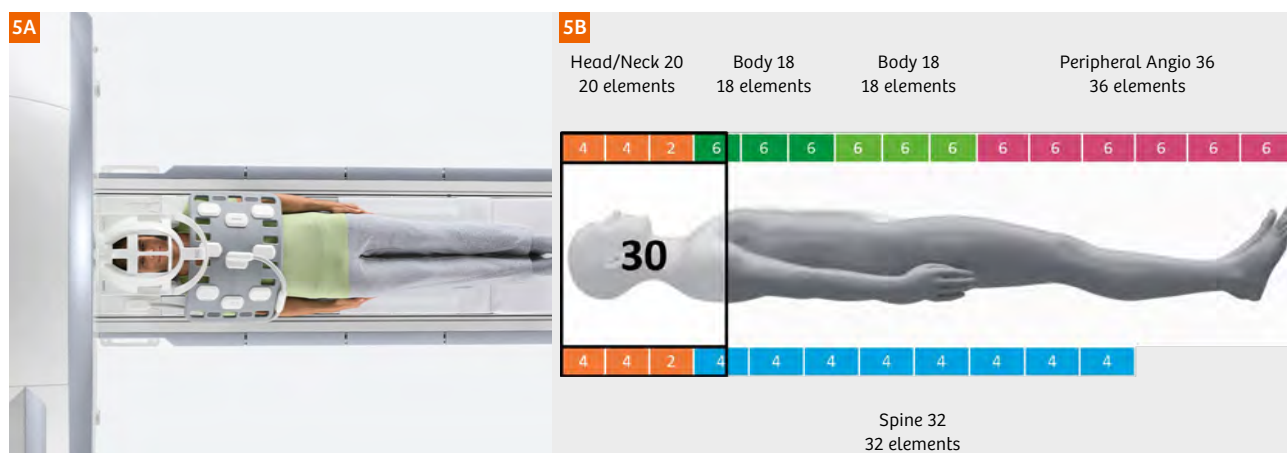


Figure 5:

(5A) Picture of the Head/Neck 20 coil and the Body 18 coil on top of the integrated Spine 32 coil. (5B) Depiction of the 30 independent channels used in head/neck imaging with max. FOV, as described under B.

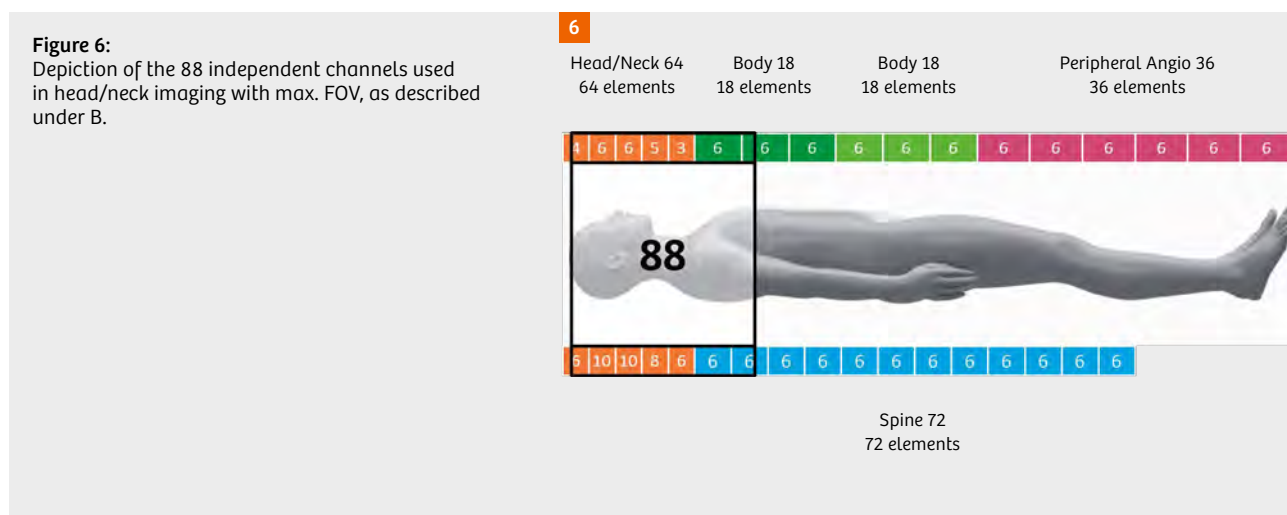


Figure 6:

Depiction of the 88 independent channels used in head/neck imaging with max. FOV, as described under B.

C. For multi-station examinations, the Head/Neck 20 coil can be combined with various other coils, e.g. the Spine 32 coil, 2–3 Body 18 coils, and the Peripheral Angio 36 coil. A multi-step whole-body examination will use up to 124 channels in total (without counting overlaps). Adding a third Body 18 coil (e.g. for obese patients, positioning two Body 18 coils side by side), even 142 channels can be used for a multi-step whole-body examination.

As a third example⁹ for the different definitions for the channel count, we look at the Head/Neck 64 coil, see Figure 6.

- A. The coil alone, as a hardware entity (“box”), has 64 elements = 64 channels, 55 in the head region and nine in the C-spine/neck region.
- B. The Head/Neck 64 coil can be used in combination with the Body 18 coil and the Spine 72 coil: For the max. FOV of the scanner, the Head/Neck 64 coil, 2 x 6 channels from the Body 18 coil and 2 x 6 channels from the Spine 72 coil can be used simultaneously in one single scan, resulting in a total of 88 channels.
- C. For multi-station examinations, the Head/Neck 64 coil can be combined with various other coils, e.g. the Spine 72 coil, 2–3 Body 18 coils, and the Peripheral Angio 36 coil. A multi-step whole-body examination will use up to 208 channels in total (without counting overlaps).

All these definitions (A.–C.) for the channel count in the example above are meaningful, but they differ by a factor of close to ten. Transparency is of utmost importance when comparing coils, otherwise it will be a comparison of apples and oranges.

An even better metric would be the “**specific coil density**”, i.e. the number of channels per length of the coil (in z-direction). Examples (both for the anterior coil only):

- For the Body 18 coil, with a length of 38.5 cm, this is **4.7 channels / 10 cm**.
- For the Body 30 coil, with a length of 46 cm, this is **6.5 channels / 10 cm**.
- For the Head/Neck 20 coil, with an “electrical” length of 35 cm, this is **5.7 channels / 10 cm**.
- For the Head/Neck 64 coil, with an “electrical” length of 35 cm, this is **18.3 channels / 10 cm**.
- For the Spine 24 coil, with a length of 120 cm, this is **2.0 channels / 10 cm**.
- For the Spine 32 coil, with a length of 120 cm, this is **2.7 channels / 10 cm**.
- For the Spine 72 coil, with a length of 120 cm, this is **6.0 channels / 10 cm**.

This “specific coil density” is the most relevant measure that should be specified for a coil, being least ambiguous and clearly related to the clinical benefits of image quality and speed.

Summary

We have defined meaningful and relevant definitions for the terms “RF channels” and “coil density” that are clearly related to clinical benefits. This standard should help to achieve a better comparability of RF systems and coils across different vendors.

⁸ Example for MAGNETOM Aera and MAGNETOM Skyra with Tim [204x48]. Other systems with a different max. FOV and/or different coil portfolio may result in different numbers.

⁹ Example for MAGNETOM Vida with Tim [228x128]. Other systems with a different max. FOV and/or different coil portfolio may result in different numbers.



Contact

Mathias Blasche
Siemens Healthcare GmbH
Karl-Schall-Str. 6
91052 Erlangen
Germany
mathias.blasche@siemens-healthineers.com

Meet Siemens Healthineers

Siemens Healthineers: Our brand name embodies the pioneering spirit and engineering expertise that is unique in the healthcare industry. The people working for Siemens Healthineers are totally committed to the company they work for, and are passionate about their technology. In this section we introduce you to colleagues from all over the world – people who put their hearts into what they do.



Oxford, UK

Hannah Hale

Hannah Hale graduated with a first-class Master's degree in Natural Sciences from the University of Cambridge, UK, which included an exchange year at MIT, Boston, USA. She specialized in Physics and Materials Science.

Hannah joined Siemens initially as an intern at Siemens Magnet Technology (SMT), Eynsham, UK. She then successfully applied to become a Magnet Engineer in the R&D team after her graduation in 2009. Over the years, Hannah has worked on a variety of projects within R&D. Highlights include developing SMT's conduction cooled test facility and leading the MgB₂ program. These are both key technical milestones in achieving helium-free magnets.

How did you first come into contact with MRI?

I applied for a scholarship scheme run by Siemens Magnet Technology (SMT) with the University of Cambridge. It sounded like a fascinating area of technology that I knew relatively little about, and I thought it would provide me with two summers of interesting employment. Little was I to know that this would be the beginning of a fulfilling career in MRI and superconducting magnet technology.

What is most fascinating about MRI?

Where to start? I know relatively little about the details of the software processing involved in descrambling all the RF signals into a meaningful image, so its very 'mystery' fascinates me. Equally my own area of expertise, the superconducting magnet, provides an abundance of fascination and interest. For starters, let's begin with the counterintuitive reality of superconductivity; provided the magnet is kept cold, it will stay at field indefinitely because current flows with zero resistance.

The contrasting scales in the superconducting magnet are incredible. Such a large, heavy object works successfully only as a result of the delicate balance between components inside. For example, a coil 1 mm out of position can make the difference between a great image or a scrambled mess. Additionally, the smallest of energy

disturbances (μJ) – equivalent to dropping a drawing pin just a few centimeters from the floor – is sufficient to result in a magnet quench and loss of field. Every day I see and walk past our magnets knowing that all there is between me and temperatures akin to outer space (-269°C) are a few millimeters of stainless steel, a thin aluminum shield, and a few layers of multilayer insulation. Cool in both senses of the word!

A superconducting magnet contains a finely tuned blend of science and technology achieved through years of experience, research, and development. However, you'd be wrong to think that after ~30 years of this technology we'd be close to "understanding it all". Far from it. The final fascination is that there is still so much we don't fully understand. As we continue to push technology and process boundaries, we are learning more about the magnet at an ever-increasing rate.

What is your role in the development of MR magnets?

Today, I am a project manager leading an exciting and challenging project to bring revolutionary technology to the 3T product portfolio. I lead a cross-functional team with members from across the business, such as R&D engineers and SCM process engineers. We have to test and prove this magnet technology before managing its

subsequent introduction into production. I see my role as the central hub of this project wheel, connecting everyone and working collaboratively to make informed and timely decisions, managing risk, and steering the project to maximize output for the effort put in. Simple, right?!

What for you are the most important developments in MR magnet technology or MRI in general?

In terms of magnet hardware, the biggest development will be the journey we are currently on; relinquishing the component's dependency on liquid helium. Liquid helium is required to keep the NbTi wire in the magnet superconducting at -269°C . However, it is both an expensive and volatile resource. High-temperature superconductors will never be cheap enough for a viable MRI, so we are restricted to using the well-established low-temperature superconductor NbTi. With sophisticated designs, we are looking to reduce the need for liquid helium. In 2014 we demonstrated a prototype dry magnet which was cooled by a separate minimal volume of liquid helium. Minimal or even no helium would make MRI system installations much simpler and cheaper for the customer and come closer to the 'plug and play' utility.

As for the future developments at the system level, digitalization and artificial intelligence are really exciting avenues to explore. We need to adopt these technologies as they are going to be at the heart of the next revolution in health-care provision: A one-stop shop for the patient with a hassle-free, streamlined, accurate, and reliable experience.

If you had one month to do whatever you wanted, what would you do?

Professionally, I would like to experience different areas of the entire MR value chain to gain a holistic understanding and appreciation. It is very easy to become so focused on your specific contribution to the product value chain (in my case, superconducting magnets) that you overlook the opportunities that link and relate to the product elsewhere. For me personally, I would also like an insight into other Siemens Healthineers businesses. I believe it is important to get out of our 'silos' because combined modalities and being able to offer the customer a single solution for all their needs is the way I see the market going. It would be a great opportunity to share knowledge and learn from others in the business. A month for all of this would barely scrape the surface though.

Being active outdoors is an important part of my personal life. I would love to have a month to go on a mountain expedition somewhere. My dream would be the Patagonian mountains if money were no object, but you don't have to go far to enjoy the wilderness. I've had some great trips with my husband in the Cairngorms, Scotland. I love the physical challenge, the outdoors, and exploring. I find it refreshing and rejuvenating. Being outside in the wilderness helps to put things in perspective, and the time away from the normal day-to-day routine gives me the opportunity for personal reflection.

Kieran O'Brien

Dr Kieran O'Brien graduated with a Ph.D. in bioengineering from the University of Auckland, New Zealand, in 2009. His work there focused on developing novel flow sequences for measuring high-velocity turbulent jets. After earning his doctorate, Kieran worked as a postdoc at the Center for Biomedical Imaging in Switzerland on ultra-high-field sequence development. He then moved to Brisbane, Australia, to join Siemens Healthineers as a senior scientist in 2013.

In his current position, Kieran works in a team of five scientists who collaborate closely with Siemens Healthineers researchers in Australia and New Zealand. Specifically, he is responsible for the University of Queensland, where he is also an adjunct research fellow. As part of the ultra-high-field research team, he works on topics such as RF pulse design, parallel transmission technology, and quantitative susceptibility mapping.



Bowen Hills, Australia



How did you first come into contact with MRI?

I was first introduced to MRI during my bachelor's project with Professor Alistair Young (University of Auckland). The

project was on strain imaging of the myocardium with DENSE MRI. My introduction to MRI was predominately from this image- or data-processing angle, and it was

meant to continue into my Ph.D. – until I came to the point where I found that the data just didn't quite match the expectations. I then embarked on a process of investigating the interaction of fluid mechanics and MR physics with Professors Alistair Young and Brett Cowan (University of Auckland) and Professor Matthew Robson (University of Oxford).

What do you find most motivating about your job?

When Niels Bohr was asked once about magnetic resonance, he said: "You know what these people do is really clever. They put little spies into molecules and send radio signals to them, and then they have to radio back what they are seeing."

Yes, I am forever fascinated by how we can utilize our technology to generate the wide variety of contrasts that MRI is known for. And yes, I am motivated to tackle the current challenges that are facing the healthcare industry. But what really motivates me is those "clever people" that Niels Bohr referred to. I enjoy the interaction with my team, our academic partners, and our clinical collaborators, who all share the same passion and excitement about MRI.

What do you think are the most important developments in MRI?

Advancing MRI technology is about pushing the boundaries. Ultra-high field is once such boundary. Back in 2015, I was very privileged to be involved in the development of Siemens' clinical ultra-high-field system, MAGNETOM Terra. I was asked to port the neuro and MSK prototypes from the research systems to the clinical system. The project was immensely satisfying, and in particular was made easier by the fact that a lot of the sequence and RF pulse design work we had undertaken at ultra-high field had already found its way into other products. This "trickle-down" or "cross-pollination" of ideas and concepts is, I believe, an important philosophy behind MRI development within the community and within Siemens Healthineers. It is one of the reasons why we always need to be pushing the boundaries.

Where do you see MRI's place in the healthcare of the future?

Magnetic resonance imaging is an unbelievably versatile tool with tremendous diagnostic potential, and we continue to make it faster and simpler to use. I believe its development has been shaped by diagnosis being the conventional practice for clinical decision-making and treatment. However, with the continued integration of a patient's data from multiple sources – such as digital health records, lab tests, and genetics – and the downward pressure on health funding, I think there will be a shift toward patient prognosis in clinical decision-making and treatment. Going forward, I believe the real challenge will therefore be to develop mathematical models that integrate and interpret a patient's data, such as an MRI scan. These mathematical models will take MRI data as one of their inputs, and the data and the model will be used to predict the patient's response to a given treatment. This will enable better outcomes for the patient at a lower cost to the healthcare system.

If you could do whatever you wanted for a month, what would you do?

My two daughters love animals. Even though my eldest is only six, she has already planned her first career as a vet or a bush ranger! But she's not sure yet. So to help her out, and if I had a month off, I would love to do a safari in Africa. If there was enough time, I'd also do an Antarctic cruise. That way, I would have set foot on every continent and given my daughter an insight into her current career plans!

The entire editorial staff at Siemens Healthineers and Denis Le Bihan extend their appreciation to all the radiologists, cardiologists, radiation oncologists, technologists, physicists, experts, and scholars who donate their time and energy – without payment – in order to share their expertise with the readers of MAGNETOM Flash.

MAGNETOM Flash – Imprint

© 2018 by Siemens Healthcare GmbH,
All Rights Reserved

Publisher:

Siemens Healthcare GmbH

Magnetic Resonance,
Karl-Schall-Str. 6, D-91052 Erlangen, Germany

Editor-in-chief:

Antje Hellwich
(antje.hellwich@siemens-healthineers.com)

Guest editor:

Denis Le Bihan, M.D., Ph.D.
NeuroSpin, Saclay, France

Editorial Board:

Renate Jerecic, Ph.D.; Wellesley Were;
Gary R. McNeal, MS (BME)

Review Board:

Daniel Fischer; Christian Geppert, Ph.D.;
Berthold Kiefer, Ph.D.; Heiko Meyer, Ph.D.;
Efrén Ojeda; Gregor Thörmer, Ph.D.

Copy Editing:

Sheila Regan, Jen Metcalf, UNIWORKS,
www.uni-works.org
(with special thanks to Kylie Martin)

Layout:

Agentur Baumgärtner,
Friedrichstr. 4, D-90762 Fürth, Germany

Production:

Norbert Moser,
Siemens Healthcare GmbH

Printer:

G. Peschke Druckerei GmbH,
Taxetstr. 4, D-85599 Parsdorf b. Munich, Germany

Note in accordance with § 33 Para.1 of the German Federal Data Protection Law: Despatch is made using an address file which is maintained with the aid of an automated data processing system.

MAGNETOM Flash is sent free of charge to Siemens Healthineers MR customers, qualified physicians, technologists, physicists and radiology departments throughout the world. It includes reports in the English language on magnetic resonance: diagnostic and therapeutic methods and their application as well as results and experience gained with corresponding systems and solutions. It introduces from case to case new principles and procedures and discusses their clinical potential. The statements and views of the authors in the individual contributions do not necessarily reflect the opinion of the publisher.

The information presented in these articles and case reports is for illustration only and is not intended to be relied upon by the reader for instruction as to the practice of medicine. Any health care practitioner reading this information is reminded that they must use their own learning, training and expertise in dealing with their individual patients. This material does not substitute for that duty and is not intended by Siemens Healthcare to be used for any purpose in that regard. The drugs and doses mentioned herein are consistent with the approval labeling for uses and/or indications of the drug. The treating physician bears the sole responsibility for the diagnosis and treatment of patients, including drugs and doses prescribed in connection with such use. The Operating Instructions must always be strictly followed when operating the MR system. The sources for the technical data are the corresponding data sheets. Results may vary.

Partial reproduction in printed form of individual contributions is permitted, provided the customary bibliographical data such as author's name and title of the contribution as well as year, issue number and pages of MAGNETOM Flash are named, but the editors request that two copies be sent to them. The written consent of the authors and publisher is required for the complete reprinting of an article.

We welcome your questions and comments about the editorial content of MAGNETOM Flash. Please contact us at
magnetomworld.team@siemens-healthineers.com

Manuscripts as well as suggestions, proposals and information are always welcome; they are carefully examined and submitted to the editorial board for attention. MAGNETOM Flash is not responsible for loss, damage, or any other injury to unsolicited manuscripts or other materials. We reserve the right to edit for clarity, accuracy, and space. Include your name, address, and phone number and send to the editors, address above.

MAGNETOM Flash is also available online:

www.siemens.com/magnetom-world

Not for distribution in the US

On account of certain regional limitations of sales rights and service availability, we cannot guarantee that all products included in this brochure are available through the Siemens sales organization worldwide. Availability and packaging may vary by country and is subject to change without prior notice. Some/All of the features and products described herein may not be available in the United States.

The information in this document contains general technical descriptions of specifications and options as well as standard and optional features which do not always have to be present in individual cases, and which may not be commercially available

in all countries. Due to regulatory reasons their future availability cannot be guaranteed. Please contact your local Siemens organization for further details.

Siemens reserves the right to modify the design, packaging, specifications, and options described herein without prior notice. Please contact your local Siemens sales representative for the most current information.

Note: Any technical data contained in this document may vary within defined tolerances. Original images always lose a certain amount of detail when reproduced.

.....
Siemens Healthineers Headquarters

Siemens Healthcare GmbH

Henkestr. 127

91052 Erlangen

Germany

Phone: +49 913184-0

siemens-healthineers.com